

# Atomic layer deposition and characterization of metal oxide thin films

Von der Fakultät 1 - MINT - Mathematik, Informatik, Physik,  
Elektro- und Informationstechnik  
der Brandenburgischen Technischen Universität Cottbus–Senftenberg  
genehmigte Dissertation  
zur Erlangung des akademischen Grades eines

Dr. rer. nat.

vorgelegt von

Ali Mahmoodinezhad

geboren am 15. Januar 1989 in Mumbai (Indien)

Vorsitzende/r: Prof. Dr. rer. nat. habil. Götz Seibold

Gutachter/in: Prof. Dr. rer. nat. habil. Jan Ingo Flege

Gutachter/in: Prof. Dr. rer. nat. habil. Joachim Wollschläger

Gutachter/in: Prof. Dr. rer. nat. habil. Christian Wenger

Tag der mündlichen Prüfung: 27. Oktober 2022



*To my family and friends*

*“for all the love that I have been privileged to get from you”*

*“for all the guidance, encouragement and support throughout my life”*





## ACKNOWLEDGEMENTS

This research project was carried out in the Chair of Applied Physics and Semiconductor Spectroscopy at the Brandenburg University of Technology Cottbus – Senftenburg during 2018 to 2022. Within these years, I have gained extensive knowledge and comprehensive research experiences. Besides, it was my pleasure to work closely with a scientific community and a huge number of researchers to whom I would very like to convey my profound gratitude for all supports.

May I take this opportunity to appreciate those academic members in the past and present for accompanying me in this scientific journey, particularly Prof. Dieter Schmeißer for introducing me to the ALD community, my supervisor Prof. Jan Ingo Flege for conducting me throughout the PhD course which lead to the completion of this doctoral thesis.

I am also grateful to my advisor Dr. Carlos Morales, co-workers Dr. Christoph Janowitz, Dr. Małgorzata Kot and Dr. Karsten Henkel for providing valuable comments and Mr. Guido Buckert for all-around technical support.

Furthermore, I wish to express kind regards to my co-authors Dr. Hassan Gargouri, Dr. Paul Plate, Mrs. Franziska Naumann, Mrs. Johanna Reck, Mr. Bernd Gruska, Mr. Adrian Blümich and Dr. Robert Meyer in the ALD group of SENTECH GmbH (Berlin) for their contribution and scientific discussion, especially forming the basis of this work.

Special thanks to prof. Christian Wenger and Dr. Marvin Zöllner from IHP GmbH (Frankfurt Oder) for XRD/GIXRD measurements and their valuable scientific discussion.

I would like to thank Prof. Iva Matolínová and Mr. Peter Kus from nanomaterials group at Charles University (Prague) for performing FESEM/EDX measurements and their support.

My acknowledgment also goes to those people in the group of Dr. David Starr and Dr. Marco Favaro for their valuable supervision and assistance to perform NAP-HAXPES experiments at SpAnTex end-station of BESSY II synchrotron (Berlin).

Nevertheless, I would like to thank all the colleagues and friends for providing great atmosphere over these years.

I kindly acknowledge the Graduate Research School (GRS) of the Brandenburg University of Technology (BTU) Cottbus – Senftenburg for funding this project within the Cluster “*Functional Materials and Film Systems for Efficient Energy Conversion (FuSion)*.”

Ali Mahmoodinezhad

July 2022

Cottbus, Germany

## ABSTRACT

This thesis describes low temperature growth of wide band gap metal oxide thin films deposited by thermal (T-) and plasma-enhanced (PE-) atomic layer deposition (ALD) techniques in which high quality materials are grown with atomic level precision.

Metal oxides are extensively investigated due to their exceptional physical and chemical properties, including relatively wide band gap, high dielectric constant and high thermal stability. This variety of properties results in a wide range of different applications. Thin films of indium oxide ( $\text{InO}_x$ ), gallium oxide ( $\text{GaO}_x$ ), zinc oxide ( $\text{ZnO}_x$ ), and quaternary  $\text{InO}_x/\text{GaO}_x/\text{ZnO}_x$  (IGZO), in addition to the well-known aluminum oxide ( $\text{AlO}_x$ ), and the catalyst cerium oxide ( $\text{CeO}_x$ ), have proven to be superior candidates for many applications; from microelectronics and optoelectronics to gas sensor devices. The demanding requirements of low-temperature deposition processes for thermal sensitive substrates, which include high layer homogeneity and conformality over large areas, makes ALD a pioneer deposition technique. Although many oxides have been grown by TALD and PEALD, the deposition of wide band gap oxides at low temperatures are rarely reported and/or being investigated.

In this work, the deposition method of the individual binary oxide films and combining the respective binary processes into the developed super-cycle growth of quaternary compound have been investigated at relatively low-temperatures by TALD and PEALD. Besides, the growth characteristics and chemical properties of the deposited films were evaluated by *in-situ* and *ex-situ* characterization techniques such as spectroscopic ellipsometry (SE) and X-ray photoelectron spectroscopy (XPS), where the influence of ALD process parameters on the growth mechanism and films composition are discussed in detail for any potential applications.

*Keywords:* Thermal atomic layer deposition, Plasma-enhanced atomic layer deposition, Indium oxide, Gallium oxide, Zinc oxide, Indium-gallium-zinc oxide, Aluminum oxide, Cerium oxide.



# ZUSAMMENFASSUNG

Diese Dissertation beschreibt das Tieftemperaturwachstum von Metalloxid-Dünnschichten mit breiter Bandlücke, die durch thermische (T-) und plasmaunterstützte (PE-) Atomlagenabscheidungstechniken (ALD) abgeschieden werden, bei denen hochwertige Materialien mit atomarer Präzision aufgewachsen werden.

Metalloxide werden aufgrund ihrer außergewöhnlichen physikalischen und chemischen Eigenschaften, einschließlich einer relativ großen Bandlücke, einer hohen Dielektrizitätskonstante und einer hohen thermischen Stabilität, ausführlich untersucht. Aus dieser Vielfalt an Eigenschaften ergibt sich ein breites Spektrum an unterschiedlichen Anwendungen. Dünnschichten aus Indiumoxid ( $\text{InO}_x$ ), Galliumoxid ( $\text{GaO}_x$ ), Zinkoxid ( $\text{ZnO}_x$ ) und quaternärem  $\text{InO}_x/\text{GaO}_x/\text{ZnO}_x$  (IGZO), zusätzlich zu dem wohlbekannten Aluminiumoxid ( $\text{AlO}_x$ ) und dem Katalysator Ceroxid ( $\text{CeO}_x$ ), haben sich für viele Anwendungen als ausgezeichnete Kandidaten erwiesen; von der Mikroelektronik und Optoelektronik bis hin zu Gassensoren. Die anspruchsvollen Anforderungen von Niedertemperatur-Abscheidungsprozessen für thermisch empfindliche Substrate, zu denen eine hohe Schichthomogenität und -konformität über große Flächen gehören, machen ALD zu einer bahnbrechenden Abscheidungstechnik. Obwohl viele Oxide durch TALD und PEALD gezüchtet wurden, wird die Abscheidung von Oxiden mit breiter Bandlücke bei niedrigen Temperaturen selten berichtet oder untersucht.

In dieser Arbeit wurden das Abscheidungsverfahren der einzelnen binären Oxidschichten und die Kombination der jeweiligen binären Prozesse zu dem entwickelten Superzyklus-Wachstum der quaternären Verbindung bei relativ niedrigen Temperaturen durch TALD und PEALD untersucht. Außerdem wurden die Wachstumseigenschaften und chemischen Eigenschaften der abgeschiedenen Schichten durch *In-situ*- und *Ex-situ*-Charakterisierungstechniken wie spektroskopische Ellipsometrie (SE) und Röntgen-Photoelektronenspektroskopie (XPS) bewertet. Dabei wurde der Einfluss von ALD-Prozessparametern auf den Wachstumsmechanismus und der Schichtzusammensetzung im Detail für mögliche Anwendungen diskutiert.

*Schlüsselwörter:* Thermische Atomlagenabscheidung, Plasmaunterstützte Atomlagenabscheidung, Indiumoxid, Galliumoxid, Zinkoxid, Indium-Gallium-Zinkoxid, Aluminiumoxid, Ceroxid.



# TABLE OF CONTENTS

<b>ACKNOWLEDGEMENTS</b> .....	<b>i</b>
<b>ABSTRACT</b> .....	<b>iii</b>
<b>ZUSAMMENFASSUNG</b> .....	<b>v</b>
<b>TABLE OF CONTENTS</b> .....	<b>vii</b>
<b>1. INTRODUCTION</b> .....	<b>11</b>
Motivation, objective and structure of this PhD thesis.....	11
<b>2. BACKGROUND AND STATE OF THE ART</b> .....	<b>14</b>
2.1 Wide band gap metal oxide thin films and their applications .....	14
2.1.1 Indium oxide ( $\text{InO}_x$ ).....	16
2.1.2 Gallium oxide ( $\text{GaO}_x$ ).....	17
2.1.3 Zinc oxide ( $\text{ZnO}_x$ ).....	17
2.1.4 Indium-gallium-zinc oxide (IGZO) .....	18
2.1.5 Aluminum oxide (Alumina; $\text{AlO}_x$ ) .....	18
2.1.6 Cerium oxide (Ceria; $\text{CeO}_x$ ) .....	18
2.2 Atomic layer deposition (ALD) .....	19
2.2.1 History .....	20
2.2.2 ALD process .....	22
2.2.3 Deposited materials.....	24
2.2.4 Precursors and co-reactants .....	25
2.2.5 Chemical and physical mechanisms .....	26
2.2.6 ALD window .....	29
2.2.7 Growth modes, nucleation and nucleation delay .....	30
2.2.8 Advantages and disadvantages .....	32
2.2.9 ALD systems.....	33
2.2.9.1 Thermal atomic layer deposition (TALD).....	34
2.2.9.2 Plasma-enhanced ALD (PEALD).....	34
<b>3. EXPERIMENTAL</b> .....	<b>38</b>

---

3.1 Characterization methods .....	38
3.1.1 Spectroscopic ellipsometry (SE) .....	38
3.1.1.1 Principles and operation .....	38
3.1.2 X-ray photoelectron spectroscopy (XPS).....	41
3.1.2.1 Principles and operation .....	41
3.1.2.2 Photoemission peak analysis and fitting .....	45
3.1.3 Field-emission scanning electron microscopy (FE-SEM) .....	51
3.1.4 Near-ambient pressure hard X-ray photoelectron spectroscopy (NAP-HAXPES).....	52
3.2 ALD system .....	53
3.2.1 Commercial SENTECH ALD system.....	54
3.2.2 Homemade BTU ALD system .....	55
3.3 Thin films deposition .....	59
3.3.1 Growth of metal oxides by SENTECH ALD reactor.....	59
3.3.1.1 InO <sub>x</sub> deposition using PEALD .....	59
3.3.1.2 GaO <sub>x</sub> deposition using PEALD .....	60
3.3.1.3 ZnO <sub>x</sub> deposition using TALD .....	62
3.3.1.4 ZnO <sub>x</sub> deposition using PEALD .....	63
3.3.1.5 IGZO deposition using PEALD .....	64
3.3.2 Homemade BTU ALD reactor .....	66
3.3.2.1 AlO <sub>x</sub> deposition using TALD.....	66
3.3.2.1.1 Ti growth .....	66
3.3.2.1.2 AlO <sub>x</sub> growth at room temperature .....	68
3.3.2.1.3 AlO <sub>x</sub> growth at 200 °C .....	68
3.3.2.2 CeO <sub>x</sub> deposition using TALD .....	70
<b>4. RESULTS AND DISCUSSION .....</b>	<b>75</b>
4.1 PEALD of InO <sub>x</sub> thin films .....	75
4.1.1 Growth and optical characteristics .....	75
4.1.2 <i>Ex-situ</i> XPS study.....	80
4.2 PEALD of GaO <sub>x</sub> thin films .....	87



---

4.2.1 Growth and optical characteristics.....	87
4.2.2 <i>Ex-situ</i> XPS study.....	89
4.3 TALD of ZnO <sub>x</sub> thin films.....	97
4.3.1 Growth and optical characteristics.....	97
4.3.2 <i>Ex-situ</i> XPS study.....	99
4.4 Bottom-up establishment of IGZO thin films.....	106
4.4.1 Growth characteristics.....	106
4.4.2 <i>Ex-situ</i> XPS study.....	109
4.4.3 <i>Ex-situ</i> structural and morphological study.....	118
4.5 TALD of AlO <sub>x</sub> on Ti-coated Si (100).....	120
4.5.1 Deposited at room temperature and 200 °C.....	120
4.5.1.1 Growth mechanism.....	120
4.5.1.2 <i>In-situ</i> XPS study.....	121
4.5.1.2.1 Oxidation of Ti by H <sub>2</sub> O exposure.....	121
4.5.1.2.2 Overview of the complete cycles.....	123
4.5.1.2.3 Qualitative analysis.....	128
4.5.1.3 <i>In-situ</i> XPS of post-deposition annealing (PDA).....	137
4.6 TALD of CeO <sub>x</sub> on SiO <sub>x</sub> and AlO <sub>x</sub> /Si (100).....	140
4.6.1 <i>In-situ</i> XPS study of ALD Ceria growth.....	140
4.6.2 Reactivity of ALD-CeO <sub>x</sub> layers.....	142
<b>5. CONCLUSIONS AND OUTLOOK.....</b>	<b>145</b>
5.1 Summary and conclusions.....	145
5.2 Future works.....	151
<b>APPENDIX.....</b>	<b>153</b>
I. List of publications.....	153
II. List of tables.....	155
III. List of figures.....	157
IV. List of abbreviations and acronyms.....	164
<b>REFERENCES.....</b>	<b>168</b>



## Chapter 1

# INTRODUCTION

### **Motivation, objective and structure of this PhD thesis**

The microelectronic devices are continuously shrinking to the nanometer scale in order to rise the number of thin film transistors (TFTs) per unit of area, and thus increasing the power while reducing costs. At the same time, thin film deposition technology is pushed toward high conformal and homogeneous layers over large areas, while there is an effort to reduce the thermal budget of the fabrication process. Besides, retaining films properties when increasing the number of stacked layers, plays an important role in manufacturing high aspect ratio of three-dimensional nanostructures for the integrated circuit (IC) industry. One of challenges in scaling down the electronic devices is to overcome the leakage current which impacts product efficiency and performance. Therefore, the use of high-k gate dielectric material would improve and/or solve such deficiency.

Nowadays, thin films of oxide-based materials have been extensively studied due to their wide variety of excellent optical and electrical properties. For example, transparent conductive oxides (TCO) show high transparency in the visible range and high charge mobility at relatively low substrate temperatures. Therefore, to comply with such properties, an accurate modification of fabrication parameters is essential and directly influences the capability of deposited films for a variety of applications, i.e. high-k gate dielectric in electronics and particularly in the optoelectronics areas.

To meet these requirements, atomic layer deposition (ALD) is an exceptional technique in which layer-by-layer growth is achieved by successive self-limiting reactions that might facilitate deposition at low temperatures ( $< 200$  °C)<sup>(1)</sup> and deliver high-quality thin films. Considering these features, ALD has become a promising technique in producing ultra-high density storage devices and

ultra-high resolution display panels.<sup>(2)</sup> Moreover, plasma-enhanced ALD (PEALD) can improve the growth rate by increasing the chemical reactions on the surface even at lower temperatures, which is particularly necessary for thermally sensitive substrates.<sup>(3)</sup> For many years, ALD has proven to be a superior deposition technique for producing high-quality metal oxide thin films where metal precursors and oxidants meet each other in a controlled cyclic process to form a layer-by-layer growth mechanism.

The represented study discusses in detail the functionality of thermal and plasma phases of ALD on the promising comprehensive wide band gap oxide materials along with their optical and spectroscopic characterizations to develop new semiconductor-based devices. For this purpose, a low-temperature full-PEALD super-cycle process of the complex IGZO films was established after intensive investigation of the corresponding individual binary oxides of  $\text{InO}_x$ ,  $\text{GaO}_x$ , and  $\text{ZnO}_x$  (in collaboration with the industry partner SENTECH Instruments GmbH). In addition, the reconfiguration of the homemade *in-situ* ALD (attached to the XPS system) was fulfilled with the capability to operate in two modes: pump- and flow-modes. Both configurations were tested and/or evaluated by deposition of two oxide-based materials (common  $\text{AlO}_x$  and catalyst  $\text{CeO}_x$ ).

This dissertation is organized into five chapters. Current **chapter one** represents the motivation and thesis configuration. **Chapter two** introduces promising metal oxide thin films and their applications, continuing with the discussion of different aspects of the ALD growth mechanisms, where a careful approach is required to obtain high-quality thin films. Subsequently, **chapter three** displays the employed materials and methods to reveal an efficient deposition of oxide-based materials. Accordingly, the characterization techniques used to evaluate the optical and chemical properties of deposited films are introduced. In **chapter four**, the analyzed data are profoundly discussed and compared with literature to indicate the advantages and potential issues of the deposited films. **Chapter five** summarizes all obtained results and discusses its potential applications. Besides, considering that the presented research is not an endpoint, an **outlook** will draw several potential research paths from which the scientific work could be extended. The provided **appendix section** lists the scientific contributions from a bilateral research collaboration with the industry, in addition to the utilized tables, figures, and abbreviations. Finally, the **reference** section reveals the cited literature and/or works in this thesis.



## Chapter 2

# BACKGROUND AND STATE OF THE ART

### 2.1 Wide band gap metal oxide thin films and their applications

Metal oxides are an important class of materials that exhibit a wide range of properties from research and technological perspectives. Oxide-based materials can potentially pave the way for current scientific challenges in fabricating low energy consumption devices and high-efficient renewable energy sources. Furthermore, thin films of metal oxides play a crucial role due to their relevance in micro/nanostructures and their ability to passivate the layers or act as buffer layers. Oxide-based semiconductors have attracted much attention as new promising materials that may replace their semiconducting counterparts, such as silicon and gallium arsenide (GaAs), to remove some obstacles in the fabrication process, i.e. diffusion of silicon into the deposited layer.<sup>(4)</sup> In fact, oxides have more freedom and can be tuned in terms of the properties at the molecular level that might lead to unusual functionalities. Nowadays, development and breakthrough in thin film deposition are sensible, particularly for the growth of complex metal oxide-based multilayers. Their prominent properties include a high dielectric constant, reactive electronic transition, and good electrical, optical, and electrochromic characteristics.<sup>(5-11)</sup> To date, a wide range of applications have been reported for metal oxides in the fields of optoelectronics<sup>(12)</sup>, sensors<sup>(13)</sup>, piezoelectric<sup>(14)</sup>, catalysts<sup>(15)</sup> and solar cells<sup>(16)</sup> because of their distinct properties as well as their superior chemical and thermal stability<sup>(17, 18)</sup>. Moreover, they are fundamentally important as heterogeneous industrial catalysts either as stand-alone catalysts (e.g., molybdenum trioxide for methane conversion to formaldehyde)<sup>(19)</sup> or in combination with other oxides and/or metals (e.g., ceria-based catalysts for auto-exhaust treatment)<sup>(20)</sup>. In fact, the nature of the oxide

influences the catalytic properties. For instance, the defects concentration<sup>(21, 22)</sup>, the oxide morphology<sup>(22, 23)</sup>, the dopants<sup>(24)</sup>, and the effects of surface polarization<sup>(25, 26)</sup> have all been found to impact catalysis directly. Furthermore, thin oxide films can be used as supports for metals in catalysis, suggesting prominent advantages in comparison with their bulk counterparts due to the strong metal-oxide interaction. In principle, oxide thin films on metal substrates can allow charge transfer between metal catalysts and the buried metal/oxide interfaces.<sup>(27, 28)</sup>

In recent years, transparent conducting oxides (TCOs) have proven to be a brilliant class of materials because of their superior optical and electrical properties.<sup>(29)</sup> Such oxides arise from the unique mixture of high transparency and electrical conductivity. Materials with low electrical resistivity ( $10^{-4}$  -  $10^{-7}$ ), such as metals, are not typically able to transmit visible light, whereas most transparent materials, such as glass, pose high electrical resistivity ( $>10^{10}$   $\Omega\cdot\text{cm}$ ) being electrical insulators. Therefore, a single material with a mixture of both mentioned properties is highly demanding for developing transparent optoelectronic devices.<sup>(30, 31)</sup> In principle, TCOs materials can be classified into two different groups, with *wide band gap* and *narrow band gap* (as shown in Fig. 2.1)<sup>(32)</sup>.

*Wide band gap TCOs* such as  $\text{InO}_x$ <sup>(33)</sup>,  $\text{GaO}_x$ <sup>(34)</sup>, and  $\text{ZnO}_x$ <sup>(35)</sup>, are transparent to visible light due to posing relatively large band gaps ( $> 3\text{eV}$ ). By doping these materials, mobility and carrier concentrations can be modified, altering their electrical conductivity.<sup>(36)</sup> On the contrary, *narrow band gap TCOs* such as cadmium oxide ( $\text{CdO}$ ) are not transparent to visible light owing to relatively low band gaps ( $< 1\text{eV}$ ).<sup>(37)</sup> However, a blue shift of their band gap ( $E_{opt}$ ) can be induced by doping, which triggers optical transparency (as indicated in Fig. 2.1). Such phenomenon is known as the Moss-Burstein effect.<sup>(38)</sup>

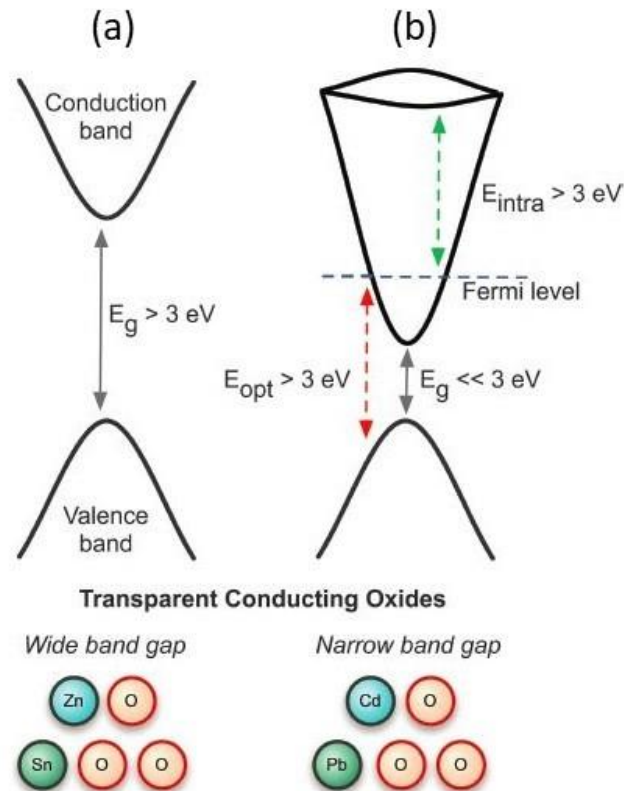


Figure 2.1. Schematic demonstration of different types of TCOs; Wide band gap (a), and narrow band gap (b) in which Fermi level denotes electron chemical potential for highly doped n-type materials.<sup>(32)</sup>

In this research project, a promising class of binary metal oxide materials ( $\text{InO}_x$ ,  $\text{GaO}_x$ ,  $\text{ZnO}_x$ ) has been investigated for subsequent deposition of the quaternary IGZO films at low temperature by ALD, probing, in addition, their promising properties for a wide range of applications from optoelectronic to photovoltaic devices. Besides, the deposition of other two metal oxide materials ( $\text{AlO}_x$  and  $\text{CeO}_x$ ) was also considered using our homemade *in-situ* ALD system, where the chemical properties of the prepared layers were *in-situ* studied by XPS for any potential applications, especially in the field of gas sensors.

### 2.1.1 Indium oxide ( $\text{InO}_x$ )

Indium oxide is a transparent conducting oxide (TCO) material that is being intensively investigated due to its good material properties, including a direct and an indirect band gaps of about 3.7 and 2.6 eV, correspondingly<sup>(39, 40)</sup>, high optical transparency in the visible range<sup>(41)</sup>, excellent electrical properties<sup>(42)</sup>,



and good chemical stability<sup>(43)</sup>. Based on these properties, In<sub>2</sub>O<sub>3</sub> has been used for numerous applications such as gas sensors<sup>(44)</sup>, optical and antistatic coatings<sup>(45, 46)</sup>, catalysts<sup>(47)</sup>, heat mirrors<sup>(48)</sup>, and electrochromic devices<sup>(49)</sup>. The electronic structure of In<sub>2</sub>O<sub>3</sub> single crystals has been comprehensively examined in several studies.<sup>(50, 51)</sup> Apart from the use of single crystals, thin In<sub>2</sub>O<sub>3</sub> films with high transparency and low electrical resistivity ( $\sim 10^{-5} \Omega \cdot \text{cm}$ )<sup>(52)</sup> are demanded due to their application in thin-film transistors<sup>(53)</sup>, organic light-emitting diodes<sup>(54)</sup>, and photovoltaics<sup>(55)</sup>.

### 2.1.2 Gallium oxide (GaO<sub>x</sub>)

Among the oxide dielectrics, gallium oxide has gained tremendous interest in recent years due to its excellent materials properties, including a wide band gap ( $\sim 5 \text{ eV}$ )<sup>(56)</sup>, a high dielectric constant<sup>(57)</sup>, a high breakdown electric field<sup>(58)</sup>, and high thermodynamic stability<sup>(59)</sup>. Thin films of Ga<sub>2</sub>O<sub>3</sub> are nowadays widely used in numerous applications, including high power and high voltage field-effect transistors<sup>(60)</sup>, photovoltaics<sup>(61)</sup>, spintronics<sup>(62)</sup>, gate dielectric, and passivation layers in III–V semiconductor-based devices to reduce the leakage current<sup>(63–65)</sup>. Owing to the possibility of controlling the electrical conductivity between insulating and semiconducting (typically n-type) behavior, and because of its high optical transparency ( $\sim 80\%$ ), gallium oxide is a promising candidate for transparent conducting oxides and thin-film transistors<sup>(66)</sup>. In addition, Ga<sub>2</sub>O<sub>3</sub> exhibits gas-dependent conducting behavior at elevated temperatures, making it one of the most suitable materials for gas sensing<sup>(67)</sup>.

### 2.1.3 Zinc oxide (ZnO<sub>x</sub>)

Zinc oxide (ZnO) has been extensively used as a transparent conducting oxide (TCO) in electronic and optoelectronic devices due to a wide band gap ( $\sim 3.3 \text{ eV}$ )<sup>(68, 69)</sup>, high electron concentration ( $> 10^{19} \text{ cm}^{-3}$ )<sup>(70)</sup>, relatively high ultraviolet (UV) emission arising from a large exciton binding energy of 60 meV<sup>(71)</sup>, high thermal stability and high dielectric constant<sup>(72)</sup>. Recent progress in processing ZnO material has paved the way for many applications in the fields of gas sensors<sup>(73)</sup>, surface acoustic wave (SAW) devices<sup>(74)</sup>, solar cell panels<sup>(75)</sup>, transparent conductors<sup>(76)</sup>, ferroelectric memories<sup>(77)</sup>, and organic light-emitting diodes<sup>(78)</sup>. ZnO is a promising alternative candidate for the indium tin oxide (ITO) of TCO materials due to its non-toxicity, availability, and posing optical and electrical properties comparable with those of the ITO features.<sup>(79, 80)</sup>

### 2.1.4 Indium-gallium-zinc oxide (IGZO)

In recent years, the quaternary oxide semiconductor indium-gallium-zinc oxide has attracted much attention due to its high optical transparency and electron mobility<sup>(81)</sup>, low leakage current<sup>(82)</sup>, and low fabrication costs<sup>(83)</sup>. These properties make IGZO a promising candidate to be utilized in TFTs for the next generation of ultrahigh-resolution organic light-emitting diode displays and flexible electronic devices.<sup>(84)</sup>

To date, several techniques have been reported to deposit binary and quaternary oxides materials, including pulsed laser deposition (PLD)<sup>(81)</sup>, radio-frequency (RF) magnetron sputtering<sup>(85)</sup>, solution processing<sup>(86)</sup>, chemical vapor deposition (CVD)<sup>(87)</sup>, and ALD<sup>(88-92)</sup> where the film quality and thus its optoelectronic properties are highly dependent on the used growth method. For example, in PLD and RF magnetron sputtering, the composition and layers thickness are difficult to control and, in addition, high-energy plasma species can damage the films and lead to the formation of interfacial defects during the deposition. Moreover, inexpensive production methods based on solution-processing are challenging to scale as well as it is very hard to optimize the properties of the films produced by these methods in a controlled way. However, metal oxide TFTs fabricated by ALD showed an excellent performance with accurate thickness controllability and highly conformal deposition.<sup>(93)</sup>

### 2.1.5 Aluminum oxide (Alumina; AlO<sub>x</sub>)

Aluminum oxide is an electrical insulator with excellent features like a high dielectric constant ( $\sim 9$ )<sup>(94)</sup>, and a relatively high thermal conductivity ( $30 \text{ W/m}^{-1}\text{K}^{-1}$ ).<sup>(95)</sup> The breakdown field for the bulk Al<sub>2</sub>O<sub>3</sub> has been reported to be  $10 \text{ MVcm}^{-1}$  increasing to  $30 \text{ MVcm}^{-1}$  for thin films.<sup>(96)</sup> ALD-prepared Al<sub>2</sub>O<sub>3</sub> has a wide band gap value of 6.7 eV, which has been documented in the literature.<sup>(97)</sup> Furthermore, thin films of Al<sub>2</sub>O<sub>3</sub> in combination with other TCOs have widened the field of applications; they have been widely investigated for optical and electronic applications such as gas diffusion barriers, interfacial buffering for high-k dielectrics, dynamic random-access memory capacitors, metal-oxide-semiconductor field-effect transistors, nanolaminates, surface passivation of photovoltaic devices and even porous silicon nanostructures.<sup>(98)</sup>

### 2.1.6 Cerium oxide (Ceria; CeO<sub>x</sub>)

Among metal-oxide semiconductors, ceria is a promising candidate for modifying the carrier concentrations based on the dual-oxidation states of the

metal cerium ( $\text{Ce}^{3+}$ ,  $\text{Ce}^{4+}$ ) when exposed to different ambient conditions (temperature and pressure) as well as the chemical environment.<sup>(99)</sup> To date, cerium oxide has been applied for a variety of applications such as catalytic converters<sup>(100)</sup>, high  $k$ -dielectric materials<sup>(101)</sup>, and as oxygen sensors<sup>(102)</sup> due to many attractive properties, including high relative permittivity<sup>(103)</sup>, durability, high refractive index as well as high transparency in the visible and near-infrared regions<sup>(104, 105)</sup>. It has also been reported that  $\text{CeO}_x$  can be used as a buffer layer (in order to avoid/suppress the chemical reactions at the layer/substrate interface) for high-temperature superconductors and ferroelectric materials.<sup>(106, 107)</sup> Moreover, ceria can be utilized as a compatible intermediate material for multilayer structures.<sup>(108)</sup>

## 2.2 Atomic layer deposition (ALD)

ALD is an exceptional growth technique capable of depositing a variety of thin film materials from the vapor phase. ALD has proven to be a promising technique in semiconductor processing and energy conversion technologies. Concerning the miniaturization and more demanding of complex materials structure in the semiconductor industry, leading to the requirement for atomic-level control of thin film growth, ALD has illustrated potential advantages over other deposition techniques such as chemical vapor deposition (CVD) and various physical vapor deposition (PVD) methods. Scaling down thickness to the order of nanometers has brought very high aspect structures that need to be deposited conformally (also called step coverage) with accurate control over growth mechanism following thickness and composition. To date, no alternative growth techniques could meet the high conformity and layer homogeneity (uniformity) achieved by ALD on high aspect complex structures. Moreover, the deposition of pinhole-free films in semiconductor-based devices has also put the focus on the ALD technique for applications in low leakage current of magnetic read/write heads<sup>(109)</sup> and diffusion barrier coatings with low gas permeability.<sup>(110)</sup> All mentioned unique characteristics of ALD process originate from a cyclic self-saturation of surface reactions that provides a layer-by-layer growth mechanism.

Therefore, ALD is definitely part of the semiconductor technology roadmap because of its ability to control growth at the atomic level in conformal deposits on very high aspect ratio structures. Figure 2.2 schematically displays the prominent features of ALD.

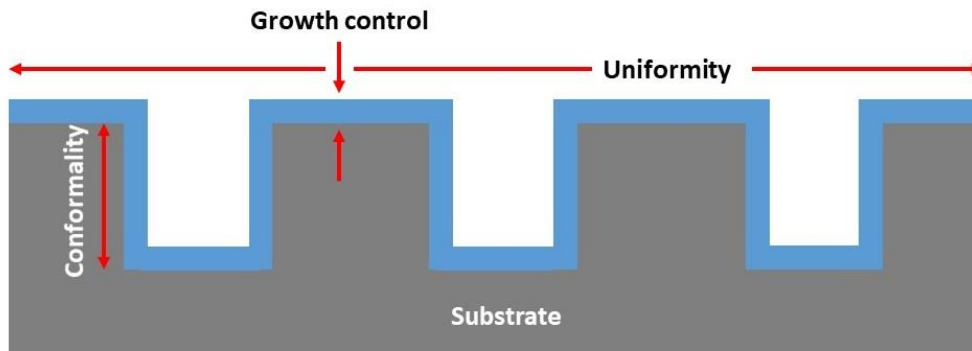


Figure 2.2. Representation of ALD unique features: precise thickness control, high conformity/step coverage and, good uniformity over large substrates.

### 2.2.1 History

The history of ALD dates back to the 1970s in Finland. ALD was initially introduced as atomic layer epitaxy (ALE) by Suntola and Antson in 1974 who developed and deposited ZnS for flat panel displays in 1977.<sup>(111)</sup> The first report on ALE process published in 1980 documents ALE application in electroluminescent displays.<sup>(112)</sup> Such displays made by ALE were publicly demonstrated in the Helsinki airport for the period from 1983 to 1998. The first commercial manufactured ALE reactor was the F-120 (Microchemistry, 1988), taking place two years after the first ALE meetings. With further developing ALE processes, many materials, metals and metal oxides were deposited nonepitaxially, hence, the more general name of ALD was adopted to refer this.<sup>(113)</sup> Nowadays, ALE is more addressed for atomic layer etching. Table 2.1 lists the used common names to refer ALD.<sup>(114)</sup>

Table 2.1. Different names of ALD.

Name	Abbreviation
Atomic layer epitaxy	ALE
Atomic layer evaporation	ALE
Atomic layer deposition	ALD
Atomic layer chemical vapor deposition	ALCVD
Atomic layer growth	ALG
Digital layer epitaxy	DLE
Molecular layer epitaxy	MLE
Molecular layering	ML
Molecular stratification	-
Molecular lamination	-
Molecular deposition	-
Chemical assembly	-

ALD has been widely introduced in a series of meetings from early 2001 and has continued through the present date as a promising deposition technique. It should be taken into account that many ALD procedures were developed from a variety of CVD processes. However, contrary to CVD, and as explained in detail in the next section, the ALD benefits from alternating chemical precursors to react with the surface in the frame of self-limiting mechanism to form the desired monolayer of material at a low-thermal budget.<sup>(115)</sup> There are several papers on the basics and applications of ALD in microelectronics and nanotechnology.<sup>(116-121)</sup>

Regarding the International Technology Roadmap for Semiconductors (ITRS), ALD is a pioneer growth technique for high dielectric gate oxides in the metal oxide semiconductor field-effect transistor (MOSFET) structure for copper diffusion barriers in backend interconnects.<sup>(122)</sup> Figure 2.3 exhibits miniaturization and requirements to control better and better the lower thickness for semiconductor technology processing by 2025.<sup>(123)</sup>

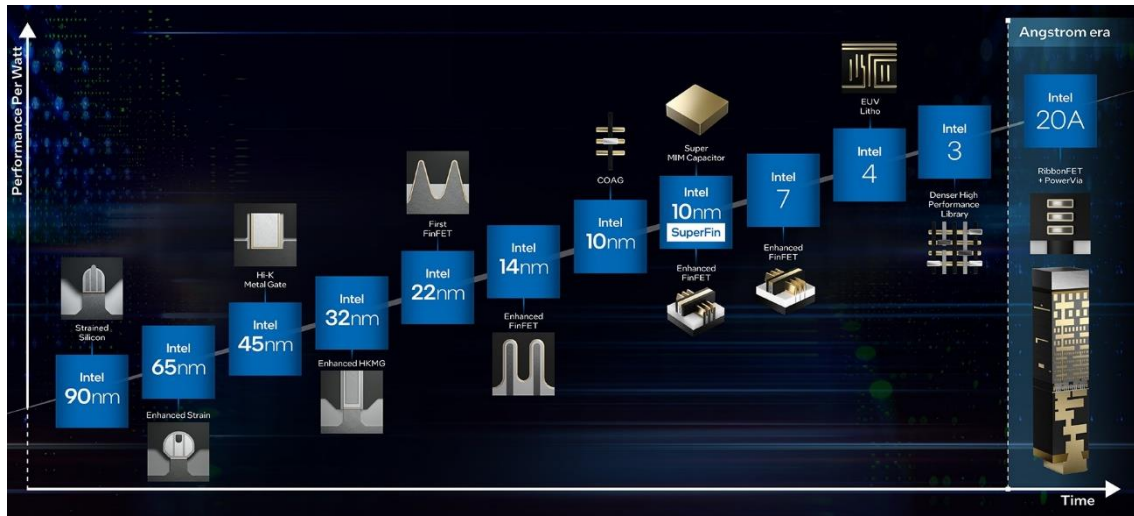


Figure 2.3. Intel process technology innovations.<sup>(123)</sup>

### 2.2.2 ALD process

A general ALD process is shown schematically in Fig. 2.4. It consists of alternating pulses of chemical precursors that reacting with the substrate. A typical ALD cycle is divided into four steps, including: (i) a precursor pulse time, where a precursor, which is typically an organometallic compound (i.e., a metal center surrounded by chemical functional groups called ligands), is pulsed into a chamber for a designated amount of time to allow the precursor fully react with the substrate surface through a self-saturation process; (ii) a purge and/or pump step using an inert carrier gas (typically  $N_2$  or Ar) to remove any remaining unreacted precursor or byproducts; (iii) a co-reactant pulse time, typically including non-metal such as O, N, S, etc., and involving a small molecule to create up to one monolayer of the desired material; and (iv) a final purge and/or pump step. These individual gas-surface reactions (called “half-cycle”) are then cycled until the appropriate film thickness is achieved.

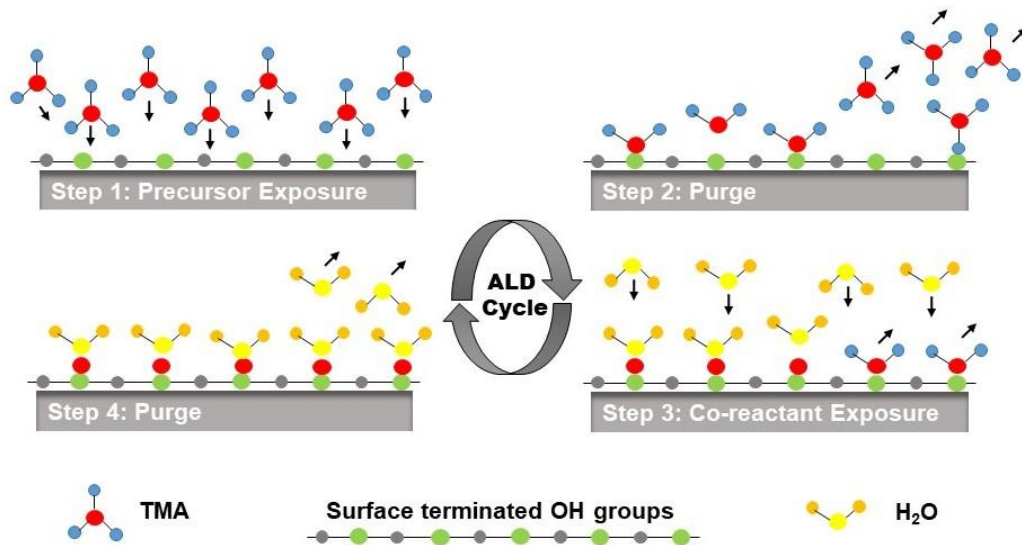


Figure 2.4. Schematic representation of an ALD-Al<sub>2</sub>O<sub>3</sub> process consisting of first half-cycle (precursor) and second half-cycle (co-reactant) in a self-limiting process that terminates when all available surface sites are occupied. The two half-cycles are separated by purging steps.

Note that as schematically shown in Figure 2.4 for the typical ALD process of the aluminum oxide, the precursor molecules and co-reactants do not react with themselves but rather with the surface occupied by the hydroxide groups. This is vital to avoid reactions between precursor and co-reactant molecules directly in the gas phase or on the surface, as this might lead to an unwanted CVD-like behavior. Therefore, for a typical ALD process, film remains extremely smooth and conformal to the original substrate because the reactions are completed during every half-cycle.<sup>(124)</sup> Nevertheless, the films are ideally continuous and pinhole-free because no surface sites are left behind within the film deposition. This phenomenon is crucial for the growth of high-quality dielectric films.<sup>(125)</sup> One superior feature of ALD is that it can be applied for very large substrates and even to parallel processing of multiple substrates. In fact, the precursors of ALD are in gas-phase molecules, and they saturate all available substrate surface independent of substrate geometry and do not need a line of sight to the substrate.<sup>(2)</sup> The parameters which limit the functionality of ALD are the high-amount of wasting precursor and the low growth rate.

### 2.2.3 Deposited materials

Figure 2.5 shows a wide range of materials deposited using ALD, including main-group of elements, transition metals, and lanthanides where the elements have been color-coded to be easily distinguished.<sup>(126)</sup> To date, ALD is a well-known growth technique capable of depositing single elements (metals) as well as complex and/or multi-component materials such as binary, ternary and quaternary films due to the prominent feature of the stepwise approach. Therefore, binary compounds consisting of metal and non-metal elements can produce a variety of metal oxides, nitrides, carbides, and chalcogenides. In principle, fabricated materials by ALD present an amorphous phase. Although depending on the applied substrate temperature, a polycrystalline phase can also form (even epitaxial growth has been achieved).<sup>(33)</sup> Among different kinds of materials deposited by ALD, metal oxides are very common because of the thermodynamic stability of metal bonded to oxygen. However, progress in the thin films made by ALD, makes it possible for complex ternary and especially quaternary compounds to grow through a super-cycle approach.

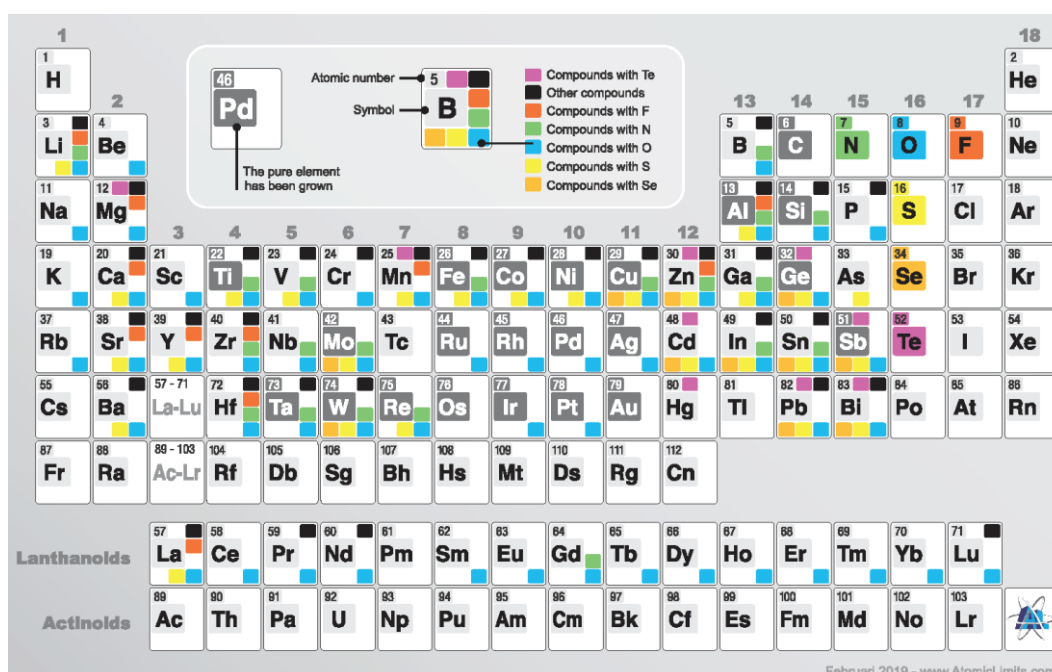


Figure 2.5. Materials deposited by ALD. Illustration of pure elements as well as different compounds by color-coding the squares.<sup>(126)</sup>



### 2.2.4 Precursors and co-reactants

In ALD, precursors are a class of molecules typically formed by metal centers surrounded by ligands and their volatility plays a pivotal role in the determining the precursor characteristics. For an ideal ALD process, the metal sources should meet some criteria: i) the metal precursor must be reactive enough towards the surface groups and leave reactive surface groups; otherwise, the ALD feature cannot occur because reactants would not undergo into surface chemical reactions; ii) the precursor molecules must not react with themselves or with its surface-adsorbed species. Besides, the metal precursors should have relatively high decomposition temperature to avoid undesirable decomposition of precursors, limiting control over the self-saturation process. Furthermore, an ALD precursor should have some demanding properties such as low cost and toxicity, easy to handle, high volatility at low temperatures, as well as not decomposing quickly, being the final factor to be easily synthesized and scaled up. An ideal and non-ideal ALD precursor has been shown in Fig.2.6.<sup>(127)</sup>

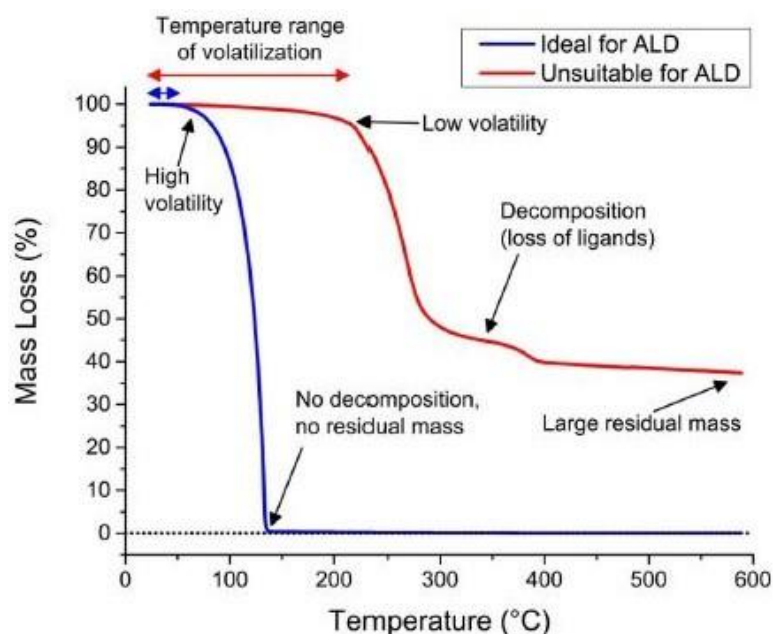


Figure 2.6. Mass loss plot of ideal and non-ideal precursors as a function of temperature. Data has been acquired using thermogravimetric (TG) analysis.<sup>(127)</sup>

Co-reactants in ALD technique are materials with specifications of volatile and small molecules such as elements ( $H_2$  or  $O_2$ ), hydrides ( $H_2O$ ,  $NH_3$ ) and alkyl compounds ( $Bet_3$  or  $AsMe_3$ ). Metal oxides are the most demanding compounds grown by ALD, where the oxygen sources or oxidants as co-reactants are  $O_2$ ,

H<sub>2</sub>O, H<sub>2</sub>O<sub>2</sub>, and many oxygen-containing organic molecules. However, according to literature O<sub>2</sub> source is restricted for oxidizing the catalytic metals that are more thermodynamically stable than their respective oxide.<sup>(127)</sup> Besides, the use of the specific oxidant depends also in the chemical nature of the organometallic precursor and the energy barrier that is needed for the oxidation. The conventional oxidant in the ALD process of metal oxides is H<sub>2</sub>O, considering some deficiencies that include: i) it cannot be easily purged out from ALD reactor, especially at low temperatures because it strongly bonded to surface. ii) not sufficiently reactive at low temperatures; therefore, relatively higher temperatures should be considered. However, using other oxidants such as O<sub>2</sub>, H<sub>2</sub>O<sub>2</sub>, O<sub>3</sub>, and O<sub>2</sub> plasma could overcome the aforementioned deficiencies that exist for H<sub>2</sub>O in the ALD process. There are some papers in which the effect of different ALD oxidants has been discussed in detail.<sup>(128-131)</sup>

### 2.2.5 Chemical and physical mechanisms

In ALD process, upon exposing precursor molecules to the substrate surface, one monolayer of adsorbed precursor saturates all available sites onto a surface. Adsorption can occur based on two main mechanisms: physisorption or chemisorption. On the one hand, physisorption is referred to intermolecular forces such as Van der Waals attraction or hydrogen bonding between the precursor and substrate surface. On the other hand, chemisorption results from a chemical reaction between the precursor and substrate surface, forming a new chemical bond. In a self-limiting chemical reaction, a precursor molecule should react only with the surface, not with itself, to comply with a layer-by-layer growth behavior. It should be noted that volatile byproducts of a chemisorption process should desorb/purge from the surface and ALD reactor to obtain desirable irreversible chemisorption.<sup>(132)</sup> Physisorption cannot be considered as a main mechanism of ALD process for two reasons. Firstly, weak intermolecular forces (often <10 kcal/mol) between the precursor and substrate surface might facilitate the desorption of the precursor from the surface in the purging step.<sup>(133)</sup> Secondly, Van der Waals forces in physisorption are not just between the adsorbed precursors and surface but also between different precursor molecules and surface, which does not have an inherent mechanism for self-limiting process. However, in many theoretical calculations of ALD processes, the physisorption of precursors onto the substrate surface plays an important role and might help in the subsequent chemisorption process.<sup>(134, 135)</sup>

In ALD chemisorption process, different mechanisms happen between the reactants as follows<sup>(132)</sup>:

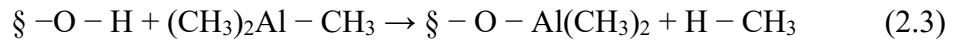
**i) Ligand-exchange.** One of the important mechanisms in the chemisorption process is referred to as ligand-exchange, where reactions involve interchanging the ligands between two species, as schematically shown below:



In which A/A' and B/B' are referred to as metal centers and their ligands, respectively. For the chemisorption process, the represented exchange is between a ligand on the substrate surface and on the precursor, which results in a new surface-precursor bond,



where  $\S$  is a notation of surface. A model of this mechanism can be simply explained based on ALD- $\text{Al}_2\text{O}_3$  process in which the chemisorption of trimethylaluminum  $[\text{Al}(\text{CH}_3)_3]$  onto a hydroxyl terminated surface releases methane as the byproduct.<sup>(114)</sup>

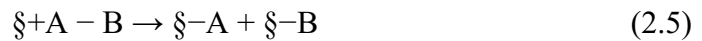


As mentioned, the first ligand-exchange (between precursor and surface OH groups) is required for the chemisorption process, interchanging can continue until the nearby active sites are available, resulting in multiple precursor surface bonds.<sup>(136)</sup>

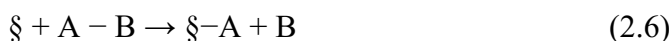
**ii) Dissociation.** Splitting a compound into two or more fragments is referred to as dissociation, which is often triggered by a form of external energy such as heat or light,



In principle, chemisorption through dissociation can occur in two ways: *classical dissociative*, which typically arises from a surface assisted pathway and lead to whole fragments of the precursor being chemisorbed to the surface.



However, it is likely that one or more of the dissociated fragments not readily chemisorb to the surface but rather desorb into the gas phase, remaining only one of the chemisorb fragments.



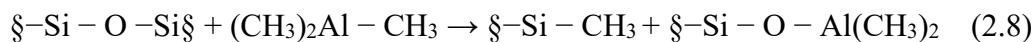
As such reactions (Eq. 2.6) are not fully considered dissociative chemisorption because not all fragments remain on the surface, one could name these reactions as *dissociative substitutions*.

The represented dissociative chemisorption typically happens onto high surface energy substrates such as platinum or ruthenium metals substrates and for metalorganic precursors by assisting in the dissociation of organic ligands.<sup>(137-139)</sup>

Besides, dissociative chemisorption can also happen for co-reactants such as O<sub>2</sub> by splitting it into its atomic counterpart that facilitates increment of its reactivity toward the next precursor pulse<sup>(140, 141)</sup>



Furthermore, dissociative chemisorption may involve substrate-bond breaking to create a binding site for a precursor fragment. For example, trimethylaluminum has been shown to undergo dissociative chemisorption onto siloxane bridges where the Si-O bond is broken and replaced with a new Si-C bond arising from one of the trimethyl ligands of Al precursor.<sup>(142, 143)</sup>



Such reactions are similar to a ligand-exchange (as discussed above) where both CH<sub>3</sub> and Al(CH<sub>3</sub>)<sub>2</sub> fragments remain bonded to the surface. However, it is categorized as dissociative chemisorption.

**iii) Association.** Association is not a very common chemisorption mechanism that happens when no bonds are broken (either in precursor or substrate surface), and a new bond is formed between a precursor and substrate. The created bond through an association mechanism is often referred to as a coordination bond. Such a mechanism only occurs after a gas-phase dissociation process and leads to an electron deficiency.



**iv) Oxidation.** Oxidation is another mechanism that can be classified into the chemisorption mechanisms for ALD process. However, it depends on the specific ALD recipe and materials. Several oxidizers include O<sub>2</sub>, H<sub>2</sub>O, and strong

oxygen sources of ozone ( $O_3$ ) and  $O_2$  plasma for removing organic fragments from metalorganic precursors via combustion reactions. These oxidants are necessary for the formation of the metal oxide as the oxygen is also incorporated into the layer.<sup>(144-146)</sup> It should be mentioned that introducing the oxygen to the substrate surface might result in partial oxidation of the surface that significantly helps to chemisorb the next cycle of metal precursor through oxidation of the ligands.<sup>(141, 147)</sup> In these cases, the chemisorption mechanism is often a mixture of both dissociation and oxidation, but it is not easy to distinguish experimentally.

### **2.2.6 ALD window**

The processing temperature range where the growth is saturated depends on the ALD mechanism, which is the so-called “ALD window” and refers to a region of nearly ideal ALD behavior between the non-ideal regions (as indicated in Fig.2.7). In principle, temperatures below or above the window generally lead to poor growth rates and/or non-ALD type deposition. At low temperatures, the reactions may not have enough thermal activation energy to comply with process completion, or the reactants could condense on the surface as a condensation effect. On the contrary, rapid desorption of the surface species or thermal decomposition of the reactants might induce a CVD process at higher temperatures. These effects directly impact the growth per cycle (GPC) so that higher and lower GPC values outside of the ALD window (at higher temperatures) could arise from decomposition and desorption of the reactants, respectively. Therefore, to benefit from the many advantages of ALD, it is necessary to stay within the designated ALD window. According to the literature, out of the temperature window, the surface reactions do not meet the process completion, which causes considerable porosity that might lead to their easy oxidation.<sup>(148)</sup>

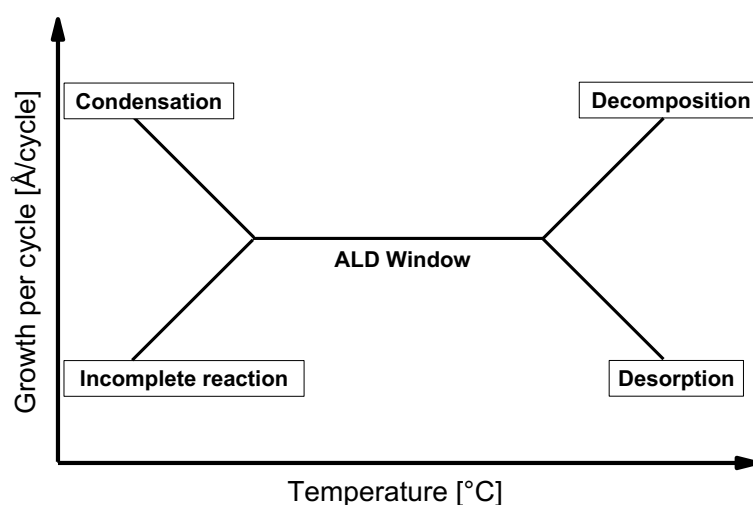


Figure 2.7. Idealized ALD temperature window, displayed by the growth per cycle as a function of temperature.

### 2.2.7 Growth modes, nucleation and nucleation delay

In ALD growth mechanism, there are three different growth modes<sup>(149)</sup>:

**i) Layer-by-layer or Frank-van der Merve (FM) growth:** In this mode, the film atoms have a stronger bond to the substrate surface than each other. In other words, each layer is completely saturated on the available sites onto the surface prior to introducing the next layer.

**ii) Island or Vollmer-Weber (VW) growth:** In this mode, the film atoms have a stronger bond between them than to the substrate surface, which triggers three-dimensional islands on the surface.

**iii) Layer-plus-island or Stranski-Krastanov (SK) growth:** In this mode, an intermediate state between the FM and VW exists where the growth of three-dimensional islands starts after full saturation of the two-dimensional layer.

In general, among the introduced growth modes, a layer-by-layer growth approach is referred as an ideal ALD process in which no more than one atomic layer of the desired material can be expected. However, it is very hard to talk about this ideal growth mode for the first cycle of ALD on a bare substrate surface. In fact, when precursor molecule adsorption is highly demanding and available active sites for chemisorption are in defect, precursor saturation is primarily controlled using the steric hindrance effect of the adsorbed ligands of

the precursor.<sup>(114, 132, 150-152)</sup> Therefore, the presence of steric hindrance might prevent the formation of a complete layer after a first ALD cycle. In the concept of two dimensional and/or layer-by-layer growth, the subsequent ALD cycle (after introducing the first ALD cycle) results in only deposition onto the unsaturated surface until one monolayer is formed.<sup>(114)</sup>

Nevertheless, in ALD process the precursor molecules have more tendency to be chemisorbed onto the deposited material rather than onto the bare substrate surface. Such behavior can be also referred as an island growth process (explained above) either in the presence or absence of surface diffusion. In the absence of surface diffusion, one could expect a linear behavior between the diameter of particles and number of cycles so that each cycle results in one monolayer of adsorbed precursor on the surface of the island.<sup>(153)</sup> However, in the presence of surface diffusion the diameter of particles deviates from linearity. Figure 2.8 schematically shows layer-by-layer deposition as well as island growth with and without diffusion. It should be noted that diffusion in ALD process has a pivotal role in thin films deposition, i.e. diffusion of trimethylaluminum precursor into the polymer film for the initial ALD cycles.<sup>(154)</sup> It has been also documented a simulation of different growth mechanisms and different diffusion effects in ALD process.<sup>(155)</sup>

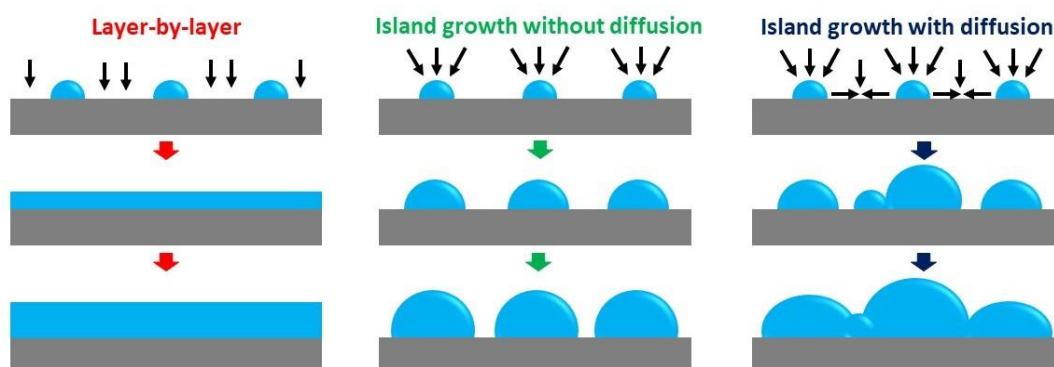


Figure 2.8. Representation of layer-by-layer growth (red), island growth without (green) and with (dark blue) diffusion.

In ALD mechanism, nucleation delay is defined as an ALD process in which a desirable nucleation process and/or a steady saturation of GPC cannot be achieved due to the absence of precursor chemisorption onto the substrate surface. In fact, the reasons might be either incompatibility of precursor chemisorption with the exposed substrate surface that triggers very slow reactions (over hundreds of ALD cycles) or lack of strong co-reactant (oxidants) to react with the

chemisorbed precursor. For the latter case, it has been reported that the using a strong oxygen source can increase the chemical reactions on the surface and reduce the amount of impurities and/or defect states.<sup>(156-158)</sup> Besides, those precursors that resist ligand-exchange such as cyclopentadienyl (Cp) often promote a nucleation delay and accordingly dissociation.<sup>(159, 160)</sup>

Therefore, the role of the substrate could have a significant impact in the chemisorption mechanisms, so that the reactivity of surface terminated –OH groups strongly depends on the nature of the substrate and differs from one substrate to other substrate.<sup>(161, 162)</sup> Moreover, different active sites and binding states on the substrate surface in addition to the role of temperature can also result in different reactivity.<sup>(163, 164)</sup> It should be noted that in case of no precursor chemisorption, a high free energy substrate might assist remarkable dissociative chemisorption of precursor ligands onto the surface, i.e., considerable chemisorption of TMA on high surface energies of platinum (Pt) and palladium (Pd).<sup>(165, 166)</sup>

### 2.2.8 Advantages and disadvantages

ALD with a layer-by-layer growth mechanism leads to several superior film properties and growth advantages such as:

- High conformity and layer homogeneity over large substrates.
- Precise control over thickness by changing the number of ALD cycles.
- Relatively low temperature deposition, especially for thermal-sensitive substrate.
- Atomic-level control of sample composition.
- Preparing pinhole-free films even at a sub-nanometer thickness scale.
- ALD delivers extremely thin films in order of atomic scale.
- Ability to deposit complex and/or multilayer structures in a continuous process.
- Preparing amorphous or crystalline films depending on substrate and temperature.
- Availability of standard recipes for pure elements, oxides, nitrides, metals, and semiconductors.

Nevertheless, some handful disadvantages of ALD can be referred to:

- A low growth rate and low precursor utilization efficiency.



- ALD requires a high purity of substrate in order to achieve high quality of films.
- Relatively high cost of ALD systems.
- The large amount of precursors is potentially wasted.

However, the abovementioned deficiencies/issues can be solved by adequate design of reactor and precursor selection. Table 2.2 compares ALD with other deposition methods.<sup>(167)</sup>

Table 2.2 An overview on comparison of ALD technique with other growth methods of chemical vapor deposition (CVD), molecular beam epitaxy (MBE), sputtering, electron beam evaporation (EB Evap.), and pulsed laser deposition (PLD).

Methods	ALD	CVD	MBE	Sputtering	EB Evap.	PLD
Low-temperature growth	✓	×	✓	✓	✓	✓
Uniformity/layer homogeneity	✓	×	fair	✓	fair	fair
Conformity/step-coverage	✓	×	poor	poor	poor	poor
Growth rate	low	✓	fair	✓	✓	✓
Film density	✓	✓	✓	✓	✓	✓
Pinhole-free	✓	✓	✓	fair	fair	fair
Preparing multilayer structures	✓	fair	✓	✓	fair	fair
Interface quality	✓	poor	✓	poor	fair	fair
Industrial applicability	✓	✓	✓	✓	✓	poor

### 2.2.9 ALD systems

For performing growth in ALD systems, activation energy is the most critical factor in enabling the exchange chemical reactions between the substrate surface groups and precursor molecules. Such activation energy can be supplied using heating the substrate. However, if thermal activation of ALD cannot sufficiently comply with the ALD mechanism, a plasma-assisted mode of ALD is employed to increase chemical reactions at the lowest possible temperatures by introducing high energy ions of radicals such as oxygen, nitrogen or hydrogen. In principle, each ALD system can operate in two different modes of either pump-

type or flow-type reactors, depending mainly on the vapor pressure of the precursors (technical details are discussed in the next chapter).

### 2.2.9.1 Thermal atomic layer deposition (TALD)

In principle, thermal atomic layer deposition (TALD) is referred to a conventional ALD process in which surface reactions occur at relatively high temperatures where no plasma source is used. To date, several examples of TALD arising from binary reaction CVD processes have been reported.<sup>(168-170)</sup> Among them, the growth of aluminum oxide layer with the use of TMA and water is the most studied among the TALD technique, and can be considered as a model for an ideal ALD based-system because of extremely high reaction enthalpy ( $\Delta H = -364$  kcal) of the overall reaction.<sup>(114, 171)</sup>

### 2.2.9.2 Plasma-enhanced ALD (PEALD)

In general, PEALD is an energy-assisted ALD technique that employs a plasma source to raise the reactivity of the incoming gas phase co-reactant(s) (e.g.,  $\text{NH}_3$ ,  $\text{N}_2/\text{H}_2$  or  $\text{O}_2$ ) to energetically activate the chemical reactions on the substrate surface at room temperature, on contrary to thermally activated processes.<sup>(3, 119, 172)</sup> Therefore, due to the presence of highly reactive plasma species, the rates of growth increase and high quality of films can be achieved at lower temperatures (even room temperature).<sup>(173)</sup> The plasma species involve all those energetic and chemically active particles formed within the discharge region, such as ions, radicals and electrons, where radicals act as highly reactive agents for film growth while ions could induce physical changes.<sup>(174)</sup> It should be taken into account that the deposition of single-element films of metals and semiconductors by TALD is not easy and/or straightforward, and with the use of introduced radicals in PEALD process those films can be grown readily.<sup>(120)</sup>

Regarding the ALD reactor design, the configuration of PEALD is more complicated than a TALD chamber, where appropriate and accurate design determines the characteristics of the produced plasma species and delivering/conducting towards the substrate surface. In principle, the reactor design of PEALD can be classified into three main configurations:

#### **i) Radical-enhanced ALD:**

Figure 2.9a displays the first ALD reactor in which thermal-based configuration of TALD is modified with a plasma generator, where plasma generation takes place externally at a relatively far distance from the substrate surface. Therefore, the generated plasma species have to travel through the reactor

between the plasma source and reaction chamber. In fact, many surface collisions happen during the flow, resulting in recombination between electrons and ions, and consequently they are lost before reaching the substrate surface. These surface collisions of plasma species might considerably decrease the radicals flux approaching the substrate surface. To have more efficiency for this plasma configuration, the choice of radicals is crucial so that hydrogen radicals show a relatively low and high probability of surface recombination on quartz and metals surfaces, respectively. However, for metallic surfaces allowing a very long radicals exposure time is required to comply ALD reactants saturation.

### **ii) Direct plasma ALD:**

Figure 2.9b shows the second ALD reactor configuration taken from plasma-enhanced chemical vapor deposition (PECVD). For the PEALD purpose, a capacitively-coupled plasma (CCP) is generated between two parallel plates (electrodes) at a radio frequency (RF) of 13.56 MHz where one plate is powered, and another one is attached to a grounded substrate. The assigned name of direct plasma ALD is because the substrate is directly located at one of the electrodes, which contributes to the plasma generation. For this configuration, gases are introduced into the ALD reactor either through a showerhead in the powered plate, named shower-head type<sup>(175)</sup> or from the side of plates, called flow-type in presence of sufficiently high-pressure<sup>(176)</sup>. According to the literature, the operational pressure during the plasma generation should be in the order of 1 Torr or < 100 mTorr.<sup>(177, 178)</sup> Note that for such configuration, the flux velocity of plasma radicals and ions is very high due to vicinity of plasma source and substrate surface which enables uniform deposition over the large area with a short feeding pulse of plasma. However, close proximity of the plasma generated species with the substrate surface might trigger surface damages due to presence of high energy ions. To overcome this issue, with variations of power as well as the operational pressure, one could tune the ions energy approaching substrate surface.

### **iii) Remote plasma ALD:**

Figure 2.9c represents the third ALD reactor configuration of PEALD in which plasma source is placed remotely from the substrate surface; therefore, high energy species of plasma cannot damage the surface as the substrate is not involved in the plasma generation. This type of plasma configuration is more demanding concerning the generation of downstream plasma where the flux of plasma radicals and species is much higher than in radical-enhanced ALD counterparts. Furthermore, contrary to direct plasma, in remote plasma ALD

substrate and plasma conditions can be varied and/or controlled independently of each other, e.g., a change in substrate temperature cannot impact the gas temperature and subsequently the density of plasma generated species.<sup>(3, 174)</sup> Therefore, remote plasma ALD could optimize the plasma operating conditions and properties, particularly for ion bombardment and the influence of plasma radiation.<sup>(179)</sup> Considering the abovementioned features, a reactor configured by remote plasma ALD would be a promising PEALD system to meet a high degree of flexibility for process design and industry purposes. Furthermore, many plasma sources can be utilized in remote plasma ALD such as inductively-coupled plasma either as a planar triple spiral antenna or cylindrical coil<sup>(180)</sup>, electron cyclotron resonance (ECR)<sup>(181)</sup>, and microwave plasma<sup>(182)</sup>.

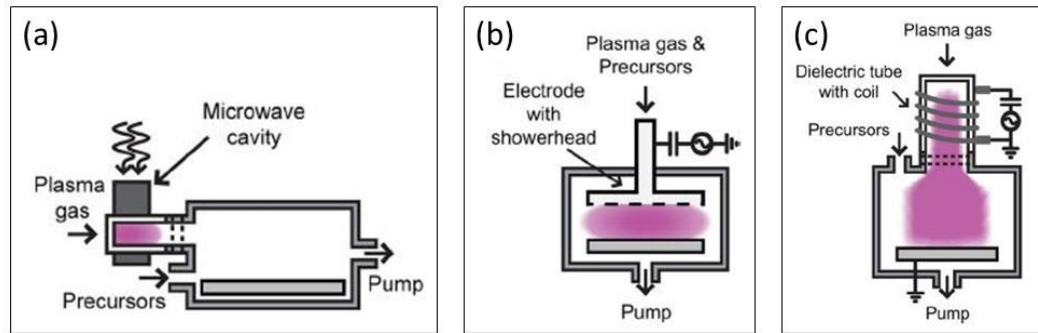


Figure 2.9. Different types of PEALD reactor configurations.<sup>(183)</sup> Radical-enhanced ALD (a), direct plasma ALD (b), and remote plasma ALD (c)

The preparation of thin films using PEALD has been proven to be as a pioneer deposition technique in the field of ALD and semiconductor technology because of superior advantages, including improved material properties<sup>(184-186)</sup>, driven lower substrate temperatures especially for thermal-sensitive substrates<sup>(187, 188)</sup>, a wide selection of precursors and substrate materials<sup>(189-191)</sup>, accurate control of film composition<sup>(192-194)</sup>, achieving higher GPC<sup>(195, 196)</sup>, and more flexibility in processing<sup>(197-199)</sup>.



## Chapter 3

# EXPERIMENTAL

### 3.1 Characterization methods

The optical and spectroscopic characterization techniques employed to investigate and probe the properties of the ALD films are discussed below.

#### 3.1.1 Spectroscopic ellipsometry (SE)

In order to ascertain the thickness and the optical constants of the ALD prepared thin films, spectroscopic ellipsometry is widely used in its characterization using polarized light. An ellipsometer measures changes in the light polarization after reflection on the surface of grown films, providing information about the roughness and thickness of the layer (ranging from sub-nanometer to a few microns), in addition to the optical characteristics of refractive index and absorption coefficient, which impact the incident polarization state of the light.<sup>(200)</sup> Thickness and roughness can be measured with a resolution in the order of angstrom by utilizing the phase information of the polarization state of light despite the inherent diffraction limitation of optical methods.<sup>(201)</sup>

##### 3.1.1.1 Principles and operation

Figure 3.1 displays an ellipsometer basic configuration based on the light reflection on a sample. In principle, the polarized light waves consisting of p and s components are irradiated onto a sample at an oblique incident angle (for an ideal condition), denoted as a Brewster angle, where the difference between the amplitude reflection coefficients ( $R_p$  and  $R_s$ ) is maximized. Besides, at this angle the measurement sensitivity increases. During an ellipsometry measurement, the change in the polarization states of the incident and reflected (transmitted) light waves are described using p- and s-polarization coordinates depending on the

oscillatory direction of its electric field as well as light wave components. The directions of the electric field vectors for p- and s-polarizations are reversed on both incident and reflection sides. Therefore, the optical film properties are determined according to the changes in amplitude and phase in the light reflection components of p- and s- polarizations, typically referred to a change in the polarization state.<sup>(202)</sup>

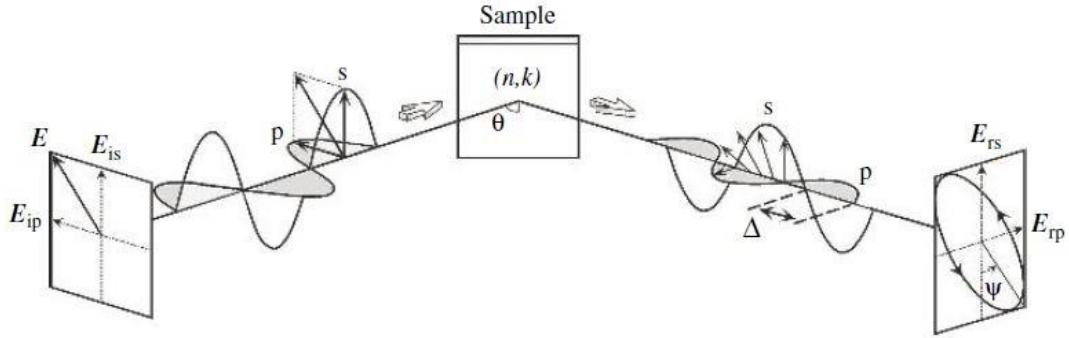


Figure 3.1. Representation of ellipsometric measurement.<sup>(202)</sup>

A complex reflectance ratio ( $\rho$ ) is applied according to the basic equation of ellipsometry to determine the films thickness and the optical constants:<sup>(200, 203)</sup>

$$\rho = \frac{R_p}{R_s} = \tan(\psi) \exp(i\Delta) \quad (3.1)$$

Where  $R_p$  and  $R_s$  refer to the light polarized parallel and perpendicular to the surface plane, respectively,  $\tan(\psi)$  shows the amplitude ratio after reflection, and  $\Delta$  is assigned to the phase shift. As ellipsometry is an indirect measurement, the use of an appropriate model should be taken into account to interpret the results. This means the acquired parameters of  $\Psi$  and  $\Delta$  are fitted with a model over a wide range of wavelengths to extract the optical properties. According to Fresnel's equations, a model is established to determine the values of the  $\Psi$  and  $\Delta$  for the desired layer and/or individual layers in a multilayer structure.<sup>(204, 205)</sup> The acquired experimental data of the  $\Psi$  and  $\Delta$  are compared with the related determined  $\Psi$  and  $\Delta$  values, and an accurate fit is performed using the root mean squared error (RMSE), given as:

$$\text{RMSE} = \sqrt{\frac{1}{2n-m-1} \sum_{i=0}^n [(\psi_i^{\text{cal}} - \psi_i^{\text{exp}})^2 + (\Delta_i^{\text{cal}} - \Delta_i^{\text{exp}})^2]} \quad (3.2)$$

In which  $n$  is referred to the number of data points in the spectra,  $m$  is assigned to the number of variable parameters in the mode, and  $cal$  and  $exp$  exhibit the calculated and experimental data, respectively. The RMSE evaluates the accuracy of the applied fitting model in comparison with the collected experimental data.

In this research, ellipsometry measurements were done using a spectroscopic ellipsometer within the UV/VIS/NIR spectral range (SENTECH SER 850 DUV) and in a wavelength range of  $\sim 290$  to  $1000$  nm at three incidence angles of  $60^\circ$ ,  $65^\circ$ , and  $70^\circ$  (Fig. 3.2). The acquired spectra were fitted based on a model consisting of the Si/SiO<sub>2</sub> substrate and the grown layer, where Tauc-Lorentz and Drude oscillators applied for the VIS range (transparent region) and the IR range, respectively. The used procedure suggests the advantages of combining all dispersion contributions to the optical model for the whole spectral range.



Figure 3.2. SENTECH spectroscopy ellipsometer.

The SENTECH UV-VIS-NIR optical spectrophotometer also provides optical information about the absorbance or band gap value of the ALD prepared films. The optical absorption of the layers is determined as a function of wavelength: monochromatic light is passed through the sample and the reference sample, and the measured light extracted from the layer is compared to the light belonging to a reference sample.<sup>(206)</sup> Based on the obtained result of transmittance measurement, the band gap is calculated, where the absorption coefficient ( $\alpha$ ) is ascertained using absorption data ( $A$ ) for each wavelength with the following equation:



$$\alpha = \frac{A}{\lambda} \quad (3.3)$$

Where  $\lambda$  is a wavelength in nm units, although it is multiplied by  $10^{-7}$  to get the absorption coefficient in the unit of  $\text{cm}^{-1}$ . Therefore, according to the obtained values, the band gap can be determined by fitting the absorption coefficient in the following Tauc's relation :<sup>(207)</sup>

$$(\alpha h\nu)^n = B (h\nu - E_g) \quad (3.4)$$

The energy of the incident photons, the absorption edge, and band gap are represented by  $h\nu$ ,  $B$ , and  $E_g$ , respectively. The value of  $n$  is either 2 for direct or 1/2 for indirect band gaps. With the use of Tauc-Lorentz plot analysis, the band gap value of the layer is determined by plotting  $(\alpha h\nu)^n$  as a function of photon energy and extrapolating the linear part of the graph.

### 3.1.2 X-ray photoelectron spectroscopy (XPS)

X-ray photoelectron spectroscopy is a surface sensitive chemical characterization technique operates based on the photoelectric effect in which the sample surface is irradiated by X-rays, generating photoelectrons. The main particularities of XPS are inherent surface sensitivity, high sensitivity to the oxidation state, and ability to probe depth chemical information of the elements (except hydrogen and helium) in the layer. In principle, XPS operates according to the photoelectric effect discovered by Heinrich Hertz in 1887 when he found irradiated surfaces emit electrons. Later in 1905, Albert Einstein fundamentally described such physical phenomena and received the Nobel Prize in physics in 1921. Robinson and Rawlinson made the first observation of the photoemission arising from X-ray irradiation in 1914, and Steinhardt and Serfass presented the first application of that effect in 1951.<sup>(208)</sup> The development of XPS technique was accomplished by Siegbahn in 1950s and 1960s, winning the Nobel Prize in 1981 for his work on high-resolution electron spectroscopy (being XPS also known as electron spectroscopy for chemical analysis (ESCA)).<sup>(209)</sup>

#### 3.1.2.1 Principles and operation

Figure 3.3 shows the schematic working principle of XPS. When X-ray interact with the core level electrons, these are photoemitted from the electronic shell.<sup>(210)</sup> In other words, the electron is emitted with a kinetic energy that depends on the difference between the photon energy and the binding energy of the particular core level. In most cases, the produced hole is filled by an electron from

a higher energy level (the valence shell) resulting in a release of energy. Although this energy is released in the form of an emitted photon, the energy can also be transferred to another electron, which is ejected from the same level with fixed kinetic energy independent of photon energy; this second ejected electron is called an Auger electron.

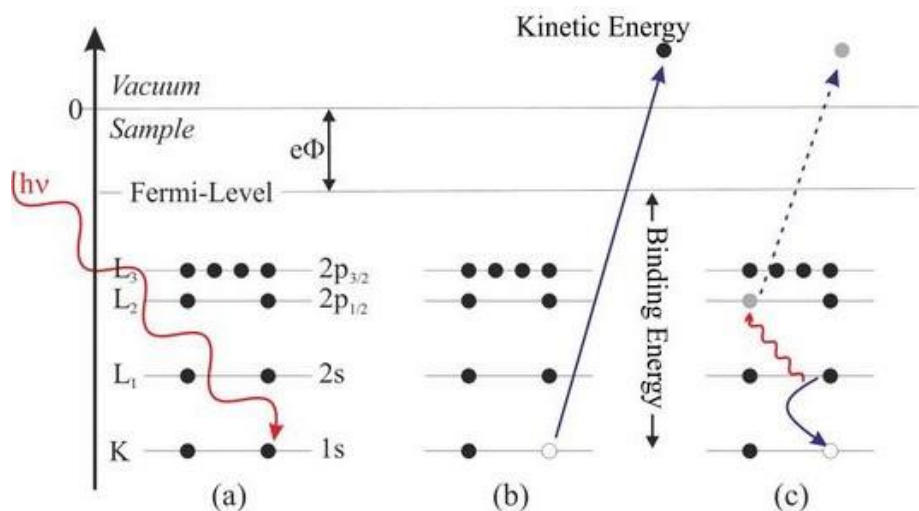


Figure 3.3. Principle of photoelectron emission and Auger relaxation effect of XPS.<sup>(211)</sup>

Finally, the kinetic energies of the photoemitted electrons are collected through a detector and subsequently the corresponding binding energies are determined based on the following equations:<sup>(210, 212)</sup>

$$h\nu = BE + KE + \Phi_{\text{spec}} \quad (3.5)$$

$$BE = h\nu - KE - \Phi_{\text{spec}} \quad (3.6)$$

Where the energy of the X-ray ( $h\nu$ ) is equal to the sum of the binding energy (BE) of the electron (means how tightly it is bound to the atom/orbital to which it is attached), the kinetic energy (KE) of the photoemitted electron, and the work function ( $\Phi$ ) of the spectrometer as a constant value. The binding energy of the photoelectron is measured with regard to the sample Fermi level (not the vacuum level), which is the reason for the presence of  $\Phi_{\text{spec}}$  (as indicated in Fig. 3.4). During the measurement, the sample and analyzer are electronically connected, establishing a potential that equilibrates the Fermi levels. It should be noticed that

equation (Eq. 3.6) only depends on the work function of the analyzer and not  $\Phi_{\text{sample}}$ .

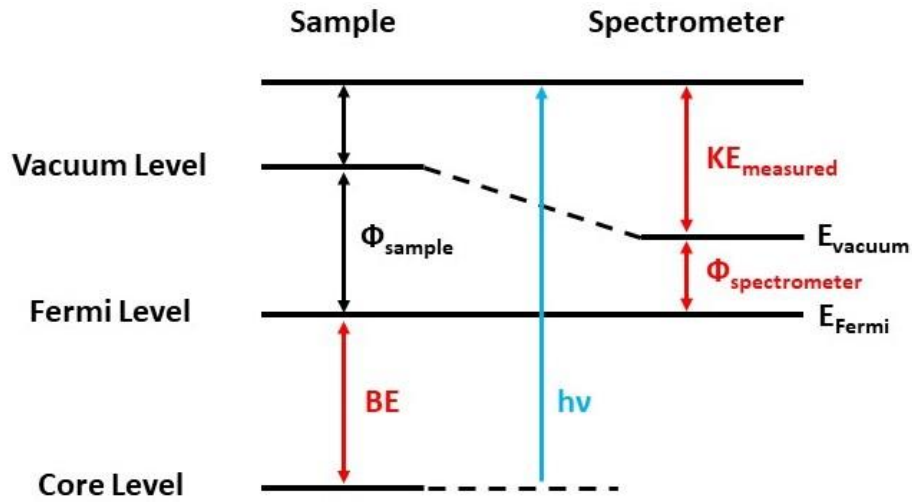


Figure 3.4. Energy level diagram of XPS basic equation.

In XPS data, the collected photoelectron peaks are identified by the element and orbital from which the electrons were ejected. Although the binding energies of the electrons are independent of the used photon energy, the kinetic energy of the electrons is the main parameter that changes with different photon energies, as described by Eq. 3.6. Any electron with binding energy lower than the applied photon energy should be emitted from the layer and accordingly observed in XPS spectra.

During XPS measurements the sample should be grounded. Although there is no shift in XPS spectrum for conducting samples,<sup>(213, 214)</sup> probable charging effects may appear, artificially shifting the spectra to higher binding energies. This issue affects samples with low electrical conductivities, such as oxide-based materials (here  $\text{InO}_x$ ,  $\text{GaO}_x$ ,  $\text{ZnO}_x$ , IGZO, as well as  $\text{AlO}_x$  and  $\text{CeO}_x$ ). In these cases, a binding energy calibration should be taken into account, where carbon is the most common element and the energy position of C 1s is taken as a reference for the calibration process of *ex-situ* prepared films.<sup>(215, 216)</sup>

The surface chemistry analysis of the layers is carried out according to the state of the different chemical bonds arising from changes in the binding energy of the electrons that are redistributed around the constituent atoms of the crystal.<sup>(217)</sup>

Prior to quantitatively analyze the *ex-situ* prepared films by XPS, a surface cleaning process is required to remove surface contamination and/or adventitious

carbon impurities. Hence, most XPS systems are commonly equipped with an  $\text{Ar}^+$  ion gun sputtering source (as an example schematically indicated in Fig. 3.5). The principle of operation is based on the electrical discharge which is produced between the anode and cathode by applying a potential in the gas cell. This type of source is also called cold cathode ion source since it uses an inert gas such as  $\text{Ar}^+$  that is continuously fed into the gas cell through the leak valve and provides a pressure difference between the gas supply and the ion source. The generated electrons in the discharge process hit the gas particles creating the cations. A permanent magnetic field over the source facilitates the acceleration of electrons and enables the discharge process to be performed at relatively low pressures. Finally, the created ions are extracted from the gas cell through an aperture and introduced into the flight tube where ions pass and are focused onto the sample surface. It should be taken into account that the sputtering process using ion source is a very common and effective surface cleaning. However, ion bombardment could physically damage the layer and/or chemically change the bonding state because of interaction between the sample and the ions.<sup>(218, 219)</sup>

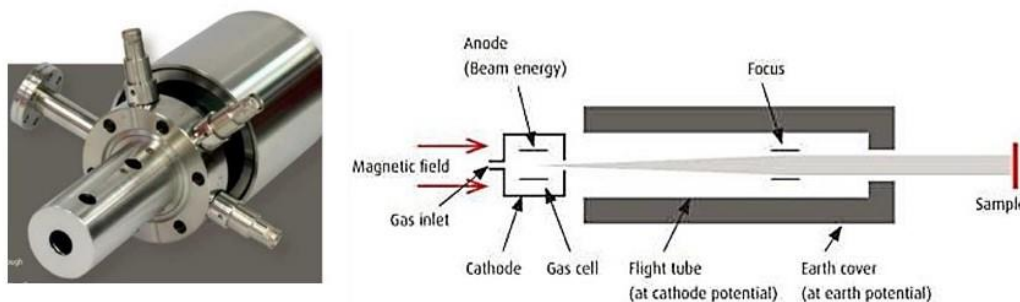


Figure 3.5. Configuration of ISE5-cold cathode ion sputter source.<sup>(220)</sup>

Furthermore, deeper probing into the materials might be required to intensively investigate not only the chemical bonding state on the surface, but within the bulk or even at the interface to the substrate. Therefore, a depth profiling approach using an ion source sputtering is applied as a surface etching process in which the layer is sputtered for a short period of time following XPS measurement and data acquisition until the sputtering has probed to the desired material depth. Note that depending on the purpose and material, such experiment might need much time to probe tens of nanometers into a sample.

### 3.1.2.2 Photoemission peak analysis and fitting

Determining the atomic concentration of the elements is one of the superior features of XPS technique that can be fulfilled after defining and confining the binding energy region, following subtraction of background and extracting of the raw area under a peak. The background selection strongly depends on the core level spectra under analysis, i.e. the general Tougaard and Shirley background shapes are typically applied for doublet (spin-orbit splitting) and single core level signals. However, the use of raw area lonely is not enough to calculate the atomic concentration, and a sensitivity factor must be employed, which is specific for each element, core level and analyzer as described in equation 3.7.

$$n_x = (I_x/S_x)/(\sum(I_i/S_i)) \quad (3.7)$$

In which  $n$ ,  $i$ ,  $S$ , and  $I$  are atomic concentration, all possible species, the sensitivity factor, and the peak raw area or intensity, respectively. In principle, the sensitivity factor consists of several individual parameters as collected in equation 3.8:

$$S = fA\sigma T(E_{kin})y\lambda(E_{kin})\theta \quad (3.8)$$

Where parameters of  $f$  and  $A$  refer to photon flux for a certain anode and area, respectively, (common to all samples and measurements),  $\sigma$  is the atomic cross section which is plotted in Figure 3.6 for some core levels versus photon energy<sup>(221)</sup>,  $T(E_{kin})$  is the transmission function of the analyzer as its determination described in the literature<sup>(222)</sup>,  $y$  is an efficiency parameter in the photoelectric process for the formation of photoelectrons of the normal photoelectron energy,  $\lambda(E_{kin})$  is the inelastic mean free path of photoemitted electrons<sup>(223)</sup>, and  $\theta$  is the magic angle of  $54.7^\circ$ <sup>(221)</sup> which is the angle between X-ray source and analyzer. The sensitivity factors differ slightly from system to system due to some instrument-specific parameters belonging to the analyzer, i.e. the transmission function (TF). It should be mentioned that the sensitivity factor, also called atomic sensitivity factor (ASF), has been explained and determined for the elements in the literature.<sup>(224)</sup> However, the given empirical values corrected for the transmission function of the used analyzer as described below.

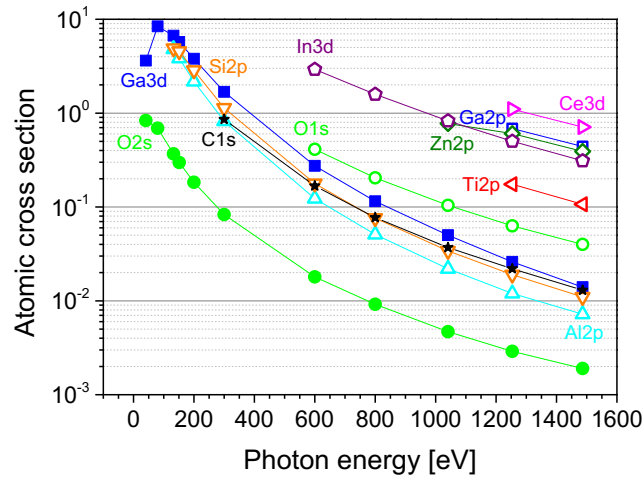


Figure 3.6. Atomic cross section of the desired elements as a function of photon energy.

To determine the TF, an *in-situ* ALD prepared  $\text{AlO}_x$  sample (at RT; thickness of  $\sim 5$  nm) was employed for XPS measurement in a medium lens size using two photon energies of Al  $K\alpha$  (1486.6 eV) and Mg  $K\alpha$  (1253.6 eV), in two different modes of the analyzer; constant analyzer energy (CAE) and constant retarding ratio (CRR). According to the following equation (Eq. 3.9), both measured spectra have the same intensity at a kinetic energy ( $E_{kin}$ ) of  $\sim 800$  eV related to the product of pass energy (PE) and retarding ratio (RR).

$$RR = \frac{(E_{kin}) - Wf}{PE} \quad (3.9)$$

In which,  $Wf$  is the work function of the material and was assumed to be zero. The transmission function of the analyzer can be calculated assuming that TF is proportional to the kinetic energy of the electrons in the CAE mode (which is mainly used for XPS measurements):

$$TF_{CAE}(E_{kin}) \approx \frac{1}{(E_{kin})^x} \quad (3.10)$$

Where the parameter of  $x$  is a correction factor that should be taken into account and can be calculated from the following equation:

$$R(E_{kin}) = \frac{[(PE)(RR)]^2}{(E_{kin})^{1+x}} \quad (3.11)$$

In which the intensity ratio ( $R(E_{kin})$ ) is determined (as given underneath) based on the intensity of the collected spectra in two different modes of CAE ( $I_{CAE}$ ) and CRR ( $I_{CRR}$ ) where two excitations of Al and Mg  $K\alpha$  were also considered.

$$R(E_{kin}) = \frac{I_{CAE}}{I_{CRR}} \quad (3.12)$$

The calculated intensity ratio is plotted as a function of the kinetic energy in both excitations (Al  $K\alpha$  and Mg  $K\alpha$ ), and then fitted following expression 3.11. Figure 3.7 shows the obtained transmission function of the analyzer in two excitations versus the kinetic energy of the electrons.

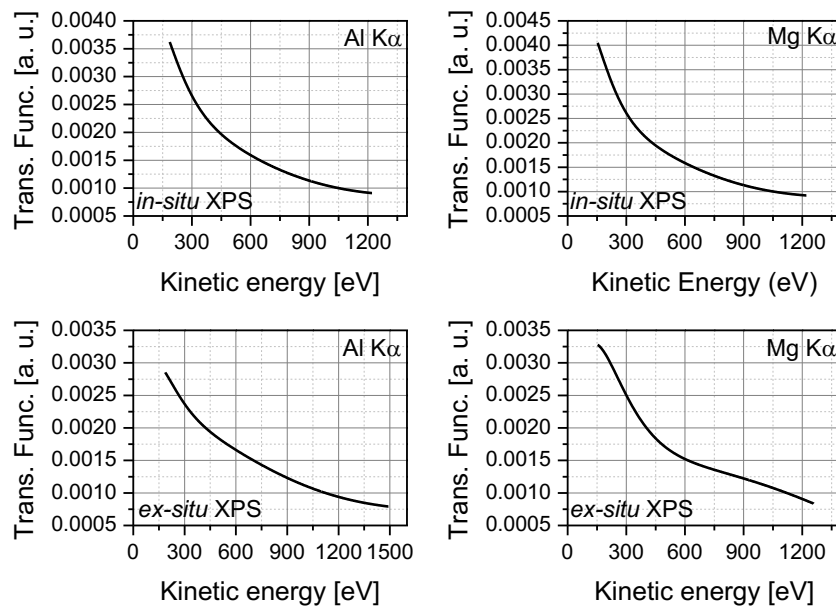


Figure 3.7. Transmission function of the *in-situ* and *ex-situ* XPS systems as a function of the kinetic energy of electrons for both excitations of Al  $K\alpha$  and Mg  $K\alpha$ .

XPS has a detection limit typically in the range of 0.1 – 1%. However, it depends on the sensitivity factor of the element and the layer matrix.<sup>(216)</sup> There are some examples in the literature in which detection limit of all elements have been predicted with a range of 0.003 to 30%.<sup>(225)</sup> Accuracy of XPS data acquisition and analysis is about  $\sim \pm 10\%$ .<sup>(226)</sup> However, it strongly depends on several factors, including peak shape, selection of background, precise peak fitting, and the correct use of ASF which could range from 4 to 5%.<sup>(227, 228)</sup> As mentioned before, XPS is a surface sensitive technique that is very sensitive to the elements located

in the surface or sub-surface regions, probably overestimating the atomic concentration from the top region compared to the layers underneath. Besides, for determining the concentration of the layers using equation 3.7, a homogeneous layer is assumed although in general this is not the real situation.

In principle, XPS is a surface sensitive technique, and its sensitivity is ascertained by how far into a sample an electron is photoemitted with a given kinetic energy. In fact, the photoelectron loses its energy when it travels through the material, process known as inelastic scattering. Such scattering can be described based on the Lambert-Beer law equation:

$$I = I_0 (e^{-\frac{d}{\lambda}}) \quad (3.13)$$

In which,  $I_0$  and  $I$  are the measured intensity of photoemitted electrons before and after passing through a sample. The parameter  $d$  is the thickness of the layer and  $\lambda$  is defined as an inelastic mean free path (IMFP) of electrons which describes how far an electron can travel through a material before losing kinetic energy.<sup>(229)</sup> The penetration depth of electrons into a material is determined based on the TPP-2M formula of QUASES-IMFP-TPP2M software (Ver. 3.0) in which IMFP values were calculated for elements, organic and inorganic compounds from measured energy loss functions for each solid with a relativistic version of the full Penn algorithm.<sup>(223, 230)</sup> Figure 3.8 represents the universal curve for estimating the IMFP as a function of kinetic energy of the electrons.<sup>(231)</sup> It should be noted that the represented universal curve is just a first approximation of IMFP.

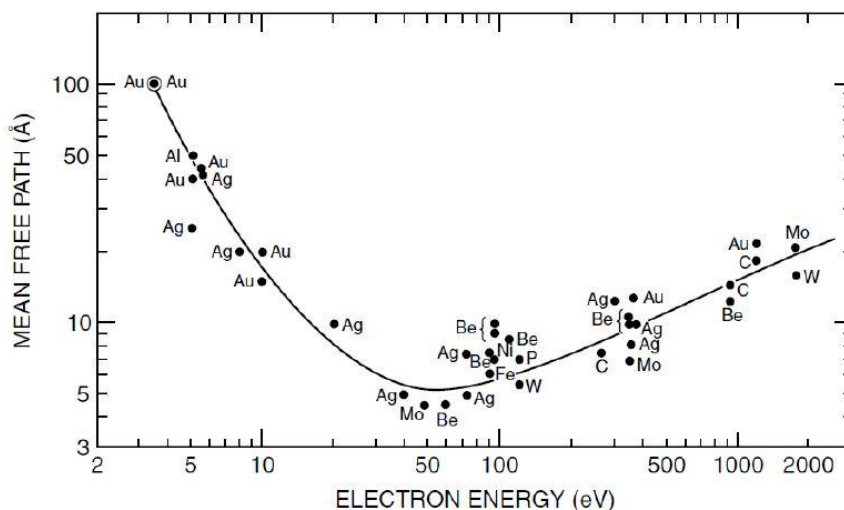


Figure 3.8. Universal curve indicating IMFP (or  $\lambda$ ) versus kinetic energy of electrons.<sup>(231)</sup>



Based on this curve, the electrons with kinetic energies of  $\sim 1$  keV posing an IMFP in order of a few nanometers. Such sampling depth is defined as the maximum depth normal to the sample surface where chemical information can be extracted.<sup>(229)</sup>

Another prominent feature of XPS is to estimate the coverage or thickness (d) of a layer A on top of a substrate B with the use of following equations:

$$I_A = I_A^\infty (1 - e^{-\frac{d}{\lambda_{IMFP}^A(E_A)} \cos\theta}) \quad (3.14)$$

$$I_B = I_B^\infty (e^{-\frac{d}{\lambda_{IMFP}^B(E_B)} \cos\theta}) \quad (3.15)$$

Where  $I_A$  and  $I_B$  are referred to the areas/intensities from the top layer and substrate, respectively.  $I_A^\infty$  and  $I_B^\infty$  are the areas/intensities from reference A and reference B.  $\lambda_{IMFP}^A$  and  $\lambda_{IMFP}^B$  is the inelastic mean free path of A and B, correspondingly. The last parameter of  $\theta$  is the angle between the path of the emitted electrons and the sample surface (also known as take-off angle). With changing that angle (tilting the sample), we can measure either bulk-sensitive ( $\theta = 90^\circ$ ) or surface-sensitive ( $\theta \leq 50^\circ$ ) XPS spectra. It should be taken into account that for the given equations a continuous and homogeneous layer is assumed.

XPS measurements were carried out after *in-situ* surface cleaning process in the XPS system (as exhibited in Fig. 3.9) using  $Ar^+$  ions created by a cold cathode ion source (ISE 5, Scienta Omicron) with an accelerating voltage and pressure of 500 eV and  $4 \times 10^{-6}$  mbar, respectively. In addition, the films were also characterized in the as-introduced state before the surface cleaning. To characterize the chemical composition of the films, XPS was performed using the hemispherical energy analyzers (Omicron EA125 for *in-situ* XPS, PHOIBOS HSA3500 for *ex-situ* XPS) with a dual Al/Mg X-ray anodes providing photon energies of 1486.6 and 1253.6 eV, respectively. The photo-emitted electrons were collected at normal emission, i.e., a take-off angle relative to the sample surface plane of  $90^\circ$  (bulk sensitive), to maximize the escape depth of the photoelectrons. Wide- (survey) and narrow-scan (core levels (CL)) XPS spectra were obtained with fixed pass energies of 50 and 20 eV and energy steps of 0.5 and 0.1 eV, respectively. When setting the pass energy to 20 eV, an overall resolution of 1.0 and 0.9 eV for Al and Mg  $K\alpha$  excitations was determined for our *ex-situ* XPS system in which those individual binary ( $InO_x$ ,  $GaO_x$ ,  $ZnO_x$ ) and quaternary (IGZO) oxides have been measured. Considering the same pass energy of 20 eV, an overall resolution of 1.0 eV was determined for Mg  $K\alpha$  excitation of *in-situ*

XPS system in which those  $\text{AlO}_x$  and  $\text{CeO}_x$  samples have been characterized. Furthermore, before performing any chemical analysis, we compared the acquired spectra for both Al and Mg  $K\alpha$  excitations to avoid spectral overlaps with additional Auger and/or satellite lines in the region of interest. The data acquisition was performed with the SpecsLab Prodigy program of *ex-situ* XPS (ver. 4.65.2-r89237, SPECS Surface Nano Analysis GmbH) and the SpecsLab processing software of *in-situ* XPS (ver. 2.39-r14670, SPECS Surface Nano Analysis GmbH); the CasaXPS software (ver. 2.3.20rev1.1e, CASA Software Ltd) was used to analyze and determine the elemental composition and particularly the metal to oxygen ratio of the films. To estimate surface composition, we weighted the raw spectral area with the respective atomic sensitivity factor, where the empirical values<sup>(224)</sup> have been corrected for the determined transmission function ( $T_F$ ) of the analyzer (as described above).

The bonding states of the main elements of the films were determined by fitting the CL spectra by peak decomposition considering a symmetric pseudo-Voigt function (Gaussian/Lorentzian product function) and a Tougaard background<sup>(232)</sup>. Prior to the fitting procedure, sample charging was corrected by calibrating the position of the main component of the C 1s CL spectra to 284.8 eV.<sup>(216)</sup> In the applied fit model, the peak widths of all chemically shifted components of a certain core level were fixed to the same value (taking into account the natural line width and the experimental resolution), while their energy positions were allowed to vary freely within a corresponding narrow energy range (typically  $\pm 0.1$  eV). The atomic concentrations of the desired elements were calculated by taking the raw area after background removal.



Figure 3.9. *In-situ* and *ex-situ* XPS systems in the chair of applied physics and semiconductor spectroscopy of BTU.

### 3.1.3 Field-emission scanning electron microscopy (FE-SEM)

The surface morphology of the prepared IGZO samples was examined using field-emission scanning electron microscopy (FE-SEM, Tescan Mira 3), as shown in Fig. 3.10. This system is also equipped with energy-dispersive X-ray spectroscopy (EDX, Bruker XFlash 6/10) to identify the elemental composition and to evaluate a homogeneous distribution of the elements. For these measurements, the working distance (WD) was fixed at 15 mm and the accelerating voltage was set to a low value of 7 kV to reduce charging effect. Besides, the maximum spatial resolution was about 2.0 nm. Further instrumental details are available elsewhere.<sup>(220)</sup>

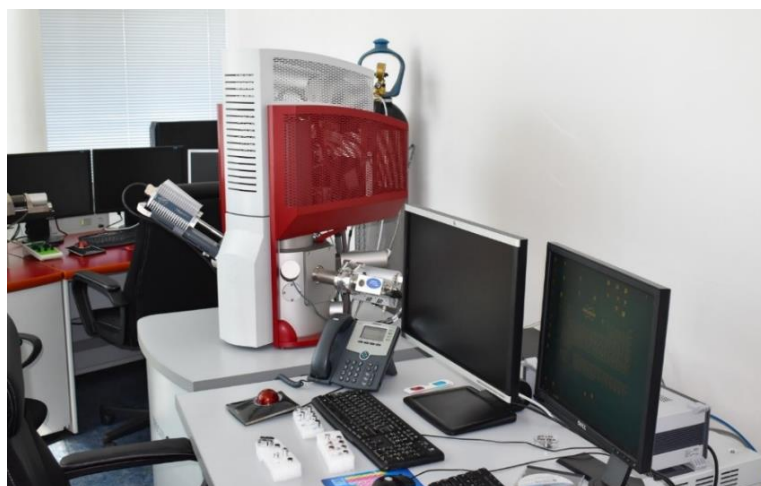


Figure 3.10. Tescan Mira3 instrument equipped with EDX. Nanomaterials group, Faculty of Mathematics and Physics, Charles University.<sup>(220)</sup>

### 3.1.4 Near-ambient pressure hard X-ray photoelectron spectroscopy (NAP-HAXPES)

The chemistry of the *in-situ* ALD prepared  $\text{CeO}_x$  layers was quantitatively investigated by SpAnTex (spectroscopic analysis with tender X-rays) end-station (Fig. 3.11), which was implanted at the KMC-1 beamline at the BESSY II synchrotron of the Helmholtz Zentrum Berlin. This station was designed for doing near-ambient pressure hard X-ray photoelectron spectroscopy (NAP-HAXPES) experiments to investigate a variety of materials from solid to liquid phases. The employed X-ray source includes a double crystal monochromator (DCM) with three pairs of *in-situ* exchangeable silicon crystals having plane directions of (111), (311), and (422), delivering photon energies ranging from 2.0 – 14.0 keV with a minimum approximated spot size of 0.4 mm (vertical)  $\times$  0.7 mm (horizontal). It should be noted that the location of such beamline is in the downstream of the focal point resulting in relatively larger spot sizes. The end-station benefits from a hemispherical energy analyzer (PHOIBOS 150 HV NAP, SPECS GmbH) where the angle between the incoming electrons and sample surface relative to the axis of the electron spectrometer pre-lens were set to  $90^\circ$  and  $\sim 5^\circ$  (polar angle), respectively. The aperture between the first differential pumping stage of the spectrometer and the analysis chamber was 0.3 mm, enabling measurements up to 30 mbar pressure. The spectrometer parameters of pass energy, step size, and dwell time were correspondingly fixed to 30 eV, 0.1 eV, and 0.2 s. The spectral acquisition was carried out using SpecsLab Prodigy software (SPECS GmbH). Further instrumental details are available at<sup>(233)</sup>.

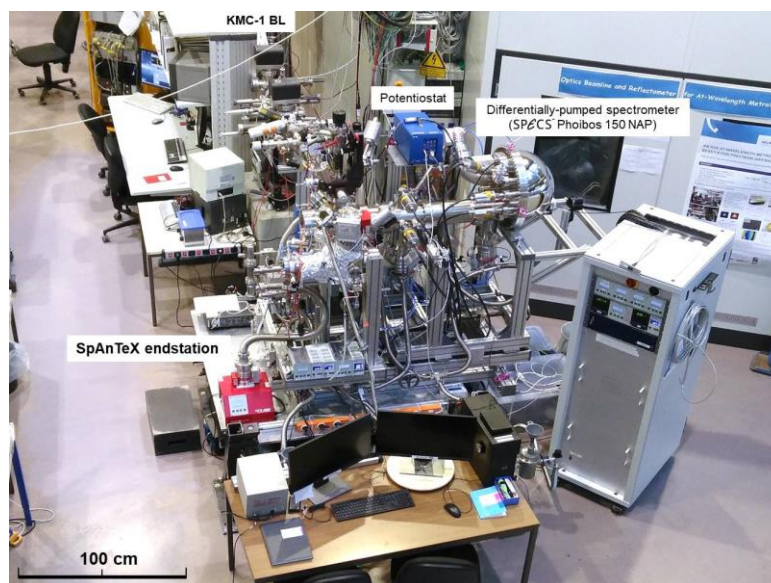


Figure 3.11. Beamline KMC-1 and SpAnTeX end-station at BESSY II, Berlin.<sup>(233)</sup>

### 3.2 ALD system

The successful preparation of high quality conformal thin films in a layer-by-layer growth mode requires an accurate and well-designed ALD system where the desired self-limiting reactions occur. However, to avoid undesirable mixing of two reactants, which results in uncontrolled deposition yielding non-conformal and rough layers, the deposition process must be made in two sequential reactant exposures under vacuum conditions. It is worth mentioning that using vacuum-base pressure during the ALD process causes the surface composition to remain unchanged or at least to reduce contamination inside of the reactor before and even during the deposition. Nevertheless, the use of *in-situ* ALD allows surface chemistry investigation of the deposited layers using a wide range of surface science techniques such as spectroscopic ellipsometry<sup>(234)</sup>, X-ray photoelectron spectroscopy<sup>(235)</sup>, Auger electron spectroscopy<sup>(236)</sup>, and low energy electron diffraction<sup>(237)</sup>. All provide detailed information on the ALD growth process.

In general, ALD systems can be divided into two standard configurations: *pump-type* (without inert gas flowing) compatible with high vapor pressure reactants, and *flow-type* with the use of inert gas flowing such as N<sub>2</sub> or Ar to deliver low/very low vapor pressure reactants through the ALD lines. Note that ALD mechanism based on the sequential pulses of reactants is typically slow for the *pump-type* ALD system in comparison with other configuration (i.e. *flow-type* ALD system). Therefore, an alternative way to expedite ALD process is to separate two half ALD cycles of reactants using purging step with introducing an

inert gas (either N<sub>2</sub> or Ar) that cleans the reactor from by-products and allows the exposures to be fulfilled closely together in a short period of time.<sup>(238-240)</sup>

### 3.2.1 Commercial SENTECH ALD system

Figure 3.12 displays the ALD system (SENTECH's SI ALD LL) developed by SENTECH for high-quality thin films and multilayers deposition using thermal or plasma processing. Such ALD system is able to be configured for depositing different classes of materials such as oxides, nitrides, and metals with high layer homogeneity and conformity from several microns scale down to nanometer size. Thermal and plasma ALD operation is supported in one reactor, allowing ultra-fast *in-situ* monitoring the layer-by-layer film growth using an ALD Real Time Monitor by spectroscopic ellipsometry through an optical shutter.

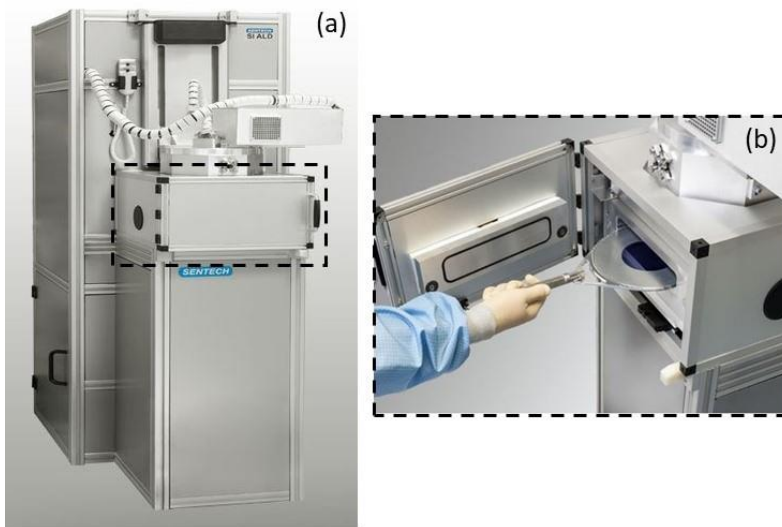


Figure 3.12. SENTECH ALD system (a), and associated load-lock chamber for introducing wafers (b).

The ALD reactor is equipped with a capacitive coupled plasma (SENTECH's CCP) source designed by SENTECH Instruments (as illustrated in Fig. 3.13) to fabricate high-quality films at lower temperatures, with lower processing time, and higher growth per cycle. This PEALD system provides a stable pulse operation in ALD cycles, synchronizing its plasma discharges to the growth process timing, triggering very efficient and stable pulsing. The plasma source is located on the upper flange of ALD reactor, operating with a radio frequency of 13.56 MHz where the substrate is placed outside the plasma



generation zone during the growth process. Therefore, according to PEALD configuration, the high energy of ions produced by plasma cannot damage the layer, and the surface does not see the light arising from plasma generation region. This configuration allows large area substrates, including wafers with a diameter of up to 200 mm. The main parts of the system are equipped with individual heaters and temperature controllers that enable applying specific temperatures to the chamber and reactants lines (three precursor lines and associated co-reactants lines), capable of heating up to 150 °C and 200 °C, respectively. Moreover, the substrate heating is carried out using a heating stage where temperature can be accurately controlled in a temperature range from room temperature to 500 °C.

The ALD process can be characterized under *operando* conditions using ALD Real Time Monitor (SENTECH's ALD-RTM; integrated into SENTECH ALD systems), which is a novel optical diagnostic tool allowing ultra-high resolution (20 ms) and a very high signal-to-noise ratio ( $\delta\Delta = 0.01^\circ$ ) of single ALD cycles, particularly for development and optimization of ALD recipes and systems. The use of spectroscopic ellipsometry operates within the wavelength ranges of UV-VIS (SE 800, SENTECH Instruments), enabling the determination of films property such as layer homogeneity, refractive index, growth rate per cycle, and thickness.

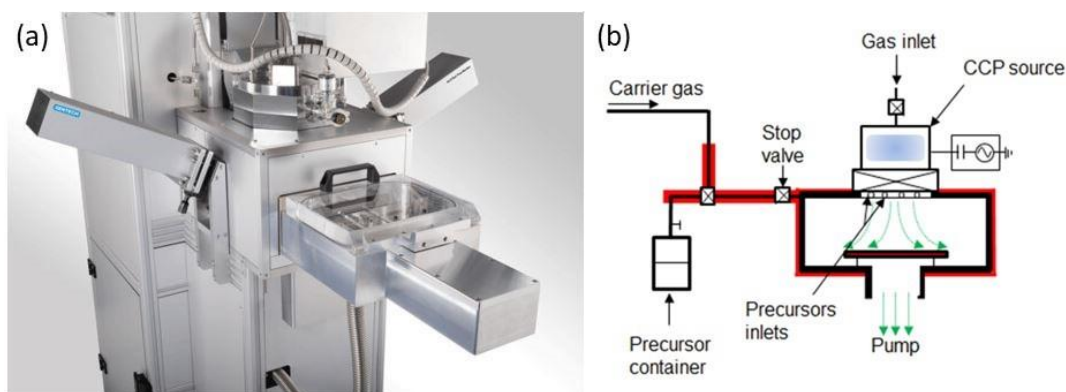


Figure 3.13. SENTECH PEALD system equipped with an *in-situ* ALD-RTM (a), and schematic representation of CCP source (b).

### 3.2.2 Homemade BTU ALD system

Figure 3.14 displays an image of our homemade *in-situ* ALD reactor capable of operating in two different ALD modes of pump and flowing approaches. From a technical point of view, the reactor is constructed from stainless steel components with an inner diameter of 20 cm. The desired sample is

loaded through an UHV-based introduction chamber and then transferred using a magnetic manipulator into a well-prepared vacuum-base pressure of the ALD reactor. It should be mentioned that the necessity of having high vacuum-base pressure ( $2 \times 10^{-8}$  mbar) is because the ALD reactor is directly attached to a XPS system for an *in-situ* characterization without exposing the sample to ambient conditions. Samples can be at room temperature or heated with or without the presence of gases using radiation heating. The temperature is initially calibrated using an infrared pyrometer (RAYMML TSSF1L, Raytek).

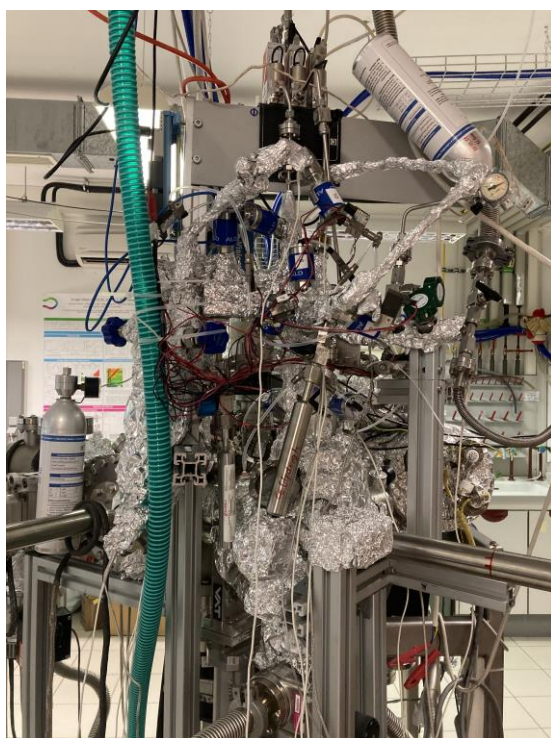


Figure 3.14. *In-situ* ALD system in the BTU's chair of applied physic and semiconductor spectroscopy.

A detailed description of ALD system is discussed below:

**i) *Flow-type reactor:*** For deposition of low-vapor pressure reactants, the use of *flow-type* reactor by ultrahigh purity nitrogen (in our case) is necessary to ease delivering materials towards the substrate. To accurately control the flux of nitrogen, two digital thermal mass flow controllers (F-201CV EL-FLOW, Bronkhorst High-Tech Inc.) with a maximum flow range of 200 sccm are applied on the individual ALD lines of precursors and co-reactants for deposition of the desired oxide-based materials. In principle, nitrogen ( $N_2$ ) is introduced from high-



purity (99.9999%) container/bottle (ALPHAGAZ) to a flux controller and then flows inside of defined ALD lines and related chamber to finally be exhausted using a scroll-pump. The designed bypass-pumping approach for the introduced ALD system enables pumping either with the turbo pump plus scroll (*pump-type*) or just with the scroll-pump that isolates turbo-pump (*flow-type*). The pressure inside of the flow tube can be manually controlled based on conductance variation using the throttle (membrane) valve placed above the exhaust pump. A capacitance manometer (UHV pressure gauge) is required to read out the flow tube pressure. ALD process is typically run under a pressure of 1 mbar. However, it depends on the reactor design and the chemical nature of reactants and/or materials.

**ii) Pump-type reactor:** The most straightforward approach is to directly introduce high vapor pressure reactants through a pressure difference between the reactor chamber (in vacuum) and the reactant vessel. A high-purity N<sub>2</sub> gas is used to reduce the purging time between sub-cycle, i.e. exposure to different reactants. The flux of N<sub>2</sub> for the purging process is precisely controlled using a mass flow controller.

**iii) Substrate heating/applying temperature to a substrate:** Our ALD system is able to heat the substrate using radiation (lamp) which is powered by a dc power supply. Temperature calibration is initially performed using a pyrometer (RAYMML TSSF1L, Raytek), where the reactor temperature could be maintained at a maximum temperature up to 350 °C.

**iv) Reactants pulsing:** Figure 3.15 shows a schematic drawing of the valves arrangement of the homemade *in-situ* ALD system, where the individual sub-lines have been designed according to the low, medium, and high vapor pressure reactants. Such ALD sub-lines configuration was done for pulse switching the reactants of metal oxide based materials such as AlO<sub>x</sub> with the use of TMA + water, and CeO<sub>x</sub> with the use of either commercial Ce(thd)<sub>4</sub> + O<sub>3</sub>. For such configuration, the gas pulse switching typically uses VCR connections with the sizes of ½ and ¼ inches, providing more flexibility and easy reconfiguration of the components to have desired arrangements. One of important benefits of VCR connections is that we can add more reactant channels to the reactor or even reconfiguring the switching valves to install a vessel (bubbler) is very straightforward. Besides, they can also be baked out to reach very low pressures.

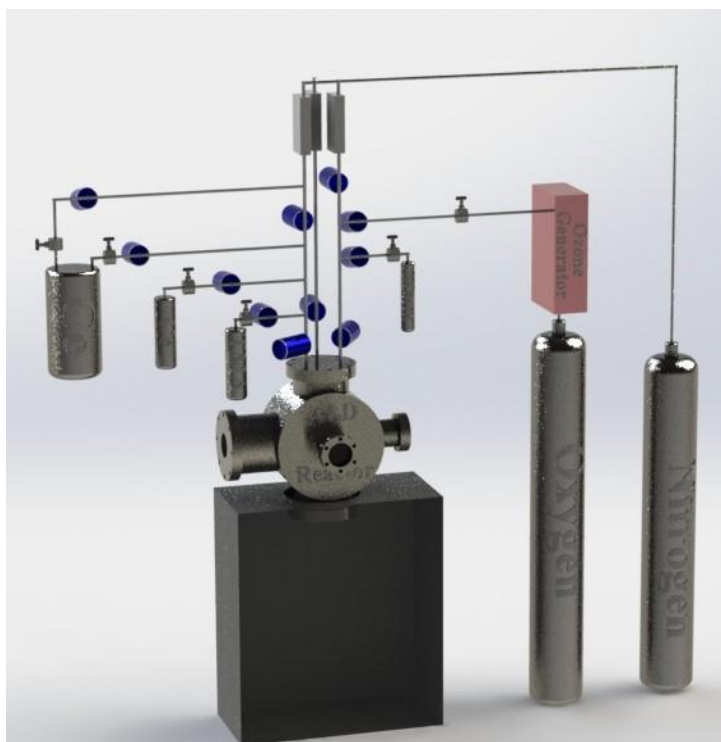


Figure 3.15. Demonstration of ALD system and applied valves.

The introduction of reactants into the ALD lines are carried out using the manual valves directly attached to the reactants container, and we can manually control the amount of materials. To digitally switch on/off pulsing reactants into the ALD lines, solenoid valves (Swagelok Inc.) are required which activate with the help of pneumatic valves (MAC Valves Inc.) and powered by a general multichannel valve driver (ADVANTECH USB-5862) interfaced to a computer. In the purge stage, all reactant valves are closed, and only  $N_2$  flows from a mass controller through the needle valve and following a solenoid valve into the corresponding line and chamber, being finally conducted to the exhaust line using turbomolecular and/or rotary pumps. Such purging process using nitrogen flow, prevents accumulation of residual particles from reactants inside the reactor. It should be mentioned that for those low vapor pressure reactants,  $N_2$  should also flow through the individual lines of reactants during pulsing to facilitate the transportation of particles towards the reactor and substrate.

**v) Running the system:** in order to operate the ALD cycling process in both pump and flow modes, a laboratory-based computer equipped with analog and digital input/output boards is utilized to monitor and control the electrical connections and ALD cycle through several application programs such as Advantech Device Manager (to control the multichannel driver and associated

valves), Mass controller (to define the flow rate), and Labview (Ver. 2020, National Instruments Corporation) where solenoid valves of ALD system can be activated. In addition, the multiple-channel pressure gauge controller (EDWARDS) monitors the pressures inside the ALD reactor.

### 3.3 Thin films deposition

This section discussed the fabrication process of the deposited wide band gap metal oxide in detail. All thin films have been prepared using TALD or PEALD techniques. For deposition of the individual binary oxides ( $\text{InO}_x$ ,  $\text{GaO}_x$ , and  $\text{ZnO}_x$ ) and their combination in a quaternary IGZO compound a commercial SENTECH ALD reactor with the capability of direct monitoring during ALD cycles was employed. In the case of the growth of the  $\text{AlO}_x$  and  $\text{CeO}_x$ , our homemade ALD reactor was utilized.

#### 3.3.1 Growth of metal oxides by SENTECH ALD reactor

##### 3.3.1.1 $\text{InO}_x$ deposition using PEALD

The indium oxide thin films were grown on 4-inch n-type Si (100) substrates at relatively low temperatures ranging from 80 to 200 °C using a PEALD system (SENTECH Instruments GmbH) equipped with a capacitively coupled plasma source as well as an ellipsometer for *in-situ* ALD real-time monitoring (SENTECH, ALD Real Time Monitor, ALD-RTM). For the determination of the ALD temperature window the substrate temperature was also increased up to 300 °C (Figure 4.2). In this deposition process, trimethylindium (TMIn) and oxygen plasma ( $\text{O}_2$ ) were periodically fed into the ALD reactor where the temperature of the precursor container was maintained at 45 °C to keep the precursor material in the solid state, i.e. below its melting point of 88 °C. This temperature warrants a sufficient vapor pressure enabling the low-temperature ALD process.

One ALD cycle was optimized to a sequence of TMIn/ $\text{N}_2$ / $\text{O}_2$ / $\text{N}_2$  with the feeding durations of 0.5 s/2 s/8 s/1 s, in which high-purity  $\text{N}_2$  (99.999%) was used as carrier and purging gas with a flow rate of 100 sccm through the reactor. These optimized pulse and purge durations are based on the evaluation of the parameter variations to achieve steady-state conditions where the deposition was controlled by the ALD-RTM for a time-efficient optimization. The optimized process parameters are listed in Table 3.1. The samples with 10 and 30 nm thick  $\text{InO}_x$  layers were prepared for X-ray photoelectron spectroscopy and spectroscopic

ellipsometry, respectively. The optical characterization was done at wafer scale, while  $10 \times 10 \text{ mm}^2$  pieces were used for the *ex-situ* XPS characterization separated from the middle of the 4-inch substrates.

To evaluate the film thickness evolution of the  $\text{InO}_x$  films, an *operando* measurement of delta ( $^\circ$ ) ellipsometric parameter was carried out. The acquired delta values were modeled using a one-layer modeling with a fixed refractive index of 1.86 (at 632.8 nm), determining the film thickness. Figure 3.16 exhibits the obtained delta and film thickness data versus ALD process time for the indium oxide thin films prepared at different temperatures. From these results, it can be clearly seen a step-like evolution (increasing and decreasing tendency) for all films at different temperatures because of the chemical adsorption of precursor and removing the ligands, where identical nucleation behavior and a linear film growth mechanism of ALD were observed.

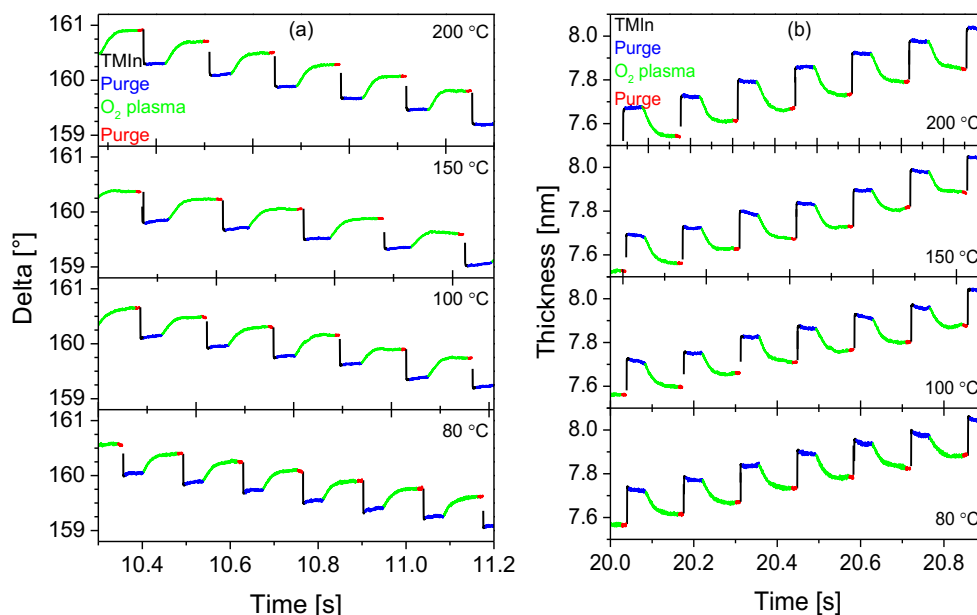


Figure 3.16. Ellipsometric parameter of delta (a), and evolution of  $\text{InO}_x$  film thickness as a function of the process time for different substrate temperatures within PEALD process (b). The thickness was obtained by modeling the *in-situ* ellipsometer data with a one-layer model with a constant refractive index of 1.86 (at 632.8 nm).

### 3.3.1.2 $\text{GaO}_x$ deposition using PEALD

The gallium oxide thin films were deposited on 4" n-type Si (100) substrates by PEALD with alternating pulses of trimethylgallium (TMGa) as Ga precursor and oxygen ( $\text{O}_2$ ) plasma as co-reacting oxidant. The deposition process

was carried out at four different substrate temperatures (80, 100, 150 and 200 °C) in the SI ALD reactor (SENTECH Instruments) equipped with a capacitively coupled plasma source as well as an ellipsometer for *in-situ* ALD real-time monitoring (SENTECH, ALD Real Time Monitor, ALD-RTM).

High-purity N<sub>2</sub> (99.999 %) was used as a carrier gas of TMGa with a flow rate of 90 sccm. The precursor line was closed during the plasma step and the nitrogen flow stopped. In this fabrication process, the plasma power and O<sub>2</sub> (high purity of 99.998 %) flow rate were set to 200 W and 150 sccm, respectively. One ALD cycle includes a 10 ms pulse of TMGa followed by a purge pulse of 2 s, an oxygen plasma pulse of 5 s, and a 2 s purge step. In this fabrication process, the GaO<sub>x</sub> layers with thicknesses of 10 and 30 nm were deposited for spectroscopic and optical characteristics, respectively, where the optical measurements were done at wafer scale. Moreover, for XPS measurements, the samples were prepared in the size of 10×10 mm<sup>2</sup> from the middle area of the wafers. The utilized PEALD parameters for deposition of the GaO<sub>x</sub> are summarized in Table 3.1.

Figure 3.17 shows the *in-situ* measurement of delta ellipsometer parameter and film thickness as a function of process time for the different applied substrate temperatures. The measurement shows film growth from the first cycle onwards, where the nucleation behavior for all four samples is very similar, and linear film growth was achieved for all applied temperatures. As typical for ALD, an increment and a reduction trend were observed in the film thickness due to precursor adsorption and ligand removal.

The film thickness increased while opening the ALD line before the actual precursor pulse. The second trend of increasing thickness is observed as soon as the precursor was dosed in the reactor. Remarkably, this double adsorption process was not attained during the first cycle of the films growth and occurs independent of substrate temperature. We assume that a certain amount of the precursor remained in the ALD line after closing due to its high volatility. When the ALD line was reopened and the flow of N<sub>2</sub> carrier gas was restarted, excess material was accidentally introduced into the reactor. Since the ALD lines were evacuated before initiating the deposition process, this double adsorption does not take place during the first cycle.

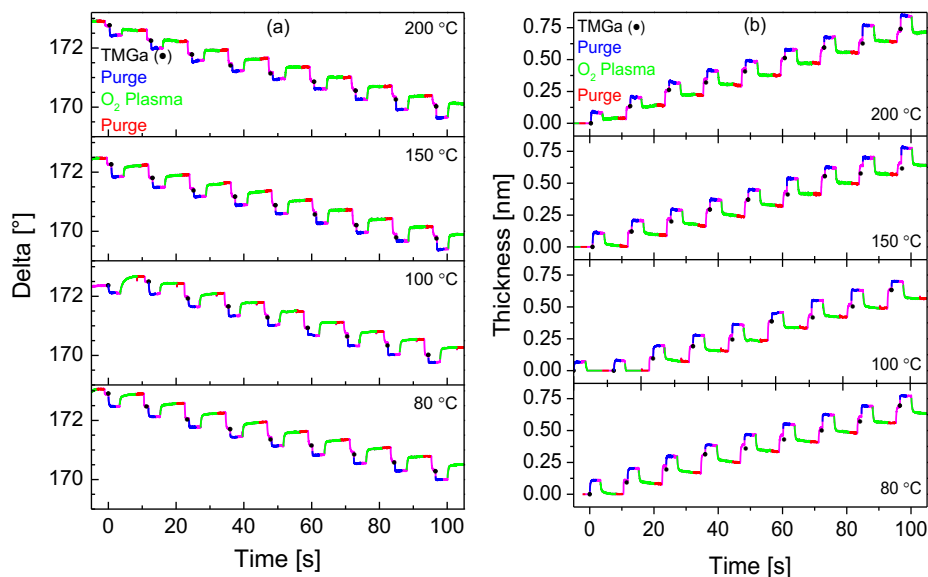


Figure 3.17. Ellipsometric parameter of delta (a), and evolution of GaO<sub>x</sub> film thickness as a function of the process time for different substrate temperatures within PEALD process (b). Color-coded of magenta denotes valve stop. The thickness was obtained by modeling the *in-situ* ellipsometer data with a one-layer model with a constant refractive index of 1.86 (at 632.8 nm).

### 3.3.1.3 ZnO<sub>x</sub> deposition using TALD

The ZnO thin films were grown on n-type Si (100) substrates at low deposition temperatures ranging from 80 to 200 °C using an ALD system (SENTECH Instruments GmbH) equipped with an ellipsometer for *in-situ* ALD real-time monitoring (SENTECH, ALD Real Time Monitor, ALD-RTM). In this gas phase process, diethylzinc (DEZ) as a source of Zn and H<sub>2</sub>O as an oxidant were subsequently fed into the ALD reactor until the desired film thickness was obtained. The ALD cycle structure was composed of a feeding sequence of DEZ/N<sub>2</sub>/H<sub>2</sub>O/N<sub>2</sub> with 40 ms/5 s/80 ms/5 s, respectively. The through-reactor flow rates of high-purity (99.999%) N<sub>2</sub> carrier (for DEZ) and purging gas and water were adjusted to 60 and 80 sccm, respectively. The ZnO<sub>x</sub> films with different thicknesses (10 and 30 nm) were grown for *ex-situ* XPS measurement and optical characterization purposes. It should be mentioned that the optical measurement was done at the wafer scale, while for XPS characterization, samples were prepared in the size of 10×10 mm<sup>2</sup> from the middle area of the wafers. Table 3.1 lists the fabrication parameters of the TALD-ZnO<sub>x</sub> films.

Figure 3.18 shows the change in the ellipsometric parameter of delta and the derived layer thickness as a function of the processing time. During the first cycle, a similar nucleation behavior was observed for all applied substrate temperatures. After the first diethylzinc pulse, there is no increase in layer thickness. This behavior is also reflected in the optical parameter delta (see Fig. 3.18 (a)). From the second cycle, the layer thickness increases. However, there are differences between the substrate temperatures. In general, it can be deduced that higher substrate temperature increases layer thickness after the DEZ pulse.

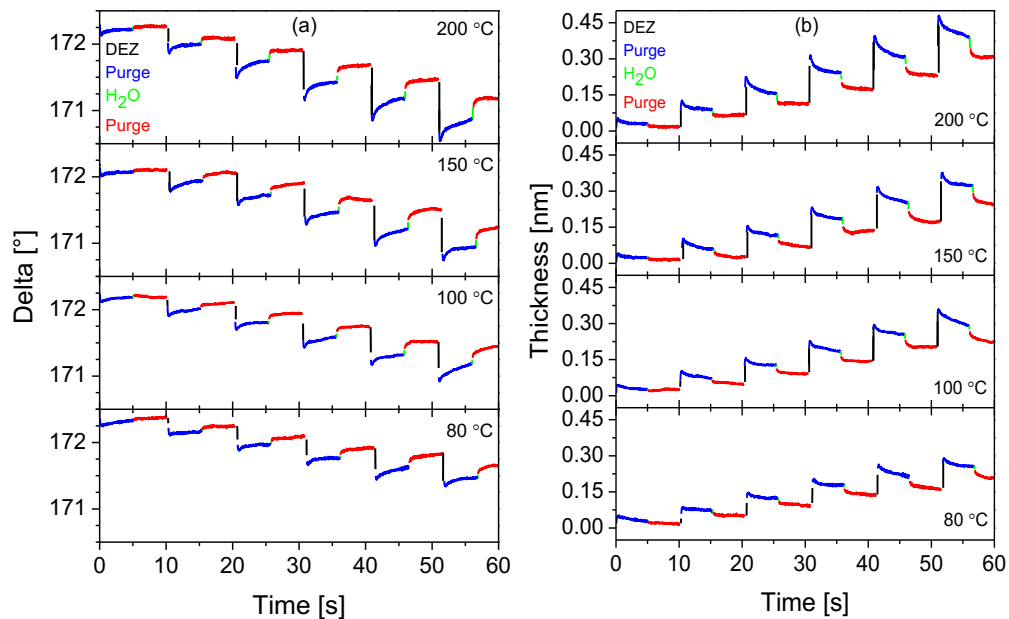


Figure 3.18. Ellipsometric parameter of delta (a), and evolution of ZnO<sub>x</sub> film thickness as a function of the process time for different substrate temperatures within TALD process (b). The thickness was obtained by modeling the *in-situ* ellipsometer data with a one-layer model with a constant refractive index of 1.86 (at 632.8 nm).

### 3.3.1.4 ZnO<sub>x</sub> deposition using PEALD

A low-temperature (150 °C) PEALD process of the zinc oxide layer using diethylzinc (DEZ) and O<sub>2</sub> plasma was established on Si (100) substrate for preparation of the quaternary PEALD-IGZO film. In this process, the ALD system (SENTECH Instruments GmbH) equipped with an ellipsometer for *in-situ* ALD real-time monitoring (SENTECH, ALD Real Time Monitor, ALD-RTM) was utilized. The ZnO<sub>x</sub> deposition was fulfilled considering the ALD pulse cycles of 0.04s DEZn/4s N<sub>2</sub>/5s O<sub>2</sub> plasma/1s N<sub>2</sub> in which high-purity N<sub>2</sub> (99.999%) with the flow rates of 120 and 150 sccm used to purge out the remaining precursor and

co-reactant, respectively. Table 3.1 lists the introduced experimental parameters of the individual PEALD and TALD prepared binary-oxides of the  $\text{InO}_x$ ,  $\text{GaO}_x$ , and  $\text{ZnO}_x$ .

TABLE 3.1. Main ALD parameters of the  $\text{InO}_x$ ,  $\text{GaO}_x$ , and  $\text{ZnO}_x$  films. Parameters are referred to plasma power ( $P_p$ ), substrate temperature ( $T_s$ ), precursor pulse duration ( $t_p$ ), co-reactant pulse duration ( $t_c$ ), purge time ( $t_{\text{purge}}$ ) and total pressure ( $P_t$ ), respectively.

Process parameters	PEALD- $\text{InO}_x$	PEALD- $\text{GaO}_x$	TALD- $\text{ZnO}_x$	PEALD- $\text{ZnO}_x$
Precursor	TMIn	TMGa	DEZ	DEZ
Co-reactant	$\text{O}_2$	$\text{O}_2$	$\text{H}_2\text{O}$	$\text{O}_2$
$P_p$ (W)	200	200	-	200
$T_s$ ( $^\circ\text{C}$ )	80, 100, 150, 200	80, 100, 150, 200	80, 100, 150, 200	150
$t_p$ (s)	0.5	0.01	0.04	0.04
$t_c$ (s)	8	5	0.08	5
$t_{\text{purge}}$ (s)	2, 1	2, 2	5, 5	4, 1
$P_t$ (Pa)	13.5	13.5	9	20

### 3.3.1.5 IGZO deposition using PEALD

The complex IGZO super-cycle was designed following a bottom-up approach, i.e. by initially defining the ALD growth characteristics (nucleation delay, growth per cycle (GPC) and total thickness) of each binary oxide and subsequently combining them in order to provide a multicomponent compound. Figure 3.19a shows the scheme of a generic super-cycle: each ALD deposit of an individual binary oxide A, B and C is carried out  $x$ ,  $y$  and  $z$  times, respectively, and then the whole super-cycle  $n$  times to achieve the desired thickness. Figure 3.19b displays the order of the ALD super-cycle in our particular case:  $[(\text{ZnO}_x)_x/(\text{GaO}_x)_y/(\text{InO}_x)_z]_n/\text{native SiO}_x/\text{Si (100)}$ . Moreover, as shown in Fig. 3.19c, IGZO thin films were deposited at  $150\text{ }^\circ\text{C}$  substrate temperature after defining a common ALD temperature window for all individual binary oxides via PEALD and TALD.

The ALD growths were carried on a SI ALD reactor configured with a capacitively coupled plasma source (SENTECH Instruments GmbH)<sup>(241)</sup> and



equipped with an ellipsometer for *in-situ* ALD real-time monitoring (SENTECH, ALD Real Time Monitor, ALD-RTM)<sup>(242)</sup>. The PEALD-IGZO films were prepared considering the sequence reactants pulses of [0.04s TMIn/4s N<sub>2</sub>/5s O<sub>2</sub> plasma/1s N<sub>2</sub>], [0.01s TMGa/2s N<sub>2</sub>/5s O<sub>2</sub> plasma/1s N<sub>2</sub>], and [0.04s DEZn/4s N<sub>2</sub>/5s O<sub>2</sub> plasma/1s N<sub>2</sub>] applied for the individual sub-oxide-cycles of the InO<sub>x</sub>, GaO<sub>x</sub>, and ZnO<sub>x</sub>, respectively. Within the ALD process, high-purity N<sub>2</sub> (99.999%) was used for purging the reactor from unreacted precursor molecules of TMIn, TMGa, and DEZn with a flow rate of 100, 90, and 120 sccm, correspondingly, where a flow rate of 150 sccm was fixed for purging the remained co-reactant of O<sub>2</sub> plasma. Table 3.2 summarizes the technical details for the PEALD (InO<sub>x</sub>, GaO<sub>x</sub>, ZnO<sub>x</sub>) and TALD (ZnO<sub>x</sub>) recipes used for each binary oxides. Finally, 4-inch n-type Si (100) wafers with a native oxide layer of about 1.7 nm were used as substrate.

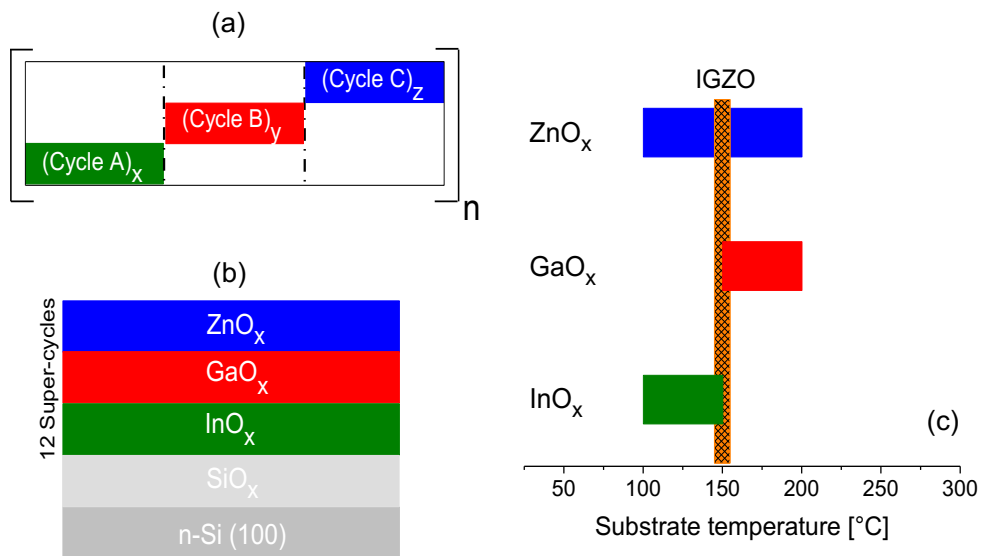


Figure 3.19. Schematic of a super-cycle approach (a), sub-layer sequence of IGZO super-cycle (b), and ALD temperature windows for individual InO<sub>x</sub>, GaO<sub>x</sub> and ZnO<sub>x</sub> deposits to evaluate the IGZO process temperature (indicated by a vertical straight line) (c).

Table 3.2 Deposition parameters for PEALD (InO<sub>x</sub>, GaO<sub>x</sub>, ZnO<sub>x</sub>) and PEALD/TALD (ZnO<sub>x</sub>) recipes of the IGZO layers. Parameters are referred to plasma power ( $P_p$ ), substrate temperature ( $T_s$ ), precursor pulse duration ( $t_p$ ), co-reactant pulse duration ( $t_c$ ), purge time ( $t_{purge}$ ) and total pressure ( $P_t$ ), respectively.

Process parameters	PEALD			TALD
	InO <sub>x</sub>	GaO <sub>x</sub>	ZnO <sub>x</sub>	ZnO <sub>x</sub>
Precursor	TMIn	TMGa	DEZ	DEZ
Co-reactant	O <sub>2</sub>	O <sub>2</sub>	O <sub>2</sub>	H <sub>2</sub> O
$P_p$ (W)	200	200	200	-
$T_s$ (°C)	150	150	150	150
$t_p$ (s)	0.04	0.01	0.04	0.04
$t_c$ (s)	5	5	5	0.08
$t_{purge}$ (s)	4, 1	2, 1	4, 1	5, 5
$P_t$ (Pa)	10	20	20	9

### 3.3.2 Homemade BTU ALD reactor

#### 3.3.2.1 AlO<sub>x</sub> deposition using TALD

The aluminum oxide thin films were deposited on 10×10 mm<sup>2</sup> of titanium (Ti)-coated Si (100) substrates at room and 200 °C temperatures using an ALD system equipped with *in-situ* XPS system. Before deposition, using thermal evaporation technique, Si wafers were coated with titanium as a buffer layer. According to the literature<sup>(243, 244)</sup>, titanium material thin films can be utilized as a barrier and/or protective coating because of their barrier and anti-corrosion properties. Nevertheless, the bilayer of Al<sub>2</sub>O<sub>3</sub>/TiO<sub>2</sub> has been reported as a promising multilayer configuration for a corrosion-resistant coating.<sup>(245, 246)</sup> Preparation details are described underneath.

##### 3.3.2.1.1 Ti growth

The pure metallic Ti wire (99.99%, Alfa Aesar) was used for Ti evaporation. As schematically demonstrated in Figure 3.20, the Ti evaporator consists of a UHV flange in which three metals feedthrough are assembled for

biasing and holding the wires. Such three legs connections allow installing two different Ti filaments configuration where one connector acts as a common bias leg. For the first configuration, three wolframs (tungsten; W) wires with length and diameter of 120 and 0.25 mm were twisted together, respectively. The provided Ti wire with a diameter of 0.25 mm is covered the middle part of the tungsten filament. The first prepared evaporator is mounted on two of three legs with the help of screws and bolts. The second evaporator includes one Ti wire with a length and diameter of 120 and 1 mm, respectively, directly installed on the common and third connection legs.



Figure 3.20. Configuration of Ti evaporator system in the BTU's chair of applied physic and semiconductor spectroscopy.

The initial pressure in the prep-chamber was in the range of  $\sim 2 \times 10^{-8}$  mbar. At this point, the Ti evaporation on Si (100) substrates was initiated by passing a current of 13 A through the desired configured legs with a voltage fixed at 4.1 V. The duration of evaporation was 95 min (appropriate time to cover the substrates entirely) in the pressure of  $\sim 4 \times 10^{-8}$  mbar. Figure 3.21 displays the performed Ti evaporation.

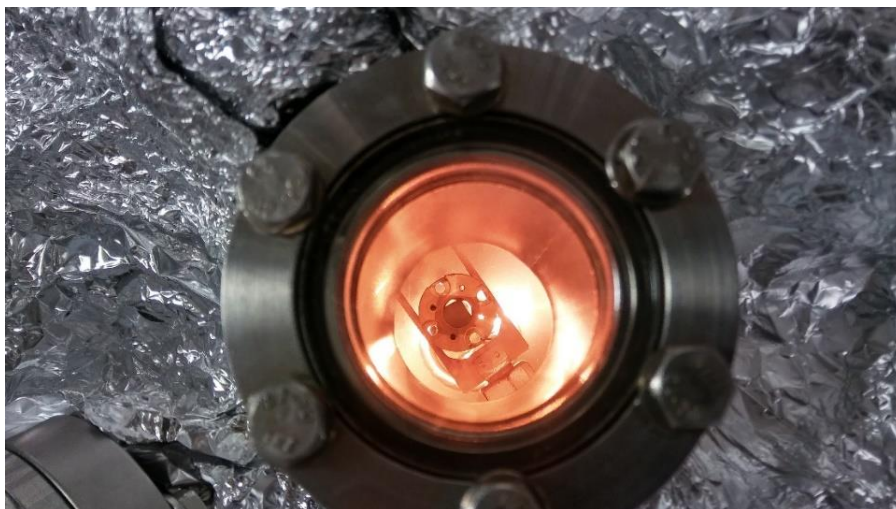


Figure 3.21. Demonstration of Ti evaporation in ALD-XPS prep-chamber of the chair of applied physic and semiconductor spectroscopy of BTU.

#### 3.3.2.1.2 AlO<sub>x</sub> growth at room temperature

The prepared substrates (Ti/Si (100)) were loaded into an *in-situ* ALD reactor with a base pressure of  $\sim \times 10^{-8}$  for the growth of aluminum oxide with trimethylaluminum (TMA) as an aluminum source and H<sub>2</sub>O as an oxidant source. A high-purity N<sub>2</sub> (99.9999%, ALPHAGAZ) with a flow rate of 50 sccm was employed in a *pump-type* approach to remove any remaining by-products of precursor and co-reactant from the ALD reactor. For this process, each ALD cycle consists of 0.5 s TMA/1 s N<sub>2</sub>/0.5 s H<sub>2</sub>O/1 s N<sub>2</sub>. The time between two cycles was set to 15 s. Two sequential (0.5 s) purging processes for individual half-cycle were used to purge the reactor efficiently. During the ALD process, the base pressure inside of the reactor slightly increased to  $\sim \times 10^{-6}$  where the individual pressures of TMA, N<sub>2</sub>, and H<sub>2</sub>O were  $\sim \times 10^{-4}$ ,  $\times 10^{-3}$ , and  $\times 10^{-3}$  mbar, respectively. It should be noted that the total number of ALD cycles was fixed to 100, and the temperature of precursor, co-reactant, and nitrogen lines was kept at room temperature. The thickness of the deposited AlO<sub>x</sub> film was determined by XPS technique analysis and estimated to be  $\sim 10$  nm.

#### 3.3.2.1.3 AlO<sub>x</sub> growth at 200 °C

For deposition of 100 cycles AlO<sub>x</sub> at 200 °C, the same growth process and associated parameters as at room temperature were considered. The reactor was also heated to 120 °C to provide a homogeneous temperature inside the chamber to avoid potential condensation at the walls, while the temperature of precursor,

co-reactant, and nitrogen lines was kept at room temperature. Figure 3.22 shows *in-situ* heating the substrate by radiation technique. The base pressure inside the reactor slightly increased to  $\sim \times 10^{-5}$ , while the individual pressures of TMA,  $N_2$ , and  $H_2O$  were kept similar to  $AlO_x$  growth at room temperature ( $\sim \times 10^{-4}$ ,  $\times 10^{-3}$ , and  $\times 10^{-3}$  mbar, respectively). The surface chemistry investigation of the half and complete cycles was done using an *in-situ* XPS system.

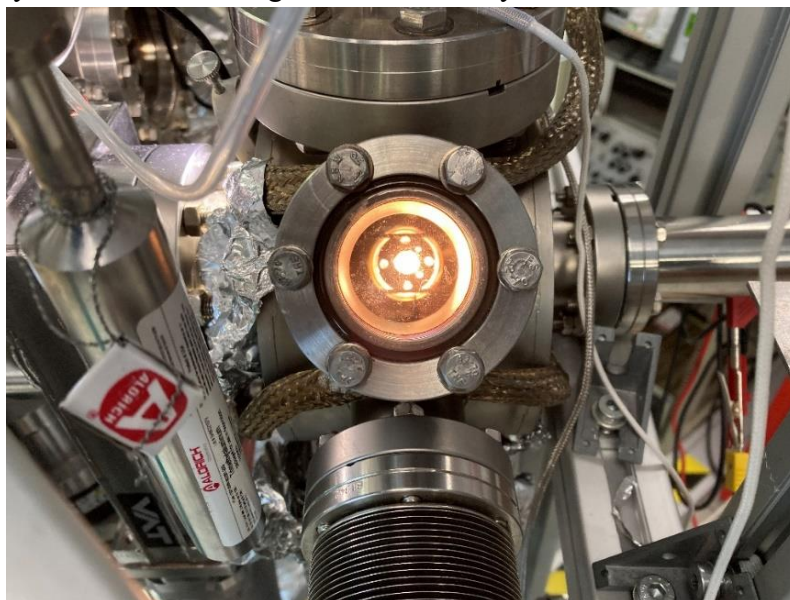


Figure 3.22. *In-situ* heating using radiation technique in ALD-XPS prep-chamber of the chair of applied physics and semiconductor spectroscopy of BTU.

Nevertheless, post-deposition annealing (PDA) in sequence temperature steps of 200 °C was carried out using heating to investigate the effect of annealing treatment on the film composition and the evolution of carbon presence, which originates as a residue from the TMA precursor during ALD cycle. The used deposition parameters of the TALD- $AlO_x$  are listed in Table 3.3.

TABLE 3.3. Main TALD parameters of AlO<sub>x</sub> films. Parameters are referred to substrate temperature ( $T_s$ ), post-deposition annealing (PDA), precursor pulse duration ( $t_p$ ), co-reactant pulse duration ( $t_c$ ), and purge time ( $t_{purge}$ ), respectively.

Process parameters	TALD-AlO <sub>x</sub>
Precursor	TMA
Co-reactant	H <sub>2</sub> O
$T_s$ (°C)	RT, 200
PDA (°C)	200 - 800
$t_p$ (s)	0.5
$t_c$ (s)	0.5
$t_{purge}$ (s)	1, 1

### 3.3.2.2 CeO<sub>x</sub> deposition using TALD

Here the growth of the cerium oxide at  $\sim 250$  °C using cerium tetrakis(2,2,6,6-tetramethyl-3,5-heptanedionato) (Ce(thd)<sub>4</sub>) (99.99%, EpiValence) as a source of cerium and ozone (O<sub>3</sub>) as a strong oxidant is reported. The CeO<sub>x</sub> thin films were deposited on different substrates of 300 nm thick SiO<sub>2</sub>, and 10 nm AlO<sub>x</sub>/Si (100) to investigate the role of different interfaces on the growth of cerium oxide thin layer. It should be noted that because of low-vapor pressure of Ce(thd)<sub>4</sub> precursor, pseudo-boost conditions are required to obtain enough vapor to be delivered to the ALD reactor chamber.<sup>(247)</sup> Transportation of the cerium precursor and ozone co-reactant onto the substrate surface was carried out in a *flow-type* fashion by high-purity (99.9999%, ALPHAGAZ) nitrogen (N<sub>2</sub>) carrier gas.

It is worth mentioning that the critical growth parameters of cerium evaporation temperature, time between two ALD cycles, and substrate temperature have been optimized in order to obtain growth rates close to 0.2 Å/cycle,<sup>(248, 249)</sup> where the remaining parameters of flow rate, temperatures of ALD reactor and lines (N<sub>2</sub>, O<sub>3</sub>) were fixed to 20 sccm, 120 °C, and 90 °C, respectively. First, different applied temperatures of 140, 160, and 180 °C to the cerium bubbler were considered (Fig. 3.23) to find the optimum vapor pressure of the Ce precursor. According to the literature,<sup>(249)</sup> the appropriate Ce(thd)<sub>4</sub> evaporation can be obtained at a temperature of 140 °C. However, in this work,

the optimum temperature was found to be 160 °C, with enough vapor pressure and fewer impurities such as sodium. Precisely the presence of sodium mainly originates from sodium hydroxide (NaOH) used to synthesis the cerium precursor.<sup>(250)</sup> Such expected impurity could be controlled via optimizing the deposition parameters.

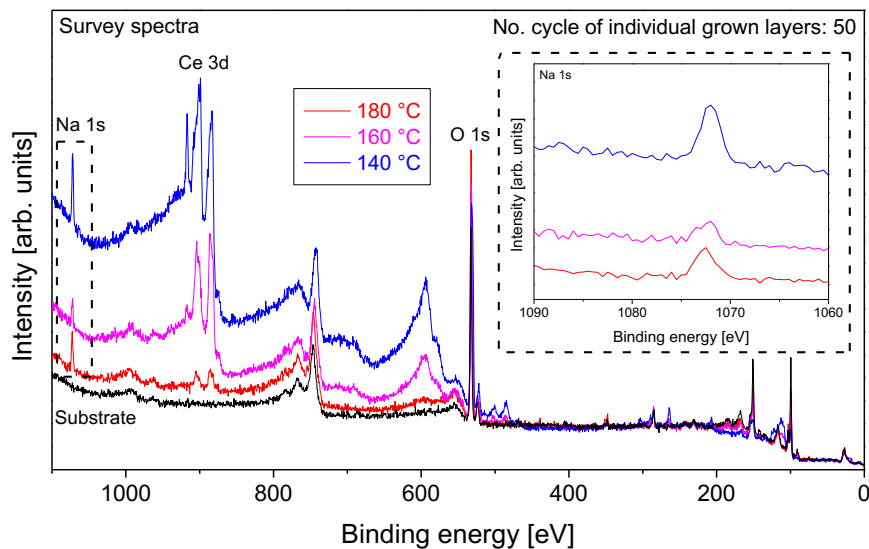


Figure 3.23. Optimizing the cerium evaporation temperature.

One important growth parameter that impacts the deposition process is the time between two ALD cycles, when the ALD reactor is purged. Figure 3.24 displays the influence of time between cycles on the intensity of the main core level spectra corresponding to the cerium oxide thin film. There is no significant change (considering the baselines) between the applied reaction times of 20, 25, and 30 s. However, it has been found that 20 s can provide enough time for chemical reactions on the substrate surface to obtain a relatively higher growth rate.

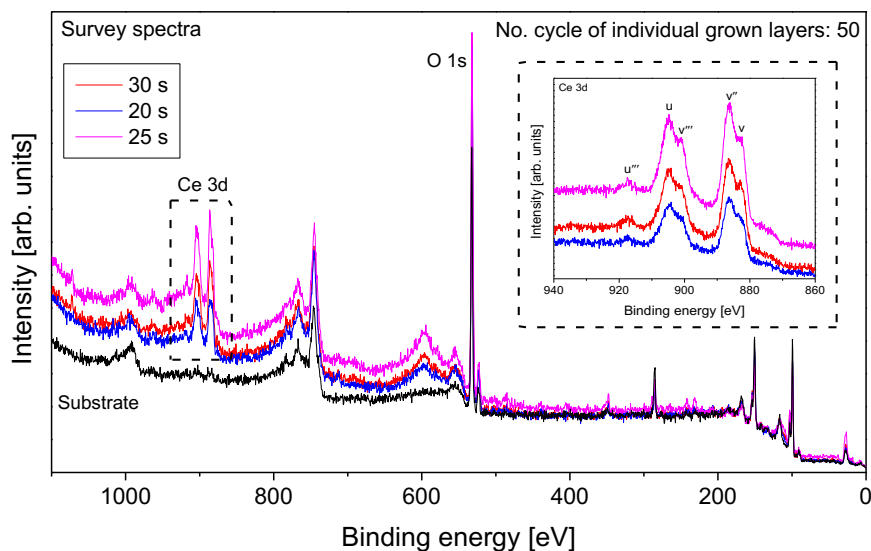


Figure 3.24. Optimizing time between two ALD cycles.

The substrate temperature is the last optimized parameter that plays an important role in ALD mechanism. The ALD window for the cerium oxide thin film using  $\text{Ce}(\text{thd})_4$  precursor and  $\text{O}_3$  is 175 to 250 °C.<sup>(249)</sup> The represented optimization of substrate temperature (Fig. 3.25) was carried out using a lamp (OSRAM, 60 W halogen lamp) and applying different voltages where the value of 7 V was found as an appropriate voltage that can deliver an estimated temperature of  $\sim 250$  °C.

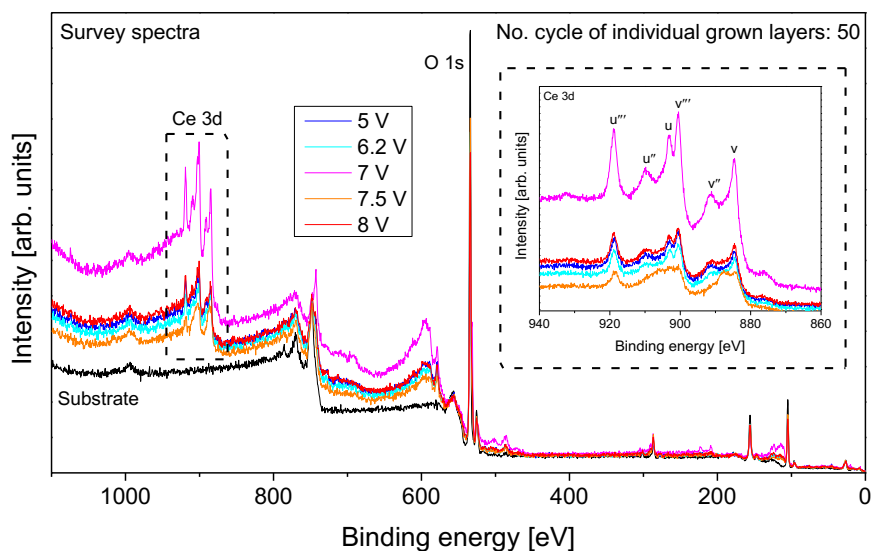


Figure 3.25. Optimizing the substrate temperature of the ALD-cerium oxide thin film.



Based on the performed optimization, the precursor evaporation and substrate temperatures were fixed to  $\sim 160$  and  $\sim 250$  °C, respectively. Besides, the temperature of the nitrogen and O<sub>3</sub> lines was kept at  $\sim 90$  °C in addition to the deposition zone (chamber's wall) temperature of  $\sim 120$  °C.

The ozone was produced from high-purity (99.9999%, ALPHAGAZ) oxygen source in an ozone generator (OXF-Series, Oxidation Technologies, LLC.), where the inlet and outlet pressures were adjusted to be 20 and 10 psi, respectively. The pulse times for Ce precursor and O<sub>3</sub> oxidizer were relatively optimized to be 1 s and 2.5 s, correspondingly, with a purging time of 1.5 s and 3 s between pulsing the reactants. It should be mentioned that the time between two ALD cycles was 20 s to provide enough reaction time on the substrate surface. Furthermore, the pressure of the Ce, N<sub>2</sub>, and O<sub>3</sub> individual pulses during the ALD cycle was recorded with the values of  $\sim 2.2$ , 2, and 1.5 mbar, respectively. The growth parameters of the cerium oxide deposited by TALD are listed in Table 3.4.

TABLE 3.4. Main parameters of TALD-CeO<sub>x</sub> films. Parameters are referred to substrate temperature ( $T_s$ ), precursor pulse duration ( $t_p$ ), co-reactant pulse duration ( $t_c$ ) and purge time ( $t_{purge}$ ), respectively.

Process parameters	TALD-CeO <sub>x</sub>
Precursor	Ce(thd) <sub>4</sub>
Co-reactant	O <sub>3</sub>
$T_s$ (°C)	$\sim 250$
$t_p$ (s)	1
$t_c$ (s)	2.5
$t_{purge}$ (s)	1.5, 3



## Chapter 4

# RESULTS AND DISCUSSION

This chapter documents the study of the promising binary oxides of  $\text{InO}_x$ ,  $\text{GaO}_x$ ,  $\text{ZnO}_x$  for a bottom-up fabrication of complex quaternary indium-gallium-zinc oxide compound, following, quantitative investigation of the synthesized IGZO films. Subsequently, the *in-situ* surface chemistry analysis of the aluminum oxide and cerium oxide samples is also documented.

### 4.1 PEALD of $\text{InO}_x$ thin films

This section discusses the optical and chemical analysis of the PEALD prepared binary indium oxide layers using  $\text{TmIn}$  and  $\text{O}_2$  plasma at low-temperatures of 80 to 200 °C.

#### 4.1.1 Growth and optical characteristics

The growth mechanism and optical properties of the low-temperature deposited indium oxide thin films were investigated by ellipsometric measurements. Figure 4.1 reveals a linear increment of the film thickness as a function of the ALD number of cycles. On the one hand, a linear behavior begins from early processing time for substrate temperatures of 80 and 200 °C. Such linearity evolution of thickness reveals that the growth of the films was taking place without any nucleation delay. During the deposition process, a slight deviation in film growth rate was observed for samples deposited at 80 and 200 °C. On the other hand, intermedium temperatures, i.e. 100 and 150 °C, show a growth delay, starting a linear evolution from 500 cycles.

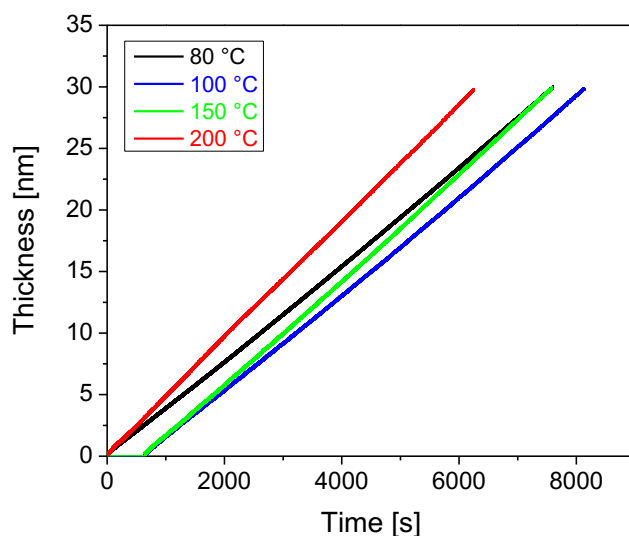


Figure 4.1. Films thickness evolution as a function of process time for PEALD-InO<sub>x</sub> films deposited at different substrate temperatures.

Figure 4.2 shows the growth per cycle (GPC), thickness inhomogeneity, and refractive index values of the InO<sub>x</sub> films as a function of substrate temperature. The GPC increases from 0.52 Å/cycle at 80 °C to 0.64 Å/cycle at 200 °C with relatively constant values around 0.56 Å/cycle in the temperature range of 100 to 150 °C. During the ALD-process optimization, a wide range of substrate temperatures was investigated from 100 to 300 °C in 25 °C steps (inset of Fig. 4.2a). The low and high GPC values at temperatures of 80 and ≥ 200 °C, respectively, could be due to incomplete surface chemical reactions at low temperatures and the thermal decomposition of TMIIn at higher temperatures.<sup>(251, 252)</sup> It should be highlighted that the obtained growth rate of ~ 0.56 Å/cycle using PEALD with TMIIn and O<sub>2</sub> plasma within a low-temperature range of 100 to 150 °C is higher than the reported indium oxide films deposited by ALD with TMIIn/H<sub>2</sub>O and TMIIn/O<sub>3</sub>, where GPC values of ~ 0.4 and 0.46 are reported.<sup>(253, 254)</sup> Probably, the presence of high-energy O<sub>2</sub> plasma ions in the PEALD process causes a significant increase in the chemical reactivity of the film surface, leading to an increase of GPC in comparison with the oxidants of H<sub>2</sub>O or O<sub>3</sub>.<sup>(34, 255)</sup> Therefore, the combination of TMIIn precursor and O<sub>2</sub> plasma offers a constant GPC within the ALD window of 100 and 150 °C, which is accompanied by a highly uniform film thickness that only exhibits a slight variation of 1.2% across the 4-inch wafers (see Fig. 4.2b). However, the film thickness homogeneity significantly decreases at a substrate temperature of 200 °C which could be related to the TMIIn decomposition. A considerable increase in GPC at a higher

deposition temperature of  $\sim 250$  °C was also observed for the ALD of indium oxide using TMIIn and  $\text{H}_2\text{O}$ .<sup>(256, 257)</sup>

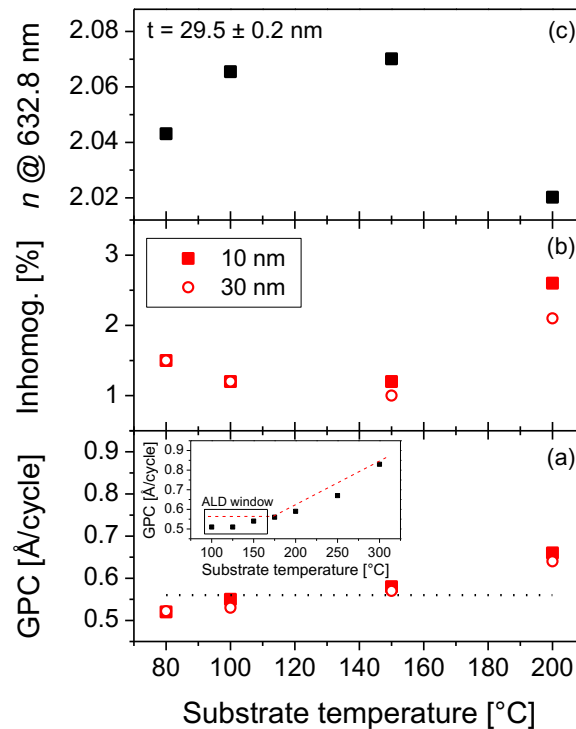


Figure 4.2. GPC (a), inhomogeneity (b), and refractive index (c) of the as-deposited PEALD- $\text{InO}_x$  films in dependence on the substrate temperature. The inset of (a) shows the GPC for a wider substrate temperature range up to 300 °C.

The applied PEALD process using TMIIn and  $\text{O}_2$  plasma delivers very high layer uniformity over large substrates and works at considerably lower deposition temperatures, making it particularly suitable for thermally sensitive substrates. Furthermore, most of the indium precursors provide more complex surface chemistry than TMIIn, which might lead to undesirable side reactions during the growth, resulting in relatively high amount of carbon in the range of  $\sim 7\%$  in the bulk.<sup>(258)</sup> On the contrary, TMIIn enables the growth of high-quality  $\text{InO}_x$  films in analogy to the metal sources of trimethylaluminum and trimethylgallium in the ALD of aluminum oxide and gallium oxide materials.<sup>(34, 242)</sup> Besides, there is a very similar reaction mechanism for the trimethyl ligands of the metal precursors (Al, Ga, In) and the oxygen plasma in the PEALD process of the corresponding oxides. Moreover, its combination with  $\text{O}_2$  plasma supports low-thermal-budget processes.

The optical properties (refractive index and band gap values) of the PEALD-InO<sub>x</sub> film were investigated by ellipsometry. Figure 4.2c shows the refractive index (at 632.8 nm) of the deposited layers, obtained using SE measurements and revealing a slight increase from 2.04 at 80 °C to 2.07 at 150 °C, with an abrupt reduction to 2.02 for the layer deposited at 200 °C. The highest refractive index of 2.07 at 150 °C is comparable to the reported values ranging from 2.07 to 2.09 for films deposited by TMIIn/O<sub>3</sub> at 100 – 250 °C<sup>(254)</sup>, close to the value of 2.09 reported for bulk indium oxide.<sup>(259)</sup> Some hypotheses could explain the changes in the refractive index. Firstly, the refractive index depends on the material density; a low refractive index value indicates that the film is less dense and possibly in an amorphous phase. In particular, reduction of the film densities may imply a porous morphology of the layers, probably causing air trapping, which would influence the optical properties of the indium oxide films.<sup>(260)</sup> Therefore, the low refractive index values at lower deposition temperatures could indicate an amorphous structure.<sup>(33)</sup> In the case of high-temperature depositions (200 °C), indium oxide films prepared by ALD with TMIIn/H<sub>2</sub>O have shown a decrease in the grain sizes while increasing the deposition temperature due to changes in the nucleation rate.<sup>(253)</sup> An abrupt reduction in the refractive index of the PEALD prepared InO<sub>x</sub> film at 200 °C might be due to the partial decomposition of TMIIn precursor resulting in reducing the order of the film as the growth velocity increases. On the contrary, when indium oxide layers are deposited by other techniques such as magnetron sputtering, CVD, and even by ALD with InCp/H<sub>2</sub>O<sub>2</sub> or dimethyl (N-ethoxy-2, 2-dimethyl-carboxylicpropanamide)indium/H<sub>2</sub>O, a densification of the films with increasing temperature has been observed.<sup>(260-263)</sup>

Figure 4.3 illustrates the extracted optical direct and indirect band gaps from the absorption coefficient spectra (as shown in the inset of Fig. 4.3) for the as-deposited PEALD-InO<sub>x</sub> films at different substrate temperatures. It can be clearly seen that the band gap values increase as the deposition temperature rises, moving from 3.0 eV at 80 °C to 3.5 eV at 200 °C. Those band gap values are in agreement with the literature<sup>(52, 261)</sup>. It should be mentioned that the obtained direct band gap of the as-deposited films is slightly lower than the reported values (3.5 to 3.6 eV) at 150 °C for the PEALD of indium oxide layers prepared with Et<sub>2</sub>InN(SiMe<sub>3</sub>)<sub>2</sub> and O<sub>2</sub> plasma.<sup>(42)</sup> Moreover, for the indirect band gap a constant value of 2.7 eV was found between 80 to 100 °C, with an increment trend to 2.9 eV at 200 °C, which is comparable to that of indium oxide single crystals, where a fundamental band gap of 2.7 and 2.9 eV was determined by photoemission spectroscopy.<sup>(264, 265)</sup> The observed tendency of the direct and indirect band gaps

with increasing substrate temperature for the prepared PEALD-InO<sub>x</sub> films might be due to the chemical state of the layers, e.g., reduced carbon contents, incorporated hydroxyl groups, more considerable atomic distances due to oxygen vacancies, changes in atomic coordination, and/or elimination of defect states, of the as-deposited layers<sup>(52, 266)</sup>. These possibilities have been investigated by XPS (see next section). Table 4.1 summarizes the optical properties of the indium oxide films.

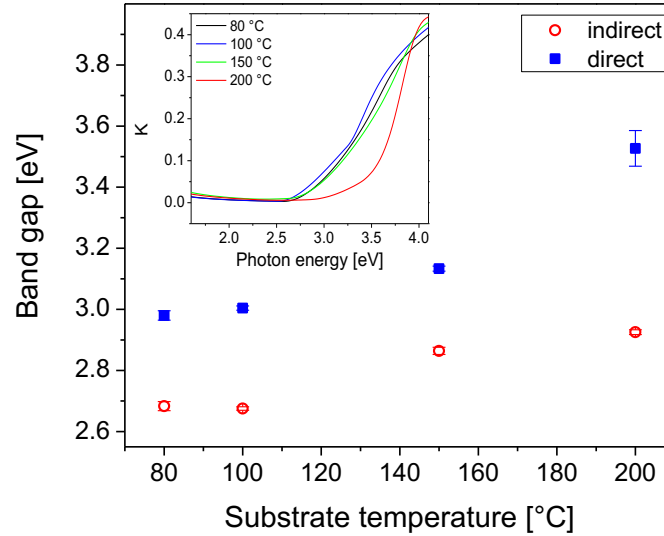


Figure 4.3. Direct (filled squares) and indirect (open circles) band gaps of the as-deposited PEALD-InO<sub>x</sub> films depending on growth temperature.

Table 4.1. Optically determined properties of InO<sub>x</sub> layers prepared by PEALD at different substrate temperatures.

$T_s$ [°C]	GPC [ $\text{\AA}/\text{cycle}$ ]	Inhomog. [%]	$n$ [@632.8nm]	Direct $E_g$ [eV]	Indirect $E_g$ [eV]
80	0.52	1.5	$2.04 \pm 0.51$	$2.98 \pm 0.02$	$2.68 \pm 0.02$
100	0.53	1.2	$2.06 \pm 0.44$	$3.00 \pm 0.01$	$2.67 \pm 0.01$
150	0.57	1	$2.07 \pm 0.36$	$3.13 \pm 0.01$	$2.86 \pm 0.01$
200	0.64	2.1	$2.02 \pm 0.34$	$3.53 \pm 0.06$	$2.92 \pm 0.01$

### 4.1.2 *Ex-situ* XPS study

The chemical composition and carbon surface contamination of the as-introduced and surface-cleaned InO<sub>x</sub> layers were evaluated by XPS. Figure 4.4 shows survey spectra acquired within the binding energy range of -5 to 1200 eV for the as-introduced films. The most intense photoemission and Auger lines correspond to the indium and oxygen signals.

It should be noted that the C 1s peak appears for all as-introduced films and probably originates from unavoidable surface contamination (adventitious carbon), which is mainly related to the exposure of the samples to air due to *ex-situ* storage and subsequent XPS characterization. Besides, the carbon signal might also arise from TMIn precursor residuals (i.e., methyl groups) that were not completely removed from the ALD reactor in the purging step. The concentration of carbon on the surface (as-introduced) and in the bulk (after surface cleaning) of the layers was calculated based on the C 1s core level spectra. The atomic concentration of carbon for the as-introduced films deposited at 100, 150 and 200 °C are nearly identical ( $17 \pm 0.1\%$ ). In contrast, the layer grown at 80 °C shows a slightly higher value, of  $19.7 \pm 0.1\%$  (as illustrated in Fig. 4.9a). Lower deposition temperatures typically trigger more carbon contamination (details are discussed below). However, after the surface cleaning (sputtering for 2 min), the carbon signal vanished completely (below the XPS detection limit). This finding proves that the carbon is located at the surface of the film and reveals that the films are carbon-free. The slight variation of the carbon concentration of the as-introduced films is likely related to the deposition process in which low temperatures induce more carbon contribution. Besides, different storage durations of the wafers before XPS analysis under non-UHV conditions (i.e. sample exposed to air) can also introduce non-deliberate impurities to the samples. Consequently, carbon-free InO<sub>x</sub> thin films can be prepared using PEALD with TMIn and O<sub>2</sub> plasma at deposition temperatures of 80 to 200 °C, suggesting high-quality films.



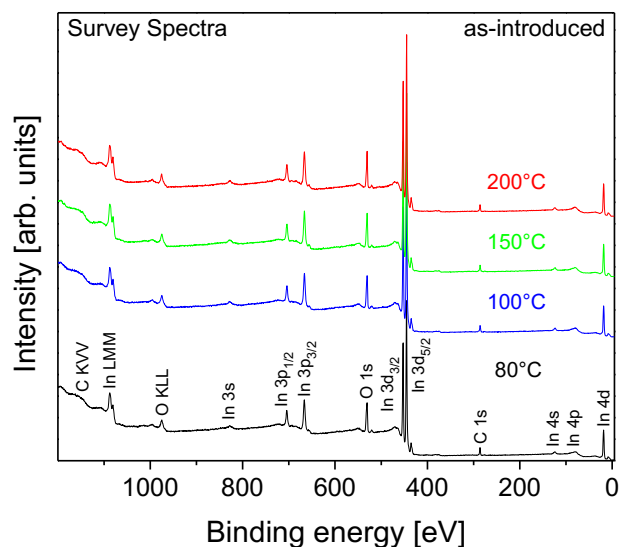


Figure 4.4. XPS survey spectra of the as-introduced PEALD-InO<sub>x</sub> films prepared at different temperatures from 80 to 200 °C, as labeled in the diagram. Al K $\alpha$  radiation was used as the excitation source.

To further prove the formation of the indium-oxygen phase in the InO<sub>x</sub> films, indium MNN Auger spectra, which is very sensitive to the indium chemical bonding states, were recorded to determine whether any metallic-like indium is present in the films or not. Figure 4.5 displays the indium MNN-Auger spectra of the InO<sub>x</sub> layers after surface cleaning. The overall lineshape with two prominent peaks at kinetic energies of  $400.1 \pm 0.2$  eV and  $406.2 \pm 0.1$  eV confirms the formation of indium oxide<sup>(267)</sup>, without any traces of metallic indium species for the films prepared at different temperatures. This fact is in agreement with the literature.<sup>(268)</sup>

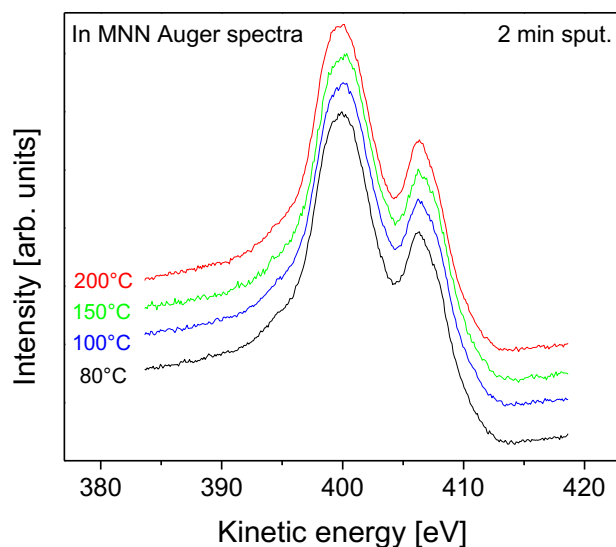


Figure 4.5. In MNN Auger XPS spectra of the surface-cleaned InO<sub>x</sub> films deposited in the temperatures range of 80 to 200 °C, as labeled in the diagram. Mg K $\alpha$  radiation was used as the excitation source.

The In 3d core level spectra of the surface-cleaned indium oxide films and their peak fitting are shown in Figure. 4.6, in which the spin-orbit-splitting peaks of the In 3d<sub>5/2</sub> and In 3d<sub>3/2</sub> are located at  $444.7 \pm 0.1$  eV and  $452.2 \pm 0.1$  eV, respectively.<sup>(52, 269)</sup> These doublet peaks exhibit an energy separation of  $7.5 \pm 0.1$  eV where the location of the In 3d<sub>5/2</sub> component is in good agreement with the reported peak position for the indium oxide.<sup>(216)</sup> The weak signals at the higher binding energy side of the main peaks (In 3d<sub>3/2</sub> and In 3d<sub>5/2</sub>) suggest the presence of OH groups and defect states; the spurious intensity on the low binding energy side is attributed to the K $\alpha$ <sub>3</sub> and K $\alpha$ <sub>4</sub> X-ray satellite lines where both peak positions and relative intensities have been fixed with respect to the main line of the In 3d<sub>3/2</sub> signal.<sup>(216)</sup>

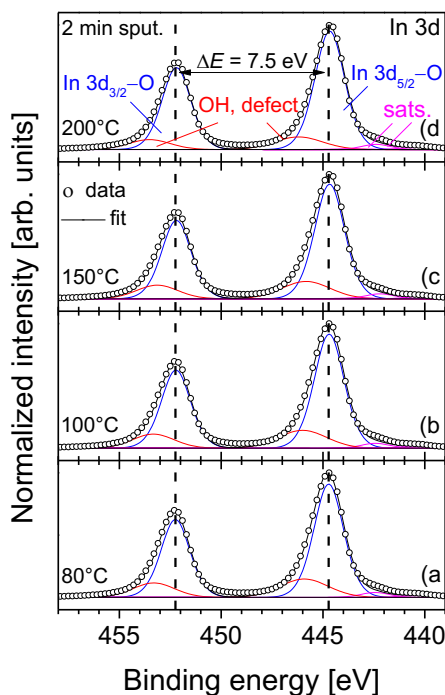


Figure 4.6. In 3d core level XPS spectra of the surface-cleaned  $\text{InO}_x$  films prepared at 80 (a), 100 (b), 150 (c), and 200 °C (d). Al  $K\alpha$  radiation was used as the excitation source.

Figure 4.7 shows the O 1s spectra of the  $\text{InO}_x$  films after surface cleaning. The O 1s can be decomposed into two components. For the surface-cleaned samples, the intense peak observed at  $530.1 \pm 0.1$  eV is assigned to O-In bonds, confirming indium oxide formation. Besides, the low peak located at  $531.4 \pm 0.3$  eV could be attributed to hydroxyl groups (oxygen bonded to hydrogen, O-H, or hydrides) and to defects in the films.<sup>(216, 270)</sup> With increasing the growth temperature from 80 to 200 °C, the O-In peak intensity (i.e., its relative weight) the area) increases from 73.7 to 82.6%, while the contributions of hydroxyl groups and defect states decrease from 26.3 to 17.4%. The energy position of the oxygen bonded to the indium peak remained nearly constant within the investigated substrate temperature range. It can be deduced that at low deposition temperatures, an incomplete surface reaction leads to more hydrogen incorporation into the layer, causing more O-H related bonds and carbon contamination. In contrast, the growth at higher temperatures facilitates the decrease of carbon and defects such as OH groups in the prepared  $\text{InO}_x$  films.<sup>(261)</sup> The formation of hydroxyl species may introduce oxygen vacancies within the indium oxide films.<sup>(271)</sup> Therefore, the O 1s core level decomposition data

corroborate the existence of hydroxyls and other defects within the PEALD-InO<sub>x</sub> films as already deduced from the In 3d core level spectra (see above); however, their signal contribution is more pronounced in the O 1s data.

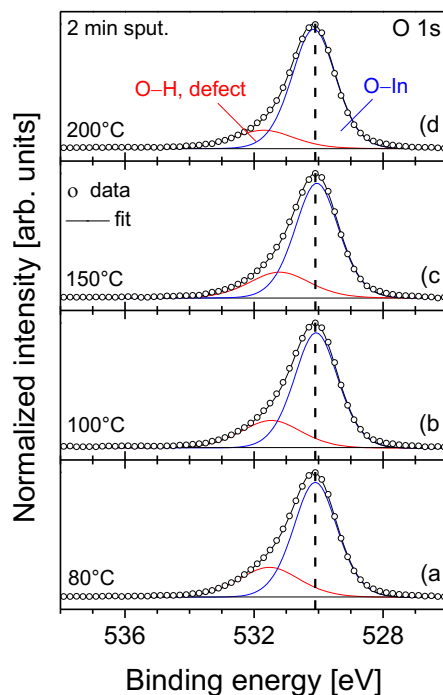


Figure 4.7. O 1s core level XPS spectra of the surface-cleaned InO<sub>x</sub> films prepared at 80 (a), 100 (b), 150 (c), and 200 °C (d). Al K $\alpha$  radiation was used as the excitation source.

An additional XPS measurement was performed on the layer deposited at 150 °C to investigate if the chemical nature of the minor peak on the shoulder of the main O-In peak is more related to bulk-like defects or hydroxyls. The take-off angle was changed to 50° to reach a higher surface sensitivity. Figure 4.8 shows the O 1s region of the as-introduced 150 °C sample (spectrum collected at 90°) and after surface-cleaning, where the spectra were collected with two different take-off angles of 50° and 90°. According to Figure 4.8a, it can be clearly seen that the as-introduced layer contains distinctly less oxygen bonded to indium (59.5%) and a higher amount of adventitious impurities (40.5%) that originate from *ex-situ* nature of this initial XPS characterization. However, after surface cleaning (Fig. 4.8b), a considerable decrease in the impurity-related signal (~23.6%) was observed. The comparison between Figures 4.8b, 4.8c shows that the change of the take-off angle in the data corresponding to the surface-cleaned film does not significantly alter the intensity of the decomposed peaks (Figs. 4.8b,

4.8c). Therefore, it can be deduced that the structural defects are present along with all the film, whereas the contribution of OH groups and adventitious carbon is more surface related.

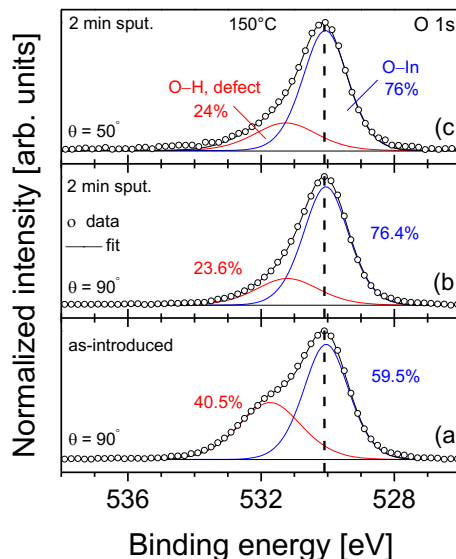


Figure 4.8. Contribution of sub-peaks in the O 1s spectra of the  $\text{InO}_x$  film prepared at 150 °C. As-introduced (a) and surface-cleaned (b, c) film with two different take-off angles of 90° (a, b) and 50° (c).

Finally, the atomic indium to oxygen ratio of the PEALD- $\text{InO}_x$  thin films was determined from the XPS peak decomposition using the total peak areas of the In 3d<sub>5/2</sub> and O 1s core levels after background removal. The In:O ratio of the surface-cleaned layers slightly increases from 0.74 at 80 °C to 0.76 at 200 °C (as depicted in Fig. 4.9b). The deviation from the ideal ratio of 2:3 reveals that the grown films exhibit oxygen vacancies for low-temperature deposition of 80 to 200 °C. However, by increasing the deposition temperature, a higher relative contribution of the In-O bonds was observed while the relative defect-related contributions decreased. Concerning the literature, an incomplete surface reaction would preferentially occur during low-temperature growth, resulting in more oxygen vacancies in the ALD process.<sup>(52)</sup> Yeom et al. reported that the indium atoms of an indium oxide film prepared by PEALD with  $\text{Et}_2\text{InN}(\text{SiMe}_3)_2$  precursor and  $\text{O}_2$  plasma have a stronger tendency to bond with oxygen at relatively low deposition temperature leading to a rise of oxygen deficiency in the films with increasing temperature.<sup>(42)</sup> According to the XPS data, the overall reduction of the O 1s intensity (relative to the In 3d intensity) indicates a net oxygen deficiency within the films that slightly increases with temperature (Fig.

4.9b). Remarkably, the as-introduced films prepared at 150 and 200 °C exhibit almost ideal indium to oxygen ratio; increasing after sputtering-cleaning. Although sputtering itself may preferentially promote the removal of oxygen compared to indium resulting in an oxygen-deficient indium oxide phase, a search in the literature shows a significant number of reports where indium-rich films are obtained for most indium precursor and co-reactant at different growth temperatures up to 300 °C,<sup>(254, 258, 260, 261)</sup>. Therefore, considering the hypotheses above, such oxygen deficiency seems to be a typical result of ALD indium oxide films. A summary of the obtained XPS results for the PEALD-InO<sub>x</sub> films is listed in Table 4.2.

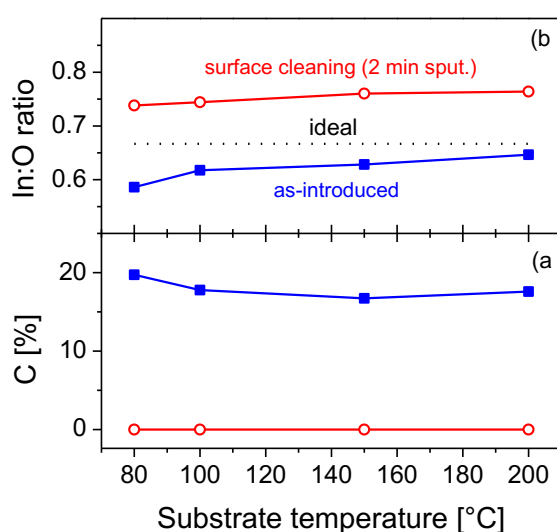


Figure 4.9. Dependence of adventitious carbon (a) and the In:O ratio (b) of the as-introduced (filled squares) and surface-cleaned (open circles) InO<sub>x</sub> films on the substrate temperature.

Table 4.2. Calculated carbon contamination, indium to oxygen ratio and relative intensities of the components in the O 1s spectra after surface cleaning (2 min sputtering).

$T_s$ [°C]	C [%]	In:O	O-H, defect [%]	O-In [%]
80	0	0.74	26.3	73.7
100	0	0.74	24.7	75.3
150	0	0.76	23.6	76.4
200	0	0.76	17.4	82.6

## 4.2 PEALD of GaO<sub>x</sub> thin films

This section discusses the optical and chemical analysis of the PEALD prepared binary gallium oxide layers using TMGa and O<sub>2</sub> plasma at low-temperatures of 80 to 200 °C.

### 4.2.1 Growth and optical characteristics

The growth mechanism and optical properties of the low-temperature deposited gallium oxide thin films were investigated by ellipsometric measurements. Figure 4.10 illustrates the linear increment of the film thickness during the PEALD process time for all applied substrate temperatures. Almost no difference was observed within the first stage of the ALD process (until the film thickness of 10 nm). However, the slopes of the curves progressively deviate with time up to a final thickness of 30 nm. This deviation indicates a reduction of the GPC from 0.70 Å/cycle (80 °C) to 0.63 Å/cycle (200 °C), as shown in figure 4.11a. This phenomenon can be explained by the reaction of the terminating hydroxyl groups forming a bridging oxygen species,<sup>(132)</sup> causing a decrease in the film thickness and changes in the nucleation behavior. This well-known effect has been already documented for other materials such as titanium oxide<sup>(272, 273)</sup>. The obtained GPC value of ~ 0.66 Å/cycle for the GaO<sub>x</sub> thin films deposited at low temperature of 80 – 200 °C is higher than the reported constant value of ~ 0.53 Å/cycle for the gallium oxide films deposited by PEALD at temperatures of 100 to 400 °C<sup>(274)</sup>.

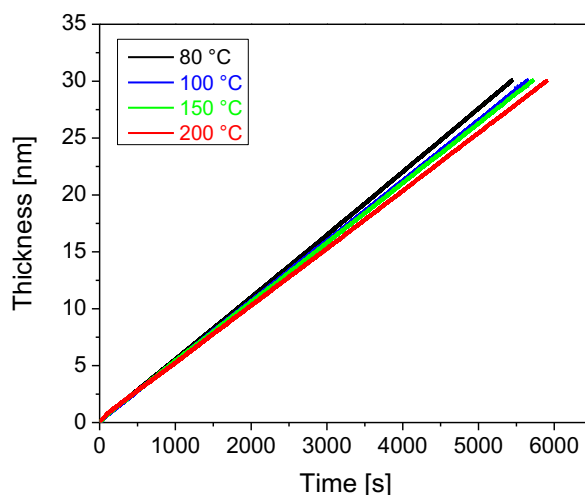


Figure 4.10. Measured thickness evolution as a function of process time up to a total thickness of 30 nm for the PEALD-GaO<sub>x</sub> films.

The growth and optical characteristics of the as-deposited 10 and 30 nm gallium oxide films were evaluated by considering the influence of temperature. The GPC, inhomogeneity, refractive index across the 4" Si wafer and band gap of the layers were determined using the Tauc-Lorentz model to fit the SE data. The used process parameters lead to similar results and very low inhomogeneity (in the range of 1.5 to 2 %) for all substrate temperatures (as shown in Fig 4.11b). These results indicate a very good process control over the large substrate area.

Figure 4.11c shows the refractive index and the band gap values of PEALD-GaO<sub>x</sub> films versus different substrate temperatures. The refractive index of the grown GaO<sub>x</sub> films at low-temperatures of 80 to 200 °C is relatively constant in the value of  $1.86 \pm 0.01$  (at 632.8 nm). The obtained value is in good agreement with the literature for the same PEALD process<sup>(274, 275)</sup> and even higher than those reported values ( $\sim 1.6 - 1.8$  at a comparable wavelength) for the gallium oxide thin films prepared by other deposition methods<sup>(276-278)</sup>. The refractive index depends on the material densification<sup>(279, 280)</sup>; therefore, amorphous films with low-density could be prone to air trapping in the layer's pores leading to an effective reduction of the refractive index (in comparison with post-annealed samples reported in the literature<sup>(61)</sup>). The band gap of the GaO<sub>x</sub> layers slightly decreases with increasing substrate temperature. However, the deviation is in the range of  $\sim 100$  meV considering the measurement error bars. The achieved result agrees with the data of Choi et al.<sup>(65)</sup>, where no significant changes in the band gap in the temperature range of 150 to 250 °C were observed for layers prepared by TALD with GTIP and water. The obtained optical band gap value of  $4.63 \pm 0.05$  eV is slightly lower than other values (4.8eV at 200 °C) reported in the literature for the same PEALD process<sup>(281)</sup>. The obtained optical properties are listed in Table 4.3.



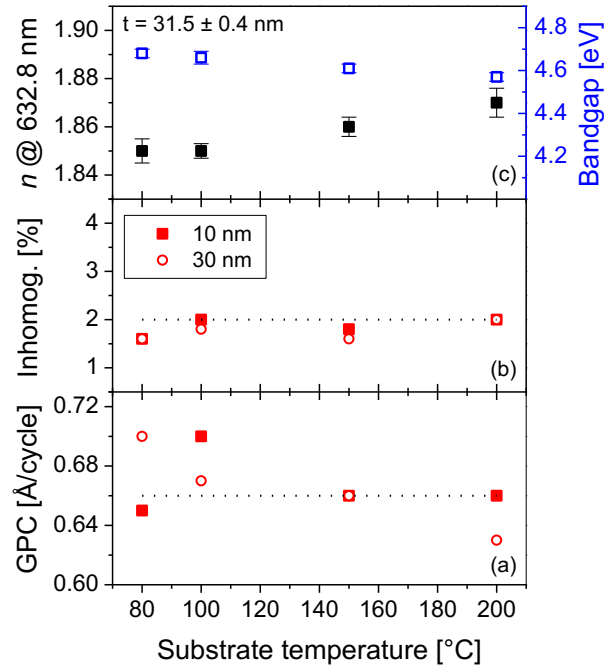


Figure 4.11. Growth rate (a), inhomogeneity across a 4" Si wafer (b), refractive index and band gap (c) of the as-deposited PEALD-GaO<sub>x</sub> layers in dependence on the substrate temperature.

Table 4.3. Summary of the optical data for the PEALD-GaO<sub>x</sub> layers prepared at different low-temperatures. The tabulated parameters are substrate temperature ( $T_s$ ), GPC, inhomogeneity (inhomog.) across 4" Si wafers, refractive index ( $n$ ), and optical band gap ( $E_g$ ).

$T_s$ [°C]	GPC [Å/cycle]	inhomog. [%]	$n$ [@632.8nm]	$E_g$ [eV]
80	0.70	1.6	1.85±0.005	4.68±0.02
100	0.67	1.8	1.85±0.003	4.66±0.03
150	0.66	1.6	1.86±0.004	4.61±0.02
200	0.63	2.0	1.87±0.006	4.57±0.02

#### 4.2.2 Ex-situ XPS study

The atomic composition of the as-introduced and surface-cleaned GaO<sub>x</sub> thin films was determined using XPS. Figure 4.12 displays the survey spectra of the as-introduced samples within the binding energy of -5 to 1350 eV. It can be

seen that the spectra contain the expected most intense photoemission and Auger lines of the gallium and the oxygen-related signals. As the samples have been exposed to the air (during preparation and *ex-situ* measurements), the C 1s spectra exhibit a contribution from adventitious carbon. Besides, the methyl groups of TMGa precursor might also introduce carbon during deposition due to an incomplete purging process. The amount of undesired carbon contamination was calculated based on the C 1s core level spectra. For the as-introduced GaO<sub>x</sub> layers, the atomic concentration of carbon was found to be almost constant ( $11.5 \pm 0.1\%$ ) for the samples grown at 100 and 150 °C, while the samples deposited at 80 and 200 °C revealed a slightly higher amount,  $17.1 \pm 0.1\%$  and  $15.2 \pm 0.1\%$ , respectively (as shown in Fig. 4.17a). However, after surface cleaning for 2 minutes, the amount of carbon significantly decreased to  $\sim 2\%$  for the lower temperatures of 80 and 100 °C, while the carbon signal completely vanished (below the XPS detection limit) for the films prepared at 150 and 200 °C. The obtained results indicate that the carbon impurity originates from the layer's surface, and the PEALD-GaO<sub>x</sub> films are carbon-free in the XPS detection range. However, the observed negligible amount of carbon for the layers of 80 and 100 °C could be related to the incomplete surface reactions at lower temperatures. It should be mentioned that the slight variation of the carbon concentration for the as-introduced layers might arise from *ex-situ* preparation of the samples and different storage time under low-vacuum environment prior to XPS characterization. Therefore, the high-quality gallium oxide thin films can be grown using PEALD process with TMGa and O<sub>2</sub> plasma at low-temperatures of 80 to 200 °C.

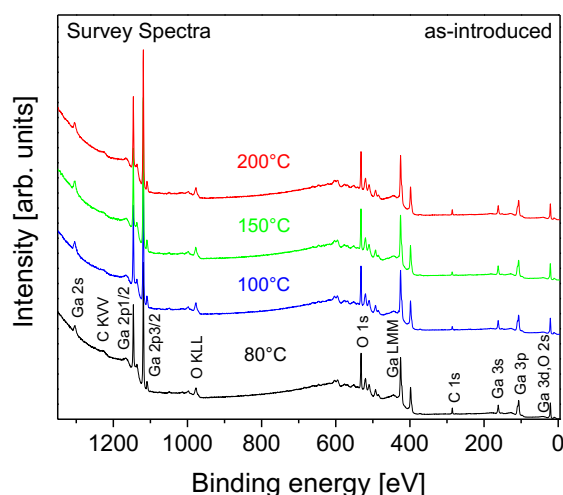


Figure 4.12. XPS survey spectra of the as-introduced PEALD-GaO<sub>x</sub> thin films prepared at different substrate temperatures. The spectra were recorded with the Al K $\alpha$  excitation source.

The formation of gallium oxide phase and investigation of whether any metallic-like gallium exists or not in the  $\text{GaO}_x$  layers, were clarified by the gallium LMM Auger spectra, that is very sensitive to the gallium chemical bonding states. Figure 4.13 shows the collected Ga LMM Auger spectra after surface cleaning of the PEALD- $\text{GaO}_x$  films prepared at different substrate temperatures of 80 – 200 °C. The formation of the gallium oxide phase without the presence of metallic species can be confirmed according to the spectra, including one intense signal located at  $1061.1 \pm 0.1$  eV and a shoulder at  $1065.1 \pm 0.1$  eV, which is in agreement with the literature.<sup>(282, 283)</sup>

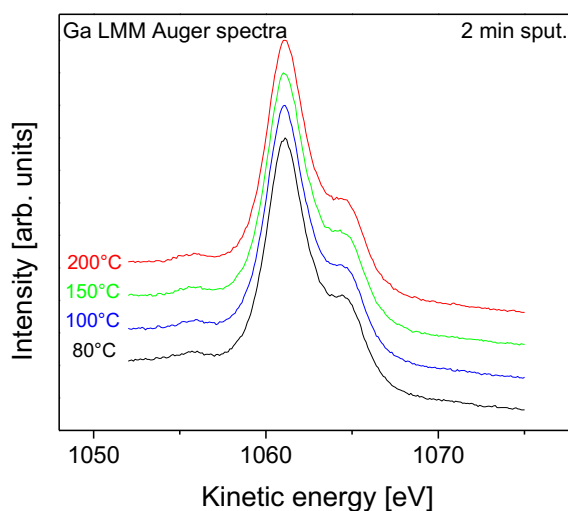


Figure 4.13. Ga LMM Auger XPS spectra of the surface-cleaned  $\text{GaO}_x$  films deposited in the temperature range of 80 to 200 °C as labeled in the diagram. Al  $K\alpha$  radiation was used as the excitation source.

Figure 4.14 illustrate the XPS fit of the Ga 2p and Ga 3d spectra after surface cleaning. From Figure 4.14a the spin-orbit splitting nature of the Ga 2p core level with doublet peaks of Ga 2p<sub>1/2</sub> and Ga 2p<sub>3/2</sub> can be seen where a binding energy separation of  $26.9 \pm 0.1$  eV was observed, which is in agreement with the literature.<sup>(216)</sup> The appeared minor peaks at a higher and lower binding energy of the main signals (Ga 2p<sub>1/2</sub> and Ga 2p<sub>3/2</sub>) could be assigned to the OH species and defect state (formation of gallium vacancy and interstitial Ga), respectively.<sup>(284, 285)</sup> Besides, weak signals that appear at the low binding energy are attributed to the  $K\alpha_3$  and  $K\alpha_4$  X-ray satellite lines, where both peak positions and relative intensities have been fixed to the corresponding signals.<sup>(216)</sup> Figure 4.14b exhibits the decomposition of the Ga 3d spectra into four sub-peaks where the presence of the highly intense peak confirms the formation of Ga-O bonds corresponding to the binary  $\text{GaO}_x$  films<sup>(274)</sup> and two further sub-peaks at the

higher and lower energy position of the Ga-O peak ( $\sim 23$  eV and  $\sim 20$  eV) could be attributed to the OH species and defect state (formation of gallium vacancy and interstitial Ga), respectively.<sup>(216, 285)</sup> Besides, there is no obvious spin-orbit splitting for the Ga 3d spectra because of the energy resolution of the analyzer combined with the low spin-orbit shift between the two Ga 3d<sub>3/2</sub> and Ga 3d<sub>5/2</sub> components. The observed weak peak at higher binding energy ( $\sim 24$  eV) is identified as the O 2s core level<sup>(216)</sup>, which might slightly impact the Ga 3d raw area and lead to deviation of the gallium concentration.

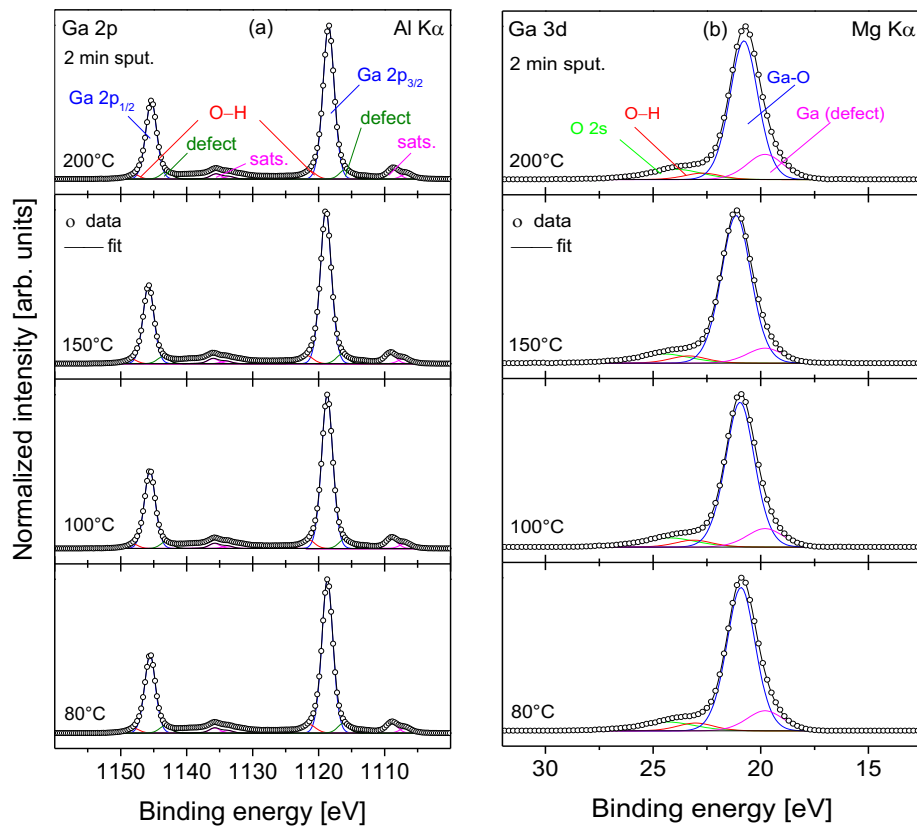


Figure 4.14. Ga 2p (a) and Ga 3d (b) XPS spectra of surface-cleaned PEALD-GaO<sub>x</sub> films grown at 80 - 200 °C. Al K $\alpha$  and Mg K $\alpha$  were used as excitation sources for the Ga 2p and Ga 3d core levels, respectively.

The O 1s XPS core level spectra of the surface-cleaned PEALD-GaO<sub>x</sub> thin films were decomposed into two distinct components, as demonstrated in Figure 4.15. The detected intense peak at a binding energy position of  $531.5 \pm 0.1$  eV is related to the O-Ga bonds that confirm the formation of gallium oxide, and the observed weak signal at a higher energy position of  $533.3 \pm 0.2$  eV might be attributed to hydroxyl groups as well as to defects in the films.<sup>(216, 278, 286)</sup> The

relative intensity of the oxygen bonded to gallium increases from 92.7 to 94.1% with rising substrate temperature from 80 to 200 °C, whereas the contribution of hydroxyl groups and defect states decreases from 7.3 to 5.9%. It should be noted that the binding energy peak position of the O-Ga remained nearly constant within the investigated substrate temperature range. Consequently, deposition of the GaO<sub>x</sub> films at lower temperatures result in more incorporated impurities such as hydroxyls (O-H) and defects in the films. At the same time, the growth at higher temperatures expedites the reduction of such impurities that might induce electron trapping in the gallium oxide layers.<sup>(287)</sup> Therefore, the obtained results from the decomposition of the O 1s spectra corroborate the presence of OH groups and defect states within the PEALD-GaO<sub>x</sub> films, as already represented from the Ga 2p and Ga 3d core levels spectra (see above). However, their relative peak intensity is more pronounced in the O 1s data.

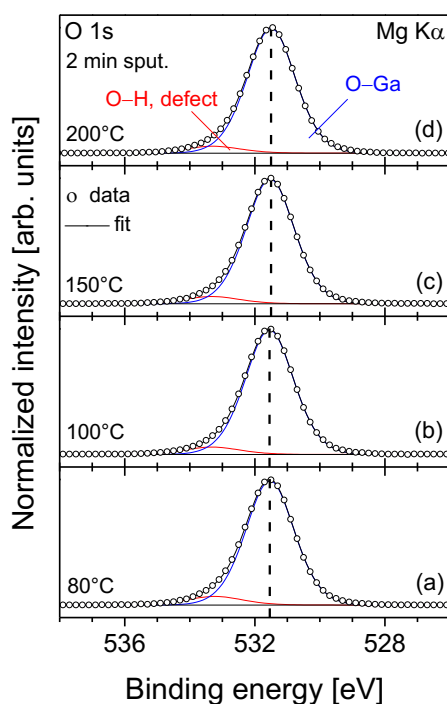


Figure 4.15. Decomposition representation of the O1s core level spectra of PEALD-GaO<sub>x</sub> layers prepared at different temperatures of 80 °C (a), 100 °C (b), 150 °C (c), and 200 °C (d). Mg K $\alpha$  radiation was used as the excitation source.

Moreover, an additional XPS measurement was carried out on one of the samples (deposited at 150 °C) to evaluate whether the observed weak signal at a higher binding energy position on the shoulder of the intense O-Ga peak is more like to be surface hydroxyls or bulk-related defects. It should be taken into

account that the sputtering process itself might create surface defects on the layer's surface. Figure 4.16 exhibits the O 1s core level signal of the sample grown at 150 °C at a normal take-off angle (90°) for the as-introduced and surface-cleaned states and at a more surface-sensitive take-off angle of 50°. Concerning Figure 4.16a, the as-introduced sample reveals a low relative intensity of O-Ga (77.7%) and a high contribution of adventitious impurities (22.3%) because of *ex-situ* preparation of the layer. However, Figure 4.16b shows that the surface cleaning (for 2 min sputtering) can decrease the amount of impurities to 6.2%. According to the obtained data of different take-off angles (Figs.4.16b, 4.16c), it can be deduced that the peak intensities of the impurities and O-Ga sub-peaks did not change significantly with changing the take-off angle from bulk-sensitive (90°) to surface sensitive (50°). However, at 50° a minor peak appeared at the low binding energy side of the main O-Ga peak and might be due to the either detecting slight part of sample holder or excess adsorbed oxygen during PEALD process that impact Ga:O ratio.<sup>(216)</sup> In consequence, the adventitious impurities are not accumulated at the surface (unlike carbon contamination); otherwise, a significant increase of the surface-sensitive signals would be expected when decreasing the take-off angle.

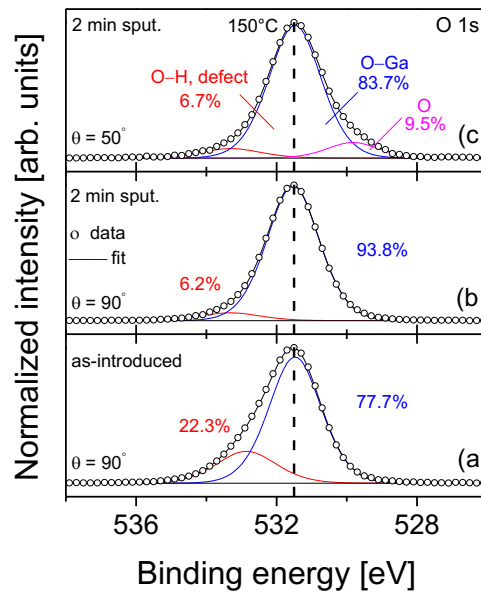


Figure 4.16. Relative intensity of the components in the O 1s spectra of the  $\text{GaO}_x$  layer prepared at 150 °C. As-introduced (a) and surface-cleaned (b, c) film with two different take-off angles of 90° (a, b) and 50° (c).

The carbon concentration and the atomic ratio (Ga:O) of the PEALD- $\text{GaO}_x$  thin films were calculated based on the main core levels of Ga 3d, O 1s, and C 1s

before and after surface cleaning (as shown in Fig. 4.17), where more bulk sensitive of the Ga 3d (posing high kinetic energy of the electrons) was employed instead of the surface sensitive Ga 2p spectra. The gallium to oxygen ratio of the  $\text{GaO}_x$  films was ascertained after XPS peak decomposition and taking the whole areas of the Ga 3d and O 1s core level peaks. Figure 4.17b represents the gallium to oxygen ratio of the as-introduced and surface-cleaned films. For the as-introduced samples, the calculated gallium to oxygen ratio remained nearly constant within the temperature range of 80 to 150 °C and slightly increased to 0.54 at 200 °C, which might be due to the reduction of adventitious impurities at relatively higher deposition temperature. However, after surface cleaning by sputtering (for 2 min), the ratio remained nearly constant (0.54) within the applied substrate temperatures. The observed deviation in the Ga:O ratio from the ideal atomic value of 2:3 reveals oxygen-rich phase of the  $\text{GaO}_x$  layers at relatively low deposition temperatures from 80 to 200 °C, which might be related to the incomplete chemisorption of the precursor at low deposition temperatures. According to the literature, the gallium oxide films grown by ALD at low temperatures are rich in oxygen, whereas high process temperatures (> 300 °C) could result in oxygen deficiencies.<sup>(65)</sup> Table 4.4 lists the XPS data of the PEALD- $\text{GaO}_x$  films.

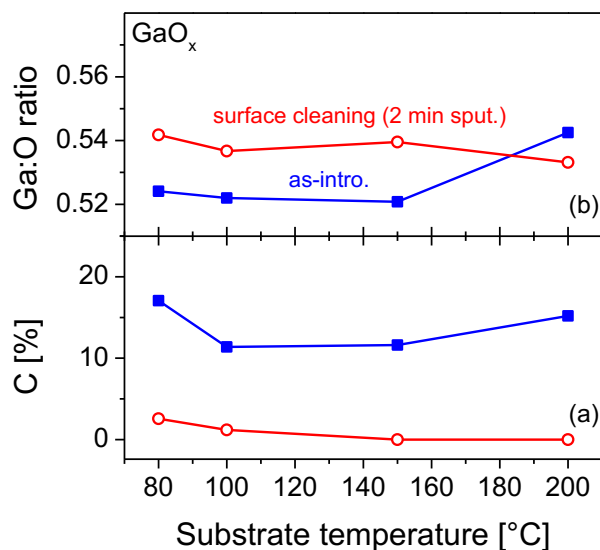


Figure 4.17. Carbon contamination (a), and gallium to oxygen ratio (b) of the PEALD- $\text{GaO}_x$  films as a function of substrate temperature.

Table 4.4. Calculated carbon contamination, gallium to oxygen ratio and relative intensities of components in O 1s spectra after surface cleaning (2 min sputtering).

$T_s$ [°C]	C [%]	Ga:O	O-H, defect [%]	O-Ga [%]
80	2.6	0.54	7.3	92.7
100	1.2	0.54	6.3	93.7
150	0	0.54	6.2	93.8
200	0	0.53	5.9	94.1



### 4.3 TALD of ZnO<sub>x</sub> thin films

This section discusses the optical and chemical analysis of the TALD prepared binary zinc oxide layers using DEZ and H<sub>2</sub>O at low-temperatures of 80 to 200 °C.

#### 4.3.1 Growth and optical characteristics

The ellipsometric measurements were carried out to evaluate the growth mechanism and optical properties of the low-temperature (80 – 200 °C) prepared zinc oxide layers. A linear film thickness evolution can be seen in Figure 4.18, in which the thickness of the films linearly increases during the growth process. Such behavior reveals that the deposition of the ZnO<sub>x</sub> films on Si substrate was fulfilled without nucleation delay. However, the observed deviation (less GPC) in the film thickness (up to 30 nm) during the deposition process is more pronounced for the films deposited at lower temperatures of 80 and 100 °C, which might be related to the incomplete surface reactions.

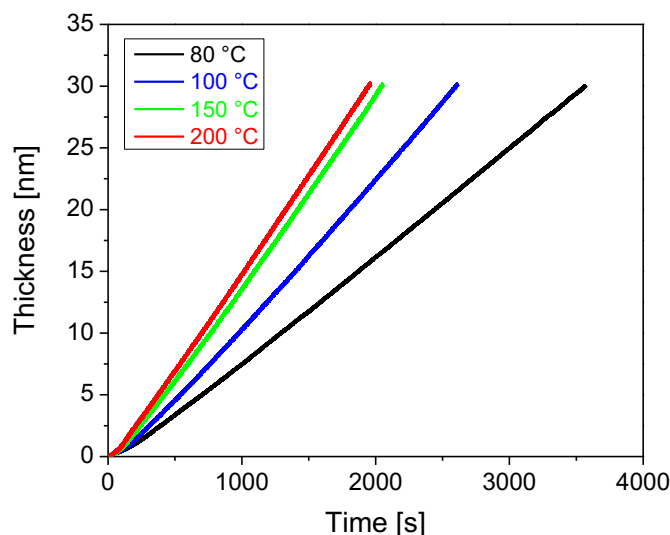


Figure 4.18. Film thickness behavior versus deposition time for TALD-ZnO<sub>x</sub> films prepared at different substrate temperatures.

Figure 4.19 displays the optical properties of the GPC, refractive index, and band gap values of the zinc oxide layers as a function of substrate temperature. From Figure 4.19a, the growth rate rises from 0.86 Å/cycle at the lower temperature of 80 °C to 1.56 Å/cycle at 200 °C. For TALD prepared ZnO<sub>x</sub> films with DEZ/H<sub>2</sub>O, a relatively constant GPC value of 1.53 Å/cycle was achieved within the temperature range of 150 to 200 °C, which can be set as the

ALD window of the ZnO<sub>x</sub> deposition. The obtained low GPC values at low-temperatures of 80 and 100 °C might be due to the lower thermal energy which could not wholly activate the surface reactions between the DEZ precursor and H<sub>2</sub>O co-reactant.<sup>(288)</sup> Besides, the acquired higher GPC values in the range of 150 to 200 °C might be due to the thermal decomposition of either the DEZ precursor at higher substrate temperatures<sup>(288, 289)</sup>. It is worth mentioning that the attained GPC value of 1.53 Å/cycle within the ALD temperature window is slightly lower than the growth rate values of ~ 1.8 and ~ 1.9 Å/cycle for the zinc oxide films using DEZ/H<sub>2</sub>O and DEZ/O<sub>3</sub>, respectively.<sup>(288, 290)</sup> Moreover, it has been reported that the growth rate of the zinc oxide film prepared by PEALD with the use of DEZ and O<sub>2</sub> plasma within the substrate temperature range of 75 – 150 °C is identical to those GPC values obtained from ALD process using DEZ and water.<sup>(291)</sup> In our case, the growth rate of the ZnO<sub>x</sub> films deposited by ALD with DEZ and water increases with substrate temperature, in agreement with the literature<sup>(288)</sup>. Finally, it has been also reported that above the ALD window the growth rate decreases with increasing temperature for the ALD process of zinc oxide-based materials.<sup>(292, 293)</sup>

The refractive index (at 632.8 nm) and band gap values of the TALD-ZnO<sub>x</sub> layers prepared at different temperatures within the range of 80 to 200 °C were investigated by SE and represented in Figure 4.19b. It can be seen that the refractive index increases with rising substrate temperature from 1.93 at 80 °C to 1.96 at 200 °C. Similar tendencies of the refractive index with the applied temperatures have been documented for the TALD- and PEALD-ZnO<sub>x</sub> layers. However, those reported values are slightly higher than the obtained refractive index of  $1.94 \pm 0.02$ .<sup>(294, 295)</sup> Nevertheless, the acquired refractive index is higher than the value of ~ 1.7 (at comparable wavelength) that has been reported for the zinc oxide films prepared by other deposition techniques such as spray pyrolysis.<sup>(296)</sup> The reason for this change in the refractive index by increasing the temperatures might be due to the phase transition from amorphous to crystalline structures as temperature rises. According to the literature, the start of crystallization for the zinc oxide films prepared by TALD with DEZ and H<sub>2</sub>O was observed at a growth temperature of  $\geq 170$  °C.<sup>(288)</sup> However, the structure and phase transition also depend on the deposition technique and process parameters, i.e., it has been reported that the PEALD of the zinc oxide films with DEZ and O<sub>2</sub> plasma facilitate the crystallization of the film even at lower temperatures of 150 °C.<sup>(291)</sup> Furthermore, the refractive index could be taken as an indication of material densification so that low refractive index values at low-temperatures reflect low-density films that result in air trapping in the layer's pores. On the

contrary, the high refractive index values could be correlated with low hydrogen incorporated films.<sup>(297)</sup> The optical band gap of the zinc oxide layers remained constant with the value of 3.1 eV within the applied substrate temperature range of 80 to 200 °C. The band gap is slightly lower than the reported value of 3.3 eV for the zinc oxide films prepared by TALD with DEZ and H<sub>2</sub>O at a temperature of 200 °C<sup>(289)</sup>. However, the achieved band gap (3.1 eV) is comparable to those band gap values of 3.15 and 3.18 eV, which have been documented for the zinc oxide layers prepared by other deposition techniques.<sup>(298, 299)</sup>

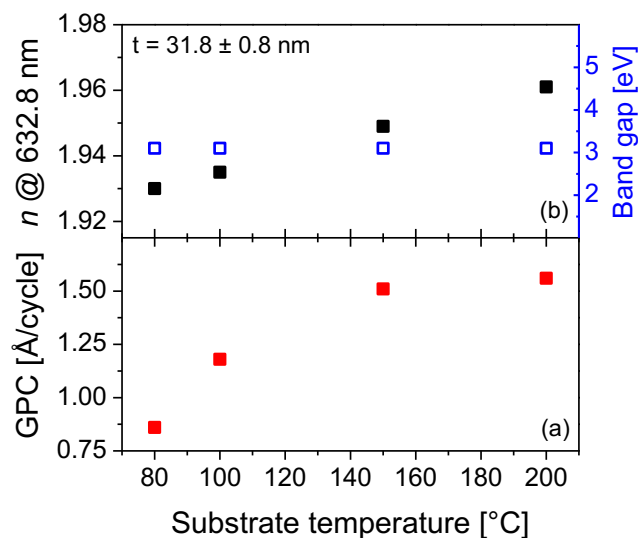


Figure 4.19. Growth rate (a), refractive index and band gap (b) of the as-deposited TALD-ZnO<sub>x</sub> layers as a function of the substrate temperature.

### 4.3.2 *Ex-situ* XPS study

The spectroscopic characterization of the as-introduced and surface-cleaned ZnO<sub>x</sub> layers was fulfilled using XPS, where the chemical states of the films as well as carbon surface contamination have been evaluated. Figure 4.20 illustrates the survey scan spectra (-5 to 1300) of the as-introduced zinc oxide films deposited at a different substrate temperature range between 80 to 200 °C. The C 1s signal appeared for all as-introduced layers, which denotes surface contamination and arises from *ex-situ* samples preparation and subsequent XPS characterization. The amount of such carbon contamination either on the layer's surface (as-introduced state) or in the bulk of the layers (after surface cleaning) because of probable insufficient purging process of byproducts from ALD reactor, can be determined from the C 1s core level spectra. The carbon contribution of the as-introduced layers decreases with increasing substrate temperature from 28.4 ± 0.1% at 80 °C to 21.4 ± 0.1% at 200 °C, while after surface cleaning (2 min

sputtering), the carbon signal completely vanished (below the XPS detection limit) for all applied temperatures (as shown in Fig. 4.25). These results reveal that the presence of adventitious carbon was only on the surface of the samples and after sputtering the films are carbon-free. Therefore, the high-quality ZnO<sub>x</sub> films can be prepared using TALD process with DEZ and HO at low-temperatures of 80 to 200 °C.

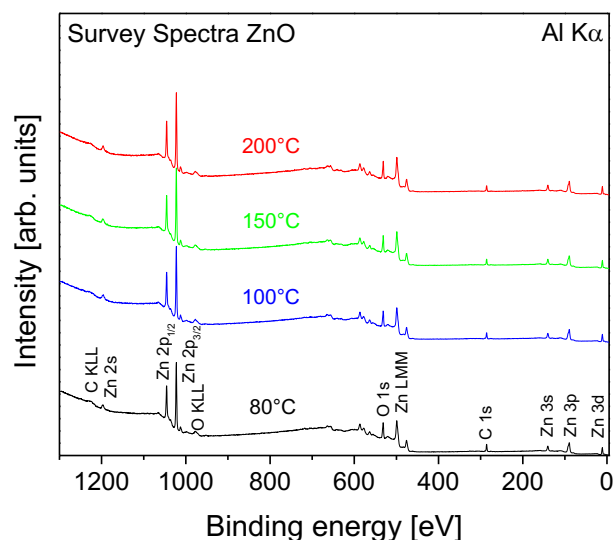


Figure 4.20. XPS survey spectra of the as-introduced TALD-ZnO<sub>x</sub> thin films prepared at different substrate temperatures. The spectra were recorded with Al K $\alpha$  excitation.

Figure 4.21 exhibits the zinc LMM Auger spectra of the surface-cleaned ZnO<sub>x</sub> samples, where the state of zinc-oxygen formation can be evaluated concerning the high sensitivity nature of the Auger spectra. The spectra show no trace of metallic-like zinc for all applied low-temperatures of 80 to 200 °C, and the overall observed signals consist of the significant peak at the kinetic energy of  $987.8 \pm 0.2$  eV and the weak peak with the kinetic energy position of  $991.1 \pm 0.5$  eV confirming the zinc oxide formation which is in agreement with literature.<sup>(267, 283)</sup>

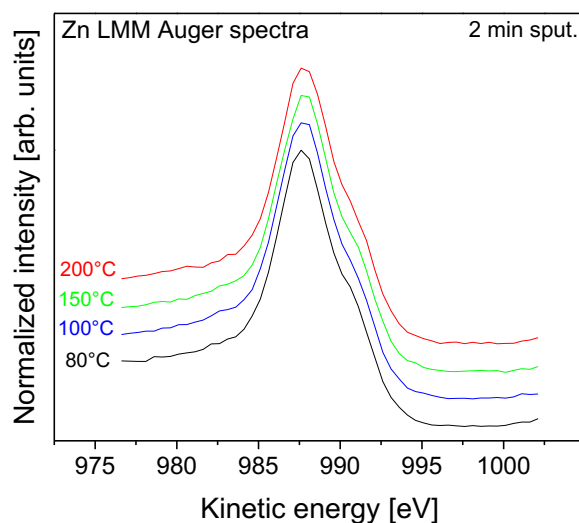


Figure 4.21. Zn LMM Auger XPS spectra of the surface-cleaned ZnO<sub>x</sub> films deposited in the temperature range of 80 to 200 °C as labeled in the diagram. Al K $\alpha$  radiation was used as the excitation source.

The Zn 2p core level peak fitting of the zinc oxide thin films at different low-temperatures is shown in Figure 4.22, where doublet signals of the Zn 2p<sub>1/2</sub> and Zn 2p<sub>3/2</sub> were located in the binding energy position of  $1044.4 \pm 0.1$  eV and  $1021.3 \pm 0.1$  eV, respectively, with a binding energy separation of  $23.1 \pm 0.1$  eV.<sup>(216, 300)</sup> The presence of minor signals at a higher binding energy of the main Zn 2p<sub>1/2</sub> and Zn 2p<sub>3/2</sub> peaks could be related to the hydroxyl species (OH groups) and defect state (oxygen vacancy).<sup>(216, 301)</sup> Besides, the observed weak signals at lower binding energy and in the middle of spectra correspond to the K $\alpha_3$  and K $\alpha_4$  X-ray satellite lines where both peak positions and relative intensities have been fixed with respect to the main lines.<sup>(216)</sup>

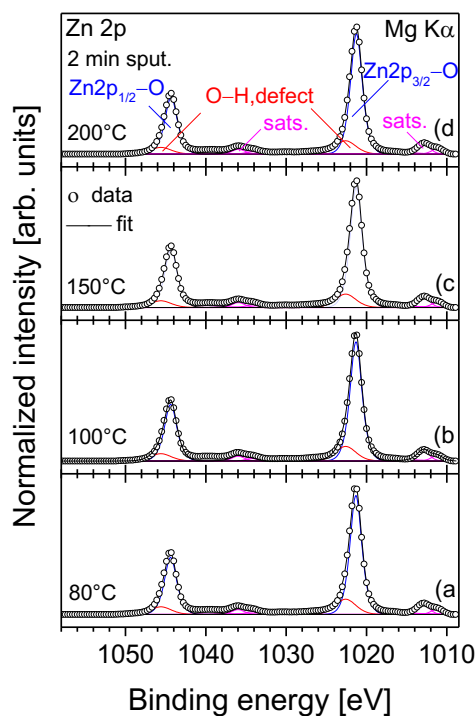


Figure 4.22. Zn 2p core level XPS spectra of the surface-cleaned ZnO<sub>x</sub> films prepared at 80 (a), 100 (b), 150 (c), and 200 °C (d). Mg K $\alpha$  radiation was used as the excitation source.

Figure 4.23 shows the O 1s core level peak fitting of the surface-cleaned ZnO<sub>x</sub> thin films, which could be decomposed into two distinct sub-peaks of O-Zn at energy positions of  $530.0 \pm 0.1$  eV, confirming zinc oxide formation and adventitious impurities (O-H, defect) at a higher binding energy of  $531.7 \pm 0.1$  eV.<sup>(302, 303)</sup> The relative intensity of the oxygen bonded to zinc slightly increases from 79.3% at 80 °C to 81.7% at 200 °C, whereas the contribution of hydroxyl groups and defect states decreases in parallel. The reduction of the impurities by increasing the temperature might be due to an incomplete surface reaction between reactants at low growth temperatures, which triggers a relatively higher amount of hydrogen impurity.<sup>(289)</sup> It should be noted that the energy position of the main O 1s component (O-Zn) remained constant within the applied substrate temperatures of 80 to 200 °C. According to the analyzed O 1s spectra, the presence of OH groups and defect states within the zinc oxide films deposited by TALD can be also verified from the Zn 2p core level spectra (as shown earlier).

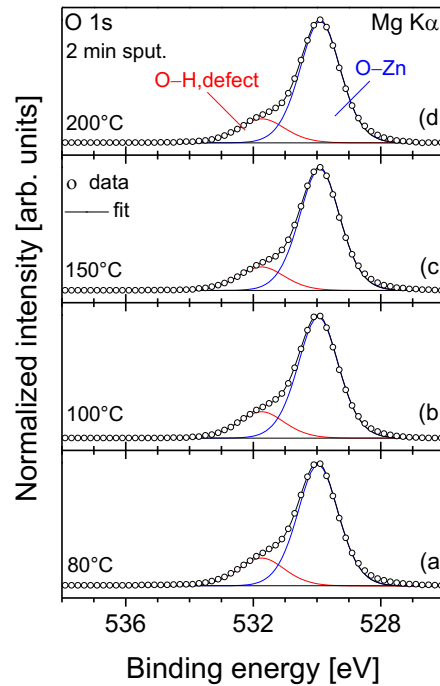


Figure 4.23. O 1s core level XPS spectra of the surface-cleaned ZnO<sub>x</sub> films prepared at 80 (a), 100 (b), 150 (c), and 200 °C (c). Mg K $\alpha$  radiation was used as the excitation source.

The observed minor impurity peak on the shoulder of the main O-Zn peak of the O 1s core level spectra can be further investigated by XPS to realize whether such signal is more like to have more content of surface hydroxyl groups or bulk-related defect states. Hence, one of the ZnO<sub>x</sub> samples (deposited at 150 °C) was employed and evaluated by considering two different take-off angles of 50° (more surface sensitive) and 90° (more bulk sensitive) in as-introduced and after surface-cleaned states (as shown in Fig. 4.24). Figure 4.24a, shows that the as-introduced layer reveals a low relative intensity of the O-Zn (54.2%) and a high amount of adventitious impurities (45.8%) arising from *ex-situ* measurement. However, the contribution of impurities reduced significantly after performing a surface cleaning (Fig. 4.24b). Concerning Figures 4.24b, and 4.24c, the peak intensity of components increased in six points when modifying the take-off angle. It can be deduced that the observed defects are more like to be created from the sputtering process, which consequently might influence the stoichiometry state of the TALD-ZnO<sub>x</sub> layers. Taking into account that the ZnO<sub>x</sub> material typically poses a peak on the shoulder of the main O-Zn signal, which is partially related to

surface stabilization via H and OH groups (because  $\text{ZnO}_x$  has a polar structure).<sup>(304)</sup>

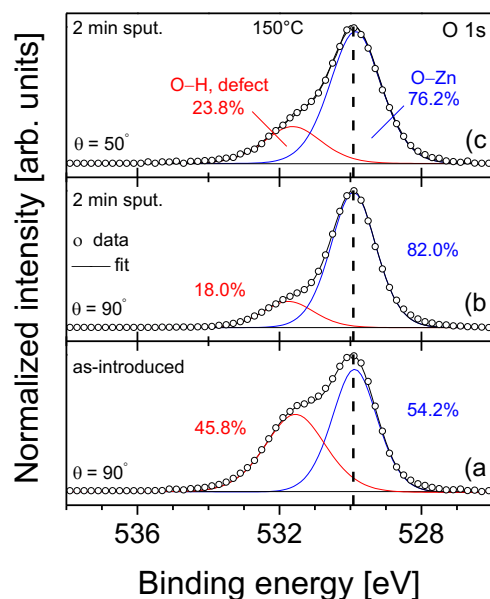


Figure 4.24. Contribution of sub-peaks in the O 1s spectra of the  $\text{ZnO}_x$  film prepared at 150 °C. As-introduced (a) and surface-cleaned (b, c) film with two different take-off angles of 90° (a, b) and 50° (c).

The atomic metal to oxygen ratio (Zn:O) of the TALD prepared zinc oxide layers was determined after peak decomposition of the Zn  $2p_{3/2}$  and O 1s core levels spectra, where the whole respective areas were considered. Figure 4.25b shows the calculated zinc to oxygen ratio of the as-introduced and surface-cleaned samples. Based on the data, the zinc to oxygen ratio of the as-introduced films decreased when rising the deposition temperature from 0.76 (at 80 °C) to 0.57 (at 100 °C), then, slightly increased and remained constant (0.59) for 150 and 200 °C. After surface cleaning using sputtering for 2 minutes, the Zn:O ratio increased to an almost constant ratio of 1.25, indicating oxygen-deficient films. According to the literature, a deviation in the zinc to oxygen ratio within the low-temperature range of 80 to 200 °C could also originate from an incomplete surface reaction that typically happens at low deposition temperatures during ALD process.<sup>(305)</sup> From analyzed O 1s spectra (Fig. 4.23), the incorporated hydroxyl groups might also induce oxygen deficiency for the  $\text{ZnO}_x$  layers, similar to that of the atomic layer deposited indium oxide films where oxygen vacancies have been observed for low-temperatures of 80 to 200 °C.<sup>(33)</sup> Furthermore, the oxygen deficiency of the ZnO material has been also reported in the literature.<sup>(306, 307)</sup> Concerning the Figure 4.24, it can be deduced that the  $\text{ZnO}_x$  layers prepared at low-temperatures



of 80 to 200 °C pose inherently defective states and doing sputtering might induce more defects which leads to a deviation in the calculated Zn:O ratio. Nevertheless, the impact of the preferential sputtering could be another reason why more oxygen atoms are removed compared to with the zinc atoms and resulting in more oxygen vacancies<sup>(308)</sup>. However, there is no indication of the metallic zinc in the Auger and Zn 2p spectra (Figs. 4.21, 4.22). The acquired XPS data of the TALD-ZnO<sub>x</sub> layers are listed in table 4.5.

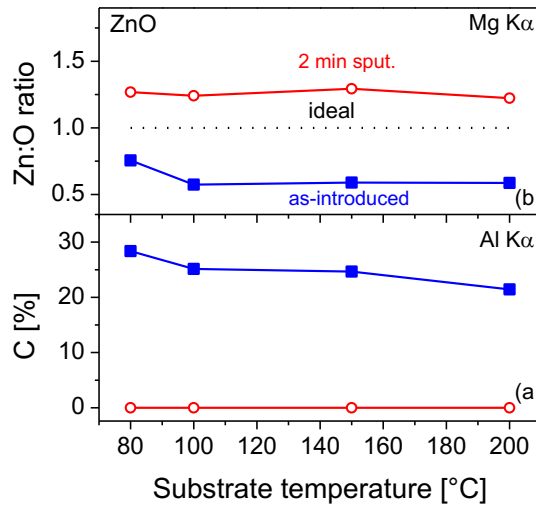


Figure 4.25. Estimated carbon contamination (a) and the Zn:O ratio (b) of the as-introduced (filled squares) and surface-cleaned (open circles) ZnO<sub>x</sub> films versus substrate temperature.

Table 4.5 Calculated carbon contamination, zinc to oxygen ratio and relative intensities of the components in the O 1s spectra after surface cleaning (2 min sputtering).

$T_s$ [°C]	C [%]	Zn:O	O-H, defect [%]	O-Zn [%]
80	0	1.41	20.7	79.3
100	0	1.40	19.8	80.2
150	0	1.43	18.0	82.0
200	0	1.35	18.3	81.7

## 4.4 Bottom-up establishment of IGZO thin films

This section discusses the optical and chemical analysis of the ALD prepared quaternary indium-gallium-zinc oxide layers after quantitative investigation of the individual binary oxides and probing a common temperature window.

### 4.4.1 Growth characteristics

As schematically shown in Fig. 3.19, the preparation of IGZO films has been done at a substrate temperature of 150 °C according to the overlapping between the three ALD temperature windows of each binary oxide: InO<sub>x</sub>, GaO<sub>x</sub> and ZnO<sub>x</sub> (more information regarding the individual deposits of GaO<sub>x</sub> and InO<sub>x</sub> can be found elsewhere,<sup>(33, 34)</sup> respectively). However, precise control of film composition requires an exact knowledge of the number of ALD-cycles corresponding to each binary oxide during the pertinent sub-cycle, which depends on the GPCs and nucleation delays over a specific surface. To illustrate how the bottom-up approach can potentially overcome the previous technical issues to design the complete IGZO super-cycle, the growth optimization of the ZnO<sub>x</sub> sub-layer should be taken into account.

Figures 4.26 and 4.27 exhibit the study of two different ALD methods of TALD and PEALD for deposition of the ZnO<sub>x</sub> where its growth on the GaO<sub>x</sub> and InO<sub>x</sub> was compared to evaluate if the underneath layer could influence the nucleation delay. On the one hand, the TALD-ZnO<sub>x</sub> approach reveals a nucleation delay on both PEALD prepared InO<sub>x</sub> and GaO<sub>x</sub> layers. On the other hand, the PEALD process for the zinc oxide showed no nucleation delay. However, a higher growth rates of 0.92 and 0.85 Å/cycle were found by *in-situ* SE measurements for the ZnO<sub>x</sub> grown on the GaO<sub>x</sub> layer in comparison with the InO<sub>x</sub>, respectively, suggesting the critical parameter is the nature of the ALD process. It should be noted that a nucleation delay would imply the use of more cycles to achieve the same composition (illustrated in Table 4.6 by the use of 12 or 2 ZnO<sub>x</sub> sub-cycles for a target composition of 1/1/1 - In/Ga/Zn- if TALD or PEALD is used, respectively).

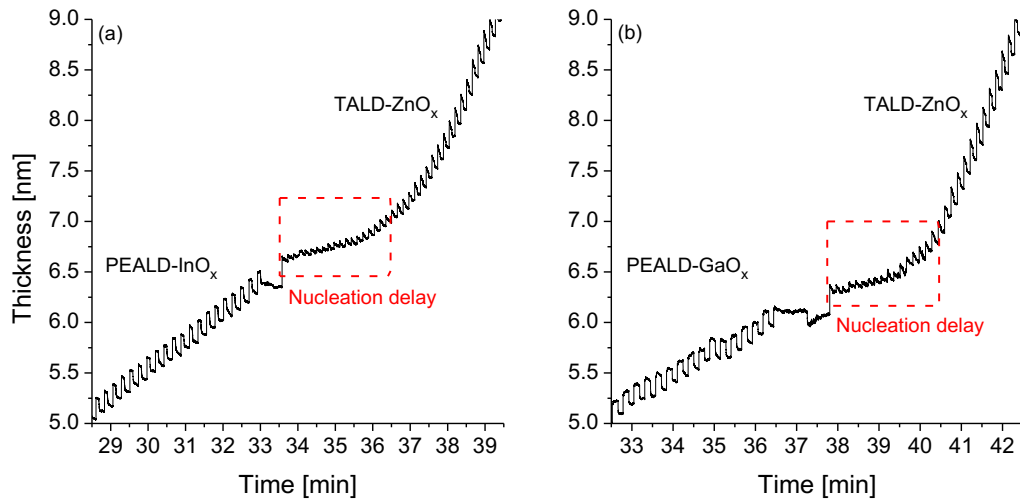


Figure 4.26. Growth evaluation of TALD prepared  $\text{ZnO}_x$  on both PEALD prepared  $\text{InO}_x$  (a), and  $\text{GaO}_x$  (b) underneath layers.

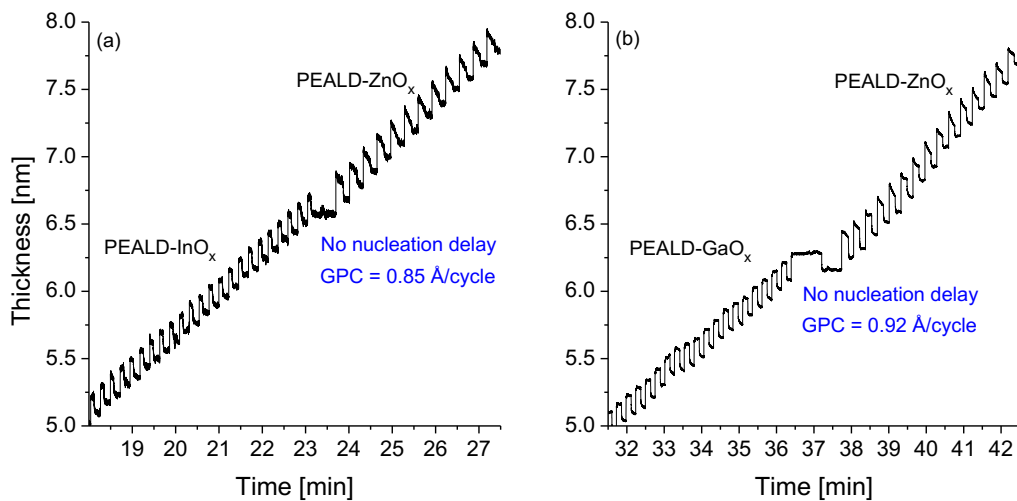


Figure 4.27. Growth evaluation of PEALD prepared  $\text{ZnO}_x$  on both PEALD prepared  $\text{InO}_x$  (a), and  $\text{GaO}_x$  (b) underneath layers. No nucleation delay for the complete PEALD process.

To precisely control the layer composition of the IGZO films, we subsequently determined the GPCs of the individual sub-layers on the respective underlying sub-layer (see Fig. 4.28). GPCs of 0.61, 0.92, and 0.72  $\text{\AA}/\text{cycle}$  were achieved for the PEALD growth of  $\text{GaO}_x$  on  $\text{InO}_x$ ,  $\text{ZnO}_x$  on  $\text{GaO}_x$ , and  $\text{InO}_x$  on  $\text{ZnO}_x$ , respectively. Table 4.6 illustrates well the differences in the needed number of cycles depending on the growth characteristics of each binary oxide sub-layer.

From the 1/1/1 sample, although the growth rates of the individual oxides do not differ significantly from one another using TALD or PEALD, more feeding cycle of the  $\text{ZnO}_x$  layer needs to be used to compensate for the nucleation delay. From the industrial scaling point of view, this translates into a waste of precursors and higher deposition process time, leading to increased production costs. In addition, compared to the TALD, the PEALD is expected to allow better mixing of the elements during the growth process and avoiding post-annealing treatments due to inherently benefiting from the high energy of ions which might increase chemical reactions on the surface. Besides, using a single ALD method (PEALD) with a single oxidant (plasma  $\text{O}_2$ ) for all sub-layers allows better optimization of the ALD recipe, facilitating the standardization of industrial film processing.

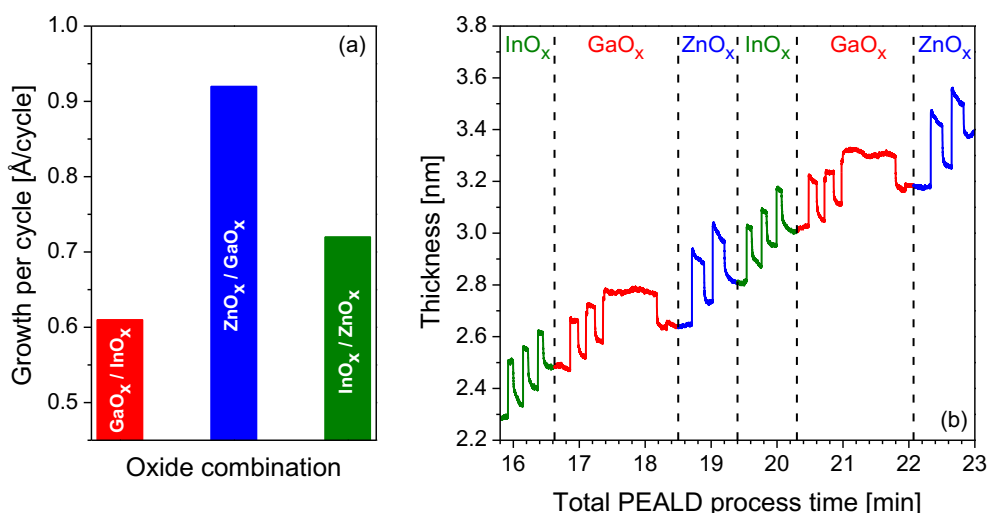


Figure 4.28. Growth rates of the respective binary oxides on the associated underlying oxides, as applied in the super-cycle (a), and *in-situ* real-time monitoring of the thickness evolution within PEALD-IGZO super-cycles comprising 3  $\text{InO}_x$ , 3  $\text{GaO}_x$ , 2  $\text{ZnO}_x$  sub-cycles (i.e., target composition of 1/1/1, see Table 4.6) (b).

Therefore, the bottom-up approach requires a deep characterization of the individual oxides and the interactions established among them, considering different recipes and a minimum number of super-cycles to establish a thick enough representative IGZO film ( $> 10$  nm) where intermixing the elements occurs. This way, a set of IGZO films deposited by PEALD were prepared with different target element ratios (In/Ga/Zn) of 1/1/1, 1/1/2, 2/1/1, and 1/2/1 (see Table 4.6). A 1/1/1 film using TALD for the  $\text{ZnO}_x$  sub-cycle was grown for comparison purposes. All films contain 12 super-cycles to ensure a final layer

thickness of  $\sim 11$  nm. The sub-cycle sequences for the PEALD series and that of TALD-ZnO<sub>x</sub> sample are given in Table 4.6, which also shows the estimated compositional ratios determined by EDX and XPS (details are discussed below). We found a good correlation between the analyzed XPS data and the target element compositions defined by the PEALD super-cycle process. Concerning collected data (Table 4.6, last row), we can deduce that observed deviations are more pronounced for the TALD-ZnO sub-layer of the IGZO compound, which indicates that this process is more challenging because of the delay in the nucleation process.

Table 4.6. Sample names, target elemental composition, sub-cycle ratio within one super-cycle, EDX actual ratio of the as-deposited layers, and XPS actual ratio of the surface-cleaned PEALD (InO<sub>x</sub>, GaO<sub>x</sub>, ZnO<sub>x</sub>) and PEALD (InO<sub>x</sub>, GaO<sub>x</sub>)/TALD (ZnO<sub>x</sub>) IGZO layers with considering the core levels of In 3d/Ga 3d/Zn 2p.

Process	Sample name	Target metal ratio In/Ga/Zn	Super-cycle ratio InO <sub>x</sub> /GaO <sub>x</sub> /ZnO <sub>x</sub>	Actual metal ratio In/Ga/Zn	
				EDX	XPS
PEALD	PE(1/1/1)	1/1/1	3/3/2	1.0/1.0/1.0	1.0/1.0/2.0
	PE(1/1/2)	1/1/2	3/3/4	1.0/1.0/2.0	1.0/1.0/3.0
	PE(2/1/1)	2/1/1	6/3/2	2.0/1.0/1.0	2.0/1.0/2.0
	PE(1/2/1)	1/2/1	3/6/2	1.0/1.4/1.0	1.0/2.0/2.0
PEALD/TALD	T(1/1/1)	1/1/1	3/3/12	1.0/1.0/2.0	1.0/1.0/3.0

#### 4.4.2 *Ex-situ* XPS study

The growth characteristics are not the only parameters that must be carefully studied to determine a specific sub-cycle, but chemical features such as composition, degree of oxidation, and impurities should also be considered. Figure 4.29 shows the survey spectra of the PEALD-IGZO films with different element ratios at a deposition temperature of 150 °C. The *ex-situ* nature of the XPS measurement results in surface contamination if no surface cleaning is performed (adventitious carbon previously described in the binary oxides) before surface cleaning. The contribution of carbon on the surface and within the sub-surface layers of as-introduced compounds was determined to be around 10%.

However, after gentle cleaning (sputtering for 35 s), carbon was reduced to only 2-4%. Further cleaning leads to complete carbon removal (carbon content below the XPS detection limit).

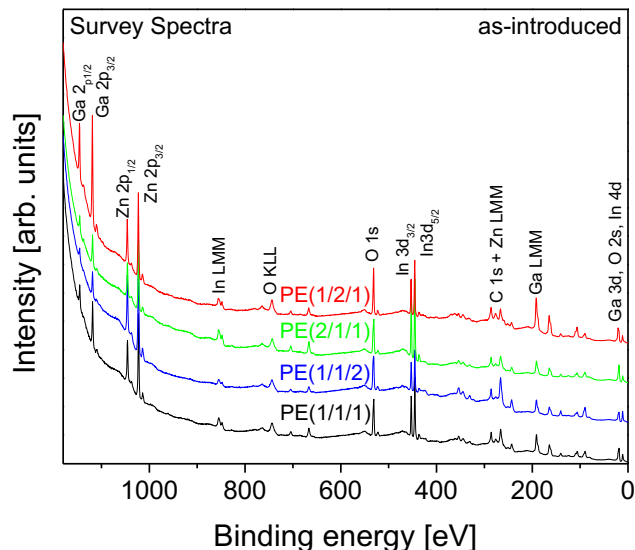


Figure 4.29. XPS survey spectra of the as-introduced PEALD-IGZO films were prepared at 150 °C. The target elemental ratios are represented as X/Y/Z. Mg K $\alpha$  radiation was used as the excitation source.

The metallic-elements Auger lines were evaluated to prove that the use of TALD leads to an almost complete oxidation state of the ZnO<sub>x</sub> sub-layer in comparison to the PEALD prepared zinc oxide sample for a common target composition of 1/1/1. Figure 4.30 displays the Zn LMM Auger spectra after gentle surface cleaning (35 s of sputtering), where the PEALD-ZnO sub-layer (Fig.4.30b) reveals a tiny component of metallic zinc ( $\sim 995.2$  eV)<sup>(267)</sup>, which suggests that the O<sub>2</sub> plasma source of ALD cannot fully oxidize the DEZ precursor of the ZnO<sub>x</sub> material at 150 °C in comparison with the H<sub>2</sub>O thermal route (Fig.4.30a). These oxidation differences could also be explained by the total number of ZnO<sub>x</sub> sub-cycles used in each case (12 and 2 for TALD and PEALD, respectively) since in the sense that more oxidant was present during the TALD approach. This example illustrates that even though the initial investigation of the binary oxides constitutes an excellent first step, complex interrelations will emerge and need to be carefully studied.

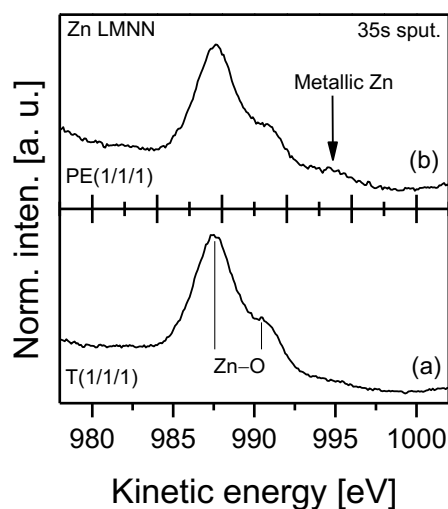


Figure 4.30. Zn LMM Auger spectra of the IGZO samples T(1/1/1) (a), and PE(1/1/1) (b). Al K $\alpha$  radiation was used as the excitation source, and the data were recorded after a gentle surface cleaning (35 s of sputtering).

XPS depth profile of the PEALD-IGZO samples is given in Fig. 4.31, where sequential sputtering steps were taken until the IGZO/substrate interface signal was detected. The obtained results reveal a nearly constant atomic concentration of the composition elements (In, Ga, Zn) through the films, with smoothly variations of the individual elements arising from different ALD sub-cycle of the In/Ga/Zn. We found that those samples with more zinc (PE(1/1/2), Fig. 4.31b) and indium (PE(2/1/1), Fig. 4.31c) contents exhibit a significant homogeneous distribution of the elements in the bulk of the films. However, the IGZO films with equal elemental ratio (PE(1/1/1), Fig. 4.31a) and more gallium contribution (PE(1/2/1), Fig. 4.31d) slightly deviate from the specified target element ratio. The formation and increment of Ga rich state during the depth profiling process might be due to a preferential sputtering phenomenon<sup>(309)</sup> (different sputtering yield for In, Ga and Zn) and/or a real increase in Ga concentration within the super-cycle deposition. From EDX data (Table 4.6), the expected target ratios can be seen for all samples except for PE(1/2/1), which reveals less Ga content (1.0/1.4/1.0). As mentioned before, we found a gradual decrease of the carbon percentage during the first sputtering cycles, which is more like adventitious carbon (due to *ex-situ* preparation and characterization) rather than probable incomplete reactions and/or insufficient purging of the precursors ligands. According to the elemental composition ratios estimated by XPS (probing surface and sub-surface regions) as documented in table 4.6, an overestimation of Zn element can be clearly seen due to the place of ZnO sub-layer on top of the

IGZO compound. The abundance of Zn contribution might be more related to the position of the  $\text{ZnO}_x$  sub-layer on top of the layers and also considering the very low kinetic energy of the collected Zn 2p electrons that induce more surface-sensitive measurement. Furthermore, the composition of the film can be controlled by selecting a specific number of cycles and/or modification of the elemental cycle ratio, which might significantly impact the material property of the super-cycle PEALD-IGZO films for promising applications.<sup>(310)</sup>

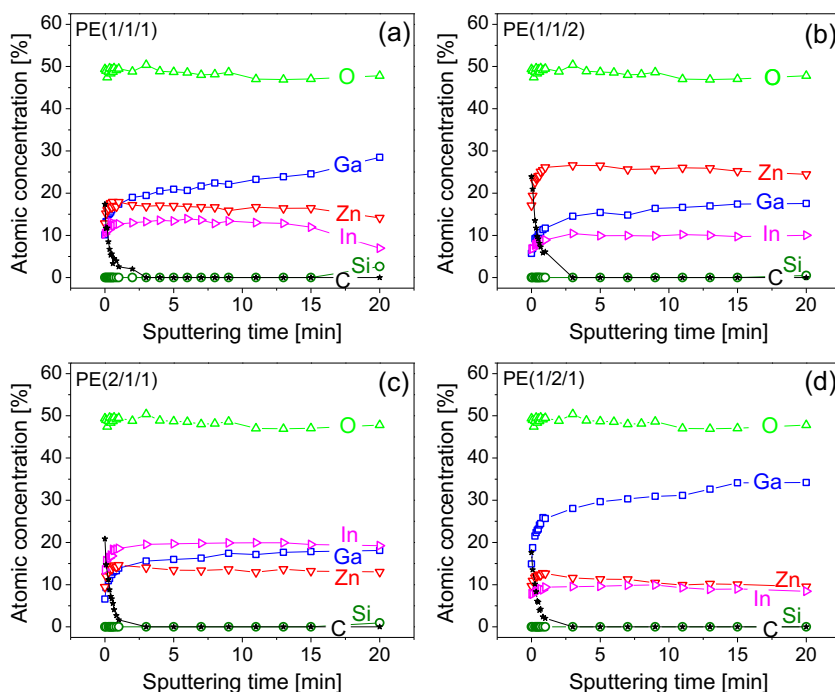


Figure 4.31. Bulk composition of the 11 nm thick IGZO films with different target element ratio of 1/1/1 (a) 1/1/2 (b) 2/1/1 (c), and 1/2/1 (d) evaluated by XPS depth profiling.

EDX measurements were carried out on the prepared IGZO samples to verify elemental composition and degree of homogeneity distribution. According to the EDX data (Figs. 4.32, 4.33), all films reveal the expected target elements ratio for the applied PEALD process (see Table 4.6) and exhibit a homogeneous distribution of the elements in correlation with the performed XPS depth profiling data (Fig. 4.31), in which nearly constant atomic concentrations of In, Ga, and Zn were observed through the films.



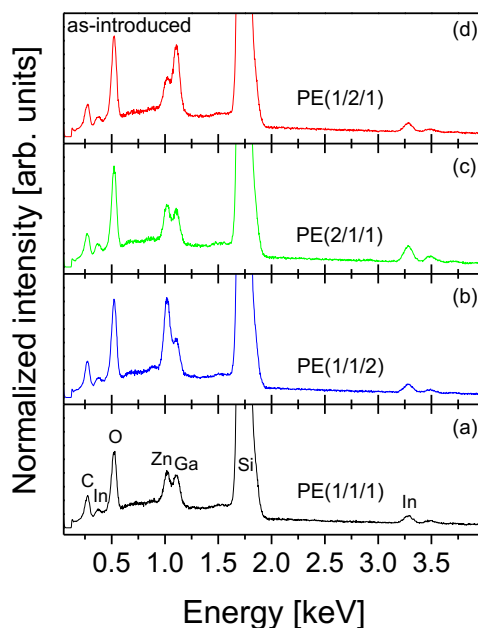


FIG. 4.32. EDX measurement of PEALD-IGZO samples.

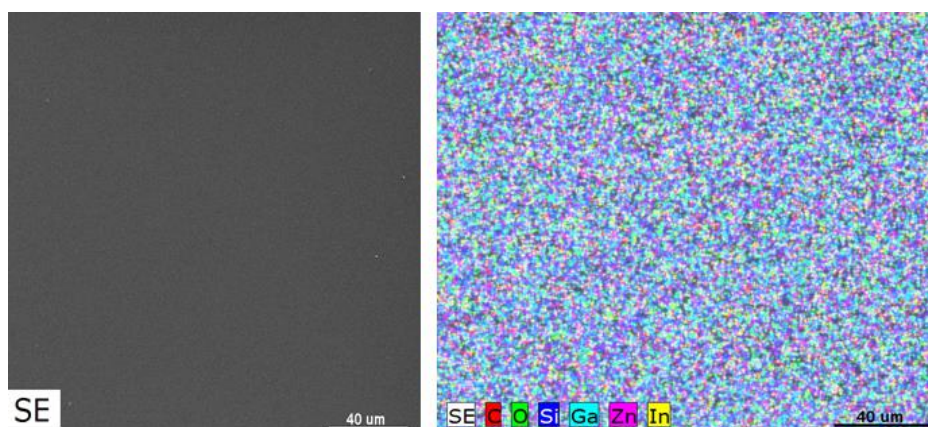


FIG. 4.33. EDX mapping image of PEALD/TALD-IGZO film related to the T(2/1/1) sample.

More in detail, Figures 4.34 and 4.35 illustrate the XPS fit of the In 3d, Zn 2p, and Ga 3d spectra after gently cleaning the film's surface. The most intense signals of the In 3d<sub>5/2</sub>, Zn 2p<sub>3/2</sub>, and Ga 3d appear at ~ 444.4 eV, ~ 1022.1 eV, and ~ 20 eV, respectively, and correspond to the metal-oxide formation of the quaternary IGZO films. The In 3d spectra are shown in Figure 4.34a with the spin-orbit-separated peaks (main lines of In 3d<sub>3/2</sub> and In 3d<sub>5/2</sub>) and the weak shoulders at the higher binding energy side of the main lines, suggesting the presence of OH groups and defect states<sup>(33)</sup>. From decomposition of the Zn 2p

spectra (see Fig. 4.34b), we found two weak signals of metallic zinc located at  $1043 \pm 0.1$  eV and  $1019.5 \pm 0.1$  eV related to the Zn  $2p_{1/2}$  and Zn  $2p_{3/2}$  signals, respectively. However, their contributions were estimated to be  $\leq 3\%$  and might arise from not complete oxidation of the PEALD process (see also Fig. 4.30). Taking advantage of the different inelastic mean free paths, in addition to the more intense Ga  $2p$  core level, we have also analyzed the more bulk-sensitive Ga  $3d$  spectra (Fig. 4.35) to clarify if the increase in Ga concentration estimated from depth profiling corresponds to changes on the Ga oxidation state. However, the analysis of Ga  $3d$  region is tricky due to the overlapping with the O  $2s$  ( $\sim 23.5$  eV) and In  $4d$  components of the In-O. In general, all core levels indicate a good oxidation degree for all samples, although defects and OH species are reported, which might indicate not ordered films probably related to the ALD low-temperature used in this investigation.

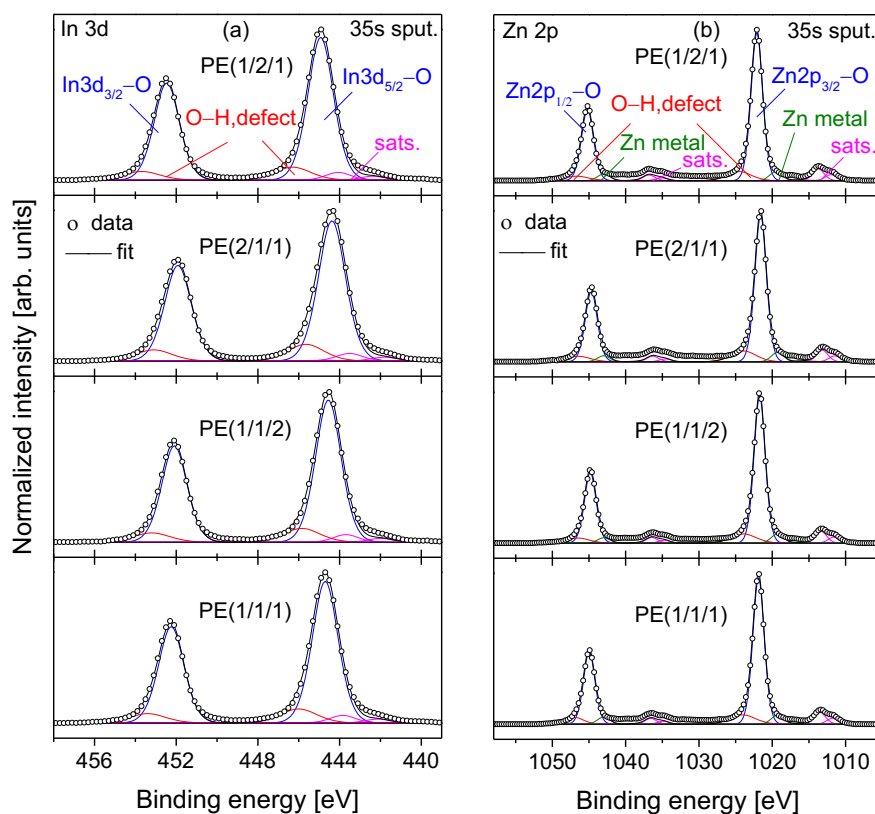


Figure 4.34. In  $3d$  (a) and Zn  $2p$  (b) XPS core levels spectra of the surface-cleaned PEALD-IGZO films prepared at  $150$  °C. The sample names are indicated within each plot. Mg  $K\alpha$  was used as the excitation source.

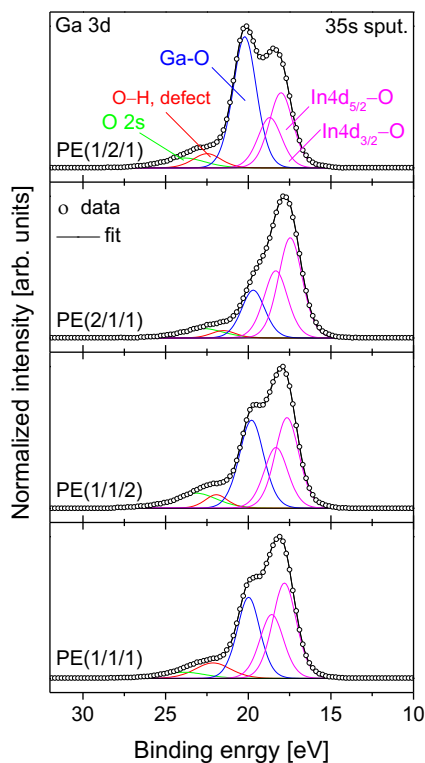


Figure 4.35. Ga 3d XPS core levels spectra of the surface-cleaned PEALD-IGZO films prepared at 150 °C. The sample names are indicated within each plot. Mg  $K\alpha$  was used as excitation source.

Auger spectra have been demonstrated to be more sensitive to slight changes in the oxidation state for many transition metal oxides.<sup>(282)</sup> Figure 4.36 shows the In MNN, Ga LMM and Zn LMM, respectively. The In MNN Auger spectra (Fig. 4.36a) depict the typical shape of indium oxide, in agreement with the literature,<sup>(268)</sup> having the main signal at  $\sim 398.2$  eV and a weaker peak at  $\sim 405.4$  eV. In the same way, the Ga LMM Auger spectra (Fig. 4.36b) of the IGZO samples present two peaks with the kinetic energies of  $\sim 1062.2$  eV and  $\sim 1065.6$  eV that confirms the formation of gallium oxide for all samples.<sup>(282)</sup> Finally, Figure 4.36c shows the Zn LMM Auger spectra appearing features for the different samples. Although the obtained spectra reveal Zn-O bonds characterized by peaks at  $\sim 987.6$  eV (main signal) and  $\sim 990.8$  eV (weak signal) for all ALD recipes, different grades of metallic Zn (not completely oxidized Zn) can be derived from contribution at  $\sim 995.2$  eV as well as relative intensity increase of the shoulder at  $\sim 990.8$  eV.<sup>(267)</sup> In this sense, samples with target element ratios of PE(1/1/2) and PE(2/1/1) exhibit typical ZnO<sub>x</sub> spectral feature which are in agreement with the reported paper<sup>(311)</sup>, while those with PE(1/1/1) and PE(1/2/1)

target ratios show incomplete oxidation of zinc. This metallic Zn contribution is more pronounced for the sample containing more gallium in the target composition PE(1/2/1). However, the sample with more indium PE(2/1/1) shows a relatively broad signal without Zn metallic phase (even though the exact number of ZnO<sub>x</sub> sub-cycles is used) which might be related to the incorporated defects in the ALD indium oxide film, which is in agreement with our previous report.<sup>(33)</sup>

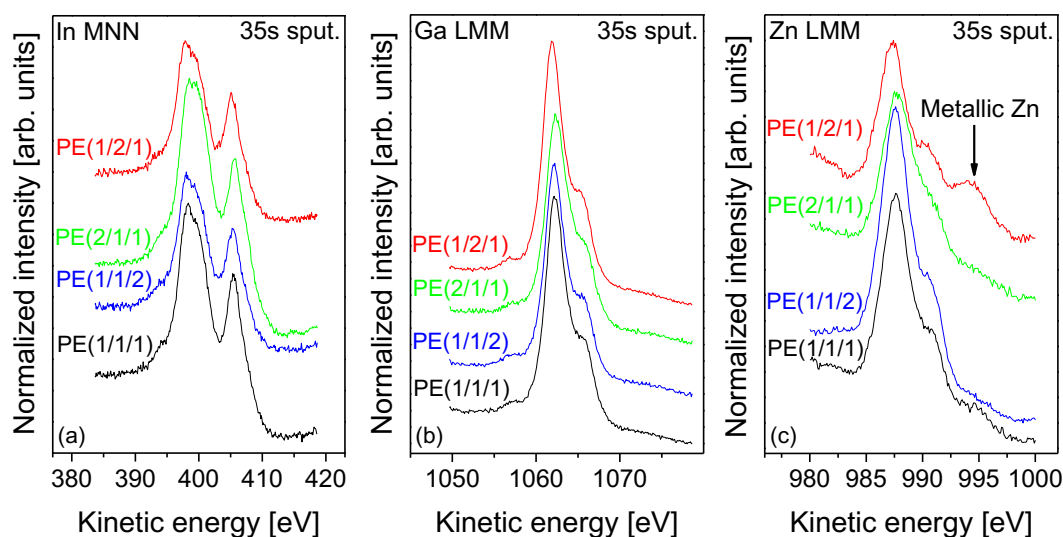


Figure 4.36. Auger XPS spectra of the surface-cleaned PEALD-IGZO films deposited in a low-temperature of 150 °C. The sample names are indicated beside each line. Excitation source of Mg K $\alpha$  radiation was used for the In MNN and Ga LMM Auger lines, while Al K $\alpha$  was applied for the Zn LMM Auger spectra.

Based on the performed analysis of the core levels spectra (see Figs. 4.34 and 4.35), the chemical properties of the cation components were investigated and compared with the target element ratio (see Table 4.6). Accordingly, the cation ratios (In/Ga and Ga/Zn) were determined by EDX as well as XPS (considering the core levels of the In 3d/Ga 3d and Ga 2p/Zn 2p), and plotted as a function of target element ratio (as shown in Fig. 4.37) with the corresponding data fitting. From XPS data, it should be remarked that the (Ga 2p)/(Zn 2p) ratio is more surface sensitive than the (In 3d)/Ga 3d) ratio due to the photoemission of the electrons. Therefore, the composition of the PEALD-IGZO films can be controlled by the definition of sub-cycle ratio within the super-cycle of the process, as can further be confirmed from EDX data which almost reflect the expected target element ratios. This enables the modification of the material properties of the super-cycle PEALD-IGZO films for promising applications.<sup>(310)</sup>

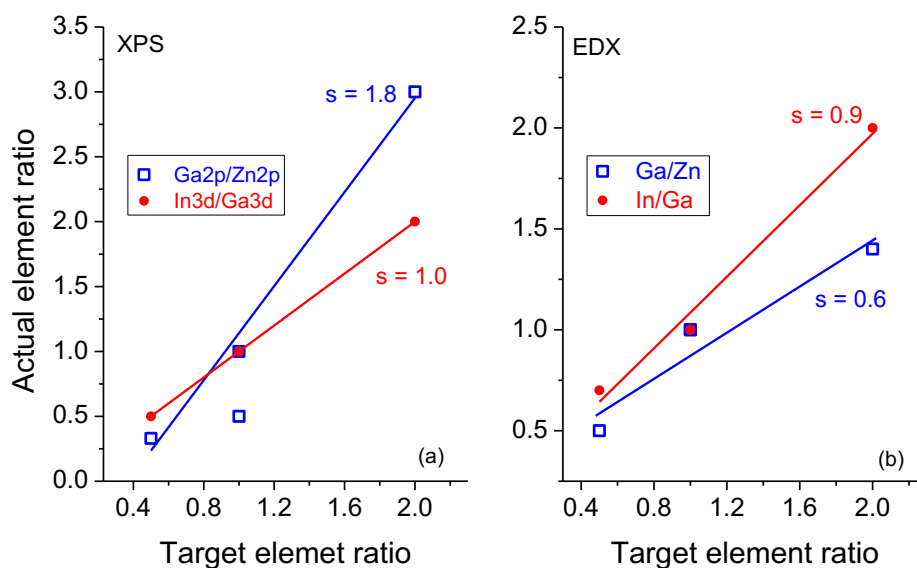


Figure 4.37. Comparison of the target and actual ratios of In to Ga (red circles) and Ga to Zn (blue open rectangles) of the PEALD-IGZO layers determined by (a) XPS, and (b) EDX. The solid lines represent the corresponding linear regressions where their slopes are given near each line.

The defect states of the PEALD-IGZO films were evaluated by XPS decomposition of the O 1s core level (as depicted in Fig. 4.38). The O 1s spectra were fitted into double sub-peaks with respect to the performed O 1s decomposition of the individual binary oxides (InO<sub>x</sub>, GaO<sub>x</sub>, ZnO), where we found the main sub-peak (oxygen-metals) located at an energy position of  $530.3 \pm 0.1$  eV. Following an equivalent procedure, two components can be used in the O 1s fitting: a unique to the O-Me (In, Ga, Zn) peak at lower binding energy (530.3 eV) and impurity related-oxygen (O-H, defects) at higher BE (531.9 eV).<sup>(33, 312)</sup> It should be taken into account that due to the energy resolution of our analyzer and the close overlapping between the individual O-Me components of the binary oxides in the O 1s spectra of the quaternary IGZO film, distinguishing between individual metals bonded to oxygen in the respective spectra is not possible. The considerable O 1s peak shifting was also detected for the sample with more indium content PE(2/1/1), which might be due to abundant oxygen deficiency and indium-rich structure, as abovementioned and in our previous report<sup>(33)</sup>. Considering the relative intensity of the sub-peaks, we found that the Ga-rich film (PE(1/2/1)) spectrum suggests fewer impurities (13.2%) with a high O-Me peak intensity of 86.8%, whereas that of In rich compound (PE(2/1/1)) delivers a higher impurity level of 16.3% with a low intensity of metals bonded to

oxygen peak (83.7%) originating from oxygen-deficiency. According to the literature, the contribution of defect states increase from growth temperature of 130 to 170 °C for the atomic layer deposited IGZO films.<sup>(313)</sup> The presence and variations of these impurities might significantly impact device performance (i.e. electrical characteristics) and ALD film quality.

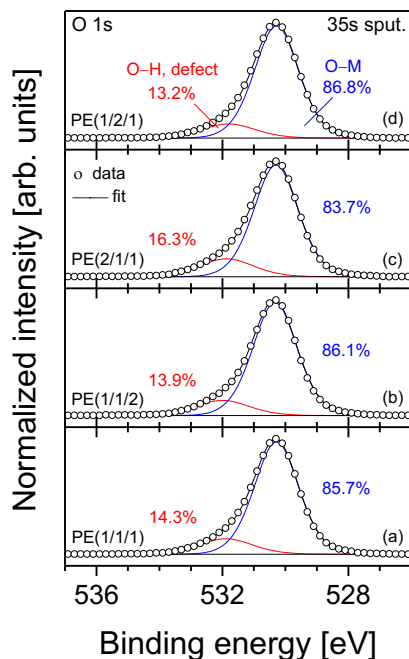


Figure 4.38. XPS O 1s decomposition of PEALD-IGZO films with different elements concentration. The target elemental ratios are represented as X/Y/Z. Mg  $K\alpha$  radiation was used as the excitation source.

#### 4.4.3 *Ex-situ* structural and morphological study

The structural properties of the PEALD-IGZO films were investigated by GIXRD measurements (Fig. 4.39). Although there were no sharp peaks in the GIXRD patterns, a broad signal appeared in the range of  $2\theta = 28^\circ\text{--}33^\circ$  could be assigned to the c-axis growth direction of IGZO peak (009)<sup>(314)</sup> and/or to the diffraction peak of (222) corresponding to the In-rich PE(2/1/1) film, which is consistent with Sheng et al., who reported the increase and widening of an already broad peak at  $32^\circ$  when the thickness of indium oxide sub-layer in PEALD-IGZO films was increased from 0.3 nm to 1.8 nm.<sup>(315)</sup> In one recent work on PEALD-InO<sub>x</sub> thin films<sup>(33)</sup>, the onset of crystallization was reported at 150 °C, precisely the temperature used in the current work. Here, the grown IGZO films shown a low degree of crystallinity. The super-cycle deposition promotes c-axis growth

with inter-diffusion<sup>(315)</sup>, resulting in a uniform and homogeneous elemental distribution from depth profiling (see Fig. 4.31), which further suppresses crystal growth<sup>(315)</sup>. It has been reported that the IGZO films prepared by sputtering and ALD techniques are in an amorphous structure at a deposition temperature of 250 °C, even after post-deposition annealing at 400 °C.<sup>(316)</sup>

In addition to the diffraction result, the surface morphology of the PEALD-IGZO film was also investigated by FE-SEM (in the inset of Fig. 4.39). A featureless and pinhole-free film surface can be seen from microscopic images, suggesting high-quality PEALD-IGZO layers resulting from a complete super-cycle-based layer-by-layer growth mechanism at low-temperatures. The present result is comparable to those amorphous ALD-IGZO films with high density grown at relatively higher temperature of 200 °C<sup>(315)</sup>. The higher morphological film quality achieved by the PEALD-IGZO process than other deposition techniques, resulting in porous films, could translate into better device performance and increase their applicability.<sup>(317)</sup>

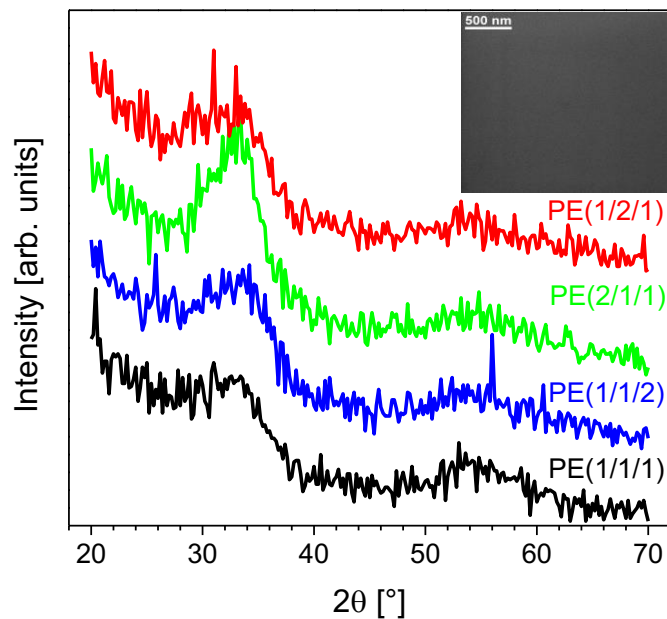


Figure 4.39. GIXRD patterns of PEALD-IGZO films with sample names labeled beside each data line. The inset shows the FE-SEM surface morphology of the PE(1/1/1) sample.

## 4.5 TALD of AlO<sub>x</sub> on Ti-coated Si (100)

In this section, the growth mechanism and the surface chemistry analysis of the AlO<sub>x</sub>/Ti samples deposited at different substrate temperatures (RT and 200 °C) using a pump-type ALD reactor are discussed for any applications in the fields of photovoltaic (as a passivation layer) and microelectronic (as a high-k gate dielectric layer). Besides, the effect of post-deposition annealing on the chemical state of the layers is also reported.

### 4.5.1 Deposited at room temperature and 200 °C

The early growth stages of the aluminum oxide thin films deposited at room temperature and 200 °C by TALD on titanium-coated Si (100) are discussed. The chemical nature of the substrate surface and the chemical reactions at the interface severely influence the film growth mechanism (here AlO<sub>x</sub>) because of potential surface diffusion, aggregation, and chemical reactivity of the reactants.<sup>(318, 319)</sup> Such effects could be investigated accurately at the beginning of the film growth when the deposited material directly contacts the substrate surface.

#### 4.5.1.1 Growth mechanism

Figure 4.40 exhibits the growth evaluation of the thin AlO<sub>x</sub> films deposited on the Ti substrates at RT and a relatively higher temperature of 200 °C. For such investigation, XPS core levels peak intensity of the Al 2p and Ti 2p were collected as a function of ALD cycles (from early stage until a final thickness of ~ 10 nm). The data were fitted using a defined layer-by-layer growth function in which the equations (see Eqs. 3.14 and 3.15 ) were applied for the film and substrates peaks, respectively.<sup>(320)</sup> It can be seen that with an increment of the ALD cycles, the Al 2p peak intensity increases exponentially as an indication of the aluminum oxide growth. In parallel, the exponential reduction of the Ti 2p peak intensity during the deposition process also confirms a layer-by-layer growth mechanism of the ALD. The function mentioned above also provides an estimation of the AlO<sub>x</sub> growth rate from both the depositing layer and the underneath substrate. At RT, the values of 0.98 and 0.97 Å/cycle were obtained, while at 200 °C nearly the same value of 1.00 Å/cycle was achieved. Therefore, according to the estimated GPC values, a self-limiting process is achieved under both substrate temperatures.



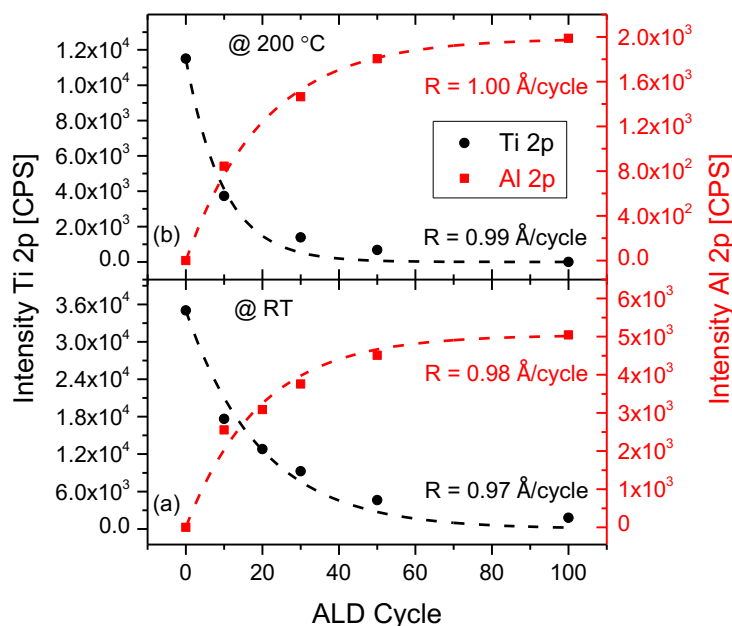


Figure 4.40. XPS peak intensities of the Al 2p (of  $\text{AlO}_x$  film) and Ti 2p (of the substrate) as a function of ALD cycle at RT (a), and at 200 °C (b).

#### 4.5.1.2 *In-situ* XPS study

##### 4.5.1.2.1 Oxidation of Ti by $\text{H}_2\text{O}$ exposure

Before growing the  $\text{AlO}_x$ , the oxidation state of the titanium substrate was investigated at RT by considering the main core level spectra of the Ti 2p and O 1s in addition to the C 1s (as shown in Fig. 4.41). For this investigation, the Ti substrate was exposed to sequential pulses (equivalent to the  $\text{H}_2\text{O}$  sub-cycle of the complete TMA/ $\text{H}_2\text{O}$  ALD process) of water at RT in parallel to *in-situ* XPS measurements to investigate the evolution of the oxidation state of the Ti. From Figure 4.41a, the spin-orbit splitting nature of the Ti 2p shows two components, Ti 2p<sub>1/2</sub> and Ti 2p<sub>3/2</sub>, at higher and lower binding energies, respectively. During the substrate oxidation with water, the main peak position of the Ti 2p<sub>3/2</sub> remained unchanged with the energy of  $\sim 453.8$  eV that could be attributed to the metallic Ti(0), while that of its counterpart (Ti 2p<sub>1/2</sub>) slightly shifted to the lower binding energies in addition to a broadening as an indication of forming Ti(IV)-oxide of  $\text{TiO}_2$  which are comparable to the data base.<sup>(267, 321)</sup> Such peak shift tendency, broadening as well as appearing satellite feature (at higher binding energy), are more pronounced for the higher number of cycles. Figure 4.41b, represents the O 1s core level spectra in which partial oxidation of Ti substrate is evident with a peak located at 531.5 eV that might be related to some adsorbed OH species from

XPS chamber. However, after introducing water to the surface by cycling process, the same peak position of  $\sim 530.4$  eV was observed where the collected signals from the higher oxidation stages show more contribution of O-Ti bonds of the  $\text{TiO}_2$  layer. The C 1s core level region is shown in Fig. 4.41c. In general, all the spectra reveal a prominent peak located at a binding energy of  $\sim 284.7$  eV, indicating C-C bonds (negligible contribution for the Ti substrate) corresponding and a minor peak appeared in the energy position of  $\sim 282.0$  eV (which is dominated in the Ti substrate) corresponds to the Ti-C (titanium carbide). A weak signal (at  $\sim 286.3$  eV) on the shoulder of the main peak represents the probable C-O (carbonyl), and its contribution increases by raising the number of  $\text{H}_2\text{O}$  cycles.

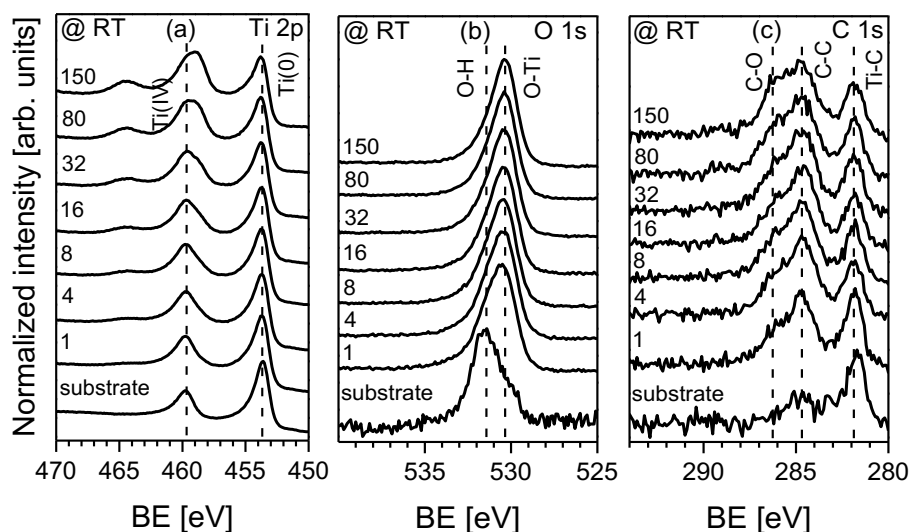


Figure 4.41. XPS core levels spectra of Ti 2p (a), O 1s (b), and C 1s (c) corresponding to the titanium substrate as a function of  $\text{H}_2\text{O}$  exposure at RT. The numbers indicate the applied ALD cycle.

Figure 4.42 demonstrates the variation of atomic concentration (at RT) for the main elements of titanium, oxygen and carbon at two different XPS take-off angles,  $90^\circ$  (bulk sensitive) and  $50^\circ$  (surface sensitive). During the oxidation of the Ti substrate via sequential pulses of  $\text{H}_2\text{O}$  (as an oxygen source), the surface is getting rich in oxygen, whereas the concentration of titanium decreases to 15.7% after 200  $\text{H}_2\text{O}$  cycles, with a saturation state of O with the percentage at 75.6%. The amount of carbon is almost constant ( $\sim 9\%$ ) within the applied cycles. However, a slight increase in carbon contamination to 11% was observed for the first cycles. In order to evaluate whether such undesired carbon contamination has more contribution to the surface or in the layer, the take-off angle of photoelectrons was altered to  $50^\circ$ . It can be seen that the concentration of carbon

increased by only one point, revealing that the carbon contamination has been introduced during the whole process and might arise from a not very clean ALD reactor. Besides, no significant change was observed for the O (78.6%) at this surface-sensitive conditions. Therefore, an almost similar 3% concentration difference (considering two applied angles) can be realized for the both C and O pointing to the formation of C-O like contamination bonds (see Fig. 4.41c) during oxidizing the Ti substrate via ALD cycles.

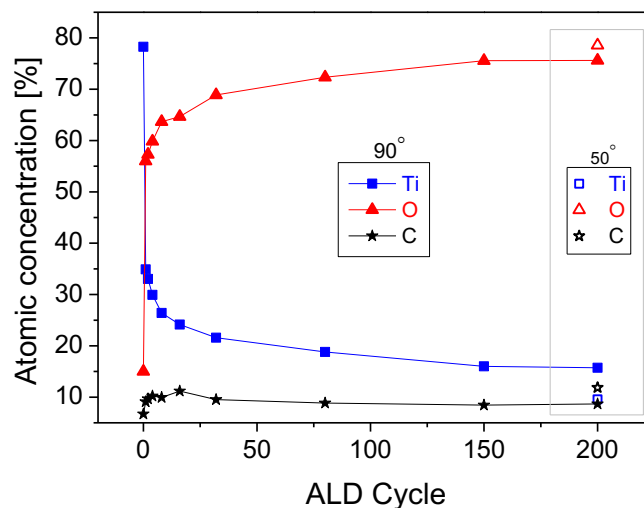


Figure 4.42. Evolution of atomic concentration corresponding to the main core levels of Ti 2p, O 1s, and C 1s as a function of ALD cycle during oxidizing Ti substrate.

The deposition of the aluminum oxide was initiated after investigating the oxidation state of the titanium substrate by H<sub>2</sub>O exposure at room temperature. Such deposition process was fulfilled along with *in-situ* XPS measurements where different ALD cycles were considered. For a better understanding the surface chemistry of the AlO<sub>x</sub> growth, the data are classified into the two parts, including the overview spectra of the significant core levels (at RT and 200 °C) and then moving to a quantitative study of the early stages of growth, where the ALD process and XPS analysis were conducted repeatedly.

#### 4.5.1.2.2 Overview of the complete cycles

Figure 4.43 shows the Ti 2p core level spectra after a series of complete cycles concerning AlO<sub>x</sub> films deposited at RT and 200 °C. The Ti 2p spectra show the expected doublet, Ti 2p<sub>1/2</sub> and Ti 2p<sub>3/2</sub> with binding energy values of about 460 and 454 eV (with an energy separation of 6 eV). The film prepared at 200 °C reveals relatively broader peaks, indicating that the Ti substrate is not completely

in the Ti(0) metallic phase rather there is a slight transition to the Ti(II) oxide phase.<sup>(267, 321)</sup> The deposition of  $\text{AlO}_x$  up to 100 cycles results in the gradual decrease of Ti 2p intensity, which is significantly pronounced for the layers at 200 °C where the signal completely vanishes after 100 ALD cycles. If we focus on the binding energy position of the dominant peaks, the layers prepared at RT show almost the same peak position until the final cycling process, whereas the growth at 200 °C reveals a slight tendency to higher binding energies due to more oxidation. It should be noted that the titanium is known as a getter material for oxygen as we saw by exposing the Ti to  $\text{H}_2\text{O}$  at RT. However, during the ALD process, the substrate surface is passivated with the  $\text{AlO}_x$  layer, which suppresses further Ti oxidation, as can be realized by comparing the Ti spectra of Figs. 4.41a and 4.42. Therefore, it can be concluded that the  $\text{AlO}_x/\text{Ti}$  deposition at RT remains the same during ALD cycles, while deposition at 200 °C could introduce a limited oxidation of the Ti substrate, which in any case could happen during the warm-up process and not during the  $\text{AlO}_x$  deposition. excess of oxygen during cycling (up to 50 cycles) and can facilitate the surface chemical reactions and film coverage (for complete 100 cycles).

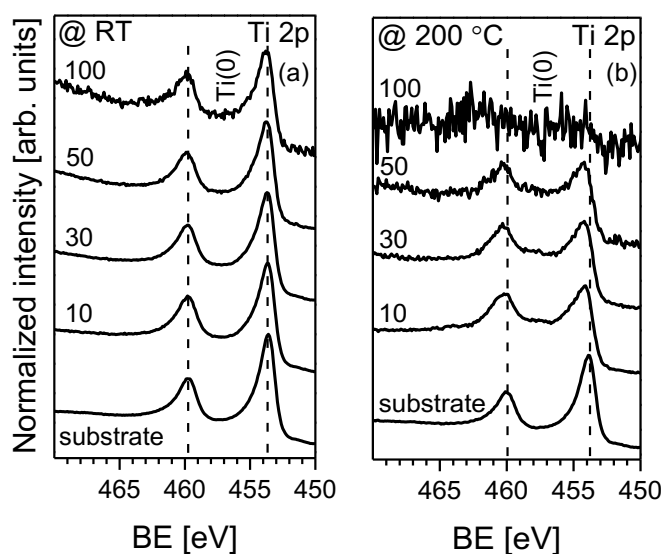


Figure 4.43. XPS Ti 2p spectra of  $\text{AlO}_x$  complete ALD cycles on Ti substrate considering different temperatures of RT (a), and 200 °C (b). The numbers indicate the applied ALD cycle.

The O 1s core level spectra corresponding to the individual complete ALD cycles of the grown  $\text{AlO}_x$  layers on the titanium substrates at RT and 200 °C is displayed in Figure 4.44. The presence of an unexpected weak and noisy signal for the O 1s spectra of the Ti substrate (at RT and 200 °C) indicates partial

adsorption of the OH species onto the substrate surface during *in-situ* sample transferring from the prep-chamber (for Ti evaporation) to the analyzer chamber. However, their contribution is negligible compared to the Ti 2p core level spectra (see above). In general, a peak shift to higher binding energies appears from 10 cycles to 100 cycles in both room and 200 °C temperatures, suggesting more oxidation and formation of O-Al. However, the layer deposited at RT shows the peak position saturation at  $\sim 532.5$  eV for the 50 and 100 ALD cycles, while for that of the 200 °C sample the saturation binding energy shift was not observed. Furthermore, comparing the line width of O 1s spectra for both temperatures, it can be deduced that setting a substrate temperature of 200 °C could reduce the amount of incorporated impurities and narrow the O 1s signal.

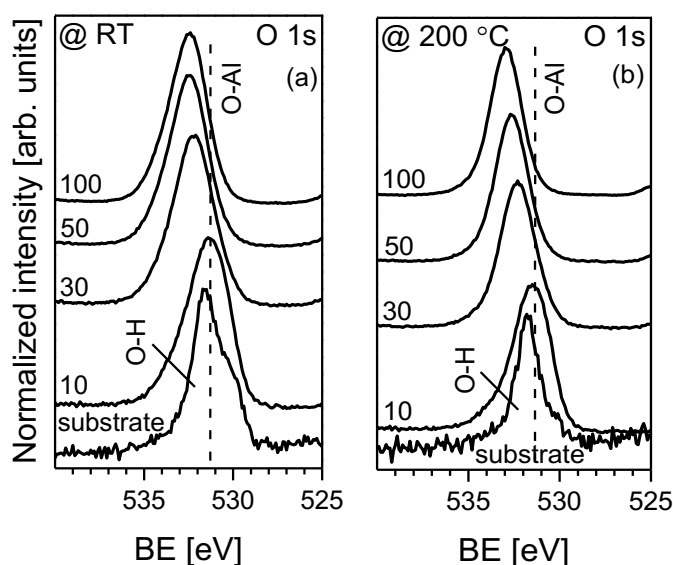


Figure 4.44. XPS O 1s spectra of  $\text{AlO}_x$  complete ALD cycles on Ti substrate considering different temperatures of RT (a), and 200 °C (b). The numbers indicate the applied ALD cycle.

Figure 4.45 illustrates the Al 2p core level spectra of the individual complete ALD cycles corresponding to the  $\text{AlO}_x$  films deposited on the Ti substrates at RT and 200 °C. The peaks show a clear shift tendency to the higher binding energies as the layer's thickness increases, pointing to the aluminum to oxygen bonds forming within the complete ALD cycles. Comparable to the O 1s spectra (Fig. 4.44), the film grown at RT reveal an energy position saturation at  $\sim 75.5$  eV for the 50 and 100 ALD cycles, whereas there is no saturation in the peak position (up to 100 cycles) for the film prepared at 200 °C.

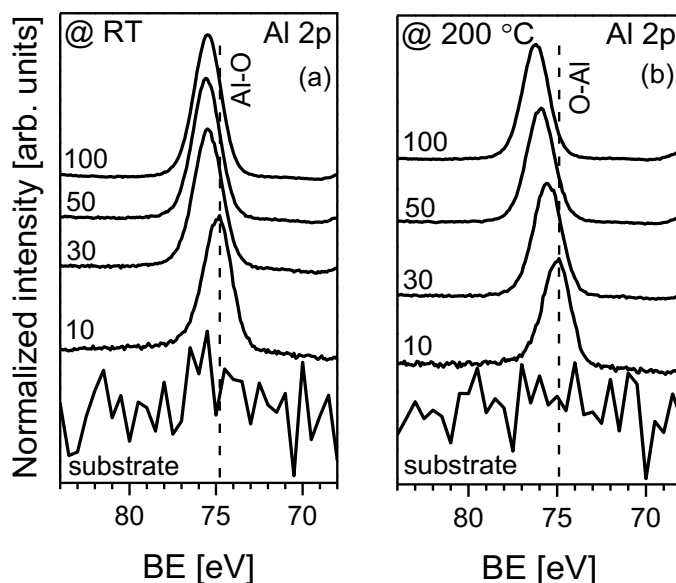


Figure 4.45. XPS Al 2p spectra of  $\text{AlO}_x$  complete ALD cycles on Ti substrate with considering different temperatures of RT (a), and 200 °C (b). The numbers indicate the applied ALD cycle.

The C 1s core level spectra of the individual complete ALD cycles of the deposited  $\text{AlO}_x$  layers on the titanium substrates at RT and 200 °C is depicted in Figure 4.46. The substrate spectra reveal clear signals at a binding energy of  $\sim 282$  eV, indicating the presence of carbon bonded to titanium as titanium carbide ( $\text{TiC}$ )<sup>(322)</sup>, in addition to an almost negligible amount of carbon located at  $\sim 285$  eV.<sup>(216)</sup> It can be seen that with increasing the ALD cycles, the carbide contribution remarkably decreases and finally vanishes after 100 cycles. From 10 cycles, the dominant carbon peak shifts to the C-C component as  $\text{AlO}_x$  thickness increases. For the RT deposition, a saturation on the energy position (at  $\sim 284.7$  eV) was found for the last two ALD cycles. Such observed shift is similar to that shown by O 1s and Al 2p core levels spectra (Figs. 4.44 and 4.45). However, for the sample at 200 °C the main peak position remained nearly constant. It is worth to mention that ALD process of aluminum oxide at temperatures above RT (here 200 °C) can considerably reduce the amount of carbon.<sup>(323)</sup> The collected noisy spectra of the C 1s corresponding to the sample prepared at 200 °C confirm that during the first ALD cycles, because of surface reaction between the reactants and Ti substrate, there is relatively more contribution of carbon in comparison with the last 100 cycles where a negligible amount of carbon was observed.

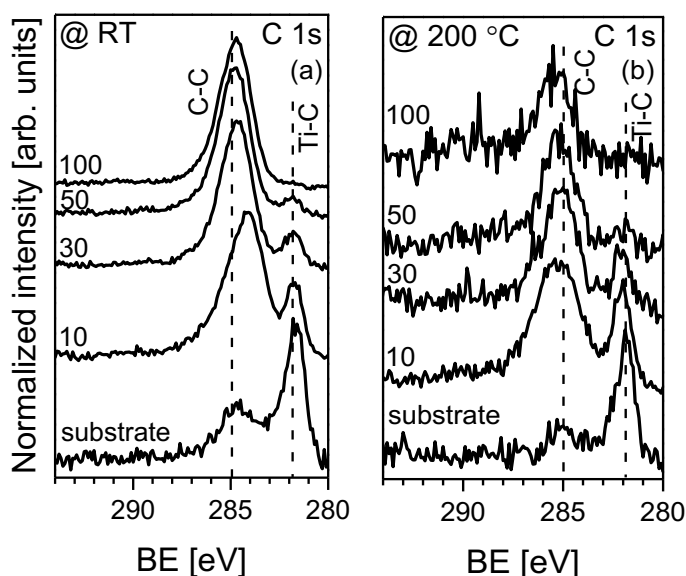


Figure 4.46. XPS C 1s spectra of  $\text{AlO}_x$  complete ALD cycles on Ti substrate with considering different temperatures of RT (a), and 200 °C (b). The numbers indicate the applied ALD cycle.

Figure 4.47 displays the dependence of atomic concentration on the ALD cycles for the prepared  $\text{AlO}_x$  samples at RT and 200 °C. The ALD cycle axis can generally be divided into the two regimes: transition regime (below 50 cycles) and steady regime (above 50 cycles). In the transition regime, the main films composition signals of aluminum and oxygen increase while those of titanium substrates and carbon contamination decrease. On the one hand, an almost steady composition signals were observed in the steady regime in which the saturation state of the main elements is evident. It can be clearly seen that Ti and C are completely disappeared at 200 °C and that of RT deposition reveals a negligible amount of Ti (below the XPS detection limit) in addition to the carbon concentration of ~ 5%. The observed abundant amount of oxygen might be related to that  $\text{H}_2\text{O}$  (oxygen source) has a less molecular weight in comparison with TMA molecules (aluminum source) causing more diffusion probability of water into the layers during deposition which leads to an excess oxygen.<sup>(324)</sup> Further analysis is discussed below.

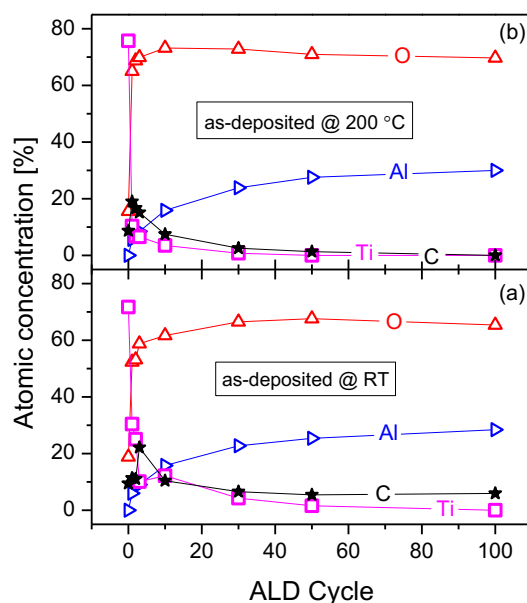


Figure 4.47. Atomic elemental concentration of AlO<sub>x</sub> films as a function of the complete ALD cycles at different temperatures of RT (a), and 200 °C (b).

#### 4.5.1.2.3 Qualitative analysis

Figure 4.48 exhibits the peak fitting corresponding to the energy region of the Ti 2p spectra for the early stage of the growth until the final ALD cycling. As discussed above, considering the energy position of the main peaks, the Ti 2p spectra are in the Ti(0) metallic phase<sup>(321)</sup>. However, there are minor amounts of the O and TiC that their contributions are negligible when compared to the major intensity of Ti 2p signals. The presence of Ti(II) oxide<sup>(321)</sup> formation is more pronounced for the sample at 200 °C with two components located at higher energy (~ 456.0 and 460.0 eV)<sup>(321)</sup> side of the main signals (Ti 2p<sub>3/2</sub> and Ti 2p<sub>1/2</sub>), respectively. In fact, the appeared partial oxidation of Ti substrate (in the first stage of ALD cycle) might arise from heating the ALD reactor during deposition which is caused to adsorb some residual gases (i.e. oxygen species) to the sample surface. Afterwards, the Ti spectra exhibits almost the same feature during the process. With increasing ALD cycle, the AlO<sub>x</sub> more passivates and/or covers the underneath titanium substrate surface where an increment of TiO<sub>x</sub> components was found due to more interface contribution and less metallic Ti signals from the bulk. For the sample prepared at RT, the Ti 2p spectra were observed even for 100 cycles, while deposition at 200 °C reveals complete coverage for 100 cycles, without any fingerprint of the Ti 2p signals. Such observation confirms the



absence of pinholes and a better chemical reaction on the surface at high substrate temperatures.

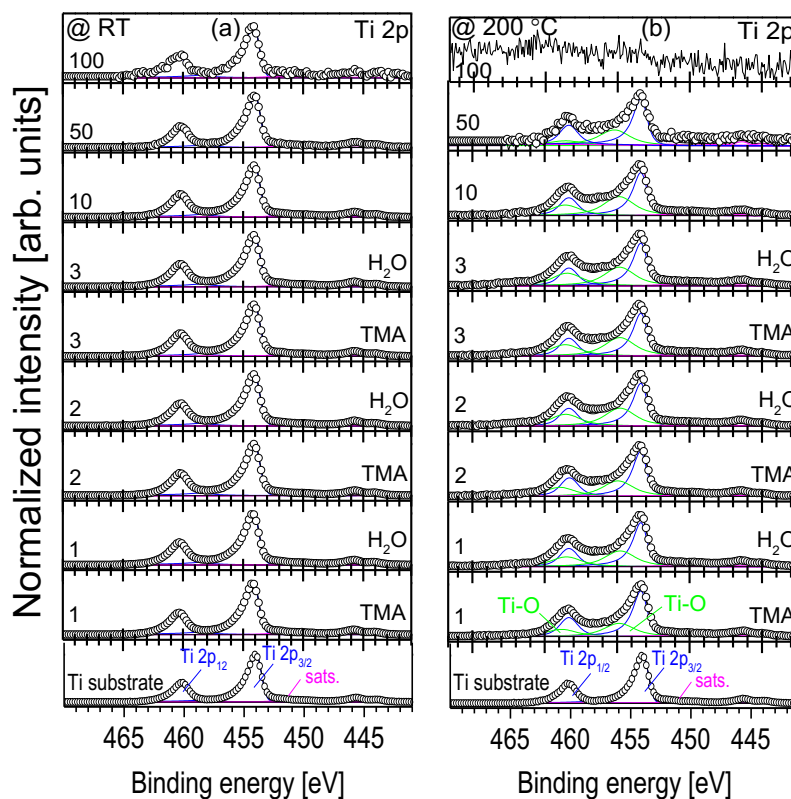


Figure 4.48. XPS Ti 2p peak decomposition of ALD- $\text{AlO}_x$  on Ti substrate considering different temperatures of RT (a), and 200 °C (b). The numbers indicate the applied ALD cycle.

The XPS O 1s core level spectra of the  $\text{AlO}_x/\text{Ti}$  are shown in figure 4.49 for both RT and 200 °C deposition temperature. The collected spectra could be decomposed into three and two components for the titanium substrate and the early stage, as well as complete ALD cycles, respectively. To minimize errors in the ratio determination (see below), a model was applied in the fitting process of the O 1s spectra, so that firstly the last 100 cycles stage (for both RT and 200 °C samples) was fitted assuming an ideal Al:O ratio of 0.66 considering the Al 2p raw area and O-Al component of the O 1s region. Afterwards, the established model (i.e., impurity-related oxygen and O-Al contributions with their corresponding fit parameters, except components area) was propagated to the stages to understand the role of different ALD cycles and temperatures on the atomic ratio (Al:O) of the  $\text{AlO}_x$  films.

As mentioned earlier, the bare Ti substrate shows a negligible amount of oxygen in comparison with the Ti 2p peak intensity (Fig. 4.48). The fitted O 1s spectrum reveals a main peak related to O-Ti and low intense contributions that could be attributed to adsorbed oxygen-related bonding (at low binding energy) and undeliberate impurities arising from the metal hydroxide groups<sup>(325)</sup> as well as small amount of carbonates and/or hydrocarbon (hydrogen bonded to carbon) (at high binding energy)<sup>(216, 322)</sup>. After initiating the ALD cycle (which starts from the first half cycle of TMA), the O 1s spectra show two distinct major and minor components, the metals-oxide (Ti-O-Al) and metal hydroxides (Ti-OH-Al), correspondingly.<sup>(325-327)</sup> However, in this decomposition, it is assumed that the available oxygen sites are more occupied by Al-O and Al-OH rather than Ti counterparts. According to the ALD mechanism, the Al-CH<sub>3</sub> ligands of the TMA precursor develop on the top during the TMA pulse, and they exchange for the Al-OH bonds after introducing the second half cycle of H<sub>2</sub>O. This is the reason to see the presence of OH species bonded to the aluminum within the ALD cycles of the AlO<sub>x</sub> using TMA and H<sub>2</sub>O reactants.<sup>(328)</sup> Typically, such ligands exchange with the oxidant cannot be done perfectly, leading to the small contributions of hydrogen and carbon residue in the prepared AlO<sub>x</sub> layer.<sup>(326, 329)</sup> The relative intensity of the OH groups increases with the number of ALD cycles, becoming more pronounced when the surface is exposed to the oxygen source (here H<sub>2</sub>O) during the early stages (up to three cycles). At the stage of 10 cycles, such undesired impurity (OH species) remarkably increased to 38.6% for RT sample, which might be an indication of interfacial reactions and/or more OH bonds at the interface between the Ti substrate and the AlO<sub>x</sub> layer, resulting in an oxygen excess (oxygen-rich) of the AlO<sub>x</sub> layers comparable to the literature.<sup>(330, 331)</sup> Whereas, 200 °C sample revealed a reduction of impurity with the amount of 19.6%. However, for 100 cycles, the contribution of hydroxides reduces to a relative weight of 33.9% (RT) and negligible contribution of 4.7% (200 °C), indicating deposition at relatively higher temperatures considerably reduces the incorporated impurities in the bulk of the layer. According to the data, the O 1s spectra shift to higher binding energies with the number of cycles. In this way, for the RT growth, the O 1s peak position remained almost constant (~ 531.2 eV) during the first 3 cycles, and afterwards, it saturates at ~ 532.9 eV for 50 and 100 cycles. On the contrary, the 200 °C deposition shows the main peak binding energy of ~ 530.9 eV up to 3 cycles, and then the energy position continually increased to ~ 532.9 eV at 100 ALD cycles.

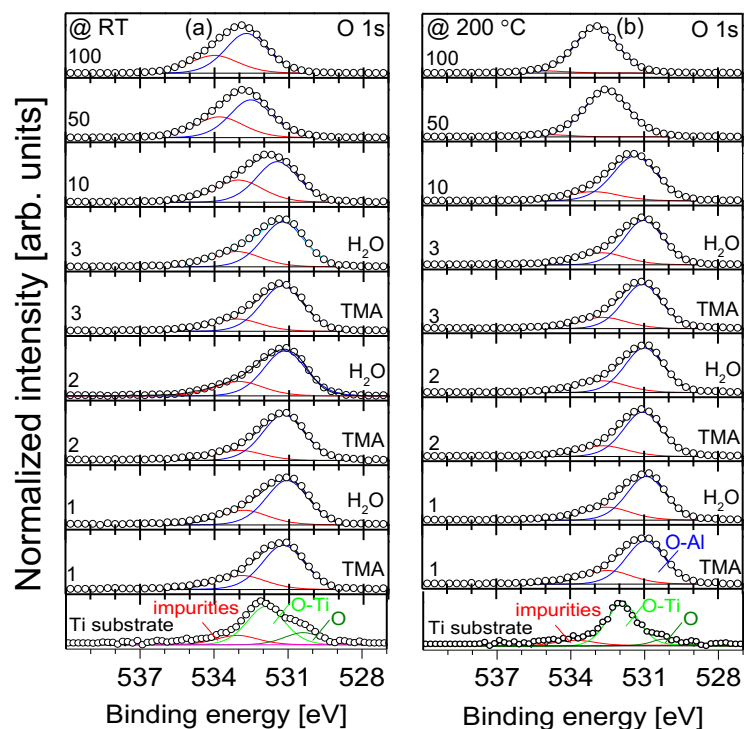


Figure 4.49. XPS O 1s peak decomposition of ALD-AIO<sub>x</sub> on Ti substrate considering different temperatures of RT (a), and 200 °C (b). The numbers indicate the applied ALD cycle.

Figure 4.50 shows the Al 2p core level spectra of the ALD-AIO<sub>x</sub> cycles on Ti substrates at RT and 200 °C. It can be fitted with three peaks, one main and two minor contributions. As it can be seen from the initial stages of the growth, the main dominant signal corresponds to the Al-O, while two minor sub-peaks could be linked to the Al-Ti (at the interface) and/or Al-(OH)<sub>x</sub> bonds (indicated with \*) at low energy position and the related impurities (hydroxides, hydrocarbon) at high binding energies.<sup>(216, 332, 333)</sup> By increasing the number of ALD cycles, the relative peak intensity of the aluminum bonded to the oxygen increases while the intensity area of those sub-peaks decreases. The presence of the minor peaks is more pronounced for the first three cycles, and their contributions considerably reduce for the complete ALD cycles of 10, 50 and 100. Considering the evolution of the Al 2p spectra, it can be deduced that the Al 2p signal of the RT sample is nearly in the same energy position of ~ 74.9 eV for the first three ALD cycles and slightly increased to an energy position saturation of 75.9 eV at 50 and 100 ALD cycles. Similar behavior was also observed for the sample prepared at 200 °C, where the binding energy of the Al 2p peak remained almost in the same energy position (~ 74.6 eV) for the early three ALD cycles.

However, with increasing the ALD cycles, a peak shift to higher binding energies continues without any saturation (comparable to the shown O 1s spectra), where the peak position of  $\sim 76.2$  eV was recorded for the total 100 cycles of ALD. The reason for these peaks shift could be explained as a result of charging effect for insulating layers such as  $\text{AlO}_x$  which increases as thickness of the layer rises.

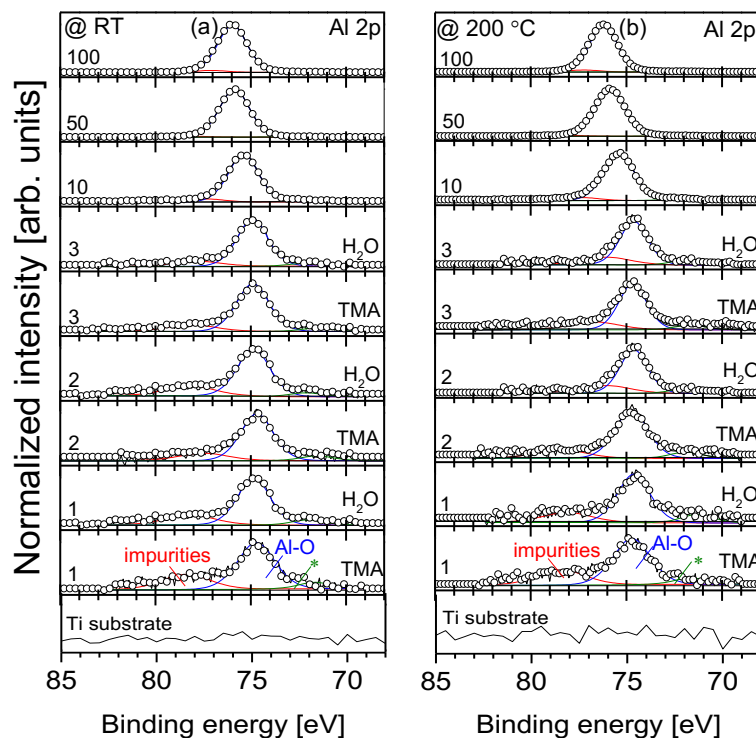


Figure 4.50. XPS Al 2p peak decomposition of ALD- $\text{AlO}_x$  on Ti substrate considering different temperatures of RT (a), and 200 °C (b). The numbers indicate the applied ALD cycle.

The C 1s core level spectra of the  $\text{AlO}_x$  samples deposited at room and 200 °C temperatures were decomposed into five components, as represented in Figure 4.51. The presence of the components from lower to higher binding energies, those contributions can be assigned to the TiC, C-related precursor bonds (arising from Al- $\text{CH}_3$ ), C-C/C-H and carbon bonded to the oxygen species (C-O/C-OH and/or C=O/O-C-O, labelled with #), respectively.<sup>(216, 334-336)</sup> It should be noted that by increasing the number of ALD cycles, the relative peak intensity of TiC decreased to only about 2% for the last complete cycles of the RT sample and completely vanished for the sample prepared at 200 °C. On the other hand, the contribution of the C-C bonds becomes more important, especially for the complete ALD cycles (10, 50 and 100). However, its peak intensity is negligible

for the 100 cycles of ALD performed at 200 °C. Moreover, considering the main C-C component of the decomposed C 1s spectra from the early deposition stages until the complete cycles, it can be realized that there is no significant shift tendency for the 200 °C film. Unlike, the layer deposited at RT reveals a slight shift to low binding energies for 10 cycles. It is worth mentioning that the peak labelled with C and located at a binding energy of  $\sim 283.9$  eV could be attributed to the remained fragments of TMA precursor that could not be completely desorbed from the ALD reactor during the purging process.<sup>(324)</sup> Based on the initial growth stages spectra, those C and C-C components are typically absorbed on the surface with TMA exposure, where the C-C signal increases with the ALD cycles while the sub-peak intensity of C increases with pulsing the TMA and decreases upon introducing H<sub>2</sub>O. During the growth process, the contributions of carbonyl and carbonates increase with the thickness, estimating a relative weight of about 19% for the last 100 ALD cycles of RT sample. Therefore, it can be concluded that deposition at temperatures above RT could reduce the amount of carbon on the surface and in the bulk of the layers.<sup>(323)</sup> Furthermore, an increase of growth temperature might facilitate oxidizing the chemisorbed TMA molecules on the surface, consequently reducing the amount of carbon.

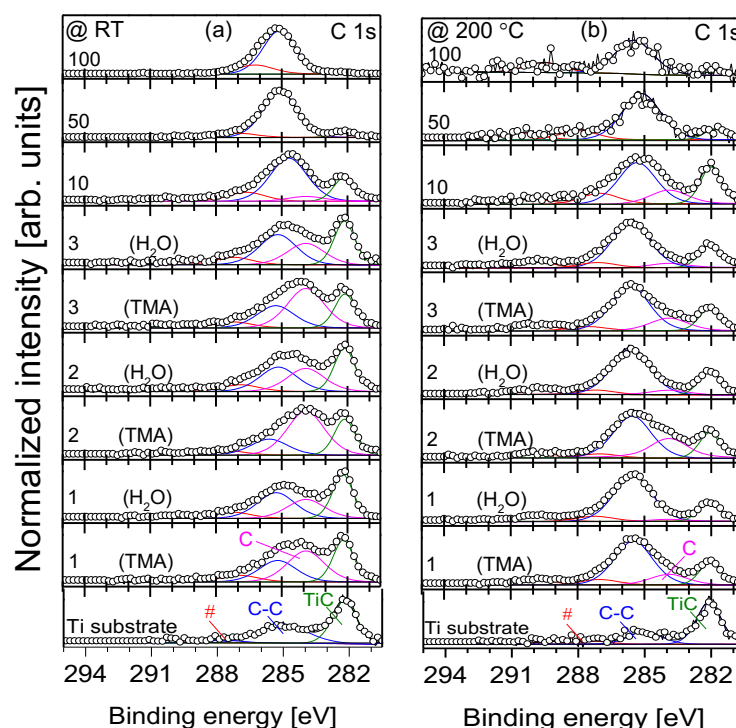


Figure 4.51. XPS C 1s peak decomposition of ALD-AlO<sub>x</sub> on Ti substrate considering different temperatures of RT (a), and 200 °C (b). The numbers indicate the applied ALD cycle.

Figure 4.52 illustrates the evolution of the aluminum to oxygen (Al:O) atomic ratio versus the number of ALD cycles, where the element ratio is calculated from the XPS decomposition of the O 1s(O-Al) and Al 2p core levels. It should be taken into account that the limited signal-to-noise ratio of the analyzed XPS spectra for the low number of ALD cycles, as well as in the determination of the baseline for background subtraction, might impact the calculated ratio in this study. Based on the obtained results, we report an excess of oxygen for the initial cycles up to 50, and more pronounced for the sample prepared at 200 °C. With an increment of the number of ALD cycles, the layers are approaching the stoichiometric state where the Al:O ratios increase from 0.37 (RT sample) and 0.34 (200 °C sample) to the expected ratio of 2:3 (as explained before, fixed for the 100 cycles growth). The observed oxygen excess and related deviations in the ratios could be due to the interface and/or nucleation effects in the deposition process. Moreover, H<sub>2</sub>O oxidant presents less molecular weight than TMA molecules, and therefore, the diffusion probability of water into the layers during ALD cycles should be taken into account, that promoting the oxygen-rich of the films.<sup>(324)</sup> Considering the surface chemistry, the oxygen atoms typically accumulate more at the interface<sup>(337)</sup>, and hence, the thin layers of the AlO<sub>x</sub> (early ALD stages between 10 and 30 cycles) exhibit more incorporated oxygen. Such interface effect is more noticeable for the applied temperature of 200 °C, which is comparable to the literature.<sup>(330)</sup> Besides, it has been reported that the aluminum oxide films are rich in oxygen at low temperatures of < 200 °C due to the considerable contribution of OH groups, resulting in a higher amount of oxygen and hydrogen in the deposited layers.<sup>(338)</sup>

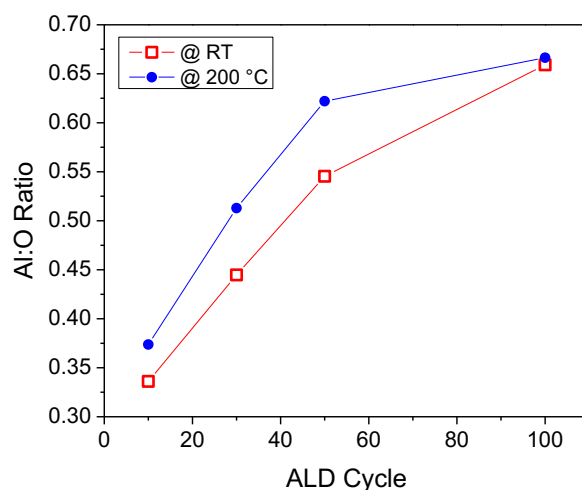


Figure 4.52. Atomic Al:O ratio of AlO<sub>x</sub> as a function of ALD cycle number.

*In-situ* XPS depth profiles of the aluminum oxide films deposited at room temperature and 200 °C are shown in Figures 4.53 and 4.54, where the atomic percentage of the composition elements is plotted as a function of the sputtering time. The inset of the figures magnifies the sputtering time zone from 0 to 300 s. In fact, the depth profile of the AlO<sub>x</sub> using the sequential sputtering steps provides useful chemical information about the distribution of the layer's elements from the surface and sub-surface regions, as well as within the bulk of the layers until reaching the films/substrates interfaces.

The acquired data reveal a homogeneous concentration of the main elements (Al and O) through the prepared AlO<sub>x</sub> layers, particularly for the sample deposited at 200 °C. A slight variation of the elements was observed for the RT sample at the initial stages of sputtering, where the atomic concentration of the aluminum and oxygen has an increasing trend. Afterwards, the amplitude of deviations decreases within the bulk of the film. The presence of carbon contamination for the first sputtering steps confirms the adventitious carbon is only at the surface of the layers, being no trace of carbon in the bulk of the films. It should be noted that the observed carbon contamination at the early sputtering stages of the 200 °C sample was negligible, suggesting the AlO<sub>x</sub> film deposited at relatively higher temperature of 200 °C is carbon-free from top to bottom of the layer.

As discussed earlier, the deposited aluminum oxide layers are rich in oxygen, as can be confirmed from depth profiling data. Such an abundant quantity of oxygen could be related to the nucleation effect and interfacial reactions between the prepared Ti substrate and the grown layer of AlO<sub>x</sub>. However, it has been reported that the pulse length of H<sub>2</sub>O (oxygen source) and the associated purging process might significantly influence the atomic percentage of oxygen in the aluminum oxide film prepared by ALD.<sup>(323)</sup> It should be taken into account that the observed oxygen-rich state of the layers has been also reported for the aluminum oxide layer deposited by PEALD at 100 °C.<sup>(187)</sup>

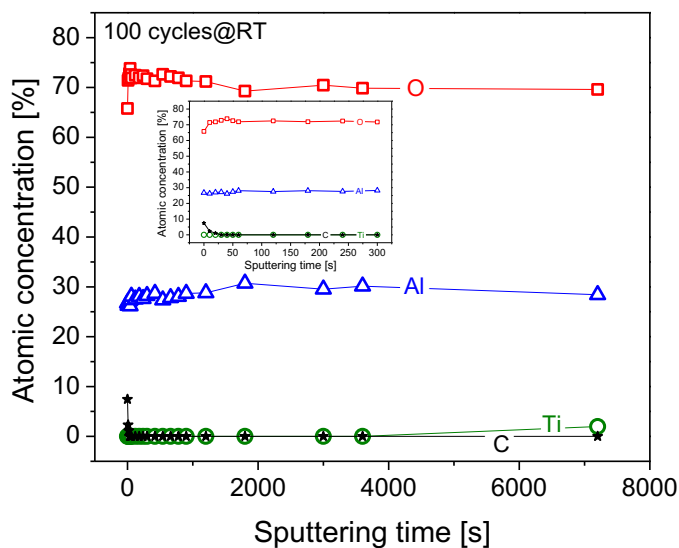


Figure 4.53. XPS depth profile of  $\text{AlO}_x$  film deposited at RT. The insert shows a narrow window of sputtering time up to 300 s.

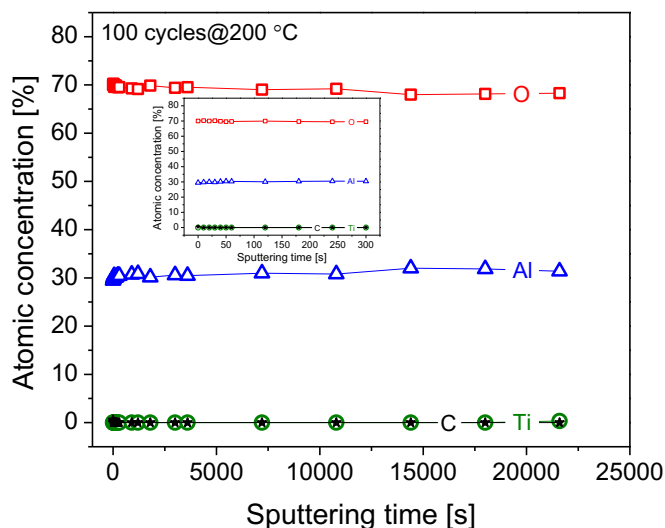


Figure 4.54. XPS depth profile of  $\text{AlO}_x$  film deposited at 200 °C. The insert shows a narrow window of sputtering time up to 300 s.

Figure 4.55 shows the XPS peak decomposition of the Al 2p, O 1s and C 1s core levels for the sample deposited at RT. The Al 2p spectra (Fig. 4.55a) reveal a single component related to Al-O at 75.7 eV before and after sputtering, where the integrated peak area was increased after sputtering, confirming the reduction of surface contamination (carbon and OH groups). In the O 1s



decomposed spectra (Fig. 4.55b), the presence of the main and minor sub-peaks could be assigned to the O-Al and impurities, respectively, in correlation with the represented data (see Fig. 4.49). According to the obtained result, the as-deposited sample shows a relatively low peak intensity of O-Al (77.6%) and a high amount of impurities (22.4%), including the adventitious carbon and OH groups. However, after 10 min sputtering, the O-Al increases (85.2%) and the contribution of incorporated hydroxides is remarkably reduced to 14.8%. It should be mentioned that a slight peak shift of  $\sim 0.3$  eV to lower binding energy was observed in the O 1s spectra of the sputtered sample for 10 min, which might be due to the partial removal of O-H under the sputtering process. Figure 4.48c shows the C 1s spectra before and after sputtering. It can be seen that the as-deposited sample was decomposed into two components of C-C and C-O. However, after 10 min sputtering, the very low intense signal dominates the spectra, indicating a negligible amount of carbon in the bulk of the film. Such noisy spectra could be fitted with three peaks, revealing more contribution of carbonates in the bulk of the layers, which might originate from incomplete reactions between the reactant molecules, which are more probable at lower temperatures.<sup>(338)</sup>

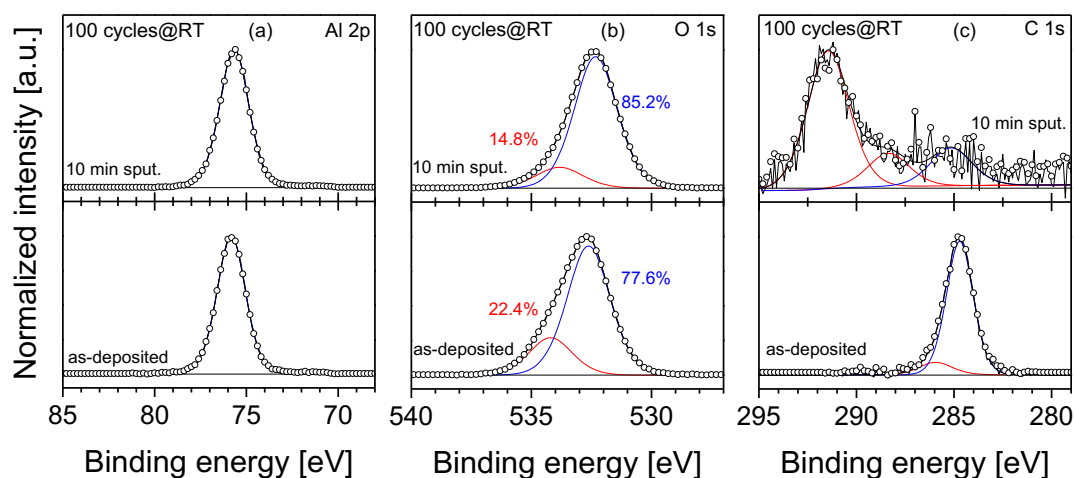


Figure 4.55. XPS surface (as-deposited) and depth (10 min sputtering) analysis of  $\text{AlO}_x$  film at RT with considering core level spectra of Al 2p (a), O 1s (b), and C 1s (c).

#### 4.5.1.3 *In-situ* XPS of post-deposition annealing (PDA)

The effect of *in-situ* post-deposition annealing (PDA) on the chemical properties of the  $\text{AlO}_x$  film deposited at RT was investigated by applying sequential thermal steps (as shown in Fig. 4.56). The collected corresponding core

level spectra of the Al 2p, O 1s and C 1s were decomposed and compared with the analyzed data of the sample prepared at RT (indicated in the bottom frame of the figures, respectively). The as-deposited and the annealed layers generally reveal almost the same energy position of  $\sim 75.8$  eV and  $\sim 532.7$  eV for the Al 2p and O 1s spectra. According to Figure 4.56a, the full width at half maximum (FWHM) of the Al 2p main signal (Al-O) slightly increased from 1.85 (for as-deposited) to 1.92 (for 1hr annealing at 200 °C), and remained constant for the following annealing steps suggesting no further re-ordering the alumina matrix. From the O 1s decomposition data (as shown in Fig. 4.56b), after the first annealing step, the contribution of the impurities decreased from 15.4% to 7.4%, while that of O-Al increased from 84.6% to 92.6% and the relative peak intensity of the components (impurities and O-Al) did not change significantly during the whole annealing steps. In Figure 4.56c, the C 1s fitted spectra for the as-deposited and annealed samples are shown. The as-grown sample reveals three distinct components that, from low to high binding energies, and could be assigned to the carbide, main signal of C-C and the minor peak of carbonyl, correspondingly. The relative intensity of Ti-C contribution was estimated to be around 1.7% for the as-deposited sample and during thermal treatment, its contribution considerably increased to 9.6% for the first annealing, then slightly decreased and remained constant (7.0%) for the next annealing steps. Concerning the result, the *in-situ* annealing process (inside of the ALD reactor) develops C-O bonds in the layer, where the corresponding relative peak intensity increases from 13.4% (1hr @ 200 °C) to 18.1% (2hrs @ 200 °C), remaining constant (19.7%) for the last two steps of annealing. Therefore, it can be concluded that PDA treatment could reduce the total amount of carbon residue, but develops carbon bonded to oxygen species to the deposited layer in agreement with the literature in which carbon contribution increased from 20.0% to 25.0% for the annealed aluminum oxide film.<sup>(339)</sup> However, it should be taken into account that the annealing process might trigger the possible diffusion of carbon from the bulk to the surface and could activates the chemical reactions on the surface. Nevertheless, it has been reported that the presence of carbon might be related to the incomplete desorption of CH<sub>3</sub> ligands of the TMA precursor.<sup>(340)</sup> Although, typically ALD of the aluminum oxide films poses less carbon contamination than other deposition methods, such as metalorganic chemical vapor deposition (MOCVD) where a relatively high amount of carbon was reported for the Al<sub>2</sub>O<sub>3</sub> films.<sup>(341)</sup> Comparing the obtained results with that of AlO<sub>x</sub> sample deposited at 200 °C, we can deduce that growth at relatively higher temperatures facilitates reduction of carbon contribution where

the layer at 200 °C (Fig. 4.51) revealed a negligible amount of C-C and no trace of TiC sub-peak.

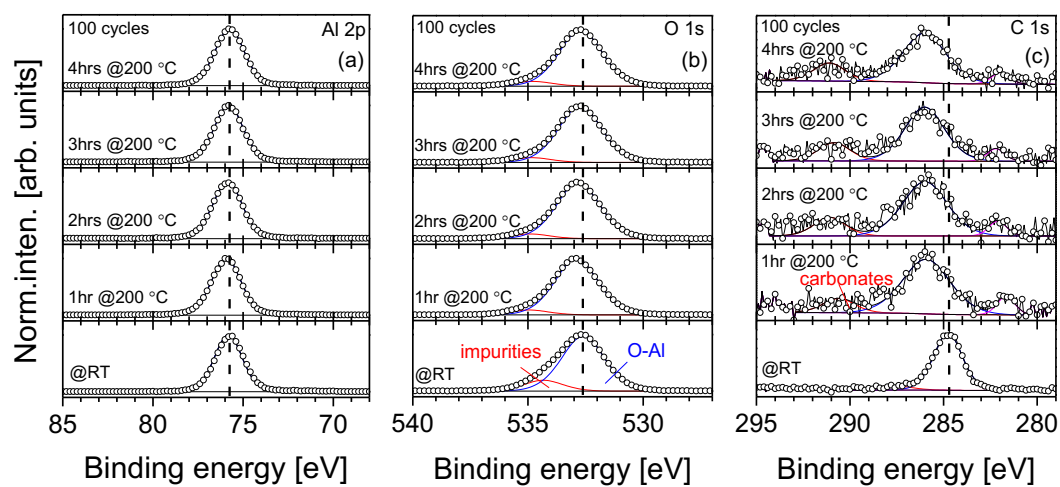


Figure 4.56. XPS peak decomposition of core levels spectra of Al 2p (a), O 1s (b), and C 1s (c) corresponding to PDA treated ALD- $\text{AlO}_x$  film grown at RT.

## 4.6 TALD of CeO<sub>x</sub> on SiO<sub>x</sub> and AlO<sub>x</sub>/Si (100)

This section discusses the role of different substrates on the growth mechanism of the CeO<sub>x</sub> layer deposited by *in-situ* ALD for any potential applications in the field of gas sensor devices. As described in the experimental chapter, the ALD reactor has been already reconfigured to use low/very low vapor pressure precursors such as Ce(thd)<sub>4</sub>. However, the optimization of the growth process (in particular controlling the temperature) is still ongoing to overcome some undesirable growth issues, including the presence of flakes that point to incomplete surface coverage for thickness below 5-10 nm.

### 4.6.1 *In-situ* XPS study of ALD Ceria growth

The role of different interfaces and thicknesses on the growth of cerium oxide thin films was investigated using an *in-situ* XPS characterization. For such study, two different substrates of 300 nm thick SiO<sub>x</sub> and 10 nm Al<sub>2</sub>O<sub>3</sub> layer (grown on Si (100) at RT, as-explained in section 4.5) by homemade *in-situ* ALD) were used for the deposition of the cerium oxide thin layers using Ce(thd)<sub>4</sub> precursor as a source of cerium and ozone (O<sub>3</sub>) as a strong oxidant. Figure 4.57 exhibits the Ce 3d core level spectra of the CeO<sub>x</sub> thin films on both SiO<sub>x</sub> and AlO<sub>x</sub> substrates, where different ALD cycles were also considered. In general, the cerium oxide spectra consists of several doublets which are related to the spin-orbit splitting (Ce 3d<sub>5/2</sub> and Ce 3d<sub>3/2</sub>) nature of Ce 3d core level, where in our case a spin-orbit shift of 18.6 and 19.6 eV was recorded for the CeO<sub>x</sub>/SiO<sub>x</sub> and CeO<sub>x</sub>/AlO<sub>x</sub> substrates, respectively, which is comparable to the data base.<sup>(267)</sup> It should be noted that the slight energy difference of 1 eV between two energies separation might arise from the interfacial reactions of two different substrates to the cerium oxide layer.

According to the collected data, the layers present a relatively rich concentration of the Ce<sup>3+</sup> state for the initial stages of ALD. The Ce 3d Ce<sup>3+</sup> spectrum is formed by four components located at around 883, 887, 901, and 905 eV, labelled as v<sup>0</sup>, v', u<sup>0</sup>, u'.<sup>(342)</sup> These components are more pronounced for the 50 cycles layer grown on the SiO<sub>x</sub> substrate, where their contributions decrease when increasing the number of ALD cycles, so called moving to the Ce<sup>4+</sup> states. The presence of peak (labeled with u''') at higher binding energy of Ce 3d region is a characteristic and/or fingerprint of Ce<sup>4+</sup> originating from a transition of the 4f<sup>0</sup> initial state to the 4f<sup>0</sup> final state.<sup>(343-345)</sup> In principle, the Ce 3d spectrum for the Ce<sup>4+</sup> oxidation state poses six peaks of v, v'', v''', u, u'', u''', corresponding to three doublets for the Ce 3d<sub>3/2</sub> and Ce 3d<sub>5/2</sub> components.<sup>(346-349)</sup> For the atomic layer

deposited cerium oxide those features are more pronounced for the higher number of ALD cycles (thicker layers) due to a transition in the oxidation state or reduction of  $\text{Ce}^{3+}/\text{Ce}^{4+}$  ratio with increasing layers thickness, comparable with other deposition methods.<sup>(350)</sup>

For the early stage of 50 cycles, initial  $\text{Ce}^{4+}$  signal was observed for  $\text{CeO}_x/\text{AlO}_x$  sample in comparison with  $\text{CeO}_x/\text{SiO}_x$  sample, with no evident  $u'''$  peak. The reason could be due to the interfacial reactions between the reactants and the insulating layer(s) (aluminum oxide in this study, or  $\text{Si}_3\text{N}_4$  from literature<sup>(351)</sup>) that inherently passivate the surface and might play as buffer layer(s) for the deposition of the cerium oxide film to favor the presence of  $\text{Ce}^{4+}$  component. Therefore, it can be deduced that the substrate surface layer influences the growth of  $\text{CeO}_2$  layer at the interface<sup>(352, 353)</sup>. Flege et al., documented that well-ordered epitaxial ultrathin cerium oxide film can be prepared on the passivated Si (111) by chlorine layer.<sup>(353)</sup> It has been reported that for other deposition techniques such as magnetron sputtering, a remarkable contribution of  $\text{Ce}^{3+}$  and  $\text{Ce}^{4+}$  were observed for 25 nm films of  $\text{CeO}_2/\text{Si}$  and  $\text{CeO}_2/\text{Si}_3\text{N}_4$ , respectively.<sup>(351)</sup>

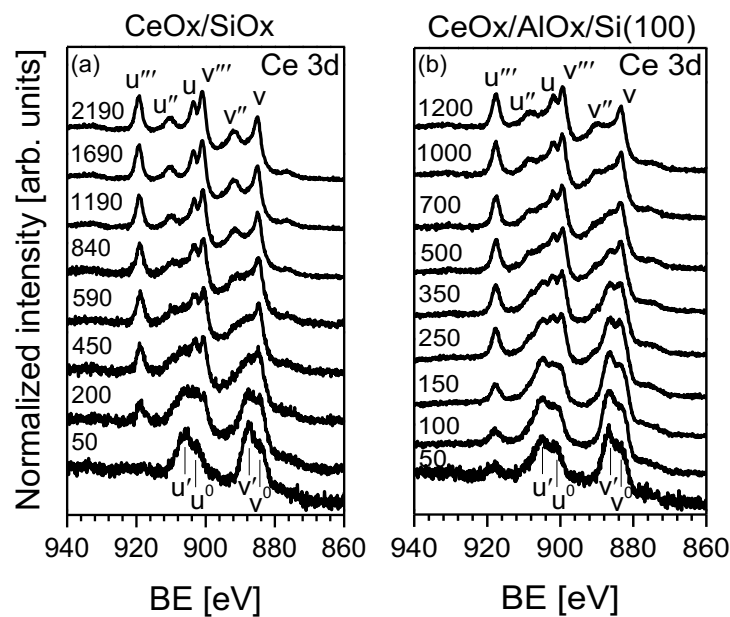


Figure 4.57. XPS Ce 3d spectra of  $\text{CeO}_x$  thin films on different substrates of  $\text{SiO}_x$  (a), and  $\text{AlO}_x/\text{Si}$  (b). The numbers indicate the applied ALD cycle.

Figure 4.58 shows C 1s XPS spectra of the cerium oxide thin films deposited on different the two substrates. First, both substrates show the fingerprint of adventitious carbon due to *ex-situ* preparation in the air before *in-*

*situ* deposition of the  $\text{CeO}_x$  layers. After characterization of the substrates (initial state), different ALD cycles were applied to investigate the role of the ceria thickness on carbon contamination. It can be seen that from bare substrate to the 50 ALD cycles, there is a slight peak transition (labelled I) from C-C to C-O (carbonyl) as the number of cycles increases. The spectra also reveal a minor component (labelled II) that could be attributed to the carbonates, and/or Ce 4s, which overlaps with C 1s.<sup>(216)</sup> The presence of such contributions (Ce 4s and carbonates) increases with the increment of the ALD cycles (as expected for the Ce 4s contribution), particularly for the cerium oxide grown on the prepared aluminum oxide substrate.

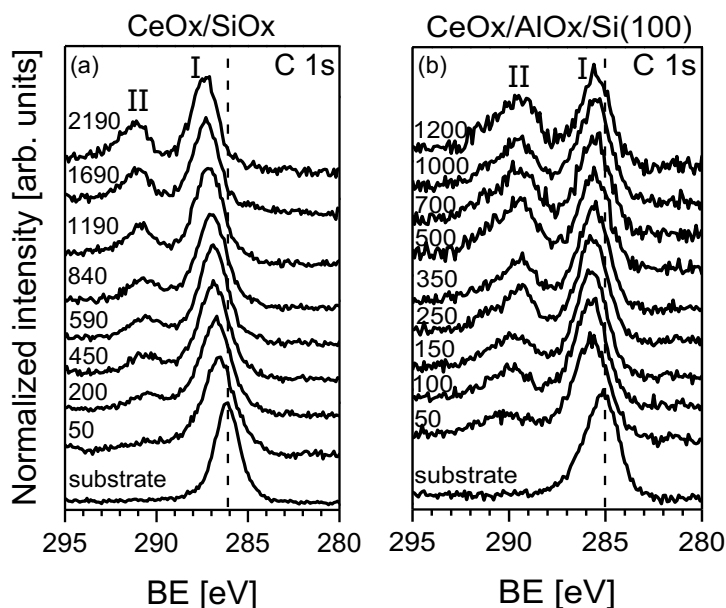


Figure 4.58. XPS C 1s spectra of  $\text{CeO}_x$  thin films on different substrates of  $\text{SiO}_x$  (a), and  $\text{AlO}_x/\text{Si}$  (b). The numbers indicate the applied ALD cycle.

#### 4.6.2 Reactivity of ALD- $\text{CeO}_x$ layers

The surface chemistry interaction of the cerium oxide film with hydrogen ( $\text{H}_2$ ) was investigated by NAP-HAXPES (as shown in Fig. 4.59). For that experiment, the  $\text{CeO}_x$  sample was deposited by ALD on the  $\text{SiO}_x$  substrate to evaluate the reduction and re-oxidation states of the film. The corresponding Ce 3d and Ce 2p core levels spectra were collected considering the photon energy and different photoelectron mean free paths. According to the decomposed Ce 3d spectrum (Fig. 4.59a), the as-introduced film reveals a mixture of  $\text{Ce}^{3+}$  and  $\text{Ce}^{4+}$  states, dominating the  $\text{Ce}^{4+}$ , with components of  $v'''$ ,  $v''$ ,  $v$ ,  $u'''$ ,  $u''$  and  $u$  belonging to  $\text{Ce}^{4+}$ , and peaks of  $v^0$ ,  $v'$ ,  $u^0$  and  $u'$  belonging to  $\text{Ce}^{3+}$ , with a fit comparable to

the literature.<sup>(350)</sup> After  $H_2/N_2$  gas exposure with a partial pressure of 20 mbar at room temperature, the slight reduction process occurs in the bulk of the film, increasing the intensity of  $Ce^{3+}$  sub-peaks. It has been reported that the cerium oxide material poses higher contribution of  $Ce^{3+}$  species after reduction process under hydrogen gas at various temperatures up to 700 °C.<sup>(354)</sup> The re-oxidation of the  $CeO_x$  layer was completed after exposing to the atmospheric air.

Figure 4.59b, shows the Ce  $2p_{3/2}$  spectrum that can be fitted by the Gaussian/Lorentzian product function into the sub-components of  $r$ ,  $r''$ ,  $r'''$  of the complete re-oxidation  $CeO_2$  which are corresponding to the three final state configurations of  $2p^54f^2$ ,  $2p^54f^1$ , and  $2p^54f^0$ , respectively, besides, two sub-signals of  $r^0$ ,  $r'$  arising from  $Ce_2O_3+CeO_2$  (appeared for as-introduced and during reduction) could be attributed to the two final state configurations of  $2p^54f^2$  and  $2p^54f^1$ , correspondingly.<sup>(355)</sup> The presence of broad signal at the energy position region of the  $r'''$  sub-component is assigned to bulk plasmons. By comparing the spectra, it can be clearly seen that the as-introduced sample reveals mixture of two cerium oxide states ( $Ce_2O_3$  and  $CeO_2$ ) where the contribution of  $Ce_2O_3$  sub-peaks are more pronounced for the reduction stage of the film that more like to be happened on the top layer region. A complete re-oxidation state of the layer was obtained by exposure to the ambient air with the major sub-signals of the  $CeO_2$  structure. Allahgholi et al., reported that the observed relatively large FWHM for the middle sub-peak ( $r''$ ) of the  $CeO_2$  could be compared with the  $v''$  component of the Ce 3d spectra, where presence of complex sub-components is likely.<sup>(355)</sup>

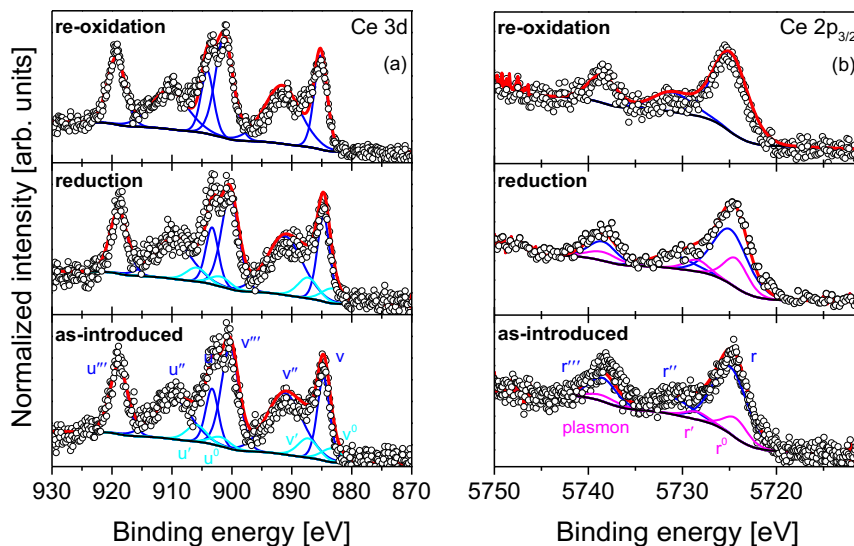


Figure 4.59. NAP-HAXPES spectra of Ce 3d (a) and Ce  $2p_{3/2}$  (b) core levels corresponding to as-introduced, after reduction and re-oxidation of the grown  $CeO_x/SiO_x$  layers.





## Chapter 5

### CONCLUSIONS AND OUTLOOK

This PhD project documents the atomic layer deposition and film properties of wide band gap metal oxides, including  $\text{InO}_x$ ,  $\text{GaO}_x$ ,  $\text{ZnO}_x$ , and their mixing as a quaternary IGZO compound. In addition, the work has also covered  $\text{AlO}_x$  and  $\text{CeO}_x$  layers. This work aimed to develop and study the ALD growth process and characterization of the aforementioned oxide-based candidates in detail. The following lines present the conclusions according to the obtained results and outlook.

#### 5.1 Summary and conclusions

- **$\text{InO}_x$**  thin films were deposited on Si (100) substrate using PEALD with  $\text{TMIIn}$  and  $\text{O}_2$  plasma at the low-temperature range of 80 to 200 °C. The prepared layers were characterized by optical and spectroscopic methods. Ellipsometry data revealed an increment of the growth rate when rising deposition temperature, where a self-saturated growth with a GPC of 0.56 Å/cycle and an excellent inhomogeneity of 1.2% (across 4-inch wafer) were achieved within the  $T_s$  range of 100–150 °C. The refractive index was found to be  $2.07 \pm 0.36$  for the layer grown at 150 °C, and it abruptly decreased to  $2.02 \pm 0.34$  at 200 °C. Besides, the films exhibit indirect and direct band gaps with the values of  $2.8 \pm 0.1$  and  $3.3 \pm 0.2$  eV, respectively. According to the XPS analysis, the films are carbon-free after surface cleaning, and a temperature-dependent off-stoichiometry was observed, suggesting oxygen vacancies in the layers where their abundance slightly increases with rising substrate temperature. For the O 1s core level decomposition, the relative contribution of hydroxyl groups and defects decreases with increasing substrate temperature while the relative intensity of the O-In component rises. Furthermore, surface-

sensitive angle-dependent XPS confirms that the defect states are homogeneously distributed within the layers.

*In conclusion*, high-quality indium oxide thin films can be deposited at large wafer scale in a low-temperature PEALD process using TMI<sub>n</sub>/O<sub>2</sub> plasma, which is suitable for high-performance optoelectronic and photovoltaic devices where low-thermal budget of processing is required.

- **GaO<sub>x</sub>** thin films were deposited on Si (100) substrate using PEALD with TMGa and O<sub>2</sub> plasma at the low-temperature range of 80 to 200 °C. The prepared layers were characterized by optical and spectroscopic methods. A constant growth rate of ~ 0.66 Å/cycle and a very high homogeneity range of 1.5 to 2% were obtained from ellipsometry measurements, confirming that the chosen substrate temperatures are within the ALD window. Moreover, the refractive index and optical band gap showed values of  $1.86 \pm 0.01$  and  $4.63 \pm 0.05$  eV, respectively. The XPS results proved that all prepared films are nearly in carbon-free, with an oxygen-rich phase of Ga:O ratio around 0.54. Besides, decomposition of the O 1s core level spectra corroborated the overwhelming presence of O-Ga bonds in the films, whose fraction increases with rising substrate temperature, whereas the relative peak intensity of the hydroxyl species and defect decreases. Further XPS investigation was carried out by collecting surface-sensitive spectra and revealed that the undesirable impurities are more presence in the bulk of the layers.

*In conclusion*, high-quality gallium oxide thin films can be grown at a large wafer scale in a low-temperature PEALD process with TMGa/O<sub>2</sub> plasma, rendering the prepared layers well suited for electronic and optoelectronic applications where low-temperature deposition is required.

- **ZnO<sub>x</sub>** thin films were deposited on Si (100) substrate using TALD with DEZ and water at the low-temperature range of 80 to 200 °C. The prepared layers were characterized by optical and spectroscopic methods. According to the ellipsometry measurement, the growth rate rises with increasing substrate temperature, where a relatively constant GPC of 1.53 Å/cycle was achieved within the ALD temperature window of 150 to 200 °C. Besides, the data also revealed the refractive index and band gap values of  $1.94 \pm 0.02$  and 3.1 eV, respectively. From the analyzed XPS

spectra, the films are carbon-free within the applied temperatures and pose a Zn:O ratio of 1.25, pointing to an oxygen-deficient state. Based on the O 1s decomposition spectra, it has been derived that the contribution of OH groups and defects decreases with increasing temperature. Concerning the surface-sensitive XPS data, the contributed impurities arise from the ZnO<sub>x</sub> bulk layers, not from the surface.

*In conclusion*, high-quality zinc oxide thin films can be deposited by TALD using DEZ and H<sub>2</sub>O in a low-temperature range of 80-200 °C with the capability to be applied in electronic and optoelectronic devices where low processing temperature is required.

- **Quaternary IGZO** thin films were deposited on Si (100) substrate by PEALD with variations in the target element ratio of the In/Ga/Zn by means of changing the ALD cycles. The deposition temperature was fixed at 150 °C according to the best overlap between the ALD windows of each grown binary oxides (InO<sub>x</sub>, GaO<sub>x</sub>, ZnO<sub>x</sub>). The prepared films composition consists of equal (1/1/1), indium rich (2/1/1), gallium rich (1/2/1), and zinc rich (1/1/2) states, where the order follows the top to bottom pattern of ZnO<sub>x</sub>/GaO<sub>x</sub>/InO<sub>x</sub>. By comparing TALD and PEALD we could discuss general ALD issues in complex super-cycles, particularly the nucleation delay of the ZnO<sub>x</sub> sub-cycle. The prepared films were characterized by a variety of techniques such as SE, XPS, GI-XRD, and FE-SEM (equipped with EDX). The GPC of the prepared PEALD binary layers of GaO<sub>x</sub> on InO<sub>x</sub>, ZnO<sub>x</sub> on GaO<sub>x</sub>, and InO<sub>x</sub> on ZnO<sub>x</sub> were determined from ellipsometry data, estimating values of 0.61, 0.92, and 0.72 Å/cycle, respectively. All films contain 12 super-cycles, resulting in a final layer thickness of about 11 nm. To further investigate the role of different preparation processes on the IGZO compound, a combination of TALD (for ZnO<sub>x</sub>) and PEALD (for GaO<sub>x</sub> and InO<sub>x</sub>) was taken into account. XPS Auger spectra of the Zn LMM reveal a complete oxidation state of the layer deposited via TALD/PEALD with the element ratio of 1/1/1. However, that PEALD sample (1/1/1) showed no complete oxidation where a weak metallic zinc signal was observed in the corresponding spectra. Based on the XPS data, the films pose a negligible amount of carbon (2-4%). Besides, O 1s decomposition spectra exhibit low and high contribution of impurities (OH group and defects) for the PEALD-IGZO samples of (1/2/1) and (2/1/1), respectively. XPS depth profiling analysis

reveals a nearly constant atomic concentration within the bulk of the films where the high homogeneous distribution of the elements was observed for the Zn- and In-rich samples (PE(1/1/2) and PE(2/1/1)). However, the PE(1/1/1) and Ga-rich PE(1/2/1) samples show an increase in the gallium content within the bulk of the films. GI-XRD and FE-SEM were used to investigate the structural and morphological properties of the IGZO films. The results represent featureless and pinhole-free films with an appeared broad diffraction peak indicating crystallization at low-temperature of 150 °C, which is more pronounced for the In-rich (2/1/1) sample. The applied target element ratio and homogenous distribution of the IGZO composition elements were confirmed by EDX measurement and associated mapping evaluation. Therefore, the new established super-cycle PEALD of IGZO film enables precise control over the fabrication process and film composition, which significantly develops its performance and productivity for any potential applications in microelectronics.

*In conclusion*, a full PEALD super-cycle process can be established at low-temperature of 150 °C for deposition of high-quality quaternary IGZO films with relatively high growth rate in absence of undesired nucleation delay.

- **AlO<sub>x</sub>** thin films were deposited via ALD with TMA and H<sub>2</sub>O on thermally Ti-coated Si (100) substrates at room temperature and 200 °C. The growth mechanism and surface chemistry using the early stages were quantitatively investigated using *in-situ* XPS. Based on the data, the AlO<sub>x</sub> follows a layer-by-layer growth behavior, where the growth per cycle was estimated to be 1.00 Å/cycle at both RT and 200 °C.

First, the oxidation state of the Ti substrate was studied by exposing the substrate to H<sub>2</sub>O at room temperature and taking into account the main core level spectra of the Ti 2p, O 1s, and C 1s. By considering the number of oxidizing cycles, a broadening of Ti spectra and more contribution of O-Ti of the O 1s, as well as carbonyl component of the C 1s, were observed. Besides, oxidizing the Ti substrate can be easily achieved during the exposure to water; Ti signal decreases while O increases until their saturation states. The carbon concentration remains almost constant during water exposure, with an estimated atomic concentration of ~ 9% and could be related to the unclean ALD reactor.

After evaluation of the Ti substrate oxidation state, the early stages of growth were studied at two different temperatures: RT and 200 °C. First, the dependence of atomic concentration on the ALD cycles was investigated, and it was found that the concentration of Al and O increased until reaching a saturation state while the atomic percentage of Ti and C decreased, vanishing for the 200 °C sample. where their contributions disappeared for 200 °C sample. However, RT sample revealed a negligible amount of Ti and ~ 5% carbon. According to the decomposition of the core levels, the O 1s spectra show two components of the metals-oxide (Ti-O-Al) and metal hydroxides (Ti-OH-Al), correspondingly, where the contribution of the hydroxides is more pronounced for the RT film than for the 200 °C sample. Thus, higher temperatures can inhibit the presence of OH groups improving the quality of the films. From C 1s spectra, the incorporated major C-C bonds and minor Ti-C component increase and decrease with the ALD cycles, respectively. Notably, carbide contribution completely disappeared for the layer prepared at 200 °C. With increasing the ALD cycles the layers approach to stoichiometric state where the Al:O ratios increase from 0.37 (RT sample) and 0.34 (200 °C sample) to the expected ratio of 2:3. XPS depth profile analysis shows a homogeneous concentration of the main elements (Al and O) within the deposition process, particularly for the sample deposited at 200 °C. Concerning the post-deposition annealing (PDA), the process develops carbonates to the layer where the relative peak intensity increases from 13.4% (1hr @ 200 °C) to 18.1% (2hrs @ 200 °C) and remains constant (19.7%) for the last two steps of annealing. Besides, annealing treatment cannot significantly reduce the carbide contribution rather slightly increase its contribution.

*In conclusion*, the ALD of AlO<sub>x</sub> film can be prepared in almost carbon-free state at relatively high temperature of 200 °C. The presence of carbon-related bonds during ALD cycles and particularly for the sample grown at RT, could be attributed to the methyl ligands of TMA precursor due to incomplete desorption in purging step and/or incomplete surface reaction at low-temperatures. PDA treatment proved that applying temperature might introduce some residual gases/particles (from ALD reactor) to the film surface during deposition. The use of Ti as a buffer layer can suppress undeliberate surface contamination and/or excess oxygen to deposit high-quality AlO<sub>x</sub> film. Although titanium substrate can be easily oxidized during experiment/measurement, ALD of AlO<sub>x</sub> passivated completely the underneath Ti substrate with preservation of the metallic state.

- **Ceria** section displays the preliminary results, and show the success reconfiguration of the homemade ALD reactor with capability to operate in two different modes of pump-type and flow-type.

To evaluate the flow-type mechanism, CeO<sub>x</sub> thin films were grown on the substrates of 300 nm thick SiO<sub>x</sub> and 10 nm AlO<sub>x</sub> grown by *in-situ* ALD on Si (100) substrate with commercial Ce(thd)<sub>4</sub> precursor and O<sub>3</sub> oxidizer at substrate temperature of ~ 250 °C. The role of different thicknesses (increasing the ALD cycles) and interfacial reactions were *in-situ* investigated by XPS. The analyzed data revealed that the layers are rich in the Ce<sup>3+</sup> state for the initial stages of ALD, which is more pronounced for the CeO<sub>x</sub> film deposited on the SiO<sub>x</sub> substrate. However, with enhancing the number of cycles a transition to Ce<sup>4+</sup> state dominates the Ce 3d core level spectra because of a reduction in the ratio of Ce<sup>3+</sup>/Ce<sup>4+</sup> with increasing layers' thickness. It has been observed that the first 50 ALD cycles of the CeO<sub>x</sub>/AlO<sub>x</sub> pose the fingerprint of Ce<sup>4+</sup> signal, which might be related to the interfacial reactions between the reactants and the insulating nature of AlO<sub>x</sub> layer, which acts as a buffer layer. Considering C 1s spectra, it can be seen that the major C-C signal replaced with the dominated C-O peak by increasing the ALD cycles. It should be noted that the high energy part of the C 1s spectra overlaps with the Ce 4s core level, which contribution increases with the ALD cycles especially for the CeO<sub>x</sub>/AlO<sub>x</sub> sample. In order to comply with sensor device requirements, the surface chemistry interaction of the CeO<sub>x</sub> with the H<sub>2</sub> gas was evaluated by NAP-HAXPES, where ceria reduction of the oxygen was observed under exposure to H<sub>2</sub>/N<sub>2</sub> gas at room temperature. The reduction is reversible after exposing the sample to atmospheric conditions at room temperature. and in the UHV condition. Upon exposing to the atmospheric air, the re-oxidation process completely occurs with the dominated Ce<sup>4+</sup> components of the Ce 3d core level spectra.

*In conclusion*, the use of insulating and/or buffer layers such as the ALD prepared AlO<sub>x</sub> can facilitate the deposition of ultrathin CeO<sub>x</sub> film which is rich in Ce<sup>4+</sup> state. Nevertheless, the growth of ceria using ALD technique, exhibits promising behavior in reduction/oxidation process that enables the fabrication of high-sensitive H<sub>2</sub> gas-based sensors.

## 5.2 Future works

Based on the performed comprehensive study of the promising binary and quaternary metal oxide thin films prepared by TALD and PEALD, further research needs to be done to achieve optimal stoichiometry at low deposition process temperatures. Nevertheless, a wide variety of metal oxide can be deposited using the introduced fabrication approach to develop an ALD process of high-quality films for functional materials and nanostructures with an extremely high surface area that certainly paves the way for manufacturing micro/nano devices.

As a possible follow-up of this intensive research, high-energy ions of  $O_2$  plasma generated from a CCP source of PEALD process might be applied for different kinds of precursors, which are rich in indium, gallium, and zinc metals, to deposit thin films of binary oxides at low-temperatures with a low amount of undesired contamination and structural defects. Afterwards, the deposition of the corresponding ternary and quaternary compounds using  $InO_x$ ,  $GaO_x$ , and  $ZnO_x$  could be studied, where the impacts of growth parameters and material composition on the physical and chemical properties of the deposited films should be extensively investigated. Furthermore, high-quality of novel transparent conducting oxide such as indium-gallium-zinc oxide (IGZO) can be optimized and synthesized as channel layers in the fabrication of thin-film-transistors (TFTs) for transparent and flexible electronics applications. The introduced binary oxides can be also combined and/or laminated with the catalytic  $CeO_x$  layer (i.e.  $CeO_x/InO_x$ ) to fabricate high sensitive  $H_2$  gas sensors. It has been already documented that the interface of heterojunction-based compounds such as  $AlO_x/ZnO_x$  can be optimized/controlled using ALD technique. Therefore, preparing other heterostructure materials such as  $ZnO_x/GaO_x$  by establishing a complete PEALD process would be a promising deposition approach to overcome the reported nucleation delay and develop interfacial properties.

Nevertheless, the use of different characterization techniques including atomic force microscopy (AFM), scanning electron microscopy (SEM)/tunneling electron microscopy (TEM), and X-ray diffraction (XRD)/grazing incidence X-ray diffraction (GIXRD) can provide comprehensive information about surface morphology and structural phase of the ALD/PEALD prepared thin films to probe more properties for any potential applications.





# APPENDIX

## I. List of publications

- **Articles:**

Janowitz, C., **Mahmoodinezhad, A.**, Kot, M., Morales, C., Naumann, F., Plate, P., Zoellner., M. H., Bärwolf, F., Stolarek, D., Wenger, C., Henkel, K., & Flege, J. I. (2022). Toward controlling the Al<sub>2</sub>O<sub>3</sub>/ZnO interface properties by *in-situ* ALD preparation. *Dalton Transactions*, 51(24), 9291.

**Mahmoodinezhad, A.**, Morales, C., Naumann, F., Plate, P., Meyer, R., Janowitz, C., Henkel, K., Kot, M., Zoellner., M. H., Wenger, C., & Flege, J. I. (2021). Low-temperature atomic layer deposition of indium oxide thin films using trimethylindium and oxygen plasma. *Journal of Vacuum Science & Technology A*, 39(6), 062406.

**Mahmoodinezhad, A.**, Janowitz, C., Naumann, F., Plate, P., Gargouri, H., Henkel, K., Schmeißer, D., & Flege, J. I. (2020). Low-temperature growth of gallium oxide thin films by plasma-enhanced atomic layer deposition. *Journal of Vacuum Science & Technology A*, 38(2), 022404.

Naumann, F., Reck, J., Gargouri, H., Gruska, B., Blümich, A., **Mahmoodinezhad, A.**, Janowitz, C., Henkel, K., & Flege, J. I. (2020). In situ real-time and ex situ spectroscopic analysis of Al<sub>2</sub>O<sub>3</sub> films prepared by plasma enhanced atomic layer deposition. *Journal of Vacuum Science & Technology B*, 38(1), 014014.

- **Conferences:**

**Mahmoodinezhad, A.**, Morales, C., Naumann, F., Plate, P., Meyer, R., Kot, M., Janowitz, C., Henkel, K., Flege, J.I. (2021). Low-temperature plasma-enhanced atomic layer deposition of indium oxide, *ALD/ALE Virtual Meeting*, AA1703, USA.

Plate, P., Marth, L., Naumann, F., **Mahmoodinezhad, A.**, Janowitz, C., Henkel, K., Flege, J.I. (2021). Super-cycle atomic layer deposition of indium gallium zinc oxide, *ALD/ALE Virtual Meeting*, AA1714, USA.

**Mahmoodinezhad, A.**, Morales, C., Naumann, F., Plate, P., Meyer, R., Kot, M., Janowitz, C., Henkel, K., Flege, J.I. (2021). Low-temperature atomic layer deposition of indium oxide thin films using trimethylindium and oxygen plasma, *DPG Virtual Spring Meeting*, O 74.8, Germany.

Morales, C., **Mahmoodinezhad, A.**, Schubert, A.M., Wenger, C., Henkel, K., Flege, J.I. (2021). Functional ultra-thin oxide films deposited by atomic layer deposition on structured substrates, *DPG Virtual Spring Meeting*, O 74.5, Germany.

Janowitz, C., **Mahmoodinezhad, A.**, Naumann, F., Plate, P., Henkel, K., Flege, J.I. (2021). XPS and UPS investigation of an ALD prepared Al<sub>2</sub>O<sub>3</sub>/ZnO heterojunction, *DPG Virtual Spring Meeting*, O 74.4, Germany.

**Mahmoodinezhad, A.**, Janowitz, C., Naumann, F., Plate, P., Gargouri, H., Henkel, K., Flege, J.I., Kot, M. (2020). Low-Temperature PEALD of Ga<sub>2</sub>O<sub>3</sub> Using TMGa and O<sub>2</sub> Plasma, *ALD/ALE 2020*, AA-TuP96, Ghent, Belgium.

**Mahmoodinezhad, A.**, Janowitz, C., Naumann, F., Gargouri, H., Henkel, K., Schmeißer, D., Flege, J.I. (2019). Spectroscopic and electrical investigations on gallium oxide PEALD-films, *E-MRS Fall Meeting*, C 7.16, Warsaw, Poland.

Blümich, A., Naumann, F., Gargouri, H., Reck, J., **Mahmoodinezhad, A.**, Janowitz, C., Henkel, K., Flege, J. I., Gruska, B. (2019). Real Time in-situ Analysis of ALD, *ICSE 8*, B-69, Barcelona, Spain.

**Mahmoodinezhad, A.**, Pożarowska, E., Henkel, K., Schmeißer, D., Flege, J.I. (2019). Depth profiling of PEALD-AIN films based on Al 2p XPS peak decomposition, *DPG Spring Meeting*, DS 14.25, Regensburg, Germany.

## II. List of tables

2.1 Different names of ALD .....	21
2.2 An overview on comparison of ALD technique with other growth methods of chemical vapor deposition (CVD), molecular beam epitaxy (MBE), sputtering, electron beam evaporation (EB Evap.), and pulsed laser deposition (PLD) .....	33
3.1 Main ALD parameters of InO <sub>x</sub> , GaO <sub>x</sub> and ZnO <sub>x</sub> films. Parameters are referred to plasma power ( $P_p$ ), substrate temperature ( $T_s$ ), precursor pulse duration ( $t_p$ ), co-reactant pulse duration ( $t_c$ ), purge time ( $t_{purge}$ ) and total pressure ( $P_t$ ), respectively. ....	64
3.2 Deposition parameters for PEALD (InO <sub>x</sub> , GaO <sub>x</sub> , ZnO <sub>x</sub> ) and PEALD/TALD ZnO <sub>x</sub> recipes of the IGZO layers. Parameters are referred to plasma power ( $P_p$ ), substrate temperature ( $T_s$ ), precursor pulse duration ( $t_p$ ), co-reactant pulse duration ( $t_c$ ), purge time ( $t_{purge}$ ) and total pressure ( $P_t$ ), respectively .....	66
3.3 Main TALD parameters of AlO <sub>x</sub> films. Parameters are referred to plasma power ( $P_p$ ), substrate temperature ( $T_s$ ), precursor pulse duration ( $t_p$ ), co-reactant pulse duration ( $t_c$ ), and purge time ( $t_{purge}$ ), respectively.....	70
3.4 Main parameters of TALD-CeO <sub>x</sub> films. Parameters are referred to plasma power ( $P_p$ ), substrate temperature ( $T_s$ ), precursor pulse duration ( $t_p$ ), co-reactant pulse duration ( $t_c$ ), purge time ( $t_{purge}$ ), respectively .....	73
4.1 Optically determined properties of InO <sub>x</sub> layers prepared by PEALD at different substrate temperatures .....	79
4.2 Calculated carbon contamination, indium to oxygen ratio and relative intensities of the components in the O 1s spectra after surface cleaning (2 min sputtering) .....	86
4.3 Summary of the optical data for the PEALD-GaO <sub>x</sub> layers prepared at different low-temperatures. The tabulated parameters are substrate temperature ( $T_s$ ), GPC, inhomogeneity (inhomog.) across 4" Si wafers, refractive index ( $n$ ), and optical band gap ( $E_g$ ).....	89
4.4 Calculated carbon contamination, gallium to oxygen ratio and relative intensities of the components in the O 1s spectra after surface cleaning (2 min sputtering).....	96
4.5 Calculated carbon contamination, zinc to oxygen ratio and relative intensities of the components in the O 1s spectra after surface cleaning (2 min sputtering)	105

4.6 Sample names, target elemental composition, sub-cycle ratio within one super-cycle, EDX actual ratio of the as-deposited layers, and XPS actual ratio of the surface-cleaned PEALD ( $\text{InO}_x$ ,  $\text{GaO}_x$ ,  $\text{ZnO}_x$ ) and PEALD ( $\text{InO}_x$ ,  $\text{GaO}_x$ )/TALD ( $\text{ZnO}_x$ ) IGZO layers with considering the core levels of In 3d/Ga 3d/Zn 2p..... 109

### III. List of figures

2.1 Schematic demonstration of different types of TCOs; Wide band gap (a), and narrow band gap (b) in which Fermi level denotes electron chemical potential for highly doped n-type materials .....	16
2.2 Representaion of ALD unique features: precise thickness control, high conformity/step coverage and, good uniformity over large substrates .....	20
2.3 Intel process technology innovations .....	22
2.4 Schematic representaion of an ALD- $\text{Al}_2\text{O}_3$ process consisting of first half-cycle (precursor) and second half-cycle (co-reactant) in a self-limiting process that terminates when all available surface sites are occupied. The two half-cycles are seperated by purging steps .....	23
2.5 Materials deposited by ALD. Illustration of pure elements as well as different compounds by color-coding squares .....	24
2.6 Mass loss plot of ideal and non-ideal precursors as a function of temperature. Data has been acquired using thermogravimetric (TG) analysis .....	25
2.7 Idealized ALD temperature window, displayed by the growth per cycle as a function of temperature .....	30
2.8 Representaion of layer-by-layer growth (red), island growth without (green) and with (dark blue) diffusion .....	31
2.9 Different types of PEALD reactor configurations. Radical-enhanced ALD (a), direct plasma ALD (b), and remote plasma ALD (c).....	36
3.1 Representaion of ellipsometric measurement .....	39
3.2 SENTECH spectroscopy ellipsometer .....	40
3.3 Principle of photoelectron emission and Auger relaxation effect of XPS .....	41
3.4 Energy level diagram of XPS basic equation.....	43
3.5 Configuration of ISE5-cold cathode ion sputter source .....	44
3.6 Atomic cross section of the desired elements as a function of photon energy	46
3.7 Transmission function of the in-situ and ex-aitu XPS systems as a function of the kinetic energy of electrons for both excitations of Al $K\alpha$ and Mg $K\alpha$ .....	47
3.8 Universal curve indicating IMFP (or $\lambda$ ) versus kinetic energy of electrons ...	48
3.9 <i>In-situ</i> and <i>ex-situ</i> XPS systems in the chair of applied physics and semiconductor spectroscopy of BTU .....	51

3.10 Tescan Mira3 instrument equipped with EDX. Nanomaterials group, Faculty of Mathematics and Physics, Charles University .....	52
3.11 Beamline KMC-1 and SpAnTeX end-station at BESSY II, Berlin.....	53
3.12 SENTECH ALD system (a), and associated load-lock chamber for introducing wafers (b) .....	54
3.13 SENTECH PEALD system equipped with an in-situ ALD-RTM (a), and schematic representation of CCP source .....	55
3.14 <i>In-situ</i> ALD system in the BTU's chair of applied physic and semiconductor spectroscopy .....	56
3.15 Demonstration of ALD system and applied valves .....	58
3.16 Ellipsometric parameter of delta (a), and evolution of InO <sub>x</sub> film thickness as a function of process time for different substrate temperatures within PEALD process (b). The thickness was obtained by modeling the <i>in-situ</i> ellipsometer data with a one-layer model with a constant refractive index of 1.86 (at 632.8 nm)....	60
3.17 Ellipsometric parameter of delta (a), and evolution of GaO <sub>x</sub> film thickness as a function of the process time for different sunstrate temperatures within PEALD process (b). Color-coded of magenta denotes valve stop. The thickness was obtained by modeling the <i>in-situ</i> ellipsometer data with a one-layer model with a constant refractive index of 1.86 (at 632.8 nm).....	62
3.18 Ellipsometric parameter of delta (a), and evolution of ZnO <sub>x</sub> film thickness as a function of the process time for different substrate temperatures within TALD process (b). The thickness was obtained by modeling the <i>in-situ</i> ellipsometer data with a one-layer model with a cnstant refractivr index of 1.86 (at 632.8 nm) .....	63
3.19 Schematic of a super-cycle approach (a), sub-layer sequence of IGZO super-cycle (b), and ALD temperature windows for individual InO <sub>x</sub> , GaO <sub>x</sub> , and ZnO <sub>x</sub> deposits to evaluate the IGZO process temperature (indicated by vertical straight line) (c) .....	65
3.20 Configuration of Ti evaporator system in the BTU's chair of applied physic and semiconductor spectroscopy .....	67
3.21 Demonstration of Ti evapoartion in ALD-XPS prep-chmaber of the chair of applied physics and sepectroscopic spectroscopy of BTU.....	68
3.22 <i>In-situ</i> heating using radiation technique in ALD-XPS prep-chamber of the chair of applied physics and semicoductor spectroscopy of BTU.....	69
3.23 Optimizing the cerium evaporation temperature .....	71

---

3.24 Optimizing time between two ALD cycles.....	72
3.25 Optimizing the substrate temperature of the ALD-cerium oxide thin film.....	72
4.1 Films thickness evolution as a function of process time for PEALD-InO <sub>x</sub> films deposited at different substrate temperatures.....	76
4.2 GPC (a), inhomogeneity (b), and refractive index (c) of the as-deposited PEALD-InO <sub>x</sub> films in dependence of the substrate temperature. The inset of (a) shows the GPC for a wider substrate temperature range up to 300 °C.....	77
4.3 Direct (filled squares) and indirect (open circles) band gaps of the as-deposited PEALD-InO <sub>x</sub> depending on growth temperature.....	79
4.4 XPS survey spectra of the as-introduced PEALD-InO <sub>x</sub> films prepared at different temperature of 80 to 200 °C as labeled in the diagram. Al K $\alpha$ radiation was used as excitation source.....	81
4.5 In MNN-Auger XPS spectra of the surface-cleaned InO <sub>x</sub> films deposited in the temperature range of 80 to 200 °C as labeled in the diagram. Mg K $\alpha$ radiation was used as excitation source.....	82
4.6 In 3d core level XPS spectra of the surface-cleaned InO <sub>x</sub> films deposited at 80 (a), 100 (b), 150 (c), and 200 °C (d). Al K $\alpha$ radiation was used as excitation source.....	83
4.7 O 1s core level XPS spectra of the surface-cleaned InO <sub>x</sub> films prepared at 80 (a), 100 (b), 150 (c), and 200 °C (d). Al K $\alpha$ radiation was used as excitation <i>Ex-situ</i> spectroscopic study.....	84
4.8 Contribution of sub-peaks in the O 1s spectra of the InO <sub>x</sub> film prepared at 150 °C. As-introduced (a) and surface-cleaned (b, c) film with two different take-off angles of 90° (a, b) and 50° (c) of the photoelectrons.....	85
4.9 Dependence of adventitious carbon (a) and the In:O ratio (b) of the as-introduced (filled squares) and surface-cleaned (open circles) InO <sub>x</sub> films on the substrate temperature.....	86
4.10 Measured thickness evolution as a function of process time up to a total thickness of 30 nm for the PEALD-GaO <sub>x</sub> films.....	87
4.11 Growth rate (a), inhomogeneity across a 4" Si wafer (b), refractive index and band gap (c) of the as-introduced PEALD-GaO <sub>x</sub> layers in dependence of the substrate temperature.....	89

4.12 XPS survey spectra of the as-introduced PEALD-GaO <sub>x</sub> thin films prepared at different substrate temperatures. The spectra were recorded with Al K $\alpha$ excitation .....	90
4.13 Ga LMM Auger XPS spectra of the surface-cleaned GaO <sub>x</sub> films deposited in the temperature range of 80 to 200 C as labeled in the diagram. Al K $\alpha$ radiation was used as excitation source .....	91
4.14 Ga 2p (a) and Ga 3d (b) XPS spectra of the surface-cleaned PEALD-GaO <sub>x</sub> films prepared at 80 - 200 °C. Al K $\alpha$ and Mg K $\alpha$ were used as excitation sources for the Ga 2p and Ga 3d core levels, respectively .....	92
4.15 Decomposition representation of the O 1s core level spectra of PEALD-GaO <sub>x</sub> layers prepared at 80 °C (a), 100 °C (b), 150 °C (c), and 200 °C (d). Mg K $\alpha$ radiation was used as excitation source .....	93
4.16 Relative intensity of the components in the O 1s spectra of the GaO <sub>x</sub> layer prepared at 150 °C. As-introduced (a) and surface-cleaned (b, c) film with two different take-off angles of 90° (a, b) and 50° (c) of the photoelectrons.....	94
4.17 Carbon contamination (a), and gallium to oxygen ratio (b) of the PEALD-GaO <sub>x</sub> films as a function of substrate temperature .....	95
4.18 Film thickness behavior versus deposition time for TALD-ZnO <sub>x</sub> films prepared at different substrate temperatures.....	97
4.19 Growth rate (a), refractive index and band gap (b) of the as-deposited TALD-ZnO <sub>x</sub> layers as a function of the substrate temperature .....	99
4.20 XPS survey spectra of the as-introduced TALD-ZnO <sub>x</sub> thin films prepared at different substrate temperatures. The spectra were recorded with Al K $\alpha$ excitation .....	100
4.21 Zn LMM Auger XPS spectra of the surface-cleaned ZnO <sub>x</sub> films deposited in the temperature range of 80 to 200 °C as labeled in the diagram. Al K $\alpha$ was used as excitation source.....	101
4.22 Zn 2p core level XPS spectra of the surface-cleaned ZnO <sub>x</sub> films prepared at 80 (a), 100 (b), 150 (c), and 200 °C (d). Mg K $\alpha$ radiation was used as excitation source .....	102
4.23 O 1s core level XPS spectra of the surface-cleaned ZnO <sub>x</sub> films prepared at 80 (a), 100 (b), 150 (c), and 200 °C (d). Mg K $\alpha$ radiation was used as excitation source.....	103



4.24 Contribution of sub-peaks in the O 1s spectra of the ZnO <sub>x</sub> film prepared at 150 °C. As-introduced (a) and surface-cleaned (b, c) film with two different take-off angles of 90° (a, b) and 50° (c) of the photoelectrons .....	104
4.25 Dependence of carbon contamination (a) and the Zn:O ratio (b) of the as-introduced (filled squares) and surface-cleaned (open circles) ZnO <sub>x</sub> films versus substrate temperature .....	105
4.26 Growth evaluation of TALD prepared ZnO <sub>x</sub> on both PEALD prepared InO <sub>x</sub> (a), and GaO <sub>x</sub> (b) underneath layers.....	107
4.27 Growth evaluation of PEALD prepared ZnO <sub>x</sub> on both PEALD prepared InO <sub>x</sub> (a), and GaO <sub>x</sub> (b) underneath layers. No nucleation delay for the complete PEALD process.....	107
4.28 Growth rates of the respective binary oxides on the associated underlying oxides, as applied in the super-cycle (a), and <i>in-situ</i> real-time monitoring the thickness evolution within PEALD-IGZO super-cycles comprising 3 InO <sub>x</sub> , 3 GaO <sub>x</sub> , 2 ZnO <sub>x</sub> sub-cycles (i.e., target composition of 1/1/1, see Table 4.6) (b) .	108
4.29 XPS survey spectra of the as-introduced PEALD-IGZO films prepared in a low temperature of 150 °C. Target elemental ratios are represented as X/Y/Z. Mg K $\alpha$ radiation was used as excitation source .....	110
4.30 Zn LMM Auger spectra of the IGZO samples T(1/1/1) (a), and PE(1/1/1) (b). Al K $\alpha$ radiation was used as excitation source and the data were recorded after a gentle surface cleaning (35 s of sputtering) .....	111
4.31 Bulk composition of of the 11 nm thick IGZO films with different target element ratio of 1/1/1 (a) 1/12 (b) 2/1/1 (c), and 1/2/1 (d) evaluated by XPS depth profiling.....	112
4.32 EDX measurement of PEALD-IGZO samples .....	113
4.33 EDX mapping image of PEALD/TALD-IGZO film related to the T(2/1/1) sample .....	113
4.34 In 3d (a) and Zn 2p (b) XPS core levels spectra of the surface-cleaned PEALD-IGZO films prepared at 150 °C. The sample names are indicated within each plot. Mg K $\alpha$ radiation was used as excitation source .....	114
4.35 Ga 3d XPS core levels spectra of the surface-cleaned PEALD-IGZO films prepared at 150 °C. The sample names are indicated within each plot. Mg K $\alpha$ was used as excitation source.....	115
4.36 Auger XPS spectra of the surface-cleaned PEALD-IGZO films deposited in a low-temperature of 150 °C. The sample names are indicated beside each line.	

Excitation source of Mg K $\alpha$ radiation was used for the In MNN and Ga LMM Auger lines, while Al K $\alpha$ was applied for the Zn LMM Auger spectra.....	116
4.37 Comparison of the target and actual ratios of In to Ga (red circles) and Ga to Zn (blue open rectangles) of the PEALD-IGZO layers determined by (a) XPS, and (b) EDX. The solid lines represent the corresponding linear regressions where its slopes are given near each line .....	117
4.38 XPS O 1s decomposition of PEALD-IGZO films with different elements concentration. The target elemental ratios are represented as X/Y/Z. Mg K $\alpha$ radiation was used as excitation source .....	118
4.39 GIXRD patterns of PEALD-IGZO films with sample names labeled beside each data line. The inset shows the FE-SEM surface morphology of the PE(1/1/1) sample.....	119
4.40 XPS peak intensities of the Al 2p (of AlO <sub>x</sub> film) and Ti 2p (of the substrate) as a function of ALD cycle at RT, and at 200 °C.....	121
4.41 XPS core levels spectra of Ti 2p (a), O 1s (b), and C 1s (c) corresponding to the titanium substrate (at RT) considering different oxidizing cycles.....	122
4.42 Evolution of atomic concentration corresponding to the main core levels of Ti 2p, O 1s, and C 1s as a function of ALD cycle during oxidizing Ti substrate	123
4.43 XPS Ti 2p spectra of AlO <sub>x</sub> complete ALD cycles on Ti substrate considering different temperatures of RT (a), and 200 °C.....	124
4.44 XPS O 1s spectra of AlO <sub>x</sub> complete ALD cycles on Ti substrate considering different temperatures of RT (a), and 200 °C.....	125
4.45 XPS Al 2p spectra of AlO <sub>x</sub> complete ALD cycles on Ti substrate considering different temperatures of RT (a), and 200 °C.....	126
4.46 XPS C 1s spectra of AlO <sub>x</sub> complete ALD cycles on Ti substrate considering different temperatures of RT (a), and 200 °C.....	127
4.47 Atomic elemental concentration of AlO <sub>x</sub> films as a function of the complete ALD cycles at different temperatures of RT (a), and 200 °C.....	128
4.48 XPS Ti 2p peak decomposition of ALD-AlO <sub>x</sub> on Ti substrate considering temperatures of RT (a), and 200 °C.....	129
4.49 XPS O 1s peak decomposition of ALD-AlO <sub>x</sub> on Ti substrate considering temperatures of RT (a), and 200 °C.....	131
4.50 XPS Al 2p peak decomposition of ALD-AlO <sub>x</sub> on Ti substrate considering temperatures of RT (a), and 200 °C.....	132

---

4.51 XPS C 1s peak decomposition of ALD- $\text{AlO}_x$ on Ti substrate considering temperatures of RT (a), and 200 °C .....	133
4.52 Atomic Al:O ratio of $\text{AlO}_x$ as a function of ALD cycle number .....	134
4.53 XPS depth profile of $\text{AlO}_x$ film deposited at RT. The insert shows a narrow window of sputtering time up to 300 s .....	136
4.54 XPS depth profile of $\text{AlO}_x$ film deposited at 200 °C. The insert shows a narrow window of sputtering time up to 300 s .....	136
4.55 XPS surface (as-deposited) and depth (10 min sputtering) analysis of $\text{AlO}_x$ film at RT with considering core level spectra of Al 2p (a), O 1s (b), and C 1s (c) .....	137
4.56 XPS peak decomposition of core levels spectra of Al 2p (a) , O 1s (b), and C 1s (c) corresponding to PDA treated ALD- $\text{AlO}_x$ film grown at RT .....	139
4.57 XPS Ce 3d spectra of $\text{CeO}_x$ thin films on different substrates of $\text{SiO}_x$ (a), and $\text{AlO}_x/\text{Si}$ (b). The numbers indicate the applied ALD cycle .....	141
4.58 XPS C 1s spectra of $\text{CeO}_x$ thin films on different substrates of $\text{SiO}_x$ (a), and $\text{AlO}_x/\text{Si}$ (b). The numbers indicate the applied ALD cycle .....	142
4.59 NAP-HAXPES spectra of Ce 3d (a) and Ce 2p <sub>3/2</sub> (b) core levels corresponding to as-introduced, after reduction and re-oxidation of the grown $\text{CeO}_x/\text{SiO}_x$ layers .....	143

#### IV. List of abbreviations and acronyms

ALCVD	Atomic layer chemical vapor deposition
ALD	Atomic layer deposition
ALE	Atomic layer epitaxy, Atomic layer evaporation
ALG	Atomic layer growth
AlO <sub>x</sub>	Aluminum oxide
ASF	Atomic sensitivity factor
AsMe <sub>3</sub>	Trimethylarsine
BE	Binding energy
Bet <sub>3</sub>	Triethylborane
CAE	Constant analyzer energy
CCP	Capacitively-coupled plasma
CdO	Cadmium oxide
Ce(dpdmg) <sub>3</sub>	Tris(N,N'-diisopropyl-2-dimethylamidoguanidinato)cerium(III)
Ce(thd) <sub>4</sub>	Cerium tetrakis(2,2,6,6-tetramethyl-3,5-heptanedionato)
Ce <sub>2</sub> O <sub>3</sub>	Silicate
CeO <sub>x</sub>	Cerium oxide
CL	Core level
CRR	Constant retarding ratio
CVD	Chemical vapor deposition
DEZ	Diethylzinc
DLE	Digital layer epitaxy
EBE	Electron beam evaporation
ECR	Electron cyclotron resonance
ESCA	Electron spectroscopy for chemical analysis
Et <sub>2</sub> InN(SiMe <sub>3</sub> ) <sub>2</sub>	Diethyl[bis(trimethylsilyl)amido]indium
FM	Frank-van der Merve
FWHM	Full width at half maximum
GaAs	Gallium arsenide
GaO <sub>x</sub>	Gallium oxide
GPC	Growth per cycle
GTIP	Gallium tri-isopropoxide
H <sub>2</sub> O	Water
H <sub>2</sub> O <sub>2</sub>	Hydrogen peroxide
IC	Integrated circuit
IGZO	Indium-gallium-zinc oxide
IMFPs	Inelastic mean free paths
InCp	Indium cyclopentadienyl

---

InO <sub>x</sub>	Indium oxide
ITO	Indium tin oxide
ITRS	International technology roadmap for semiconductors
KE	Kinetic energy
MBE	Molecular beam epitaxy
ML	Molecular layering
MLE	Molecular layer epitaxy
MOCVD	Metalorganic chemical vapor deposition
MOSFET	Metal oxide semiconductor field effect transistor
NaOH	Sodium hydroxide
NAP-HAXPES	Near-ambient pressure hard X-ray photoelectron spectroscopy
NH <sub>3</sub>	Ammonia
OH	Hydroxide
PDA	Post deposition annealing
PE	Pass energy
PEALD	Plasma-enhanced atomic layer deposition
PECVD	Plasma-enhanced chemical vapor deposition
PLD	Pulsed laser deposition
PVD	Physical vapor deposition
RF	Radio frequency
RMSE	Root mean squared error
RT	Room temperature
RTM	Real time monitor
SAW	Surface acoustic wave
SCCM	Standard cubic centimeters per minute
SE	Spectroscopic ellipsometry
Si <sub>3</sub> N <sub>4</sub>	Silicon nitride
SIMS	Secondary ion mass spectrometry
SiO <sub>2</sub>	Silicon dioxide
SK	Stranski-Krastanov
TALD	Thermal atomic layer deposition
TCOs	Transparent conducting oxides
TF	Transmission function
TFTs	Thin film transistors
TG	Thermogravimetric
TiC	Titanium carbide
TMA	Trimethylaluminum
TMGa	Trimethylgallium

TMIn	Trimethylindium
UHV	Ultra-high vacuum
UV	Ultraviolet
VIS/NIR	Visible/near-infrared
VW	Vollmer-Weber
XPS	X-ray photoelectron spectroscopy
ZnOx	Zinc oxide



## REFERENCES

- (1) M. D. Groner, F. H. Fabreguette, J. W. Elam and S. M. George, *Chem. Mater.* **16**, 639-645 (2004).
- (2) C. S. Hwang, *Atomic Layer Deposition for Semiconductors*, Springer US: New York, 2014.
- (3) H. B. Profijt, S. E. Potts, M. C. M. van de Sanden and W. M. M. Kessels, *J. Vac. Sci. Technol. A* **29**, 050801 (2011).
- (4) K. G. Grigorov, G. I. Grigorov, M. Stoyanova, J. L. Vignes, J. P. Langeron, P. Denjean and J. Perriere, *Appl. Phys. A* **55**, 502-504 (1992).
- (5) G. Mavrou, S. Galata, P. Tsipas, A. Sotiropoulos, Y. Panayiotatos, A. Dimoulas, E. K. Evangelou, J. W. Seo and C. Dieker, *J. Appl. Phys.* **103**, 014506 (2008).
- (6) M. Gutowski, J. E. Jaffe, C.-L. Liu, M. Stoker, R. I. Hegde, R. S. Rai and P. J. Tobin, *Appl. Phys. Lett.* **80**, 1897-1899 (2002).
- (7) K. Takada, H. Sakurai, E. Takayama-Muromachi, F. Izumi, R. A. Dilanian and T. Sasaki, *Nature* **422**, 53-55 (2003).
- (8) V. V. Sysoev, B. K. Button, K. Wepsiec, S. Dmitriev and A. Kolmakov, *NanoLett.* **6**, 1584-1588 (2006).
- (9) X. Su, Z. Zhang and M. Zhu, *Appl. Phys. Lett.* **88**, 061913 (2006).
- (10) D. R. Rosseinsky and R. J. Mortimer, *J. Adv. Mater.* **13**, 783-793 (2001).
- (11) C. G. Granqvist, *Solar Energy Materials and Solar Cells* **92**, 203-208 (2008).
- (12) X. Yu, T. J. Marks and A. Facchetti, *Nat. Mater.* **15**, 383-396 (2016).
- (13) C. Wang, L. Yin, L. Zhang, D. Xiang and R. Gao, *Sensors* **10**, 2088-2106 (2010).
- (14) L. Wang Zhong and J. Song, *Science* **312**, 242-246 (2006).
- (15) S. Royer and D. Duprez, *ChemCatChem* **3**, 24-65 (2011).
- (16) S. S. Shin, S. J. Lee and S. I. Seok, *APL Materials* **7**, 022401 (2018).
- (17) J. Lee, M. Christopher Orilall, S. C. Warren, M. Kamperman, F. J. DiSalvo and U. Wiesner, *Nat. Mater.* **7**, 222-228 (2008).
- (18) H. J. Bolink, E. Coronado, J. Orozco and M. Sessolo, *J. Adv. Mater.* **21**, 79-82 (2009).
- (19) C. M. Friend, K. T. Queeney and D. A. Chen, *Appl. Surf. Sci.* **142**, 99-105 (1999).
- (20) A. Trovarelli, C. de Leitenburg, M. Boaro and G. Dolcetti, *Catalysis Today* **50**, 353-367 (1999).



- (21) S. Polarz, J. Strunk, V. Ischenko, M. W. E. van den Berg, O. Hinrichsen, M. Muhler and M. Driess, *Angewandte Chemie International Edition* **45**, 2965-2969 (2006).
- (22) M. S. Chen and D. W. Goodman, *Science* **306**, 252-255 (2004).
- (23) A. Vittadini, M. Casarin, M. Sambri and A. Selloni, *J. Phys. Chem. B* **109**, 21766-21771 (2005).
- (24) Q. Fu and T. Wagner, *Surf Sci.* **574**, L29-L34 (2005).
- (25) G. Parravano, *J. Chem. Phys.* **20**, 342-343 (1952).
- (26) A. M. Kolpak, I. Grinberg and A. M. Rappe, *Phys. Rev. Lett.* **98**, 166101 (2007).
- (27) H.-J. Freund, *Surf Sci.* **601**, 1438-1442 (2007).
- (28) Q. Fu and T. Wagner, *Surface Science Reports* **62**, 431-498 (2007).
- (29) S. Ghose, M. S. Rahman, J. S. Rojas-Ramirez, M. Caro, R. Droopad, A. Arias and N. Nedev, *J. Vac. Sci. Technol. B* **34**, 02L109 (2016).
- (30) G. Thomas, *Nature* **389**, 907-908 (1997).
- (31) T. Minami, *Semicond. Sci. Technol.* **20**, S35-S44 (2005).
- (32) W. Aron, *Chemical communications* v. **49**, 448-450 (2012).
- (33) A. Mahmoodinezhad, C. Morales, F. Naumann, P. Plate, R. Meyer, C. Janowitz, K. Henkel, M. Kot, M. H. Zoellner, C. Wenger and J. I. Flege, *J. Vac. Sci. Technol. A* **39**, 062406 (2021).
- (34) A. Mahmoodinezhad, C. Janowitz, F. Naumann, P. Plate, H. Gargouri, K. Henkel, D. Schmeißer and J. I. Flege, *J. Vac. Sci. Technol. A* **38**, 022404 (2020).
- (35) P. F. Carcia, R. S. McLean, M. H. Reilly and G. Nunes, *Appl. Phys. Lett.* **82**, 1117-1119 (2003).
- (36) S. K. Vasheghani Farahani, T. D. Veal, P. D. C. King, J. Zúñiga-Pérez, V. Muñoz-Sanjose and C. F. McConville, *J. Appl. Phys.* **109**, 073712 (2011).
- (37) M. Burbano, D. O. Scanlon and G. W. Watson, *J. Am. Chem. Soc.* **133**, 15065-15072 (2011).
- (38) N. F. Mott, *Rev. Mod. Phys.* **40**, 677-683 (1968).
- (39) P. Malar, B. C. Mohanty and S. Kasiviswanathan, *Thin Solid Films* **488**, 26-33 (2005).
- (40) R. L. Weiher and R. P. Ley, *J. Appl. Phys.* **37**, 299-302 (1966).
- (41) K. L. Chopra, S. Major and D. K. Pandya, *Thin Solid Films* **102**, 1-46 (1983).
- (42) H. I. Yeom, J. B. Ko, G. Mun and S. H. K. Park, *J. Mater. Chem. C* **4**, 6873-6880 (2016).
- (43) M. Girtan and G. Folcher, *Surf. Coat. Tech.* **172**, 242-250 (2003).
- (44) C. Cantalini, W. Wlodarski, H. T. Sun, M. Z. Atashbar, M. Passacantando and S. Santucci, *Sens. Actuator B-Chem.* **65**, 101-104 (2000).
- (45) Z. Qiao and D. Mergel, *Physica Status Solidi (A)* **207**, 1543-1548 (2010).
- (46) R. Mientus and K. Ellmer, *Surf. Coat. Tech.* **142-144**, 748-754 (2001).
- (47) K. R. Reyes-Gil, E. A. Reyes-García and D. Raftery, *J. Phys. Chem. C* **111**, 14579-14588 (2007).

- (48) C. M. Lampert, *Sol. Energy Mater.* **6**, 1-41 (1981).
- (49) C. G. Granqvist, *Appl. Phys. A* **57**, 19-24 (1993).
- (50) C. Janowitz, V. Scherer, M. Mohamed, A. Krapf, H. Dwelk, R. Manzke, Z. Galazka, R. Uecker, K. Irmscher, R. Fornari, M. Michling, D. Schmeißer, J. R. Weber, J. B. Varley and C. G. Van de Walle, *New Journal of Physics* **13**, 085014 (2011).
- (51) J. Haerberle, M. Richter, Z. Galazka, C. Janowitz and D. Schmeißer, *Thin Solid Films* **555**, 53-56 (2014).
- (52) W. J. Maeng, D.-w. Choi, K.-B. Chung, W. Koh, G.-Y. Kim, S.-Y. Choi and J.-S. Park, *ACS Appl. Mater. Inter.* **6**, 17481-17488 (2014).
- (53) Z. Yuan, X. Zhu, X. Wang, X. Cai, B. Zhang, D. Qiu and H. Wu, *Thin Solid Films* **519**, 3254-3258 (2011).
- (54) P. Görrn, M. Sander, J. Meyer, M. Kröger, E. Becker, H. H. Johannes, W. Kowalsky and T. Riedl, *J. Adv. Mater.* **18**, 738-741 (2006).
- (55) C.-Y. Huang, G.-C. Lin, Y.-J. Wu, T.-Y. Lin, Y.-J. Yang and Y.-F. Chen, *J. Phys. Chem. C* **115**, 13083-13087 (2011).
- (56) H. Peelaers and C. G. Van de Walle, *physica status solidi (b)* **252**, 828-832 (2015).
- (57) M. Orita, H. Ohta, M. Hirano and H. Hosono, *Appl. Phys. Lett.* **77**, 4166-4168 (2000).
- (58) Y. Yao, R. F. Davis and L. M. Porter, *J. Electron. Mater.* **46**, 2053-2060 (2017).
- (59) S. J. Pearton, J. Yang, P. H. Cary, F. Ren, J. Kim, M. J. Tadjer and M. A. Mastro, *Appl. Phys. Rev.* **5**, 011301 (2018).
- (60) M. Higashiwaki, K. Sasaki, A. Kuramata, T. Masui and S. Yamakoshi, *Appl. Phys. Lett.* **100**, 013504 (2012).
- (61) F. K. Shan, G. X. Liu, W. J. Lee, G. H. Lee, I. S. Kim and B. C. Shin, *J. Appl. Phys.* **98**, 023504 (2005).
- (62) H. Hayashi, R. Huang, H. Ikeno, F. Oba, S. Yoshioka, I. Tanaka and S. Sonoda, *Appl. Phys. Lett.* **89**, 181903 (2006).
- (63) G. W. Paterson, P. Longo, J. A. Wilson, A. J. Craven, A. R. Long, I. G. Thayne, M. Passlack and R. Droopad, *J. Appl. Phys.* **104**, 103719 (2008).
- (64) H. Lee, K. Kim, J.-J. Woo, D.-J. Jun, Y. Park, Y. Kim, H. W. Lee, Y. J. Cho and H. M. Cho, *Chem. Vapor. Depos.* **17**, 191-197 (2011).
- (65) D.-W. Choi, K.-B. Chung and J.-S. Park, *Thin Solid Films* **546**, 31-34 (2013).
- (66) S. Stepanov, V. Nikolaev, V. Bougrov and A. Romanov, *Rev. Adv. Mater. Sci* **44**, 63-86 (2016).
- (67) M. Fleischer and H. Meixner, *J. Appl. Phys.* **74**, 300-305 (1993).
- (68) W. H. Hirschwald, *Acc. Chem. Res.* **18**, 228-234 (1985).
- (69) K. Ellmer, *Journal of Physics D: Applied Physics* **34**, 3097-3108 (2001).
- (70) S.-K. Hong, T. Hanada, H. Makino, Y. Chen, H.-J. Ko, T. Yao, A. Tanaka, H. Sasaki and S. Sato, *Appl. Phys. Lett.* **78**, 3349-3351 (2001).

- (71) M. Scharrer, X. Wu, A. Yamilov, H. Cao and R. P. H. Chang, *Appl. Phys. Lett.* **86**, 151113 (2005).
- (72) Ü. Özgür, Y. I. Alivov, C. Liu, A. Teke, M. A. Reshchikov, S. Doğan, V. Avrutin, S. J. Cho and H. Morkoç, *J. Appl. Phys.* **98**, 041301 (2005).
- (73) S. Pizzini, *J. Electrochem. Soc.* **136**, 1945 (1989).
- (74) G. S. Kino and R. S. Wagers, *J. Appl. Phys.* **44**, 1480-1488 (1973).
- (75) J. A. Aranovich, D. Golmayo, A. L. Fahrenbruch and R. H. Bube, *J. Appl. Phys.* **51**, 4260-4268 (1980).
- (76) M. J. Brett, R. W. McMahon, J. Affinito and R. R. Parsons, *J. Vac. Sci. Technol. A* **1**, 352-355 (1983).
- (77) C.-S. Son, S.-M. Kim, Y.-H. Kim, S.-I. Kim, Y. T. Kim, K. H. Yoon, I.-H. Choi and H. C. Lopez, *Journal of the Korean Physical Society* **45**, 685-688 (2004).
- (78) A. Facchetti and T. Marks, *Transparent electronics: from synthesis to applications*, John Wiley & Sons, 2010.
- (79) K. Elmer, A. Klein and B. Rech, *Transparent conductive zinc oxide: basic and applications in thin film solar cells*, Springer-Verlag, Berlin, 2008.
- (80) S. Kumar and B. Drevillon, *J. Appl. Phys.* **65**, 3023-3034 (1989).
- (81) K. Nomura, H. Ohta, A. Takagi, T. Kamiya, M. Hirano and H. Hosono, *Nature* **432**, 488-492 (2004).
- (82) N. Su, S. Wang, C. Huang, Y. Chen, H. Huang, C. Chiang and A. Chin, *IEEE Electron Device Lett.* **31**, 680-682 (2010).
- (83) M. Yu, Y. Yeh, C. Cheng, C. Lin, G. Ho, B. C. Lai, C. Leu, T. Hou and Y. Chan, *IEEE Electron Device Lett.* **33**, 47-49 (2012).
- (84) J. Yeon Kwon and J. Kyeong Jeong, *Semicond. Sci. Technol.* **30**, 024002 (2015).
- (85) D. S. Ginley and J. D. Perkins, in *Handbook of Transparent Conductors*, ed. D. S. Ginley, Springer US, Boston, MA, 2011, DOI: 10.1007/978-1-4419-1638-9\_1, pp. 1-25.
- (86) E. Fortunato, P. Barquinha and R. Martins, *J. Adv. Mater.* **24**, 2945-2986 (2012).
- (87) G. T. Dang, T. Kawaharamura, M. Furuta and M. W. Allen, *IEEE Electron Device Lett.* **36**, 463-465 (2015).
- (88) M. I. Hossain, A. Mohammad, W. Qarony, S. Ilhom, D. R. Shukla, D. Knipp, N. Biyikli and Y. H. Tsang, *RSC Advances* **10**, 14856-14866 (2020).
- (89) D. Dick, J. B. Ballard, R. C. Longo, J. N. Randall, K. Cho and Y. J. Chabal, *The Journal of Physical Chemistry C* **120**, 24213-24223 (2016).
- (90) X. Wang, S. M. Tabakman and H. Dai, *J. Am. Chem. Soc.* **130**, 8152-8153 (2008).
- (91) Z. Xing, J. Xiao, T. Hu, X. Meng, D. Li, X. Hu and Y. Chen, *Small Methods* **4**, 2000588 (2020).

- (92) M. H. Cho, H. Seol, A. Song, S. Choi, Y. Song, P. S. Yun, K. Chung, J. U. Bae, K. Park and J. K. Jeong, *IEEE Trans. Electron Devices* **66**, 1783-1788 (2019).
- (93) Y.-Y. Lin, C.-C. Hsu, M.-H. Tseng, J.-J. Shyue and F.-Y. Tsai, *ACS Appl. Mater. Inter.* **7**, 22610-22617 (2015).
- (94) E. P. Gusev, M. Copel, E. Cartier, I. J. R. Baumvol, C. Krug and M. A. Gribelyuk, *Appl. Phys. Lett.* **76**, 176-178 (2000).
- (95) E. Dorre and H. Hubner, *Alumina: Properties, Processing and Applications*, Springer-Verlag, Berlin, 1984.
- (96) H. C. Lin, P. D. Ye and G. D. Wilk, *Appl. Phys. Lett.* **87**, 182904 (2005).
- (97) J. W. Liu, A. Kobayashi, K. Ueno, J. Ohta, H. Fujioka and M. Oshima, *e-j. surf. sci. nanotechnol.* **10**, 165-168 (2012).
- (98) J. S. Ponraj, G. Attolini and M. Bosi, *Critical Reviews in Solid State and Materials Sciences* **38**, 203-233 (2013).
- (99) A. F. P. W. S. Trovarelli, Catalysis by ceria and related materials, <http://site.ebrary.com/id/10719510>.
- (100) T. X. T. Sayle, M. Molinari, S. Das, U. M. Bhatta, G. Möbus, S. C. Parker, S. Seal and D. C. Sayle, *Nanoscale* **5**, 6063-6073 (2013).
- (101) C. Zhao, C. Z. Zhao, M. Werner, S. Taylor and P. Chalker, *Nanoscale Res. Lett.* **8**, 456 (2013).
- (102) N. Izu, W. Shin, I. Matsubara and N. Murayama, *Sens. Actuator B-Chem.* **100**, 411-416 (2004).
- (103) R. K. Sharma, A. Kumar and J. M. Anthony, *JOM* **53**, 53-55 (2001).
- (104) P. F. Wahid, K. B. Sundaram and P. J. Sisk, *Optics & Laser Technology* **24**, 263-266 (1992).
- (105) N. T. McDevitt and W. L. Baun, *Spectrochim. Acta* **20**, 799-808 (1964).
- (106) J. Qiao and C. Y. Yang, *Materials Science and Engineering: R: Reports* **14**, 157-201 (1995).
- (107) B. K. Moon, H. Ishiwara, E. Tokumitsu and M. Yoshimoto, *Thin Solid Films* **385**, 307-310 (2001).
- (108) M. A. A. M. van Wijck, M. A. J. Verhoeven, E. M. C. M. Reuvekamp, G. J. Gerritsma, D. H. A. Blank and H. Rogalla, *Appl. Phys. Lett.* **68**, 553-555 (1996).
- (109) A. Paranjpe, S. Gopinath, T. Omstead and R. Bubber, *J. Electrochem. Soc.* **148**, G465 (2001).
- (110) H. Chatham, *Surf. Coat. Tech.* **78**, 1-9 (1996).
- (111) T. Suntola and J. Antson, *Finland Patent*, 4058430, 1977.
- (112) M. Ahonen, M. Pessa and T. Suntola, *Thin Solid Films* **65**, 301-307 (1980).
- (113) S. M. George, *Chem. Rev.* **110**, 111-131 (2010).
- (114) R. L. Puurunen, *J. Appl. Phys.* **97**, 121301 (2005).
- (115) M. Ritala, H. Parala, R. Kanjolia, R. D. Dupuis, S. Alexandrov, S. J. Irvine, R. Palgrave, I. P. Parkin, J. Niinisto and S. Krumdieck, *Chemical*

- vapour deposition: precursors, processes and applications, Royal Society of Chemistry, 2008.
- (116) S. M. George, A. W. Ott and J. W. Klaus, *The Journal of Physical Chemistry* **100**, 13121-13131 (1996).
- (117) C. H. L. Goodman and M. V. Pessa, *J. Appl. Phys.* **60**, R65-R82 (1986).
- (118) T. Suntola, *Thin Solid Films* **216**, 84-89 (1992).
- (119) M. Leskelä and M. Ritala, *Thin Solid Films* **409**, 138-146 (2002).
- (120) H. Kim, *J. Vac. Sci. Technol. B* **21**, 2231-2261 (2003).
- (121) M. Ritala and M. Leskelä, *Nanotechnology* **10**, 19-24 (1999).
- (122) International Technology Roadmap for Semiconductors, <http://www.itrs.net/>).
- (123) Intel process technology innovations, <https://www.intel.com/content/www/us/en/newsroom/resources/press-kit-accelerated-event-2021.html#gs.4842e7>).
- (124) F. H. Fabreguette, R. A. Wind and S. M. George, *Appl. Phys. Lett.* **88**, 013116 (2006).
- (125) M. D. Groner, J. W. Elam, F. H. Fabreguette and S. M. George, *Thin Solid Films* **413**, 186-197 (2002).
- (126) Overview of the materials prepared by ALD, <https://www.atomiclimits.com/2019/01/28/overview-of-all-materials-prepared-by-atomic-layer-deposition-ald-an-up-to-date-and-colorful-periodic-table-to-download/>).
- (127) H. C. M. Knoops, S. E. Potts, A. A. Bol and W. M. M. Kessels, in *Handbook of Crystal Growth (Second Edition)*, ed. T. F. Kuech, North-Holland, Boston, 2015, DOI: <https://doi.org/10.1016/B978-0-444-63304-0.00027-5>, pp. 1101-1134.
- (128) S. Seo, W. J. Woo, I.-k. Oh, H. Kim and B. Shong, *ECS Meeting Abstracts* **MA2019-02**, 1152-1152 (2019).
- (129) P. Repo and H. Savin, *Energy Procedia* **92**, 381-385 (2016).
- (130) J. Castillo-Saenz, N. Nedev, B. Valdez-Salas, M. Curiel-Alvarez, M. I. Mendivil-Palma, N. Hernandez-Como, M. Martinez-Puente, D. Mateos, O. Perez-Landeros and E. Martinez-Guerra, *Coatings* **11**, 1266 (2021).
- (131) F. Campabadal, O. Beldarrain, M. Zabala, M. C. Acero and J. M. Rafi, 2011.
- (132) R. L. Puurunen, *Chem. Vapor. Depos.* **9**, 249-257 (2003).
- (133) T. Muneshwar and K. Cadien, *J. Appl. Phys.* **124**, 095302 (2018).
- (134) S. T. Barry, A. V. Teplyakov and F. Zaera, *Acc. Chem. Res.* **51**, 800-809 (2018).
- (135) Y. Duan, J.-M. Lin and A. V. Teplyakov, *The Journal of Physical Chemistry C* **119**, 13670-13681 (2015).
- (136) T. Weckman and K. Laasonen, *Phys. Chem. Chem. Phys.* **17**, 17322-17334 (2015).
- (137) Q. M. Phung, G. Pourtois, J. Swerts, K. Pierloot and A. Delabie, *The Journal of Physical Chemistry C* **119**, 6592-6603 (2015).

- (138) X. Qin and F. Zaera, *The Journal of Physical Chemistry C* **122**, 13481-13491 (2018).
- (139) J. Lu and J. W. Elam, *Chem. Mater.* **27**, 4950-4956 (2015).
- (140) B. Hammer and J. K. Nørskov, *Surf Sci.* **343**, 211-220 (1995).
- (141) J. A. Singh, N. F. W. Thissen, W.-H. Kim, H. Johnson, W. M. M. Kessels, A. A. Bol, S. F. Bent and A. J. M. Mackus, *Chem. Mater.* **30**, 663-670 (2018).
- (142) M. Bartram, T. Michalske and J. Rogers Jr, *The Journal of Physical Chemistry* **95**, 4453-4463 (1991).
- (143) E. L. Lakomaa, A. Root and T. Suntola, *Appl. Surf. Sci.* **107**, 107-115 (1996).
- (144) J. B. Kim, D. R. Kwon, K. Chakrabarti, C. Lee, K. Y. Oh and J. H. Lee, *J. Appl. Phys.* **92**, 6739-6742 (2002).
- (145) R. K. Ramachandran, J. Dendooven, J. Botterman, S. Pulinthanathu Sree, D. Poelman, J. A. Martens, H. Poelman and C. Detavernier, *Journal of Materials Chemistry A* **2**, 19232-19238 (2014).
- (146) J. Provine, P. Schindler, J. Torgersen, H. J. Kim, H.-P. Karthaler and F. B. Prinz, *J. Vac. Sci. Technol. A* **34**, 01A138 (2015).
- (147) T. Aaltonen, A. Rahtu, M. Ritala and M. Leskelä, *Electrochemical and Solid-State Letters* **6**, C130 (2003).
- (148) J. W. Elam, M. Schuisky, J. D. Ferguson and S. M. George, *Thin Solid Films* **436**, 145-156 (2003).
- (149) K. Oura, *Surface science : an introduction*, Springer, Berlin, 2003.
- (150) V. Vandalon and W. M. M. Kessels, *J. Vac. Sci. Technol. A* **35**, 05C313 (2017).
- (151) S. D. Elliott, G. Dey and Y. Maimaiti, *J. Chem. Phys.* **146**, 052822 (2017).
- (152) M. Ylilammi, *Thin Solid Films* **279**, 124-130 (1996).
- (153) R. L. Puurunen and W. Vandervorst, *J. Appl. Phys.* **96**, 7686-7695 (2004).
- (154) C. A. Wilson, R. K. Grubbs and S. M. George, *Chem. Mater.* **17**, 5625-5634 (2005).
- (155) F. Grillo, J. A. Moulijn, M. T. Kreutzer and J. R. van Ommen, *Catalysis Today* **316**, 51-61 (2018).
- (156) Q. Tao, K. Overhage, G. Jursich and C. Takoudis, *Thin Solid Films* **520**, 6752-6756 (2012).
- (157) A. Gharachorlou, M. D. Detwiler, X.-K. Gu, L. Mayr, B. Klötzer, J. Greeley, R. G. Reifengerger, W. N. Delgass, F. H. Ribeiro and D. Y. Zemlyanov, *ACS Appl. Mater. Inter.* **7**, 16428-16439 (2015).
- (158) R. C. Longo, S. McDonnell, D. Dick, R. M. Wallace, Y. J. Chabal, J. H. G. Owen, J. B. Ballard, J. N. Randall and K. Cho, *J. Vac. Sci. Technol. B* **32**, 03D112 (2014).
- (159) T. Aaltonen, P. Alén, M. Ritala and M. Leskelä, *Chem. Vapor. Depos.* **9**, 45-49 (2003).
- (160) S.-S. Yim, D.-J. Lee, K.-S. Kim, S.-H. Kim, T.-S. Yoon and K.-B. Kim, *J. Appl. Phys.* **103**, 113509 (2008).

- (161) A. Mameli, B. Karasulu, M. A. Verheijen, A. J. M. Mackus, W. M. M. Kessels and F. Roozeboom, *ECS Trans.* **80**, 39-48 (2017).
- (162) A. Mameli, M. J. M. Merkx, B. Karasulu, F. Roozeboom, W. M. M. Kessels and A. J. M. Mackus, *ACS Nano* **11**, 9303-9311 (2017).
- (163) B. A. Morrow and A. J. McFarlan, *J. Non-Cryst. Solids* **120**, 61-71 (1990).
- (164) P. J. Pallister and S. T. Barry, *J. Chem. Phys.* **146**, 052812 (2016).
- (165) J. Lu, B. Liu, N. P. Guisinger, P. C. Stair, J. P. Greeley and J. W. Elam, *Chem. Mater.* **26**, 6752-6761 (2014).
- (166) L. Vitos, A. V. Ruban, H. L. Skriver and J. Kollár, *Surf Sci.* **411**, 186-202 (1998).
- (167) J. S. Becker, Ph.D. thesis, Harvard University, 2003.
- (168) S. M. George, O. Sneh, A. C. Dillon, M. L. Wise, A. W. Ott, L. A. Okada and J. D. Way, *Appl. Surf. Sci.* **82-83**, 460-467 (1994).
- (169) H. Virola and L. Niinistö, *Thin Solid Films* **249**, 144-149 (1994).
- (170) M. Ritala, M. Leskelä, L.-S. Johansson and L. Niinistö, *Thin Solid Films* **228**, 32-35 (1993).
- (171) M. R. Shaeri, T.-C. Jen and C. Y. Yuan, *International Journal of Heat and Mass Transfer* **78**, 1243-1253 (2014).
- (172) S. E. Potts and W. M. M. Kessels, *Coordination Chemistry Reviews* **257**, 3254-3270 (2013).
- (173) J. L. van Hemmen, S. B. S. Heil, J. H. Klootwijk, F. Roozeboom, C. J. Hodson, M. C. M. van de Sanden and W. M. M. Kessels, *J. Electrochem. Soc.* **154**, G165 (2007).
- (174) M. A. Lieberman and A. J. Lichtenberg, *Principles of plasma discharges and materials processing*, John Wiley & Sons, 2005.
- (175) J.-S. Park, H.-S. Park and S.-W. Kang, *J. Electrochem. Soc.* **149**, C28 (2002).
- (176) J. H. Lee, Y. J. Cho, Y. S. Min, D. Kim and S. W. Rhee, *J. Vac. Sci. Technol. A* **20**, 1828-1830 (2002).
- (177) W.-J. Lee, I.-K. You, S.-O. Ryu, B.-G. Yu, K.-I. Cho, S.-G. Yoon and C.-S. Lee, *Jpn. J. Appl. Phys.* **40**, 6941-6944 (2001).
- (178) C.-W. Jeong, B.-i. Lee and S.-K. Joo, *Materials Science and Engineering: C* **16**, 59-64 (2001).
- (179) H. B. Profijt, P. Kudlacek, M. C. M. van de Sanden and W. M. M. Kessels, *J. Electrochem. Soc.* **158**, G88 (2011).
- (180) S. M. Rosnagel, A. Sherman and F. Turner, *J. Vac. Sci. Technol. B* **18**, 2016-2020 (2000).
- (181) E.-J. Lee, M.-G. Ko, B.-Y. Kim, S.-K. Park, H.-D. Kim and J.-W. Park, *Journal of the Korean Physical Society* **49**, 1243-1246 (2006).
- (182) M. de Keijser and C. van Opdorp, *Appl. Phys. Lett.* **58**, 1187-1189 (1991).
- (183) S. B. S. Heil, J. L. van Hemmen, C. J. Hodson, N. Singh, J. H. Klootwijk, F. Roozeboom, M. C. M. van de Sanden and W. M. M. Kessels, *J. Vac. Sci. Technol. A* **25**, 1357-1366 (2007).

- (184) O.-K. Kwon, S.-H. Kwon, H.-S. Park and S.-W. Kang, *J. Electrochem. Soc.* **151**, C753 (2004).
- (185) S. Choi, J. Koo, H. Jeon and Y. Kim, *Journal of the Korean Physical Society* **44**, 35-38 (2004).
- (186) S. J. Yun, J. W. Lim and J.-H. Lee, *Electrochemical and Solid-State Letters* **7**, C13 (2004).
- (187) A. Niskanen, K. Arstila, M. Ritala and M. Leskelä, *J. Electrochem. Soc.* **152**, F90 (2005).
- (188) S. E. Potts, W. Keuning, E. Langereis, G. Dingemans, M. C. M. van de Sanden and W. M. M. Kessels, *J. Electrochem. Soc.* **157**, P66 (2010).
- (189) L. Wu and E. Eisenbraun, *J. Vac. Sci. Technol. B* **25**, 2581-2585 (2007).
- (190) N. E. Lay, G. A. Ten Eyck, D. J. Duquette and T.-M. Lu, *Electrochemical and Solid-State Letters* **10**, D13 (2007).
- (191) J. W. Lim, J. B. Koo, S. J. Yun and H.-T. Kim, *Electrochemical and Solid-State Letters* **10**, J136 (2007).
- (192) H. Kim and S. M. Rosnagel, *Thin Solid Films* **441**, 311-316 (2003).
- (193) H. Kim, S. Woo, J. Lee, H. Lee and H. Jeon, *Journal of Physics D: Applied Physics* **43**, 505301 (2010).
- (194) H. C. M. Knoops, A. J. M. Mackus, M. E. Donders, M. C. M. van de Sanden, P. H. L. Notten and W. M. M. Kessels, *Electrochemical and Solid-State Letters* **12**, G34 (2009).
- (195) S. W. Choi, C. M. Jang, D. Y. Kim, J. S. Ha, H. S. Park, W. Y. Koh and C. S. Lee, *Journal of the Korean Physical Society* **42**, 975-979 (2003).
- (196) J.-H. Kim, W.-J. Lee and S.-G. Yoon, *Integr. Ferroelectr.* **68**, 63-73 (2004).
- (197) Y. H. Kim, J. Moon, C. H. Chung, S. J. Yun, D. J. Park, J. W. Lim, Y. H. Song and J. H. Lee, *IEEE Electron Device Lett.* **27**, 896-898 (2006).
- (198) J. Choi, S. Kim, J. Kim, H. Kang, H. Jeon and C. Bae, *J. Vac. Sci. Technol. A* **24**, 900-907 (2006).
- (199) L. Wu and E. Eisenbraun, *Electrochemical and Solid-State Letters* **11**, H107 (2008).
- (200) A. W. John, D. J. Blaine, M. H. Craig, N. H. James, A. S. Ron and L. B. Corey, 1999.
- (201) H. G. Tompkins and W. A. McGahan, *Spectroscopic ellipsometry and reflectometry: a user's guide*, Wiley, 1999.
- (202) H. Fujiwara, *Spectroscopic ellipsometry: principles and applications*, John Wiley & Sons, 2007.
- (203) D. E. Aspnes, J. B. Theeten and F. Hottier, *Phys. Rev. B* **20**, 3292-3302 (1979).
- (204) J. G. E. Jellison, *Thin Solid Films* **313-314**, 33-39 (1998).
- (205) G. E. Jellison, *Thin Solid Films* **234**, 416-422 (1993).
- (206) H.-H. Perkampus, *UV-VIS Spectroscopy and its Applications*, Springer Science & Business Media, 2013.



- (207) L. Guo, X. Shen, G. Zhu and K. Chen, *Sens. Actuator B-Chem.* **155**, 752-758 (2011).
- (208) R. Steinhardt and E. Serfass, *Anal. Chem.* **23**, 1585-1590 (1951).
- (209) C. Nordling, E. Sokolowski and K. Siegbahn, *Phys. Rev.* **105**, 1676-1677 (1957).
- (210) S. Hüfner, *Photoelectron spectroscopy: principles and applications*, Springer Science & Business Media, 2013.
- (211) EAgle, [http://www.eagle-regpot.eu/EAgle-Equipment\\_XPS.html](http://www.eagle-regpot.eu/EAgle-Equipment_XPS.html).
- (212) P. Van der Heide, *X-ray photoelectron spectroscopy: an introduction to principles and practices*, John Wiley & Sons, 2011.
- (213) J. H. Thomas, C. E. Bryson and T. R. Pampalone, *Journal of Vacuum Science & Technology B: Microelectronics Processing and Phenomena* **6**, 1081-1086 (1988).
- (214) J. H. Thomas Iii, C. E. Bryson Iii and T. R. Pampalone, *Surf. Interface Anal.* **14**, 39-45 (1989).
- (215) C. Wagner, L. Gale and R. Raymond, *Anal. Chem.* **51**, 466-482 (1979).
- (216) J. F. Moulder, W. F. Stickle, P. E. Sobol and K. D. Bomben, *Handbook of X-ray photoelectron spectroscopy: a reference book of standard spectra for identification and interpretation of XPS data.* , Perkin-Elmer, Waltham, MA, 1992.
- (217) W. Priyantha, G. Radhakrishnan, R. Droopad and M. Passlack, *J. Cryst. Growth* **323**, 103-106 (2011).
- (218) J. L. Sullivan, S. O. Saied and I. Bertoti, *Vacuum* **42**, 1203-1208 (1991).
- (219) D. R. Baer, M. H. Engelhard, A. S. Lea, P. Nachimuthu, T. C. Droubay, J. Kim, B. Lee, C. Mathews, R. L. Opila, L. V. Saraf, W. F. Stickle, R. M. Wallace and B. S. Wright, *J. Vac. Sci. Technol. A* **28**, 1060-1072 (2010).
- (220) Field emission scanning electron microscope, <https://nano.mff.cuni.cz/nanomaterials-group/instruments/field-emission-scanning-electron-microscope>.
- (221) J. J. Yeh and I. Lindau, *At. Data Nucl. Data Tables* **32**, 1-155 (1985).
- (222) P. Ruffieux, P. Schwaller, O. Gröning, L. Schlapbach, P. Gröning, Q. C. Herd, D. Funnemann and J. Westermann, *Rev. Sci. Instrum.* **71**, 3634-3639 (2000).
- (223) S. Tanuma, C. J. Powell and D. R. Penn, *Surf. Interface Anal.* **21**, 165-176 (1994).
- (224) C. D. Wagner, L. E. Davis, M. V. Zeller, J. A. Taylor, R. H. Raymond and L. H. Gale, *Surf. Interface Anal.* **3**, 211-225 (1981).
- (225) A. G. Shard, *Surf. Interface Anal.* **46**, 175-185 (2014).
- (226) B. D. Ratner and D. G. Castner, *Surface analysis: the principal techniques* **2**, 374-381 (2009).
- (227) C. R. Brundle and B. V. Crist, *J. Vac. Sci. Technol. A* **38**, 041001 (2020).
- (228) G. Greczynski and L. Hultman, *Progress in Materials Science* **107**, 100591 (2020).
- (229) C. J. Powell, *J. Vac. Sci. Technol. A* **38**, 023209 (2020).

- (230) H. Shinotsuka, S. Tanuma, C. J. Powell and D. R. Penn, *Surf. Interface Anal.* **47**, 871-888 (2015).
- (231) G. A. Somorjai, *Chemistry in two dimensions: surfaces*, Cornell University Press, 1981.
- (232) M. Jo, *Surf Sci.* **320**, 191-200 (1994).
- (233) F. Schaefers, M. Mertin and M. Gorgoi, *Rev. Sci. Instrum.* **78**, 123102 (2007).
- (234) Y. J. Cho, N. V. Nguyen, C. A. Richter, J. R. Ehrstein, B. H. Lee and J. C. Lee, *Appl. Phys. Lett.* **80**, 1249-1251 (2002).
- (235) Y. Yamamoto, T. Matsuura and J. Murota, *Surf Sci.* **408**, 190-194 (1998).
- (236) J. W. Elam, C. E. Nelson, R. K. Grubbs and S. M. George, *Thin Solid Films* **386**, 41-52 (2001).
- (237) M. Pessa, O. Jylhä, P. Huttunen and M. A. Herman, *J. Vac. Sci. Technol. A* **2**, 418-422 (1984).
- (238) T. Suntola and J. Hyvarinen, *Annual Review of Materials Science* **15**, 177-195 (1985).
- (239) T. S. Suntola, A. J. Pakkala and S. G. Lindfors, *Journal*, 1983.
- (240) M. Ylilammi, *J. Electrochem. Soc.* **142**, 2474-2479 (1995).
- (241) K. Henkel, H. Gargouri, B. Gruska, M. Arens, M. Tallarida and D. Schmeißer, *J. Vac. Sci. Technol. A* **32**, 01A107 (2014).
- (242) F. Naumann, J. Reck, H. Gargouri, B. Gruska, A. Blümich, A. Mahmoodinezhad, C. Janowitz, K. Henkel and J. I. Flege, *J. Vac. Sci. Technol. B* **38**, 014014 (2020).
- (243) L. Escobar-Alarcón, E. Haro-Poniatowski, M. A. Camacho-López, M. Fernández-Guasti, J. Jiménez-Jarquín and A. Sánchez-Pineda, *Surface Engineering* **15**, 411-414 (1999).
- (244) M. Ritala, M. Leskelä, L. Niinistö, T. Prohaska, G. Friedbacher and M. Grasserbauer, *Thin Solid Films* **249**, 155-162 (1994).
- (245) A. I. Abdulagatov, Y. Yan, J. R. Cooper, Y. Zhang, Z. M. Gibbs, A. S. Cavanagh, R. G. Yang, Y. C. Lee and S. M. George, *ACS Appl. Mater. Inter.* **3**, 4593-4601 (2011).
- (246) E. Marin, L. Guzman, A. Lanzutti, W. Ensinger and L. Fedrizzi, *Thin Solid Films* **522**, 283-288 (2012).
- (247) M. Becht, T. Gerfin and K. H. Dahmen, *Chem. Mater.* **5**, 137-144 (1993).
- (248) M. Coll, J. Gazquez, A. Palau, M. Varela, X. Obradors and T. Puig, *Chem. Mater.* **24**, 3732-3737 (2012).
- (249) J. Päiväsäari, M. Putkonen and L. Niinistö, *J. Mater. Chem.* **12**, 1828-1832 (2002).
- (250) K. J. Eisentraut and R. E. Sievers, *J. Am. Chem. Soc.* **87**, 5254-5256 (1965).
- (251) H. S. Nalwa, *Handbook of thin film materials*, Academic Press, San Diego, 2002.
- (252) J. W. Klaus, S. J. Ferro and S. M. George, *Thin Solid Films* **360**, 145-153 (2000).

- (253) D.-J. Lee, J.-Y. Kwon, J. I. Lee and K.-B. Kim, *J. Phys. Chem. C* **115**, 15384-15389 (2011).
- (254) A. U. Mane, A. J. Allen, R. K. Kanjolia and J. W. Elam, *J. Phys. Chem. C* **120**, 9874-9883 (2016).
- (255) W.-H. Kim, W. J. Maeng, K.-J. Moon, J.-M. Myoung and H. Kim, *Thin Solid Films* **519**, 362-366 (2010).
- (256) J. A. Libera, J. N. Hryn and J. W. Elam, *Chem. Mater.* **23**, 2150-2158 (2011).
- (257) A. W. Ott, J. M. Johnson, J. W. Klaus and S. M. George, *Appl. Surf. Sci.* **112**, 205-215 (1997).
- (258) Q. Ma, Y. Shao, Y. Wang, H. Zheng, B. Zhu, W. Liu, S. Ding and D. W. Zhang, *IEEE Electron Device Lett.* **39**, 1672-1675 (2018).
- (259) O. Medenbach, T. Siritanon, M. A. Subramanian, R. D. Shannon, R. X. Fischer and G. R. Rossman, *Mater. Res. Bull.* **48**, 2240-2243 (2013).
- (260) R. E. Agbenyeke, E. A. Jung, B. K. Park, T.-M. Chung, C. G. Kim and J. H. Han, *Appl. Surf. Sci.* **419**, 758-763 (2017).
- (261) Q. Ma, H.-M. Zheng, Y. Shao, B. Zhu, W.-J. Liu, S.-J. Ding and D. W. Zhang, *Nanoscale Res. Lett.* **13**, 4 (2018).
- (262) L.-j. Meng and M. P. dos Santos, *Thin Solid Films* **322**, 56-62 (1998).
- (263) C. Wang, V. Cimalla, G. Cherkashinin, H. Romanus, M. Ali and O. Ambacher, *Thin Solid Films* **515**, 2921-2925 (2007).
- (264) A. Walsh, J. L. F. Da Silva, S.-H. Wei, C. Körber, A. Klein, L. F. J. Piper, A. DeMasi, K. E. Smith, G. Panaccione, P. Torelli, D. J. Payne, A. Bourlange and R. G. Egdell, *Phys. Rev. Lett.* **100**, 167402 (2008).
- (265) V. Scherer, C. Janowitz, A. Krapf, H. Dwelk, D. Braun and R. Manzke, *Appl. Phys. Lett.* **100**, 212108 (2012).
- (266) R. Sarhaddi, N. Shahtahmasebi, M. Rezaee Rokn-Abadi and M. M. Bagheri-Mohagheghi, *Physica E Low Dimens. Syst. Nanostruct.* **43**, 452-457 (2010).
- (267) Thermo Fisher Scientific X-ray photoelectron spectroscopy database, <https://www.thermofisher.com/de/de/home/materials-science/learning-center/periodic-table/lanthanide-rare-earth/cerium.html>.
- (268) Z. M. Detweiler, S. M. Wulfsberg, M. G. Frith, A. B. Bocarsly and S. L. Bernasek, *Surf Sci.* **648**, 188-195 (2016).
- (269) R. W. Hewitt and N. Winograd, *J. Appl. Phys.* **51**, 2620 (1980).
- (270) M. Z. Atashbar, B. Gong, H. T. Sun, W. Wlodarski and R. Lamb, *Thin Solid Films* **354**, 222 (1999).
- (271) D. Kim, T. Nam, J. Park, J. Gatineau and H. Kim, *Thin Solid Films* **587**, 83-87 (2015).
- (272) B. Abendroth, T. Moebus, S. Rentrop, R. Strohmeyer, M. Vinnichenko, T. Weling, H. Stöcker and D. C. Meyer, *Thin Solid Films* **545**, 176-182 (2013).
- (273) P. Malet and G. Munuera, *J. Chem. Soc. Faraday Trans.1* **85**, 4157-4166 (1989).

- (274) I. Donmez, C. Ozgit-Akgun and N. Biyikli, *J. Vac. Sci. Technol. A* **31**, 01A110 (2012).
- (275) H. Altuntas, I. Donmez, C. Ozgit-Akgun and N. Biyikli, *J. Vac. Sci. Technol. A* **32**, 041504 (2014).
- (276) E. Kobayashi, M. Boccard, Q. Jeangros, N. Rodkey, D. Vresilovic, A. Hessler-Wyser, M. Döbeli, D. Franta, S. De Wolf, M. Morales-Masis and C. Ballif, *J. Vac. Sci. Technol. A* **36**, 021518 (2018).
- (277) O. M. Bordun, I. Y. Kukharsky, B. O. Bordun and V. B. Lushchanets, *Journal of Applied Spectroscopy* **81**, 771-775 (2014).
- (278) C. V. Ramana, E. J. Rubio, C. D. Barraza, A. Miranda Gallardo, S. McPeak, S. Kotru and J. T. Grant, *J. Appl. Phys.* **115**, 043508 (2014).
- (279) K. Taniguchi, M. Tanaka, C. Hamaguchi and K. Imai, *J. Appl. Phys.* **67**, 2195-2198 (1990).
- (280) W. Rzodkiewicz and A. Panas, *Acta Phys. Pol. A* **116** (2009).
- (281) H.-P. Ma, H.-L. Lu, T. Wang, J.-G. Yang, X. Li, J.-X. Chen, J.-J. Tao, J.-T. Zhu, Q. Guo and D. W. Zhang, *J. Mater. Chem. C* **6**, 12518-12528 (2018).
- (282) C. C. Surdu-Bob, S. O. Saied and J. L. Sullivan, *Appl. Surf. Sci.* **183**, 126-136 (2001).
- (283) G. Schön, *J. Electron Spectrosc.* **2**, 75-86 (1973).
- (284) X. Zhang and S. Ptasińska, *Scientific Reports* **6**, 24848 (2016).
- (285) P. Bogusławski, E. L. Briggs and J. Bernholc, *Phys. Rev. B* **51**, 17255-17258 (1995).
- (286) S. Ghose, S. Rahman, L. Hong, J. S. Rojas-Ramirez, H. Jin, K. Park, R. Klie and R. Droopad, *J. Appl. Phys.* **122**, 095302 (2017).
- (287) M. Uenuma, R. Ando, M. Furukawa and Y. Uraoka, *physica status solidi (b)* **257**, 1900368 (2020).
- (288) J. Lim and C. Lee, *Thin Solid Films* **515**, 3335-3338 (2007).
- (289) D. Saha, A. K. Das, R. S. Ajimsha, P. Misra and L. M. Kukreja, *J. Appl. Phys.* **114**, 043703 (2013).
- (290) S. Keun Kim, C. Seong Hwang, S.-H. Ko Park and S. Jin Yun, *Thin Solid Films* **478**, 103-108 (2005).
- (291) S.-H. K. Park, C.-S. Hwang, H.-S. Kwack, J.-H. Lee and H. Y. Chu, *Electrochemical and Solid-State Letters* **9**, G299 (2006).
- (292) P. Boryło, K. Matus, K. Lukaszewicz, J. Kubacki, K. Balin, M. Basiaga, M. Szindler and J. Mikuła, *Appl. Surf. Sci.* **474**, 177-186 (2019).
- (293) E. B. Yousfi, B. Weinberger, F. Donsanti, P. Cowache and D. Lincot, *Thin Solid Films* **387**, 29-32 (2001).
- (294) P. C. Rowlette, C. G. Allen, O. B. Bromley, A. E. Dubetz and C. A. Wolden, *Chem. Vapor. Depos.* **15**, 15-20 (2009).
- (295) J. W. Elam and S. M. George, *Chem. Mater.* **15**, 1020-1028 (2003).
- (296) E. Muchuweni, T. S. Sathiaraj and H. Nyakoty, *Heliyon* **3**, e00285 (2017).
- (297) C. R. Ottermann and K. Bange, *Thin Solid Films* **286**, 32-34 (1996).

- (298) E. Bacaksiz, S. Aksu, S. Yilmaz, M. Parlak and M. Altunbaş, *Thin Solid Films* **518**, 4076-4080 (2010).
- (299) C. Muiva, S. T. Sathiaraj and K. Maabong, *Materials Science Forum* **706-709**, 2577-2582 (2012).
- (300) D. Cabrera-German, G. Molar-Velázquez, G. Gómez-Sosa, W. de la Cruz and A. Herrera-Gomez, *Surf. Interface Anal.* **49**, 1078-1087 (2017).
- (301) V. Ischenko, S. Polarz, D. Grote, V. Stavarache, K. Fink and M. Driess, *Advanced Functional Materials* **15**, 1945-1954 (2005).
- (302) S. Major, S. Kumar, M. Bhatnagar and K. L. Chopra, *Appl. Phys. Lett.* **49**, 394-396 (1986).
- (303) K. Ogata, T. Komuro, K. Hama, K. Koike, S. Sasa, M. Inoue and M. Yano, *physica status solidi (b)* **241**, 616-619 (2004).
- (304) D. Schmeißer, K. Henkel and C. Janowitz, *EPL (Europhysics Letters)* **123**, 27003 (2018).
- (305) E. Przeździecka, Ł. Wachnicki, W. Paszkowicz, E. Łusakowska, T. Krajewski, G. Łuka, E. Guziewicz and M. Godlewski, *Semicond. Sci. Technol.* **24**, 105014 (2009).
- (306) M. Chen, X. Wang, Y. H. Yu, Z. L. Pei, X. D. Bai, C. Sun, R. F. Huang and L. S. Wen, *Appl. Surf. Sci.* **158**, 134-140 (2000).
- (307) Z. G. Wang, X. T. Zu, S. Zhu and L. M. Wang, *Physica E Low Dimens. Syst. Nanostruct.* **35**, 199-202 (2006).
- (308) J.-M. Lee, K.-K. Kim, S.-J. Park and W.-K. Choi, *Appl. Phys. Lett.* **78**, 3842-3844 (2001).
- (309) S. Lian, H. Yang, J. J. Terblans, H. C. Swart, J. Wang and C. Xu, *Thin Solid Films* **721**, 138545 (2021).
- (310) Y. H. Hwang and B.-S. Bae, *J. Display Technol.* **9**, 704-709 (2013).
- (311) Y.-S. Min, C.-J. An, S.-K. Kim, J.-W. Song and C.-S. Hwang, *Bulletin of the Korean Chemical Society* **31**, 2503-2508 (2010).
- (312) M. Fang, L. Qi, C. Zhang and Q. Chen, *J. Mater. Sci.: Mater. Electron.* **27**, 10252-10258 (2016).
- (313) S.-M. Yoon, N.-J. Seong, K. Choi, G.-H. Seo and W.-C. Shin, *ACS Appl. Mater. Inter.* **9**, 22676-22684 (2017).
- (314) Y. Shin, S. T. Kim, K. Kim, M. Y. Kim, S. Oh and J. K. Jeong, *Scientific Reports* **7**, 10885 (2017).
- (315) J. Sheng, T. Hong, H.-M. Lee, K. Kim, M. Sasase, J. Kim, H. Hosono and J.-S. Park, *ACS Appl. Mater. Inter.* **11**, 40300-40309 (2019).
- (316) M. H. Cho, M. J. Kim, H. Seul, P. S. Yun, J. U. Bae, K.-S. Park and J. K. Jeong, *Journal of Information Display* **20**, 73-80 (2019).
- (317) K. Ide, M. Kikuchi, M. Ota, M. Sasase, H. Hiramatsu, H. Kumomi, H. Hosono and T. Kamiya, *Jpn. J. Appl. Phys.* **56**, 03BB03 (2017).
- (318) V. E. Henrich and P. A. Cox, *The surface science of metal oxides*, Cambridge university press, 1996.
- (319) R. J. Lad, *Surface Review and Letters* **02**, 109-126 (1995).

- (320) M. P. Seah, in *Practical Surface Analysis*, eds. D. Briggs and M. P. Seah, John Wiley and Sons, Chichester, 2 edn., 1990, vol. 1, ch. 5, p. 245.
- (321) C. D. Wagner, A. V. Naumkin, A. Kraut-Vass, J. W. Allison, C. J. Powell and J. R. Rumble Jr, NIST standard reference database 20, <http://srdata.nist.gov/xps/>).
- (322) J. Musschoot, Q. Xie, D. Deduytsche, S. Van den Berghe, R. L. Van Meirhaeghe and C. Detavernier, *Microelectron. Eng.* **86**, 72-77 (2009).
- (323) R. Matero, A. Rahtu, M. Ritala, M. Leskelä and T. Sajavaara, *Thin Solid Films* **368**, 1-7 (2000).
- (324) I. Iatsunskiy, M. Kempniński, M. Jancelewicz, K. Załęski, S. Jurga and V. Smyntyna, *Vacuum* **113**, 52-58 (2015).
- (325) M. E. Simonsen, C. Sønderby, Z. Li and E. G. Søgaard, *Journal of Materials Science* **44**, 2079-2088 (2009).
- (326) L. G. Gosset, J. F. Damlencourt, O. Renault, D. Rouchon, P. Holliger, A. Ermolieff, I. Trimaille, J. J. Ganem, F. Martin and M. N. Séméria, *J. Non-Cryst. Solids* **303**, 17-23 (2002).
- (327) T. Henke, M. Knaut, C. Hossbach, M. Geidel, M. Albert and J. W. Bartha, *Surf. Coat. Tech.* **309**, 600-608 (2017).
- (328) A. C. Dillon, A. W. Ott, J. D. Way and S. M. George, *Surf Sci.* **322**, 230-242 (1995).
- (329) S. K. Kim, S. W. Lee, C. S. Hwang, Y.-S. Min, J. Y. Won and J. Jeong, *J. Electrochem. Soc.* **153**, F69 (2006).
- (330) O. Renault, L. G. Gosset, D. Rouchon and A. Ermolieff, *J. Vac. Sci. Technol. A* **20**, 1867-1876 (2002).
- (331) V. Naumann, M. Otto, R. B. Wehrspohn and C. Hagendorf, *J. Vac. Sci. Technol. A* **30**, 04D106 (2012).
- (332) Y. J. Cho, K.-B. Chung and H. S. Chang, *Thin Solid Films* **649**, 57-60 (2018).
- (333) W. Suk Yang, Y. Kwan Kim, S.-Y. Yang, J. Hwak Choi, H. Soo Park, S. In Lee and J.-B. Yoo, *Surf. Coat. Tech.* **131**, 79-83 (2000).
- (334) D. Wilson, R. Williams and R. Pond, *Surface and Interface Analysis: An International Journal devoted to the development and application of techniques for the analysis of surfaces, interfaces and thin films* **31**, 385-396 (2001).
- (335) N. Vandecasteele and F. Reniers, *J. Electron Spectrosc.* **178**, 394-408 (2010).
- (336) R. Liang, X. Su, Q. Wu and F. Fang, *Surf. Coat. Tech.* **131**, 294-299 (2000).
- (337) V. Naumann, M. Otto, R. B. Wehrspohn, M. Werner and C. Hagendorf, *Energy Procedia* **27**, 312-318 (2012).
- (338) J. L. van Hemmen, S. B. S. Heil, J. H. Klootwijk, F. Roozeboom, C. J. Hodson, M. C. M. van de Sanden and W. M. M. Kessels, *J. Electrochem. Soc.* **154**, G165-G169 (2007).

- (339) E. Ghiraldelli, C. Pelosi, E. Gombia, G. Chiavarotti and L. Vanzetti, *Thin Solid Films* **517**, 434-436 (2008).
- (340) R. L. Puurunen, A. Root, S. Haukka, E. I. Iiskola, M. Lindblad and A. O. I. Krause, *J. Phys. Chem. B* **104**, 6599-6609 (2000).
- (341) Q.-Y. Shao, A.-D. Li, H.-Q. Ling, D. Wu, Y. Wang, Y. Feng, S.-Z. Yang, Z.-G. Liu, M. Wang and N.-B. Ming, *Microelectron. Eng.* **66**, 842-848 (2003).
- (342) S. Deshpande, S. Patil, S. V. N. T. Kuchibhatla and S. Seal, *Appl. Phys. Lett.* **87**, 133113 (2005).
- (343) D. R. Mullins, S. H. Overbury and D. R. Huntley, *Surf Sci.* **409**, 307-319 (1998).
- (344) Y. A. Teterin, A. Y. Teterin, A. M. Lebedev and I. O. Utkin, *J. Electron Spectrosc.* **88-91**, 275-279 (1998).
- (345) L. Qiu, F. Liu, L. Zhao, Y. Ma and J. Yao, *Appl. Surf. Sci.* **252**, 4931-4935 (2006).
- (346) E. Paparazzo, G. M. Ingo and N. Zacchetti, *J. Vac. Sci. Technol. A* **9**, 1416-1420 (1991).
- (347) P. Burroughs, A. Hamnett, A. F. Orchard and G. Thornton, *Journal of the Chemical Society, Dalton Transactions*, DOI: 10.1039/DT9760001686, 1686-1698 (1976).
- (348) M. Romeo, K. Bak, J. El Fallah, F. Le Normand and L. Hilaire, *Surf. Interface Anal.* **20**, 508-512 (1993).
- (349) A. Kotani, T. Jo and J. C. Parlebas, *Adv. Phys.* **37**, 37-85 (1988).
- (350) A. Gupta, T. S. Sakthivel, C. J. Neal, S. Koul, S. Singh, A. Kushima and S. Seal, *Biomaterials Science* **7**, 3051-3061 (2019).
- (351) C. Anandan and P. Bera, *Appl. Surf. Sci.* **283**, 297-303 (2013).
- (352) S. Vangelista, R. Piagge, S. Ek, T. Sarnet, G. Ghidini and A. Lamperti, *MRS Advances* **2**, 3005-3010 (2017).
- (353) J. I. Flege, B. Kaemena, J. Höcker, F. Bertram, J. Wollschläger, T. Schmidt and J. Falta, *Appl. Phys. Lett.* **104**, 131604 (2014).
- (354) K. Bak and L. Hilaire, *Appl. Surf. Sci.* **70-71**, 191-195 (1993).
- (355) A. Allahgholi, J. I. Flege, S. Thieß, W. Drube and J. Falta, *ChemPhysChem* **16**, 1083-1091 (2015).